

UNIVERSITÀ DEGLI STUDI DI NAPOLI FEDERICO II

DIPARTIMENTO DI SCIENZE DELLA TERRA, DELL'AMBIENTE E DELLE RISORSE



**PH.D. IN
EARTH SCIENCE, ENVIRONMENT AND RESOURCES
XXIX CICLO**

PH.D THESIS

**ANCIENT ROMAN MORTARS: MIX DESIGN,
MINERALOGICAL COMPOSITION AND MINEROGENETIC
SECONDARY PROCESSES**

TUTOR

PROF. PIERGIULIO CAPPELLETTI

COTUTOR

PROF. VINCENZO MORRA

DR. EMANUELE GOTTI

Ph.D CANDIDATE

CONCETTA RISPOLI

2014-2017

TABLE OF CONTENTS

Abstract	4
Introduction	5
Chapter 1. Geological outlines of studied archaeological sites	8
1.1 Campania geological setting	8
1.2 Bay of Naples.....	11
1.2.1 Campi Flegrei.....	12
1.2.2 Sarno River plain	13
1.2.3 Sorrento Peninsula	15
Chapter 2. Archaeological background	17
2.1 Piscina Mirabilis	17
2.2 Terme di Baie.....	23
2.3 Villa del Capo	31
2.4 Villa del Pezzolo	34
Chapter 3. Analytical methods	37
3.1 Optical studies and modal analysis on thin sections	37
3.2 Sample pretreatment according to UNI 11305	39
3.3 X-Ray Powder Diffraction analysis (XRPD)	40
3.4 Scanning electron microscopy (SEM) and Microanalyses (EDS)	43
3.5 X-RAY Fluorescence (XRF)	47
3.6 Thermal analysis	50
3.7 Mercury intrusion porosimetry (MIP)	52
Chapter 4. <i>Piscina Mirabilis</i>: materials and results	55
4.1 Materials	55
4.2 Results.....	57
4.2.1 Macroscopic observation	57
4.2.2 Petrography	58

4.2.3 XRPD analysis	66
4.2.4 Micro-morphology and chemical analysis (SEM-EDS).....	68
4.2.5 XRF analysis.....	78
4.2.6 X-ray Differential and Gravimetric Thermal Analysis (DTA-TGA)	79
4.2.7 Mercury intrusion porosimetry (MIP)	82
Chapter 5. Terme di Baia: materials and results.....	85
5.1 Materials	85
5.2 Results.....	88
5.2.1 Macroscopic observation	88
5.2.2 Petrography	89
5.2.3 XRPD analysis	93
5.2.4 Micro-morphology and chemical analysis (SEM-EDS).....	95
5.2.5 XRF analysis.....	104
5.2.6 X-ray Differential and Gravimetric Thermal Analysis (DTA-TGA)	105
5.2.7 Mercury intrusion porosimetry (MIP)	108
Chapter 6. Villa del Capo: materials and results.....	110
6.1 Materials	110
6.2 Results.....	111
6.2.1 Macroscopic observation	111
6.2.2 Petrography	113
6.2.3 XRPD analysis	121
6.2.4 Micro-morphology and chemical analysis (SEM-EDS).....	124
6.2.5 XRF analysis.....	133
6.2.6 Differential and Gravimetric Thermal Analysis (DTA-TGA)	135
6.2.7 Mercury intrusion porosimetry (MIP)	138
Chapter 7. Villa del Pezzolo: materials and results	140
7.1 Materials	140
7.2 Results.....	141
7.2.1 Macroscopic observation	141
7.2.2 Petrography	143
7.2.3 XRPD analysis	149

7.2.4 Micro-morphology and chemical analysis (SEM-EDS).....	152
7.2.5 XRF analysis.....	163
7.2.6 Differential and Gravimetric Thermal Analysis (DTA-TGA)	164
7.2.7 Mercury intrusion porosimetry (MIP)	167
Chapter 8. Standard hydraulic mortar.....	169
8.1 Realization	169
8.2 Results.....	170
8.2.1 Differential and Gravimetric Thermal Analysis (DTA-TGA)	170
8.2.2 Mercury intrusion porosimetry (MIP)	172
Chapter 9. Discussions	173
Chapter 10. Conclusions.....	184
Acknowledgments.....	187
Bibliography.....	188

ABSTRACT

Aim of this study is the characterization of ancient Roman mortars collected in a) *Piscina Mirabilis*, b) *Terme di Baia*, c) *Villa del Capo* (commonly called *Bagni della Regina Giovanna*) and d) *Villa del Pezzolo* sites. All investigated location are placed in two important geological, archaeological and historical areas of Campania Region: *Campi Flegrei* and *Sorrento Peninsula*.

Goals of this research project were: a) to improve the knowledge of Roman construction techniques by means of detailed microstructural and compositional examination of 1) cementitious binding matrix and 2) aggregates, to point out both mortars' mix-design and provenance of raw materials, along with b) the study of secondary minerogenetic processes and c) comparing the obtained results with the modern mortars.

Thanks to the permission by Superintendence of Archeological Heritage of Campania, it was possible to take out small, non-invasive, and representative samples of mortars.

The collected samples were used for an integrated analytical program using multiple methodologies such as: optical microscopy (OM) on thin sections, X-ray powder diffraction (XRPD), scanning electron microscopy analysis (SEM), energy-dispersion X-ray spectroscopy (EDS), X-ray fluorescence (XRF), thermal analyses (TGA-DTA) and mercury intrusion porosimetry (MIP). This research activity was performed in collaboration with CTG (Group Technical Center) of Italcementi Heidelberg Group at Bergamo (Italy).

Results have shown that building materials used in studied archaeological sites had a local provenance, and are very well consistent with the surrounding geological setting.

A relevant characteristic detected in all samples is the evident hydraulicity of these mortars, as shown by the reaction rims of pozzolanic materials; this feature is supported by the Hydraulicity Index and thermal analyses investigations.

Extremely interesting is composition of cementitious binding matrix characterized by various products of reaction, including amorphous gel-C-A-S-H, calcite, tobermorite (*Piscina Mirabilis* samples) and hydrocalumite (*Villa del Capo* samples). In particular, these two late secondary minerogenetic products fill pore space and thus enhancing bonding in pumice clasts.

The difference between ancient Roman mortars and modern hydraulic mortar was mainly related to porosity.

keywords: ancient Roman mortars, mineralogical and petrographic analysis, *Campi Flegrei*, *Somma Vesuvius*, standard hydraulic mortars.

Introduction

Since ancient times humans made mortars, artificial products deriving from transformed geological materials. Mortars are composite materials, consisting of hydraulic or aerial binding material, aggregates and additives, passive or active, which react with the binding material and are modified during their setting (Moropoulou et al., 2000).

Their use has been various, such as for the production of bedding mortar in the masonry buildings, the frescoes and decorations realization using the most valuable mortars, the concretes production for maritime constructions etc.... The large use of these materials was not simply based on the development of their specific functions but also from the historical period and location where they were made.

The excellent preservation state of many products made in the Roman period demonstrates the high technological level achieved by these construction workers.

Although evidences (*Plino il Vecchio*) show that Egyptians knew “the way” to produce lime, it began largely used by Greeks and especially by Romans that diffused it since the third century. B.C. (Collepari, 2003). A lot of documents about the acquired knowledge in the construction field have been passed down thanks to these civilizations. Several writers have treated the building art of the roman builders such as: Cato in *De Agricola* (160 B.C.), M. Vitruvius Pollio (I century B.C.), in the ten books of *De Architectura* and Plinio il Vecchio (23 - 9 A.D.) with the treat called *Naturalis Historia*.

The roman builders knew that thanks to the combination of lime with special volcanic deposits (*pozzolana*), mortar became hydraulic allowing the underwater hardening and also giving greater mechanical strength to it (Collepari, 2003). The use of *pozzolana* marked a revolutionary progress in the construction, due to the ability of mixture to cure also underwater (hydraulic limes) and with a higher speed than that required by the carbonation process of slaked lime. When the volcanic material was not available, they were implied fragments of artificial materials such as bricks and ceramics, which have the same hydraulic properties of *pozzolana*.

Roman mortars have been object of many archaeometric scientific studies. Some works were focused on the mineralogical and petrographic features of the mortar constituents to go back at the old production technology used by the Roman builders (Sanchez-Moral et al., 2004; Moropoulou et al., 2005; Silva, 2005; Jackson and Marra, 2006; Belfiore et al., 2009, Jackson et al., 2009, 2010). Other works were based on the study of hydraulic properties of *pozzolana*, with details of the processes leading to the formation of hydrated phases such as calcium silicate

hydrate (CSH) and calcium aluminate hydrate (CAH) (Massazza 2001; Moropoulou et al., 2004; Jackson et al., 2006; Fernández et al. 2010).

The aims of this research project were: a) improve the knowledge of Roman construction techniques by means of detailed microstructural and compositional examination of 1) cementitious binding matrix and 2) aggregates, to point out both mortars' mix-design and provenance of raw materials, along with b) the study of secondary minerogenetic processes and c) comparing the obtained results with the modern mortars.

Several archaeological sites were chosen for mortars sampling, in particular those related both to ancient Roman structures built in subaerial environment, submerged later on by seawater, and structures which had been in contact for long times with "fresh" water (e.g. thermal baths and cisterns). Such Roman structures are located in the Baia area (*Piscina Mirabilis* and *Terme di Baia*) and all along the Sorrento coast (*Villa del Capo* or *Bagni della Regina Giovanna* at Massa Lubrense and *Villa del Pezzolo* at Seiano) (Figure 1).



Figure 1: archaeological site location.

Due to the complexity and the importance of archaeological sites the sampling was an crucial step of the study for meaningful analytical results.

The sampling was achieved in cooperation with archaeologists and thanks to authorization and the supervision of Archaeological Superintendence of Campania (courtesy of Dr. Budetta and Dr. Talamo).

They were taken 45 samples (13 *Piscina Mirabilis*; 9 *Terme di Baia*; 13 *Villa del Capo*; 10 *Villa del Pezzolo*) for which it was necessary to follow specific criteria such as little invasiveness,

representativeness and limited samples size and visual impact; a photographic campaign before and after sampling was also carried out to witness the sampling procedure.

Besides, it was done an archive research at Superintendence offices to be aware about the areas which were object of a restoration work.

The collected samples were used for an integrated analytical program using multiple methodologies such as: optical microscopy (OM) on thin sections, X-ray powder diffraction (XRPD), scanning electron microscopy analysis (SEM), energy-dispersion X-ray spectroscopy (EDS), X-ray fluorescence (XRF), thermal analyses (TGA-DTA) and mercury intrusion porosimetry (MIP). This research activity was performed in collaboration with CTG (Group Technical Center) of Italcementi Heidelberg Group at Bergamo (Italy).

The study of these geomaterials is very interesting to understand the "secrets" of such enduring resistance; because actually the cisterns or *Villae* built by the Romans resisted over two thousand years to the strength of waves and weathering of seawater. They are a tangible example of a transformation product of geological materials (namely geomaterials) that can last so long during the eras.

Even today the concept of "durability" is of great interest. The current concrete technologists trying constantly to improve their formulations to achieve new special concrete to be able to resist to the aggressive agents such as seawater and sulphates.

Chapter 1

Geological outlines of studied archaeological sites

The Roman structures of interest are located in Campania Region in particular all along the Campania coast from Baia (*Campi Flegrei*) to Punta Campanella (Sorrento Peninsula).

The geological settings and lithostratigraphy described hereafter are mainly represented by geomaterials such as those used in the past as raw materials for mortars productions.

1.1 Campania geological setting

The geology of Campania is dominated by the Southern Apennine chain located between the Central Apennine chain to the north and the Calabria-Peloritani Terrane to the south (Bonardi et al., 2009) (Figure 1.1). Apennine Platform domain (Mostardini and Merlini, 1986; Bonardi et al., 2009; Cosentino et al., 2010; Vitale et al., 2016) includes several basins to platform Middle Triassic to Lower Miocene successions. At shallow-crustal scale, they are tectonically sandwiched between the basin successions of the Ligurian Accretionary Complex (Vitale et al. 2016) on the top, and the Lagonegro–Molise basin units at the bottom, in turn overlying the buried Apulian carbonates (Figure 1.1). The Apennine orogeny was the result of the closure of the Ligurian basin, characterized by deep basin deposits overlying an oceanic to thinned continental lithosphere, with the subduction of the westernmost area beneath the European Plate starting from the Eocene (e.g. Jolivet et al., 2003; Rosenbaum and Lister 2004; Vignaroli et al., 2009; Carminati et al., 2012; Vitale et al., 2016). In the Late Oligocene, the ocean–continent transition (OCT) succession of the Frido unit (Bonardi et al., 1988; Vitale et al., 2016) was firstly subducted, reaching very low-temperature/high-pressure (VLT/HP) metamorphic conditions and then tectonically exhumed before the middle Tortonian. On the contrary, the easternmost Ligurian successions were frontally accreted and detached from their Mesozoic basements in the Burdigalian (Ciarcià et al. 2012). In the Middle-Late–Miocene, the Apennine platform and Lagonegro–Molise basin realms were dominantly affected by thick- and thin-skinned tectonics, respectively (Vitale et al., 2016). The Lagonegro–Molise basin was completely closed in the uppermost Miocene with the overthrusting of the allochthonous wedge onto the Apulian platform carbonates. Subsequently, the Early Pliocene to Middle Pleistocene ramp-dominated thrust faults deformed the buried Apulian carbonates. The Eocene to Middle Pleistocene tectonic evolution of the southern Apennines is characterized by some crucial stages that sensibly controlled the kinematics of this orogen (e.g., Faccenna et al., 2001; Roure et al., 2012; Mazzoli et al. 2014;

Vitale et al., 2016). Following an early period related to the subduction of oceanic-OCT lithosphere, the Early Miocene thrust migration rate increased concurrently with (1) the frontal accretion of non-metamorphic Ligurian Accretionary Complex successions, essentially driven by the downgoing lithosphere roll-back (Malinverno and Ryan, 1986; Faccenna et al., 1996); (2) the opening of the Ligurian–Provençal back-arc basin and (3) the counterclockwise rotation of the Sardinia–Corsica block. In the Middle Miocene, the tectonic wedge migration rate suffered a drop with the end of the rotation of the Sardinia–Corsica block. This abrupt change was possibly a consequence of the termination of the down going slab penetration beyond the 660 km transition zone in the lower mantle (Faccenna et al., 2001). In the Late Miocene, the extension-shortening system eastward shifted, as recorded by: (1) the Tyrrhenian basin opening; (2) the tectonic imbrication of the easternmost side of the Apennine Platform domain and (3) the closure of the Lagonegro–Molise basin. In this stage the thrust front rate achieved the maximum values (Vitale et al., 2016). The Miocene–Pliocene transition marks a critical step in the orogenic evolution of the southern Apennines. In this period several geodynamic events occurred, including: (1) the break-off of the downgoing slab with the rebound and uplift of the chain and the SE migration of the lithosphere tear, starting from the Early Pliocene from the northern area of the southern Apennines (Ascione et al. 2012); (2) the subsequent interruption of the roll-back mechanism. As consequence, (1) and (2) produced: (3) the docking of the allochthonous prism onto the western margin of the Apulian platform with a fall of horizontal velocities and an increase in exhumation rates (as reconstructed by thermochronological data; Mazzoli et al. 2008); (4) the transition from a thin to a thick tectonics, with the inversion as thrust faults of inherited normal faults in the buried Apulian carbonates (Shiner et al. 2004).

Finally, in the Middle Pleistocene the crustal thickening, in the external area of the southern Apennines, ended. Subsequently, extensional structures related to the Tyrrhenian Sea opening overprinted the entire chain. The tectonic vergences resulting from the kinematic analysis on thrust faults, folds, and stretching lineations (Vitale et al., 2016) indicate dominant E/SE and E/NE vergences (in the present coordinates), respectively, for Lower Miocene and Plio-Pleistocene. However, several studies described regional to local shortening structures characterized by unusual vergences ranging from NW to NNE, frequently described as out-of-sequence thrusts (Vitale et al., 2016).

These structures are located in the carbonates of the Apennine domain, commonly involving the Miocene-earliest Pliocene thrust-top deposits.

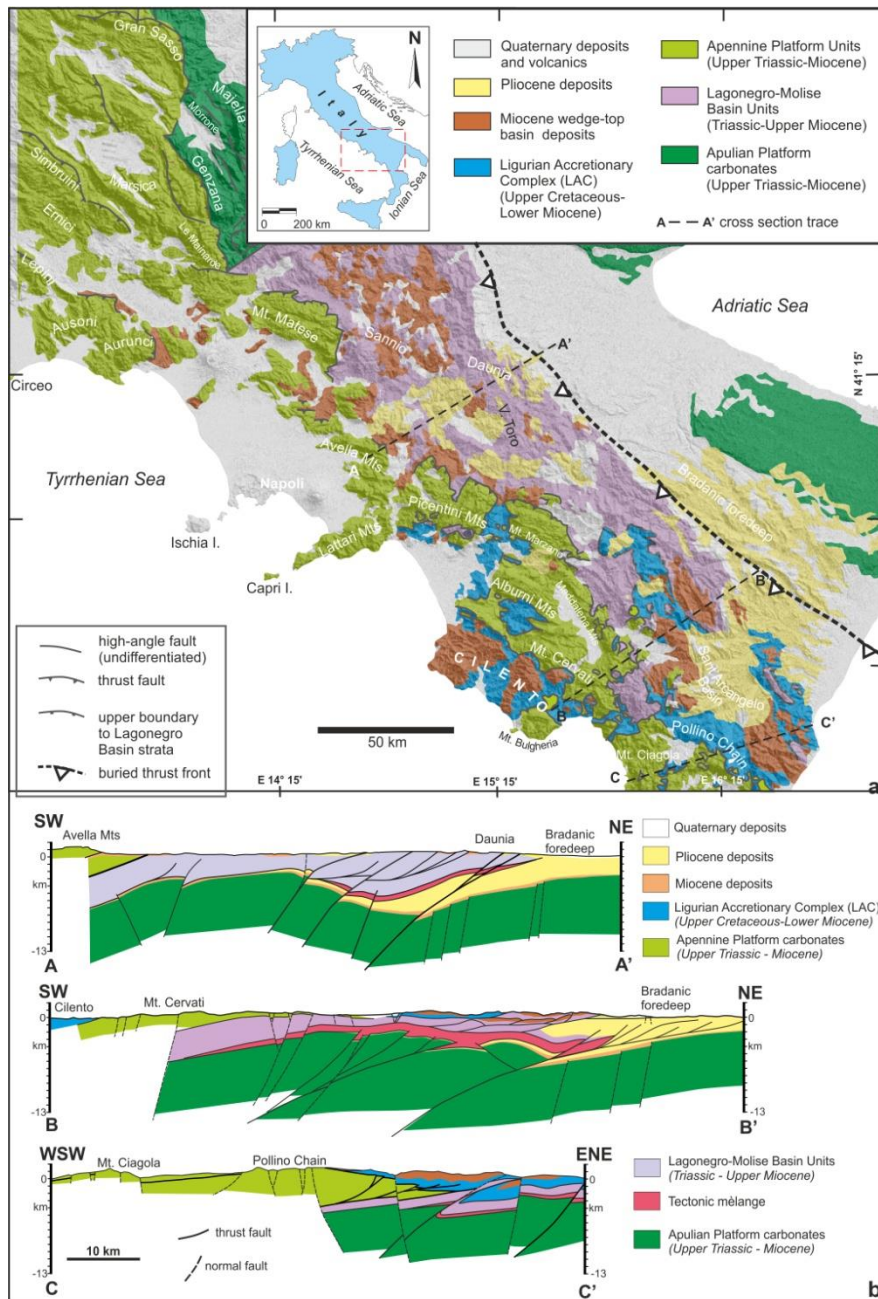


Figure 1.1: Geological sketch map and southern Apennine geological sections (Vitale et al., 2016).

1.2 Bay of Naples

The Bay of Naples area as defined here extends from ancient Cumae to Stabiae (Figure 1.2), also considering the *Campi Flegrei* and the peri-Vesuvian area (De Bonis et al., 2016).

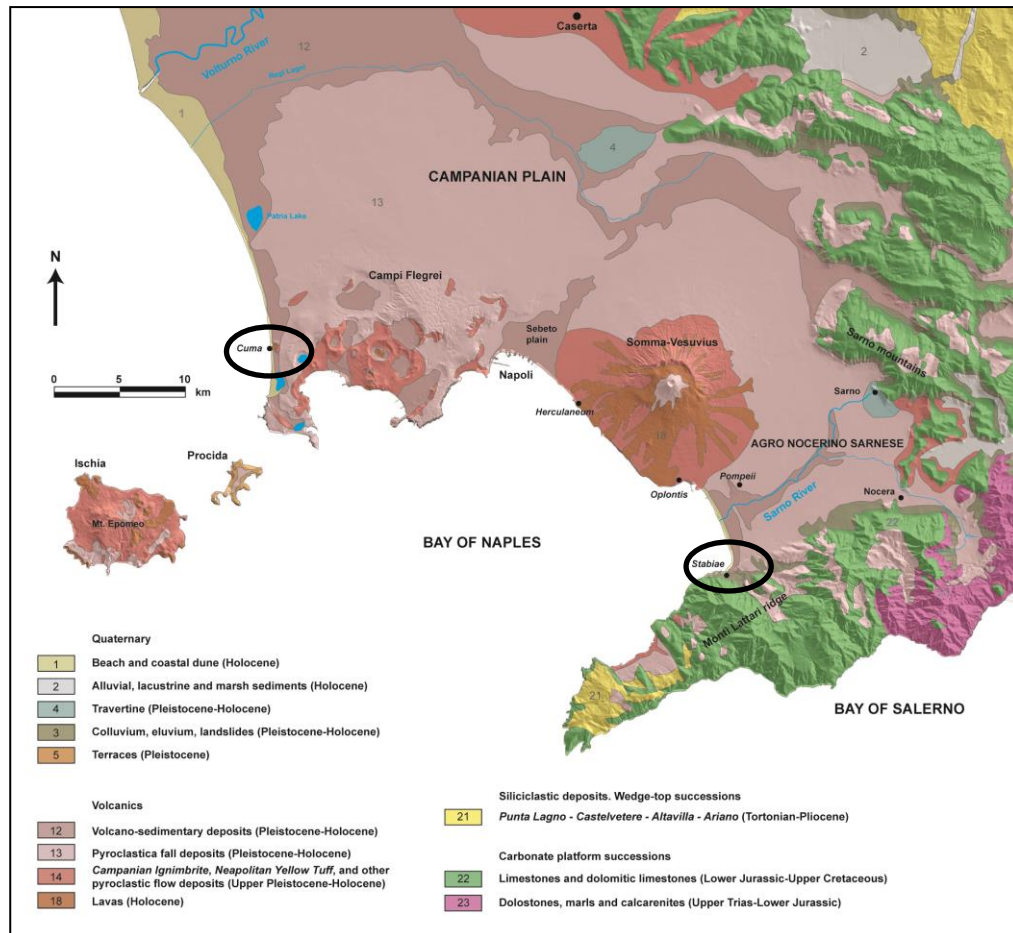


Figure 1.2: Geological sketch map of the Bay of Naples (De Bonis et al., 2016).

The area is comprised in the southern area of the Campanian Plain, a structural depression including the Volturno river floodplain ridge to the N, the Southern Apennine chain to the N/E, the Sarno Mountains to the E, and by the Monti Lattari ridge to the S. During the Quaternary period, alluvial and volcanic sediments filled the area. While volcanic deposits provide the main sediment supply for the Campanian Plain, they also cover the surrounding mountain slopes, occasionally leading to the generation of hazardous debris flows for the urban settlements located at foothills (De Vita et al., 2012). All along the Bay of Naples these deposits can vary in their composition as a function of the nearby outcropping lithologies.

Due to the different sources of sediments present in the surroundings of the Campanian Plain, volcanics fragments are mixed with detrital quartz/carbonate bearing sediments in the northern area of *Campi Flegrei* and with carbonates only on the southern area of the bay.

Moreover, volcanic products in the Bay of Naples area can be distinguished by their petrographic composition. Sediments from *Campi Flegrei* are mostly composed by alkali feldspar (sanidine), clinopyroxene (diopside/salite), trachytic scoriae, pumice and biotite, whereas in the Somma-Vesuvius area they also contain leucite and garnet (Morra et al., 2013).

The Bay of Naples is one of the most important archaeological areas of Italy and, due to its fertile soils, propitious climate and geomorphology, has always been an optimum location for human settlements since pre-historic times (Grifa et al., 2013).

1.2.1 *Campi Flegrei*

The *Campi Flegrei* area is a volcanic field located immediately W of the city of Naples (Figure 1.3). Its volcanic history was characterized by a great number of eruptions of mainly monogenetic edifices, which emplaced huge volumes of pyroclastic rocks and very sporadic lava flows. In particular, two high-magnitude eruptions, that of the Campanian Ignimbrite (39 ka) (De Vivo et al., 2001; Fedele et al., 2008) and that of the Neapolitan Yellow Tuff (15.4 ka) (Deino et al., 2004) emplaced the largest amount of products, also forming a large caldera (Morra et al., 2010).

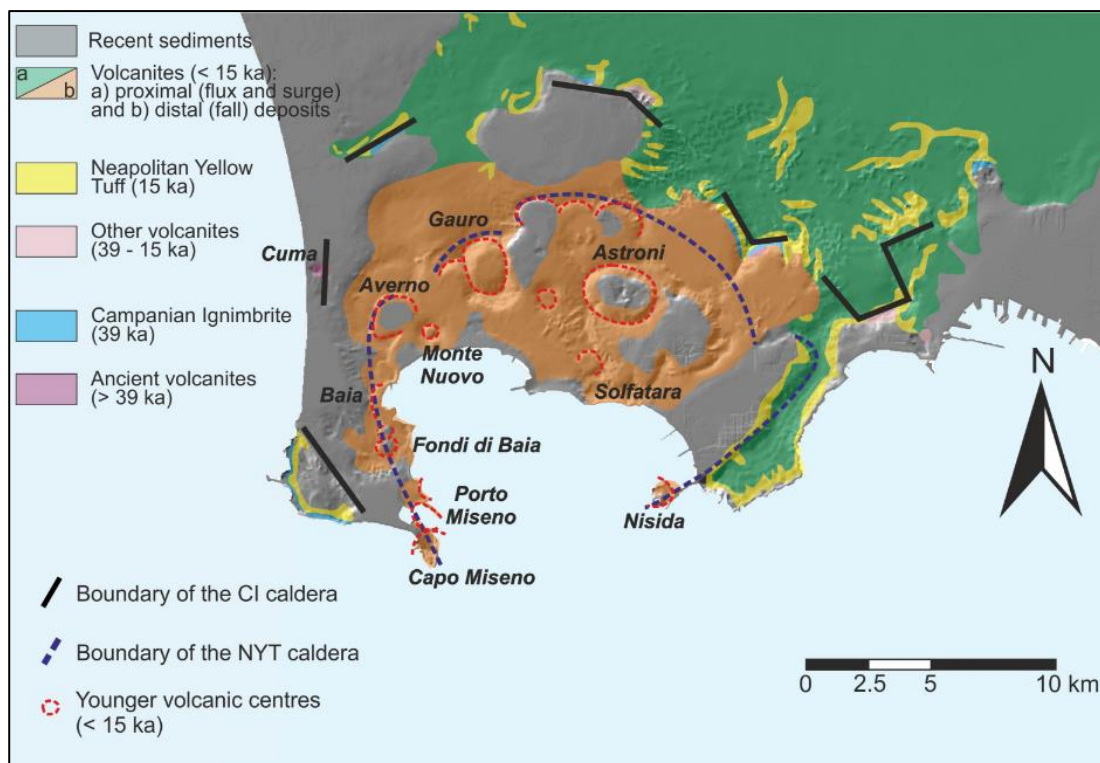


Figure 1.3: Geological sketch map of *Campi Flegrei* (Morra et al., 2010).

From a petrological point of view, Phlegraean products belong to shoshonitic series, among which trachytes are the most common lithotype. The main mineral phases are clinopyroxene, plagioclase, sanidine, biotite and magnetite; olivine is present only in the less evolved rocks. The accessory minerals are zircon, brown amphibole and titanite, whereas nepheline and exotic minerals can be found in the most evolved products (Melluso et al., 2012).

Phlegraean volcanism also includes the activity developed on the islands of Ischia and Procida. The two islands are characterised by volcanological and petrological similarities with the continental area of *Campi Flegrei* (Morra et al., 2010).

1.2.2 Sarno River plain

The Sarno floodplain, also known as Agro Nocerino-Sarnese, is the Southern part of the Campanian Plain. The area is dominated by the Somma-Vesuvius central volcanic complex and is bordered by the Sarno Mountains to the N/E and by the Monti Lattari ridge to the South, both formed by Meso-Cenozoic carbonates (Figure 1.4). These mountains are mantled by colluvium with interbedded fallout deposits. Alluvial fan sedimentation has been active in the plain during the Late Pleistocene period to the Holocene period, emplacing principally volcanoclastic and carbonate deposits (Zanchetta et al., 2004). The area has ever been an optimum for human settlements since pre-historic times, due to its fertile soils and propitious climate. At present it is one of the most densely inhabited areas of the world, lying just in the surroundings of an active volcano (Somma- Vesuvius).

Somma-Vesuvius is a stratovolcano formed by an alternation of effusive and explosive eruptions, and Mount Somma represents the oldest volcano, which concluded its activity with the formation of a caldera, where Vesuvius successively formed. The history of SommaVesuvius is marked by four major Plinian eruptions (22 ka “Pomici di Base”, 89 ka “Mercato Pumice”, 43 ka “Avellino Pumice” and AD 79 “Pompeii Pumice”), whose pyroclastic deposits are widely dispersed in the surrounding area (Santacroce et al., 2008). The first historical Plinian eruption, recorded in the archaeological layers and largely used as a stratigraphic marker for the Bronze Age, is the “Avellino Pumice” eruption (4300 ka), which deposited large volumes of pyroclastic falls and flows, resulting in a significant hiatus in the occupation of the Southern Campanian Plain (Laforgia et al., 2009). The A.D. 79 is the most known historic event, directly observed by Plinius the Younger, who carefully described the catastrophic eruption destroying the cities of Pompeii, Herculaneum, Oplontis, Stabiae and other minor settlements. Successively, two subplinian events, the AD 472 Pollena eruption and the AD 1631, also had a strong impact on the area. Then

the volcano entered its period of modern activity, characterized by semi persistent, mild activity up to the 20th century (AD 1944) (Marturano et al., 2009). From a petrological point of view the Somma-Vesuvius products show alkaline potassic affinity ranging from slightly (KS) to strongly silica-undersaturated (HKS) (Conticelli et al., 2004). Slightly undersaturated rocks range in composition from K-trachybasalts to trachytes, characterized by plagioclase and clinopyroxene (plus olivine and leucite in the less evolved products, biotite, K-feldspar and amphibole in the intermediate/evolved ones).

The rocks of the mildly undersaturated series are represented by phonotephrites, tephriphonolites, and phonolites with phenocrysts of plagioclase, clinopyroxene and leucite (plus K-feldspar and biotite in the most evolved tephriphonolites and phonolites). The highly undersaturated rocks range from leucite-tephrite to leucite-phonolite, generally showing strongly porphyritic textures characterized by phenocrysts of clinopyroxene, plus minor leucite and olivine. Garnet is a common accessory phase (Morra et al., 2010).

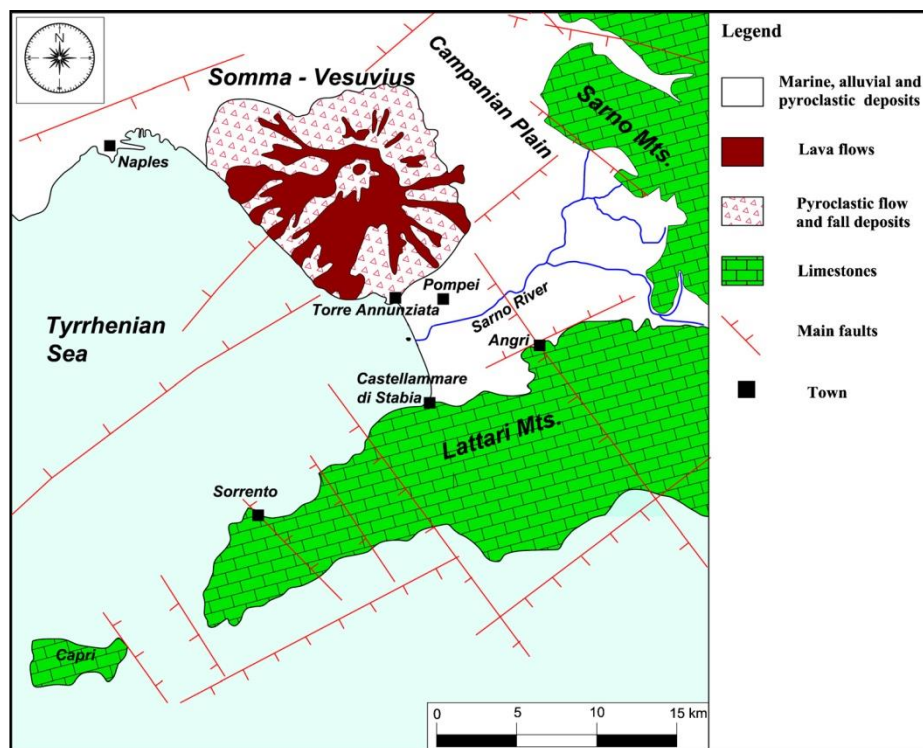


Figure 1.4: Geological sketch map of Sarno River plain (modified after Di Maio et al., 2014).

1.2.3 Sorrento Peninsula

The Sorrento Peninsula is a WSW–ENE elongated horst and lowered to the west, which separates two semi-grabens, the Gulf of Naples in the Campania Plain to the North, and the Gulf of Salerno in Sele Plain to the south (Cinque and Robustelli, 2009; Pappone et al., 2010; Aucelli et al., 2016) (Figure 1.5).

The structural framework is characterized by NW dipping homoclinal blocks which are dissected by faults with NW–SE, NE–SW and E–W trends (Brancaccio et al., 1991; Carannante et al., 2000).

The structural setting is the result of Late Miocene–Pliocene compressive tectonics and of the subsequent Plio-Quaternary transcurrent and extensional tectonics (Brancaccio et al., 1991; Iannace et al., 2015; Aucelli et al., 2016).

Mesozoic carbonate platform limestones and subordinated dolostones of Upper Cretaceous succession crop out in the Sorrento Peninsula promontory and were overlain by a transgressive Miocene succession and, locally, overlain by Pleistocene calcareous breccias and Pleistocene–Holocene pyroclastic rocks (Figure 1.5).

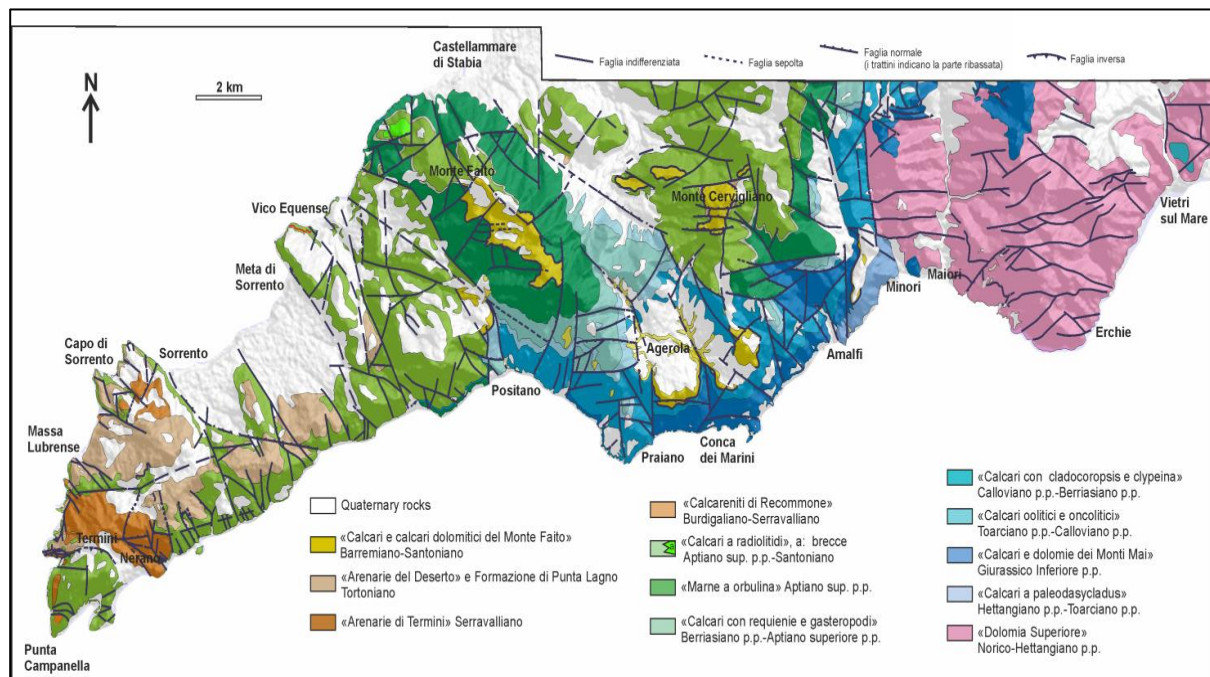


Figure 1.5: Geological sketch map of Sorrento Peninsula (modified after Vitale et al., 2016).

The whole promontory is also carpeted by a pyroclastic unit emitted by Somma Vesuvius and the volcanoes of the *Campi Flegrei*, with a thickness varying between a few centimetres (Iannace et al., 2015). The most important eruption producing these deposits during the Holocene, was the Vesuvius eruption of 79 AD. The 79 AD pyroclastic unit rests directly on the Mesozoic rocks or

on eruption units of Middle-Late Pleistocene. Therefore, between 18 ka ago and 79 A.D. the Lattari Mts. did not receive any significant fallout deposits, because during this time span, the Vesuvius Plinian eruptions were dispersed in other directions (NE to E; Santacroce et al., 2008, Aucelli et al., 2016). During the 79 A.D. eruption, the Lattari ridge was completely mantled by loose pyroclastic deposits, with a thickness ranging between 1 and 2.5 m of pumice and ash (Sigurdsson et al., 1982; Santacroce et al., 2008; Cinque and Robustelli, 2009). This cover has been almost totally removed from the steepest hill slopes of the Lattari Mts. by mass wasting and fluvial denudation; whereas, on less inclined hill slopes some parts of the cover have been preserved.

Chapter 2

Archaeological background

2.1 *Piscina Mirabilis*

The *Piscina Mirabilis* is located in the present day Municipality of Bacoli, in Miseno (the ancient *Misenum*), up the hill facing the sea in the bay of Naples (Figure 2.1). It was realized during the Augustan Age.



Figure 2.1: *Piscina Mirabilis* location, Miseno (Southern Italy).

In fact, during the war with *Pompeius*, *Augustus* ordered the construction of a harbour complex west of Puteoli (Pozzuoli), named *Portus Julius* (Figure 2.2), where an old Greek dam was restored to create an artificial lake, *Lacus Lucrinus*, which was then connected by a channel to another lake, *Lacus Avernus*, which was traditionally considered one of the entrances to the underworld. Later, this harbor was seen as less ideal, because of silting problems, and a new complex was built further west at *Misenum*, where two lakes were connected, becoming the base of the western Mediterranean war fleet (Amalfitano et al., 1990).

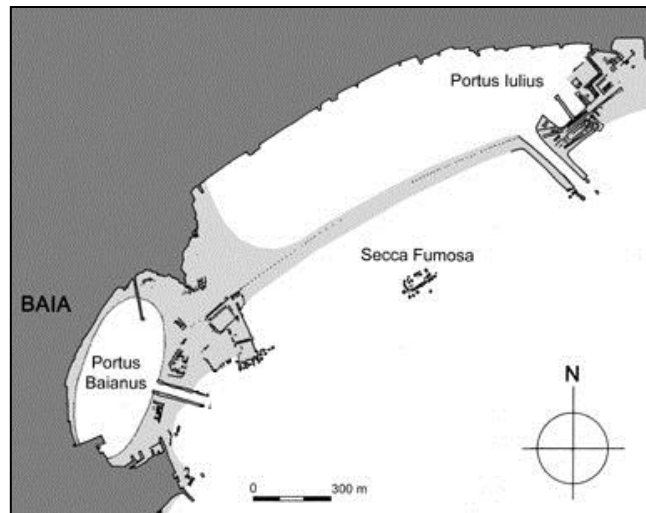


Figure 2.2: the ancient Portus Iulius (modified after Brandon et al., 2008).

This major naval base needed large quantities of fresh water for the base itself and for the ships, which was the principal reason why *Augustus* had a new aqueduct built (Passchier and Schram 2005).

For this purpose, the “Serino aqueduct” was constructed, probably between 33 and 12 B.C., when Marcus Vipsanius Agrippa was *curator aquarum* in Rome. The *caput aquae* of the aqueduct was the Acquaro-Pelosi spring in the village of Serino, in the province of Avellino (the ancient *Abellinum*) (De Feo and Napoli 2007).

The aqueduct provided the Roman fleet of *Misenum* and supplied water for the demand of the important commercial harbour of *Puteoli* as well as drinking water for big cities such as Cumae (Cuma) and Neapolis (Naples).

The main channel of the aqueduct was approximately 96 km long, with 7 main branches corresponding to approximately 49 km. for a total length of around 145 km. The Serino aqueduct is one of the largest aqueduct systems in the Roman world (Amalfitano et al., 1990). The Serino aqueduct filled several reservoirs in the section beyond Naples and, in particular, the *Piscina Mirabilis*. It was located up the hill facing the sea in order to easily refurnish of water the *Classis Praetoria Misensis*.

The *Piscina Mirabilis* is a gigantic reservoir 70m long, 25.50m large and 15m deep (Hodge 2002; Tolle-Kastenbein 2005), which gets its name from the eighteenth century antiquarian tradition, with clear reference to the impressiveness of its plan as well as the remarkable architectonic effect. It is dug in a tuff hill and has two step entrances in the northwest, the Ancient Roman entrance (Figure 2.3) and southeast corners, the latter closed. Forty-eight pillars, arranged on four rows serving as a support to the barrel vault, divide it into five principal aisles on the long sides and thirteen secondary aisles on the short sides, lending to it the majestic look of a cathedral.

In particular, one of the five principal aisles and one of the thirteen secondary aisles (constituting the ancient Roman reservoir) are respectively shown in Figure 2.4a and 2.4b.

The *Piscina Mirabilis* can be considered one of the biggest Roman reservoirs ever known until now with a volumetric capacity of 12,600m³ of water (Amalfitano et al., 1990; Hodge, 2002; Tolle-Kastenbein, 2005; De Feo and Napoli, 2007).

The water coming from Serino flew into it near the northwest entrance, as shown in Figure 2.3. In particular, in Figure 3.1.4c, the zone interested by the entry of the water is shown, near the northwest staircase. The long walls were realized in *opus reticulatum* (reticular work) with brick bonding courses and by the technique of the tufa stone pillars, both covered with a thick waterproof layer of *cocciopesto* (pounded terracotta).

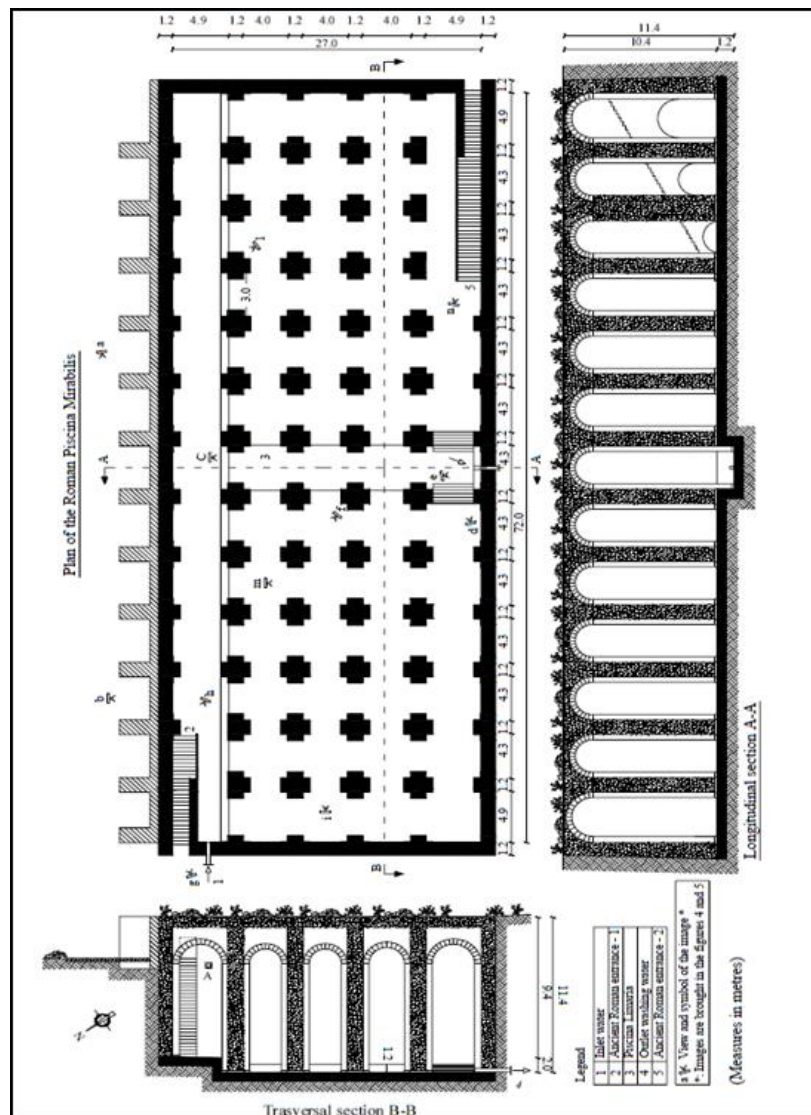


Figure 2.3: Plan and section of the *Piscina Mirabilis* (modified after De Feo et al., 2010).



Figure 2.4: Images of the *Piscina Mirabilis*: a) a longitudinal aisle; b) a cross aisle; c) the northwest staircase (inlet water).

Different material used in the construction of the ancient reservoir can be observed, with tuffs used as a base material (widely present in the area of *Campi Flegrei*) and a layer of *cocciopesto* used for the waterproofing of the structure (Figure 2.5).



Figure 2.5: pillar covered with a tick waterproof layer of *cocciopesto*.

There is a basin of 1.10 m, probably a polishing pool, that is a waste-bath for the maintenance of the reservoir, in the floor of the nave (Figure 2.6). It was used as a *piscina limaria* for the periodical cleaning of the reservoir (Hodge, 2002; Tolle-Kastenbein 2005; De Feo and Napoli 2007).



Figure 2.6: internal *piscina limaria*.

The water, through a series of doors opening in the vault along the central nave (Figure 2.7), was raised through hydraulic engines on the covering terrace of the reservoir, which was also floored with *cocciopesto* and from there, canalized towards the built-up area. These doors appear casually opened in the roof, with an irregular realization being noted.



Figure 2.7: examples of openings in the barrel vault are visible.

Along the north-west external side, in the course of the first century A.D. twelve vault-covered little rooms in *opus reticolatum* with angular brick bonding courses were added (Figure 2.8), in the second of which is kept a *signinum* floor with labyrinth-shaped mosaic tesserae and a central white inlaid panel with polychrome limestone tiles, which seems to date back to a more ancient phase (Adam 1988; Amalfitano et al., 1990; Passchier and Schram 2005).



Figure 2.8: outside barrel vaults.

Close to the *Piscina Mirabilis* there are two other large cisterns, probably belonging to large villas, the Grotta Dragonaria and Cento Camerelle (Nerone's jail). In Pozzuoli, the aqueduct served several cisterns, notably the *Piscina Cardito* (55 x 16 m) from the second century, and the *Piscina Lusciano* (35 x 20 m) from the first century AD. In Baiae, a tunnel with two cisterns, known as the *Crypta Romana*, was filled by the aqueduct (Adam 1988; Passchier and Schram 2005; De Feo and Napoli 2007).

2.2 Terme di Baia

The hillside overlooking the bay of Baia is entirely covered with the remains of buildings built on a series of terraces. The area that has been excavated from the 1920s onwards and open to the public, known as the Archaeological Park or *Terme di Baia* covers some 40.000 square meters lying between two roads running along the brow of the hill (Figure 2.9).

The rest of hillside, occupying a further 150,000 square meters and called the Monumental Park, has recently been provided with a visitors' route and joined up with the Archaeological Park. Here too you can now inspect a series of highly important archaeological remains while enjoying a beautiful panorama and the luxuriant Mediterranean maquis.

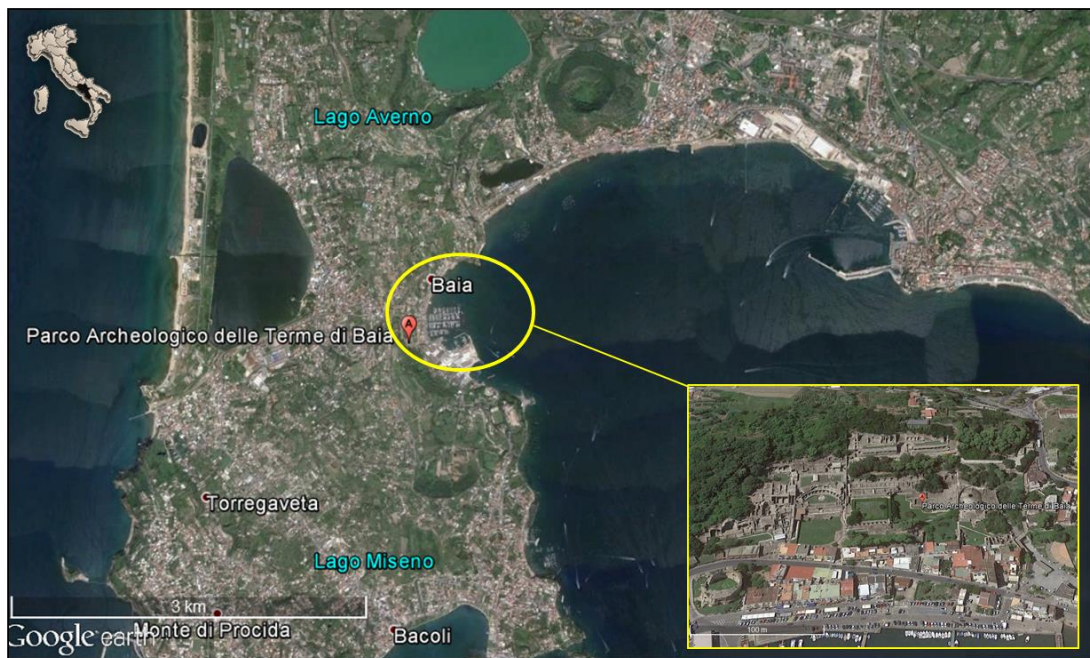


Figure 2.9: *Terme di Baia* location, Baia (southern Italy).

The Archaeological Park

A glance at the map (Figure 2.10) shows a series of residential buildings grouped in separate nuclei, which bear all the marks of having been constructed under imperial supervision: this was in all likelihood the *Palatium Baianum*, or at least part of it. The buildings continued to be used in one way or another up to medieval times, and even in some cases until the early 1990s (Amalfitano et al., 1990). They have thus lost almost all their original decoration (e.g. stucco work and marble facing). This nudity largely dispels their original splendor, but the impressive scale and sophistication of surviving architecture does give some idea of it.

Scholars have sought to give an identity to the endless succession of buildings by dividing the area into five areas: *Villa dell’Ambulatio*, *Mercurio*, *Sosandra*, *Venere*, and *Piccole Terme* (Figure 2.10)

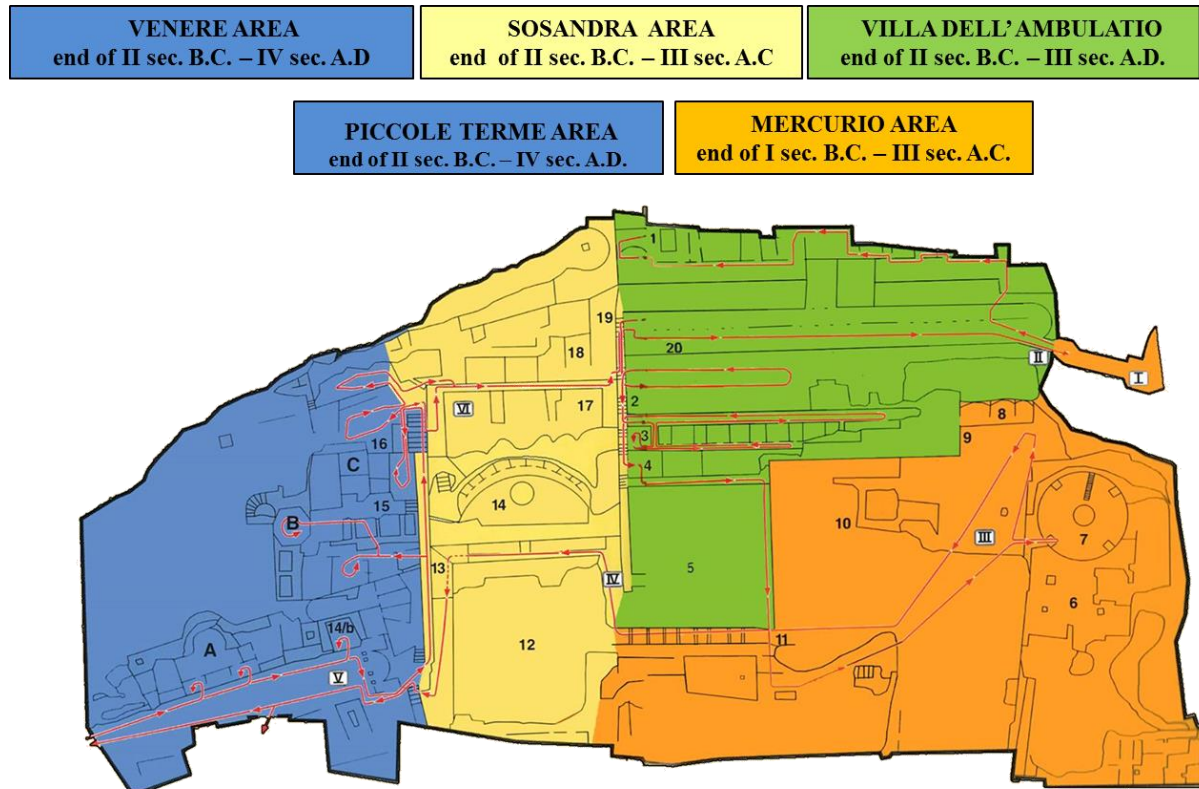


Figure 2.10: Planimetry of Archaeological Park of Baia (modified after Di Bonito and Giammelli, 1992).

The buildings are located along a hillside, descending from the ridge on successive terraces so that each lower level functions as the substrate for the building above it. This construction technique was an extension of that used in building the villas of the late Republican era involving artificial foundations. Two commanding flights of steps serve to both link and distinguish the various levels of each area. The map also clearly shows which areas were built on the same orientation, indicating not only that they date from the same period but also, that they served similar purposes (D’Antonio, 2003).

The **Area of the *Villa dell’Ambulatio*** (green in Fig 2.10) is laid out on six terraces, the first three of which display a coherent overall design (Figure 2.11).

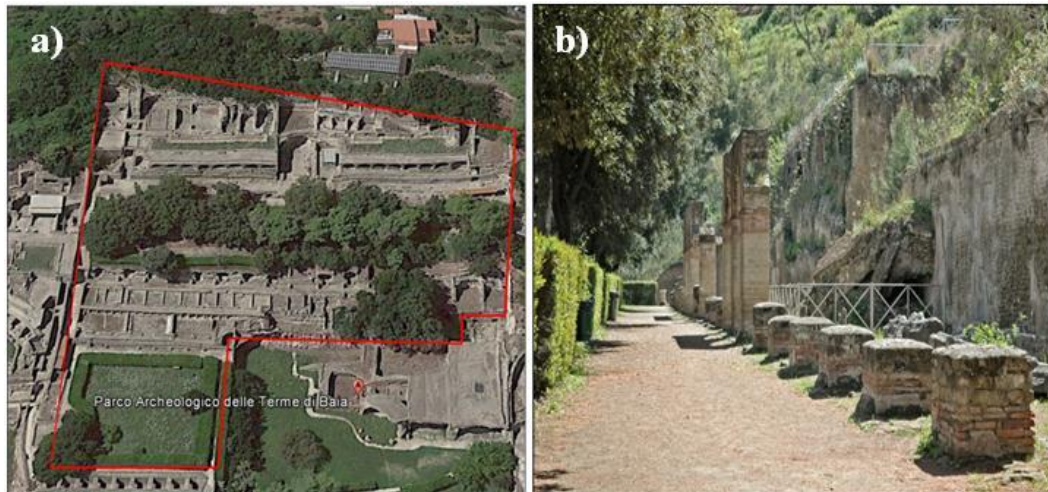


Figure 2.11: Villa dell' Ambulatio area, a) visible part; b) details .

The highest terrace (1 in Figure 2.10), is occupied by the domestic quarters, with the peristyle, living rooms and cubiculi opening off a large main room (*oecus*) overlooking the bay. The flooring throughout was originally decorated either with marble (*opus sectile*) or in black and white mosaic. At first terrace (2 in Figure 2.10) merely shored up the buildings above, but it was soon provided with a double curtain wall in *opus reticulatum* and turned into a covered walkway (*ambulatio*), from which the area gets its name. It is divided down the middle with a row of pillars and linking arches, and has a large central room situated beneath the one on the terrace above (Amalfitano et al., 1990). The servants' quarters on this terrace, dating from the 1st century AD, were evidently restructured much later, probably for use as *hospitalia*, accommodation for people using the nearby baths. This obviously came about after the imperial era, when this site passed into public ownership. Terrace 4 (Figure 2.10) was also substantially modified: built originally with a series of blind arches and semicolumns, it was subsequently incorporated into rooms built below. The lowest level (5, Figure 2.10) was seriously damaged in post-Roman times by people searching for underwater springs; it was occupied by a large garden, bounded to the west by the long containing wall of the level above (Amalfitano et al., 1990).

The *Sosandra* area (in yellow, Figure 2.10), comprising the central segment of the whole complex, features four phases of construction between the mid. -1st century BC and the 2nd century AD. It is laid out on four levels, once again with the residential quarters on the upper two levels (Amalfitano et al., 1990) (Figure 2.12a).

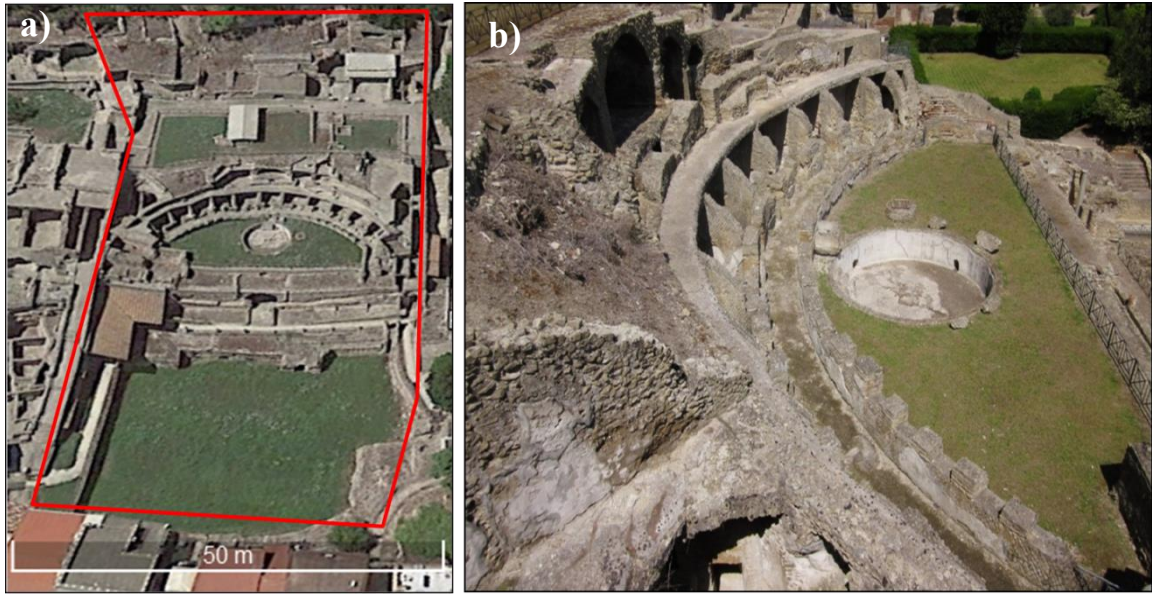


Figure 2.12: Sosandra area, a) visible part; b) semicircular edifice.

The top terrace is occupied by service rooms, and the next one down has dining and living rooms and also a small steam bath (*laconicum*) with stucco decoration, overlooking the bay and preceded by a colonnade. All these rooms were very well appointed, with mosaic flooring, notably one dating from the 2nd century AD adorned with actors' masks and with a centerpiece featuring a theatrical scene, and also sculptures. In the largest room, the statue known first as *Aspasia* and subsequently as *Aphrodite Sosandra* stood in the central recess in the rear well (Amalfitano et al., 1990). In the room next door stood a statue of *Hermes*; the head was stolen but subsequently retrieved and is now in the National Archaeological Museum of Naples, as is the *Aphrodite Sosandra*. Both sculptures were produced in a workshop of copyists that catered for commissions from the imperial household from the Augustan era until the last year of reign of Hadrian. The workshop was certainly located in Baia, possibly on the premises of imperial residence. In 1954, during work to consolidate this terrace, archaeologists found a deposit of discarded fragments of plaster sculptures used as casts for making copies. These are now displayed in one of rooms of Archaeological Museum of *Campi Flegrei* (D'antonio, 2003).

The lower two levels are completely different in character. They are occupied by a very striking architectonic ensemble, with a semicircular edifice up above and below it a large open-air site traditionally pool (*piscine*) (Fig 2.12b). The former resembles a theatre with a terrace instead of the stands (*cavea*), a round pool in the middle of the orchestra and an architectonic façade with alcoves and columns. It seems to have been a theater-nymphaeum, used for spectacles based on marine subject complete with water features and waterfalls (Ling, 1979).

As for the *piscine*, there is nothing to suggest that it was used for bathing, although the area has never been excavated down to the foundation lying some 6 meters below the present ground level. It might perhaps have been the *ebeterion* (place of recreation for the youth) that the historian Cassius Dio record Nero having built in Baia for the sailors stationed at Misenum. In fact the layout recalls the complex at Pompeii comprising the Theatre and the Palestra of the Gladiators; this area may have served the same purpose, with the added attraction of a plentiful water supply, exploited in fountains and waterfalls both in the open air and below ground. The room at the center of the portico beneath lies on the same axis as the semicircular pool of the theatre- *nymphaeum* and another chamber hollowed out of the cliff behind it. Here too there is ample evidence of transformations made after the restructuring carried out in the 2nd century AD. In the portico of *piscine* a series of rooms were created by the rather clumsy insertion of long partition walls, and the space inside the *nymphaeum* was similarly divided up (D'Antonio, 2003). The **Area of Mercurio** (in orange, Figure 2.10) takes its name from the *Tempio di Mercurio*. It comprises two groups of buildings, prevalently for bathing, situated to the north-east and south-west (Figure 2.13).



Figure 2.13: *Mercurio* area, a) visible; b) indoor of the *Tempio di Mercurio*.

We know little about the former because the buildings lie below ground, with water up to the level of the vaults; moreover various parts were destroyed when new housing was put up and during construction of the road along the north-east of the site. Structures in *opus reticulatum* indicate that there were already buildings here in the late Republican or early Imperial era, subsequently restructured in *opus latericium* during the 2nd century AD (D'Antonio, 2003). In one of these rooms the fine head of Omphalos Apollo in Pentelic marble was found, also a copy of a Greek bronze in the late Severe Style like the Aspasia and Hermes found in the *Sosandra* area all made in the same local workshop. The group of buildings to the south-west, on the other

hand, were all put up during the Severus reigns, as we can tell from the use of red brickwork. These were particularly sumptuous premises in term of both design, as in the octagonal room with dome and wall recesses, and decoration, with elaborate wall painting and relief stucco work. It could in fact have been part of Alexander Severus's palace, which would have extended down to the shoreline, where during the 1920s various architectonic fragments dating from his reign were found in the sea (Ling, 1979).

The **Venere area** (in blue, Figure 2.10) gets its name from “rooms of Venus”, as they were called by eighteenth century scholars. These are three rooms on the lower level adorned with fine stucco work on the ceiling in the manner of boudoirs (Di Bonito and Giammelli., 1992). The area comprises three groups of buildings dating from different periods on the lower, intermediate and upper levels, the latter known as the *Piccole Terme* (Figure 2.14).

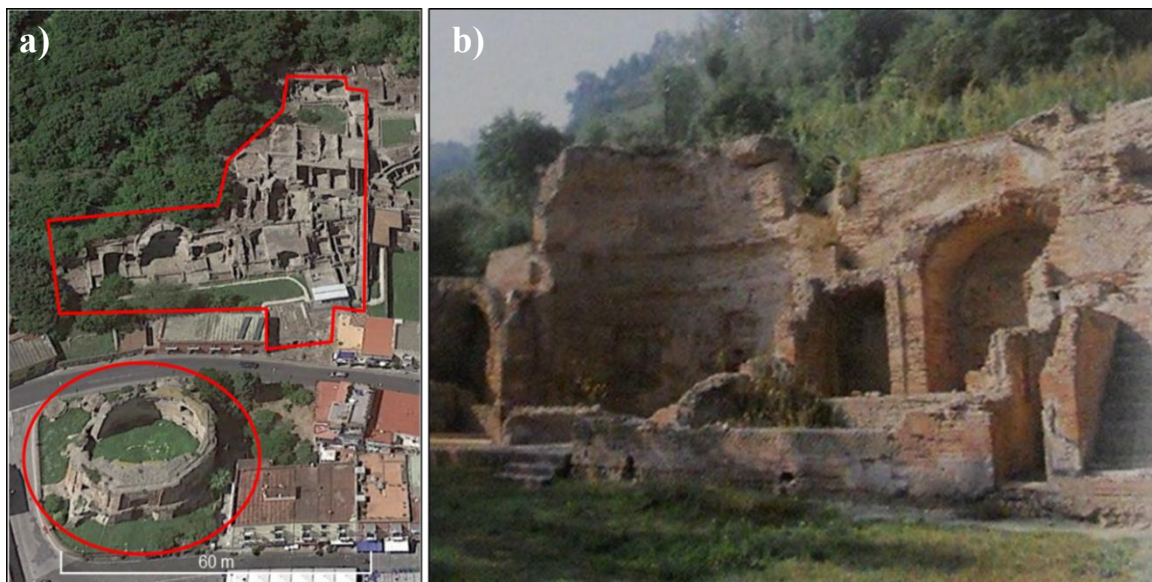


Figure 2.14: Venere area, a) visible part; b) detail

The eastern side of the lower level was completely disrupted by the construction of the coast road with modern buildings along it, leaving the large bath house, the *Tempio of Venere*, sticking out like a sore thumb (D'Antonio, 2003). The development on this level, clearly a separate entity with respect to the levels above since it has a different orientation, comprises two groups of buildings standing on the western side of a large uncovered area, only partially excavated, which was probably a garden. Along the northern side there are a fountain, a small room with a female herm in the center and mosaic featuring a cherub with baby hare, possibly representing Autumn, and an exedra or summer dining-room, all dating from 2nd century AD (Ling, 1979). The succession of rooms on the western side date from two different periods. To the north there are three chambers (the so-called rooms of Venus) originally used for bathing and dating from the

beginning of the 1st century AD (Amalfitano et al., 1990). The scant remains of stucco work in bas relief on the ceiling have been thoroughly blackened by the torches held by travelers on the Grand Tour; moreover, these rooms were inhabited for a long period. The stucco work featured subjects drawn from the *palestra* and the baths as we know from drawings made by Francesco Bartoli in the years 1700-1724 (now conserved at Eton College) (Di Bonito and Giammelli, 1992). This decoration can be dated to the middle years of the 1st century AD. Subsequently the rooms were turned into water tanks and service rooms, including a kitchen with a cooking range and sinks. The buildings at the southern end of the western side constitute a large bathing establishment built during the reign of Hadrian. It is arranged round a large rectangular hall with an apse at the centre of the lower level, roofed with half-dome vaults and perfectly aligned with the *Tempio di Venere*. It is entirely occupied by a basin filled from fountains and water jets, probably a nymphaeum with on either side two large rooms with a Greek cross ground-plan, roofed with cross vaulting (Di Bonito and Giammelli, 1992).

This large complex, built at the same time as the radical transformation carried out in the adjacent *Sosandra* area, was probably used by Emperor Hadrian. He is known to have spent long periods in Baia, and he died here in 138 AD. Furthermore, it was during his reign, as Carlo Gasparri has established, that the repertoire of the local workshop of sculptors was renewed, taking as models Greek works in the late-Severe style dating from the 5th century BC (Ling, 1979). This corresponded to the idealized conception held Hadrian of Athenian civilization between the end of the Persian wars and the age of Pericles (Ling, 1979). An impressive ramp of broad steps along the north side of the *Venere* area led up to the intermediate level, comprising an artificial terrace supported by robust vaults filling in the large gap between the lower and upper levels. On account of its very poor state of conservation, this terrace has remained largely uninvestigated (Di Bonito and Giammelli, 1992). The buildings date from the 1st- 4th century AD, and comprise a double row of service and store rooms, leading to an octagonal chamber, probably a bath house, aligned with the *laconicum* above it. Built above these rooms there was a baths suite whose individual rooms caved in and are now virtually unrecognizable. The unheated rooms lay to the north, including the *frigidarium* with its wall recesses and central pool; to the south the remains of *suspensurae* indicate the heated rooms; with an octagonal *laconicum*. In the courtyard in front of the suite we can identify other service rooms and a ramp leading down to a large underground room, also probably used for bathing, now inaccessible (D'Antonio, 2003).

The so-called *Piccole Terme* (Figure 2.15), are built on two levels and occupy the upper western side of this level, standing against the hillside.

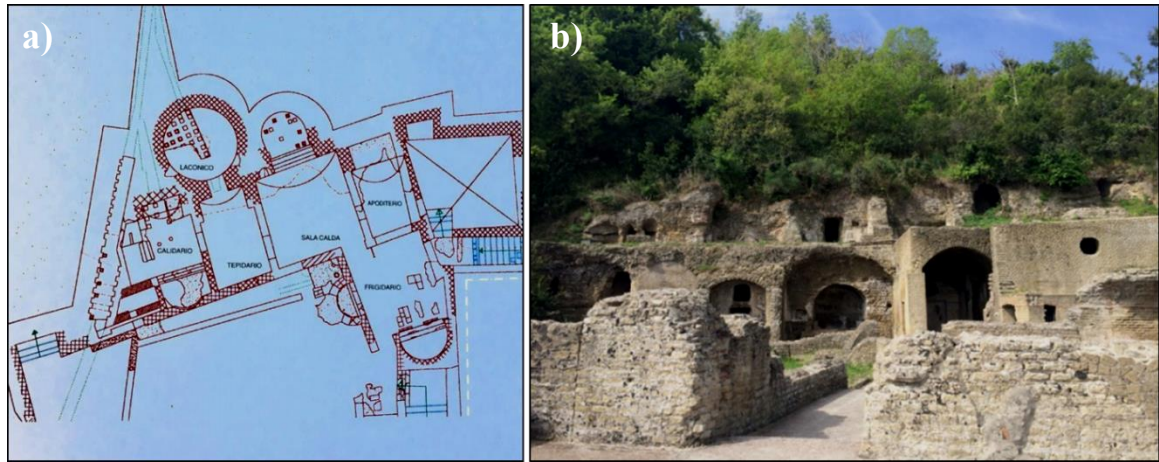


Figure 2.15: *Piccole Terme* : a) planimetry; b) detail.

They exploit the hot springs inside the hill by means of tunnels. This is one of the oldest examples of baths suites known to us: the original structure, dating from the middle of the 1st century BC, comprised simply a rotunda in *opus reticulatum*, where bathers would take the *sudation*, and a pool of cold water, *frigidarium*. This structure was probably part of a *villa* dating from the late-Republican period, of which more remains may well come to light during excavations above and below there remains (D'Antonio, 2003). Further bathing facilities were added over the next 100 years, including the *calidarium* and *tepidarium* built opposite the *laconicum*, probably when the baths were opened to the public (Ling, 1979). In the final phase, dating from the 2nd century AD, the original *frigidarium* was turned into another heated room, and a larger cold room was built on the north-east side of courtyard, provided with two pools. To the south, water tanks were added and a long channel was cut into the hillside to convey hot vapor to the baths. In the area to north, still awaiting excavation two colossal statues were found representing the heavenly twins, Castor and Pollux (Ling, 1979). They are copies in pentelic marble based on originals by Polycletes, active in Athens in the mid- 5th century BC, produced in the local workshop in the mid-2nd century AD (Di Bonito and Giannelli, 1992). They are now on display in the National Archaeological Museum of Naples.

2.3 *Villa del Capo*

On the tip of the Cape of Sorrento (Naples) there are the remains of the famous Roman *Villa del Capo*, dating back to the first imperial age (I century AD).



Figure 2.16: *Villa del Capo* location, Sorrento Peninsula (Southern Italy).

Today, ancient references and comparisons with other Roman *villae* of the Gulf of Naples, from Posillipo to punta Campanella (cf. Strabone V 47) give us account of its ruins.

The *Villa del Capo di Sorrento*, which the popular tradition knew as *I bagni della regina Giovanna* (the baths of Queen Giovanna) or *Villa of Pollio Felice*, had an extent of about two hectares.

The property maybe included, besides the seaside *villa*, also a *domus*, more upstream, used predominantly for agricultural purposes. The two units were connected with slip roads and tunnels, whereas, the differences in height of the promontory were settled with artificial terraces (Budetta et al., 2013) (Figure 2.17).

The *villa* is accessible either overland or oversea. The current secondary sloping road of Massa traces out to a large extent the ancient access road to the *villa*. A little bridge connected the promontory to the actual cape and surmounted the access to the internal basin. Not far away, an entrance led into the rooms of the house. These were arranged around a *peristilium* – whose porch floor was in *cocciopesto* – surrounded by a series of room. Other rooms with different functions were arranged, instead, into several levels on the promontory (Russo, 2006).

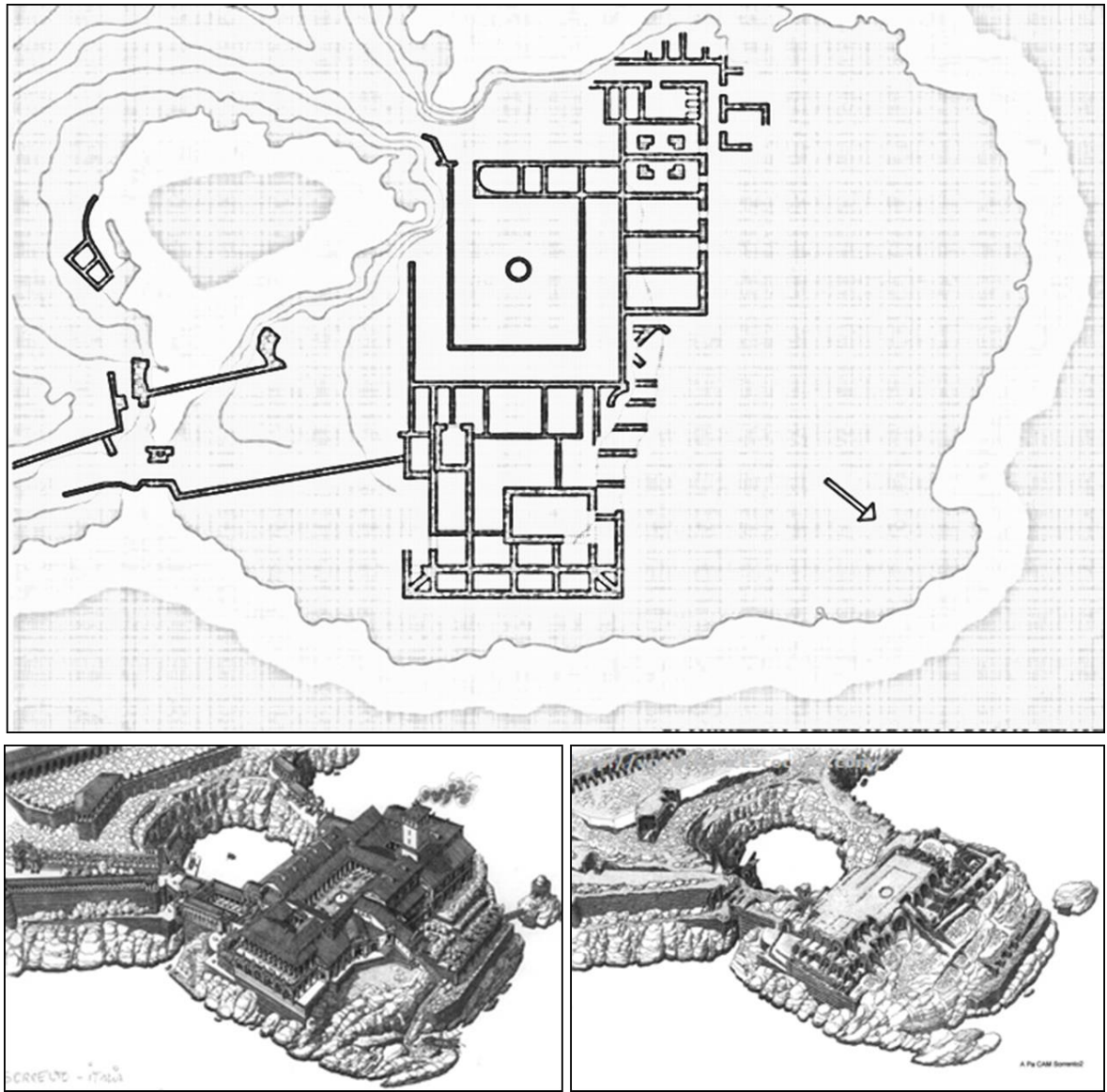


Figure 2.17: planimetry and reconstruction of *Villa del Capo* (FrancESCO Conti drawings).

The eastern part – with mosaic floors – acted as the lodging house, while, the other block of barer rooms, on the western part, was assigned to the servants and to the service rooms, as we can see from the presence of a kitchen. The two units were separated by a secondary entrance on the sea, which allowed the passage to the lower buildings up to the seaside stores, on the outermost strip of the cape.

Without any doubt, the compound was also provided with a spa, although it is impossible to establish its precise location only analyzing the ruins (Budetta et al., 2013). The information by Vitruvio, according to which the apse of the *calidarium* was south-west oriented for the maximum sun exposure during the day, may be of some help. A continuous water-supply could justify a location upstream.

The architecture seems to take a great advantage of the landscape beauties. The rooms show the greatest usability of the scenery, also thanks to some tricks: divergent walls, wide windows, up to the sophisticated solution of a promenade around the little harbour, with a panoramic viewpoint into the internal part of the apse overlooking the entrance. The most evocative element of the landscape is a natural basin, which the masters used wisely as a dock and swimming pool. It was scenically furnished as we can see from the two examples of the Grotta Azzurra in Capri and the Grotta of Sperlonga (Russo, 2006). The two western small islands show several wall structures and, therefore, it is likely that were connected to the promontory with a bridge. Considering that the promontory obstructed the access to Sorrento, it is probable that it was equipped with a lighthouse. The productive activities of the *villa*, the *negotium*, were bound to the fields, on the upperpart of the *villa*, and to the sea (Mingazzini, 1946). The fields produced oil and the high-quality wine of Sorrento (*Strabone, Oratio, Macedonius* and *Plinius*), while, the sea supplied fish and shellfish, one of the Romans' favourite dishes. Everything, architecture and decoration, was functional to the *luxuria* and *otium*. Even the shaded areas – the roof – gardens and the *pergolae* – veiled the sunny trails and reflected the desire to live well as the greatest expression of luxury.

2.4 Villa del Pezzolo

Remains of a Roman *villa* are visible near the eastern side of the Marina d'Equa bay, at the foot of the promontory of Vico Equense, in the Sorrento peninsula (Figure 2.18).

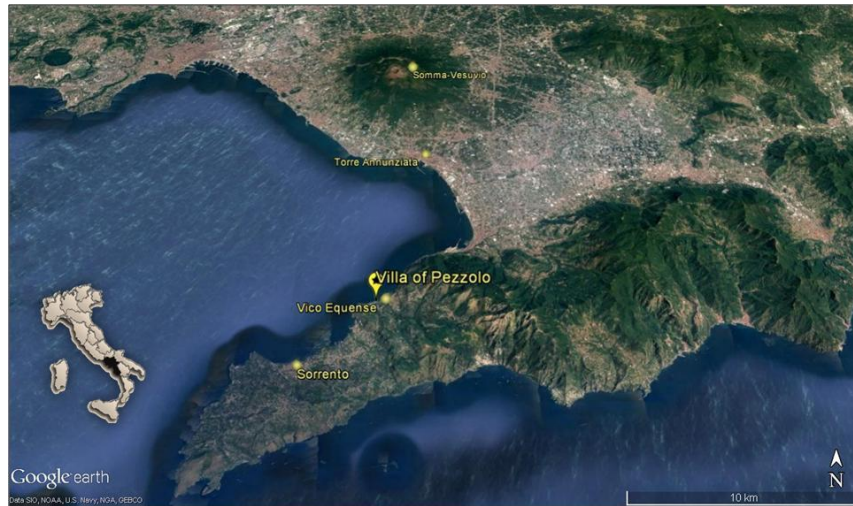


Figure 2.18: Villa del Pezzolo location, Sorrento Peninsula (Southern Italy).

Rooms were seriously damaged by sea erosion and for this reason is almost impossible to recognize the original building plan. However, thanks to the analysis of a) geological stratigraphy and b) building techniques, three building phases can be identified (Aucelli et al., 2015) (Figure 2.19).

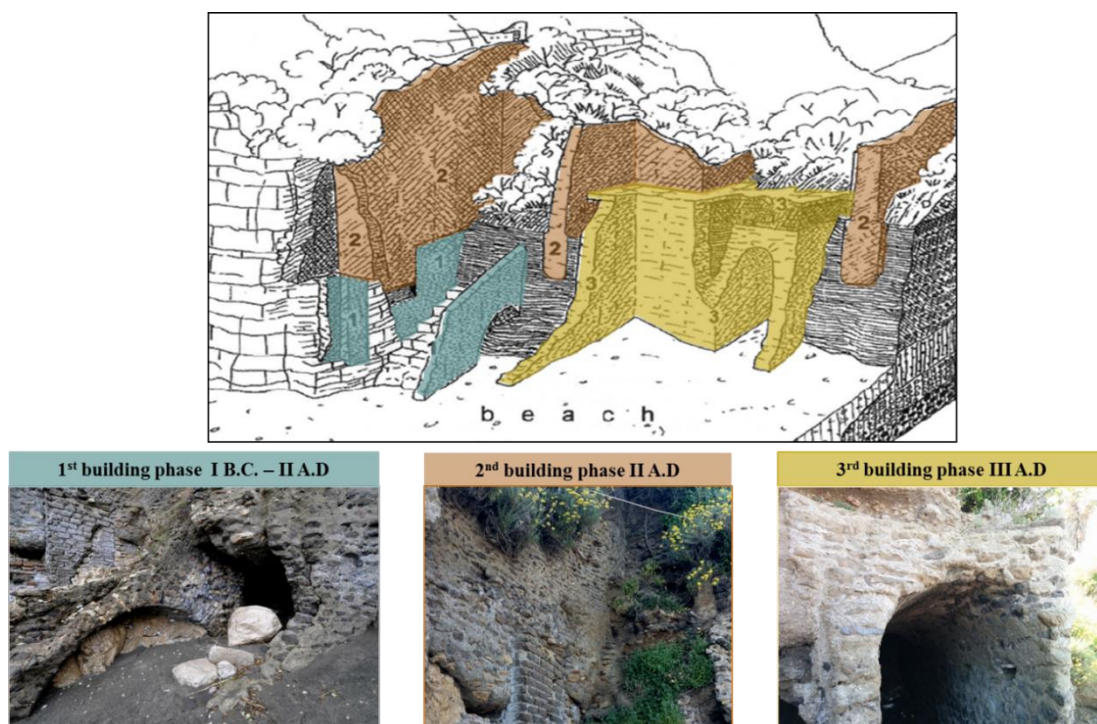


Figure 2.19: Sketch and picture of the *Villa* archaeological remains on the beach (modified after Cinque et al., 2000).

The first phase occurred between the first century B.C. and the middle of the first century A.D. This first *villa* was erected on Cretaceous limestone flanking the bay and had a staircase descending to the beach (Figure 2.20). The coastline, however, was more embayed than it is today (Cinque et al., 2000). The first villa was severely damaged and partially buried as a result of the A.D. 79 eruption. In particular, the lower part of the staircase descending to the beach was covered with a 6 m succession of deposits that starts at the bottom with fallout and surge deposits (Figure 2.21) and continues upwards into debris flow and alluvial deposits related to the so-called Durece event (Cinque et al., 2000).



Figure 2.20: evidence of A.D. 79 eruption: base surge of Somma-Vesuvius volcano (~12 km far).



Figure 2.21: “Durece”, typical lithofacies of reworked pyroclastic deposits.

When the alluvial events ended, the *villa* was rebuilt. Judging from the building materials and the techniques used, the second construction phase can be ascribed to the first half of the second century A.D., when the coastal plain had already aggraded as a result of the Durece deposition (Cinque and Robustelli, 2009). During this period, the resumption of landscape stability encouraged the reconstruction of the seaside *villa*, likely by the same owners.

The masonry work performed in the second phase included the restoration of certain preexisting rooms on the calcareous slope and the extension of the compound, with new rooms constructed on the newly forming alluvial delta.

After the dismantling of the alluvial delta by wave action, the *villa* was rebuilt a second time. The third building phase consists of the restoration and adaptation of the rooms resting on the terrace and the construction of a new route down to the beach via an inclined tunnel (Figure) that started from rooms within the *villa* and emerged at the sea cliff. The architectural forms and materials used suggest that the third phase of building and its correlative geomorphological stage occurred in the third century A.D. (Cinque et al., 2000).

The decoration of the Roman *villa* is documented by some sporadic marble findings, now kept at the National Archaeological Museum of Naples.

Chapter 3

Analytical methods

Knowledge of mineralogical composition, and microstructural properties, of cement-based materials is very important for the understanding of their chemical and physical properties (Rispoli et al., 2016). In order to obtain these information, the following analyses were carried out:

- Optical studies on thin sections and modal analyses (OM),
- Mechanical separation of the different constituent phases (matrix, ceramic fragments, aggregates), according to the UNI 11305: 2009
- X-ray powder diffraction (XRPD);
- Scanning electron microscopy (SEM) and microanalyses (SEM-EDS);
- X-ray fluorescence (XRF);
- Thermal analyses (TGA-DTA);
- Mercury intrusion porosimetry (MIP).

3.1 Optical studies and modal analysis on thin sections

General outline

Optical microscopic methods are commonly applied using a polarizing microscope to study thin sections of samples. Thin sections are very thin slices of rocks and geomaterials, that are essentially two dimensional cross sections through the sample, that are mounted (and embedded in epoxy resins) on clear, flat glass slides (Middendorf et al., 2005).

The reduction of thickness of the material (commonly to 20-30/ μm) permits light to pass through crystalline or amorphous materials and for the detailed analysis and recognition, by an experienced operator, of the geomaterial's components.

As regards mortar, a piece of it, with dimensions of between 7 to 20 cm, is removed (sawn without using water if necessary to avoid dissolution of soluble material) from a part of a characteristic mortar sample. It is then dried at 40° C (to avoid dehydration of components, especially gypsum if present, and physical damage due to thermal shock), until mass constancy is reached. After this it has to be impregnated with warmed low viscosity epoxy resin (Middendorf et al., 1998).

The sample is then ground flat with a lapping or polishing machine using an abrasive paste, suspended in water, petroleum or oil, with hardness adequate for the removal of binder and aggregate.

The sample fixed to the slide must be reduced to a thickness of about 20 - 30 micron plane-parallel to the microscope slide through successive sawing, milling and lapping (Middendorf et al., 2005). Indications for traditional building practice and the provenance of raw materials can also be obtained. The result of petrographic and textural investigations has to be presented in a report with regard to features relevant for building preservation. Illustration of features, using photographs if possible, or with annotated drawings is desirable.

The modal analysis is based on the method of counting points, with the use of a specific ocular reticle and criteria for the determination of the mineralogical phases and constituents of the mortars such as: C-A-S-H gel, scoriae, zeolites, etc

The analysis is considered to be quantitative, and it is performed counting at least 1500 points for each thin section and allows to create a database useful for statistical analysis, through the identification and the counting point by point of the individual constituents of the mortar with maximum detail.

Moreover, the analysis allows to obtain a classification of samples based on composition in order to detail, distribute and evaluate the proportionality relationship between the individual mineralogical phases and the other constituents.

Analytical details

Polarised Light Microscopy (PLM) in thin section was performed to observe the textural features and the petrographic composition of the samples. Image acquisition was carried out using a Leica DFC280 camera and Leica Q Win image analysis software (Figure 3.1).

Modal analyses were performed on representative thin sections (selected on the basis of microscopic observation and typology of mortars) using counting grids, in size 10x10, of at least 1500 points, using Leica Qwin software for image analyses.

In the intersection of the grid (10x10), points are counted in order to be associated with the mineral phases or constituents (including pores). In the counts are excluded aggregates having dimensions greater than 4mm in diameter, to discard any errors due to excessive weight of a single granule.

The modal analysis can be considered representative since the maximum uncertainty of percentage for a total amount of 1500 points is about 2.6% (Howarth, 1998).



Figure 3.1: Polarizing microscope Leica Laborlux 12 pol.

3.2 Sample pretreatment according to UNI 11305

General outline

In order to analyze separately binder, aggregate, ceramic fragments and neoformed products, samples underwent a preliminary treatment, before carrying out the following analysis, according to the UNI 11305: Cultural heritage - historical mortars - guidelines for the mineralogical-petrographic, physical and chemical characterization of mortars.

Analytical details

Sample disintegration is performed with extreme caution using an agate mortar, preventing the crushing the main components of the mortars (aggregate and ceramic fragments).

Separation of the components was performed with a binocular microscope (WILD M38) and with the assistance of tools such as forceps, scalpels and spatula (Figure 3.2).

It was used a quantity of material not less than 5g but always representative of the mortar under examination

radiates the beam in all directions. This phenomenon is known as “scattering” (Moore and Reynolds, 1997).

In 1912 Bragg postulated that the diffraction from a crystal can occur whenever the following law is satisfied (Bragg, 1913):

$$n\lambda = 2d_{hkl} \sin \theta$$

Where:

- n is an integer
- λ is the X-ray wavelength
- d is the lattice spacing
- θ is the diffraction angle

The Bragg's law defines a very strict relationship between λ and θ for any crystal or mineral structure (Figure 3.4).

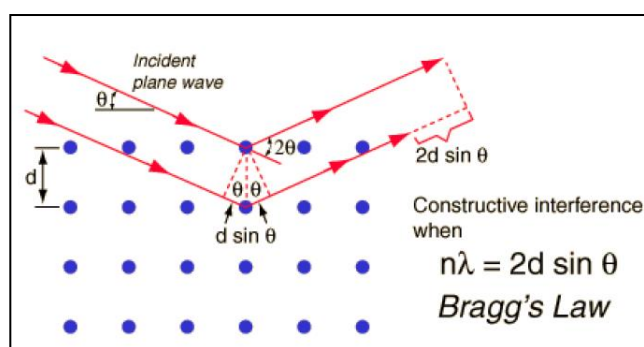


Figure 3.4: Bragg's Law (modified after Moore and Reynolds, 1997).

The most common technique to apply the Bragg's law to identify unknown minerals in a powder is to use a X-radiation characterized by a specific wavelength, λ , to measure the diffraction angle θ of the radiations diffracted by the powder, and to compare these angles with a database listing the diffraction angles of scheduled mineral phases, which depend by their d-spacing (Cullity, 1978). The instrument which allows to carry out this analysis is called diffractometer.

The most widespread diffractometers are based on the so-called “Bragg-Brentano (semi-) focalizing geometry” (Figure 3.5). Two settings are possible, i.e. θ/θ and $\theta/2\theta$ types with horizontal or vertical geometry. In $\theta/2\theta$ diffractometer, both sample and detector move with angular velocities equal to 1:2. In θ/θ diffractometer, the sample does not move, whereas the X-ray tube and the detector rotate with the same angular velocity (Cullity, 1978; Moore and Reynolds, 1997).

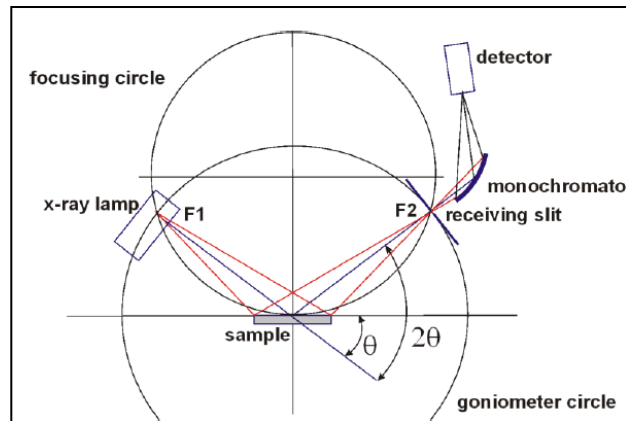


Figure 3.5: Bragg- Brentano focalizing geometry. The goniometer or diffractometer circle is defined by the source (F1) and receiving slit (F2) and has fixed radius. The sample is located in the central part of the diffractometer circle and is tangent to the focusing circle. (modified after Mottana, 1988).

Although different geometries are possible, all the instruments are composed of the same basic components:

- X-ray source (X-ray tube)
- collimation system
- goniometer
- sample lodge
- X-ray detector (\pm radiation monochromator)

The X-ray tube produces a X-ray beam, by streaming electrons across a high voltage potential (15-45 kV). Current is applied to a tungsten filament (cathode) in a vacuum. Electrons are then accelerated into a metal target (anode), producing X-ray radiations. The most common anode materials are Cu and Mo (heavily absorbing sample), Co (for ferruginous samples), Fe, W and Cr.

X-ray powder diffraction (XRPD) analyses are reported on a XY diagram, where the horizontal scale is calibrated in $^{\circ}2\theta$ and the vertical scale shows the intensity of the diffracted X-rays. XRD patterns of a mono- or poly-crystalline matrix are constituted by a sequence of characteristic peaks, with various intensities at specific 2θ positions. Each sequence of peaks is diagnostic for each mineral structure, in agreement with the Bragg's law. Comparing the XRPD pattern of any crystalline mixture, as a rock sample, with the standard minerals of available database, it is possible to identify the mineral compounds by an automated search-match procedure between the measured peaks and the standard ones. Several databases exist, among which worldwide used are the ICDD-PDF (International Centre for Diffraction Data, PDF Powder Diffraction Files) and the ICSD (Inorganic Crystal Structure Database).

In addition to microscopical analyses, XRPD analysis is suitable for identification and differentiation of binders and kinds of aggregates within a mortar, if they are crystalline.

Analytical details

XRPD samples were prepared by dry crushing samples by hand in agate mortar, in order to prevent the loss of information on soluble phases. Operative conditions of XRPD analyses were the following: CuK α radiation, 40 kV, 40 mA, 2θ range from 4° to 70°, equivalent step size 0,017° 2θ , 30 s per step counting time on a modular Panalytical X'Pert Pro diffractometer equipped with a RTMS X'Celerator detector (Figure 3.6). The software for identification of mineral phases was Panalytical Highscore Plus 2.2 with ICSD database.



Figure 3.6: Panalytical X'Pert Pro diffractometer equipped with a RTMS X'Celerator detector, at DISTAR, University Federico II, Naples.

3.4 Scanning electron microscopy (SEM) and Microanalyses (EDS)

General outline

The scanning electron microscope (SEM) is an electronic instrument used for inspecting topographies of sample materials allowing a high-resolved and high-zoomed observation up to enlargements of 1-10 μm . This technique is based on the interaction between an incident electron beam and sample surface. The electron beam is focused and accelerated at high potential, by means of magnetic lenses, on the specimen, and its interaction generates several electromagnetic

radiations such as backscattered electrons, secondary electrons, Auger electrons, characteristic X-rays, and visible light (Middendorf et al., 2005).

High-resolution imaging of surface morphology is generated by secondary electrons. The efficiency of production of backscattered electrons is strongly related to the material's atomic number. The higher the atomic number the brighter the material image.

Using SEM the structure of a mortar can be analyzed at high magnifications and in three dimensions on rough, broken surfaces to directly visualize the structural components of the mortar.

If the SEM is equipped with an X-ray detector (EDS) a quali/quantitative determination of the chemical elements within the components of the sample is possible. The samples which are analyzed with SEM should be small and need to be covered with a conductive layer of gold and/or carbon, that facilitates the removal of electrical charges from the sample, which otherwise interferes with image formation (Middendorf et al., 2005).

The hydrated hydraulic phases in cement or hydraulic lime mortars are mostly too fine to identify with conventional petrographic microscopy and can be rarely identified by XRD since most of these phases are poorly crystalline or amorphous. Analyses at higher magnifications allow the recognition of the microstructure of such hydrated hydraulic phases (e.g. needle-shaped calcium silicate-hydrates – CASH –, hexagonal portlandite plates, etc.) and with EDS, the chemical composition of the phases can be determined (Callebaut et al., 2001).

This analysis was performed also to determine the major chemical composition of the binder, lime lumps, and the volcanic glass fragments (pumice) of the collected samples.

Furthermore, for lime lumps and binder, hydraulicity index (HI) was calculated according to the method of Boynton (1966) as follows:

$$\mathbf{HI = (SiO_2 + Al_2O_3 + Fe_2O_3) / (CaO + MgO)}$$

Generally, lime with HI values less than 0.1 may be considered aerial lime (common lime), values of HI between 0.1 - 0.2 indicate a weakly hydraulic lime, HI between 0.2 - 0.4 indicate a moderately hydraulic lime and finally HI between 0.4 - 0.6 indicate a highly hydraulic lime (Zawawi, 2006).

The analyses on lumps were performed in their central portion, to reduce the level of contamination; whereas the analyses of binder were performed on homogeneous areas of the binder, without aggregate.

Regarding SEM-EDS data on volcanic glass fragments were selected all analyses that close between 98 to 100 %, besides in order to exclude the possibility of analyzing altered pumice, due to the fact that often mortars were in subaerial environment from more than two thousand

years, the alteration indexes have been calculated as: CIA (Chemical Index of Alteration), WIP (Weathering Index of Parker) and W index.

Chemical Index of Alteration (CIA) was proposed by Nesbitt and Young (1982) and it is the most widely used chemical index to determine the degree of weathering.

This index, works correctly when Ca, Na, and K decrease as the intensity of weathering increases (e.g., Duzgoren and Aydin, 2003) and can be calculated using molecular proportion:

$$\text{CIA} = [\text{Al}_2\text{O}_3 / (\text{Al}_2\text{O}_3 + \text{CaO}^* + \text{Na}_2\text{O} + \text{K}_2\text{O})] \times 100$$

where CaO* is the amount of CaO incorporated in the silicate fraction only.

The CIA values are directly represented on A-CN-K ($\text{Al}_2\text{O}_3 - \text{CaO} + \text{Na}_2\text{O} - \text{K}_2\text{O}$) diagram; high CIA values reflect the removal of labile cations relative to stable residual constituents during weathering, and low CIA values indicate the near absence of chemical alteration (Nesbitt and Young, 1982). The samples can be subdivided into different weathering states according to their CIA values: strong weathering, intermediate weathering and weathering to fresh rock (Figure 3.7a).

WIP is a weathering index that provides a relative measure of the removal of elements, which include most of the mobile cations, during weathering (Parker, 1970). As this index includes many chemical components, it may be more reliable than a simple index, which only relies on one or two components. The smaller the measured WIP value, the greater the intensity of weathering (Ng et al., 2001). This index is calculated as follows:

$$\text{WIP} = 100 \times (2\text{Na}_2\text{O}/0.35) + (\text{MgO}/0.9) + (2\text{K}_2\text{O}/0.25) + (\text{CaO}/0.7)$$

WIP and CIA can be correlated through a WIP/CIA diagram, since generally at great values of CIA coincide smaller WIP values with stronger weathering (Figure 3.7b).

W index is an alternative statistical empirical index of chemical weathering that is extracted by the principal component analysis (PCA) of a large dataset derived from unweathered igneous rocks and their weathering profiles (Ohta and Arai, 2007).

W index is extracted using statistical empirical laws, and possesses a number of unique properties that are not found in conventional indices: for example, it is sensitive to chemical changes that occur during weathering because it is based on eight major oxides, whereas most conventional indices are defined by between two and four oxides.

W can be calculated using the formula:

$$\text{W} = 0.203 \times \ln(\text{SiO}_2) + 0.191 \times \ln(\text{TiO}_2) + 0.296 \times \ln(\text{Al}_2\text{O}_3) + 0.215 \times \ln(\text{Fe}_2\text{O}_3) - 0.002 \times \ln(\text{MgO}) - 0.448 \times \ln(\text{CaO}) - 0.464 \times \ln(\text{Na}_2\text{O}) + 0.008 \times \ln(\text{K}_2\text{O}) - 1.374$$

The W values are represented on M-F-W diagram, where M and F vertices characterize mafic and felsic rock source (Fig 3.7c), respectively, while the W apex identifies the degree of

weathering of these sources, independent of the chemistry of the unweathered parent rock (Ohta and Arai, 2007).

The equations used to calculate M and F are here reported:

$$M = -0.395 \times \ln(\text{SiO}_2) + 0.206 \times \ln(\text{TiO}_2) - 0.316 \times \ln(\text{Al}_2\text{O}_3) + 0.160 \times \ln(\text{Fe}_2\text{O}_3) + 0.246 \times \ln(\text{MgO}) + 0.368 \times \ln(\text{CaO}) + 0.073 \times \ln(\text{Na}_2\text{O}) - 0.342 \times \ln(\text{K}_2\text{O}) + 2.266$$

$$F = 0.191 \ln(\text{SiO}_2) - 0.397 \times \ln(\text{TiO}_2) + 0.020 \times \ln(\text{Al}_2\text{O}_3) - 0.375 \times \ln(\text{Fe}_2\text{O}_3) - 0.243 \times \ln(\text{MgO}) + 0.079 \times \ln(\text{CaO}) + 0.392 \times \ln(\text{Na}_2\text{O}) + 0.333 \times \ln(\text{K}_2\text{O}) - 0.892$$

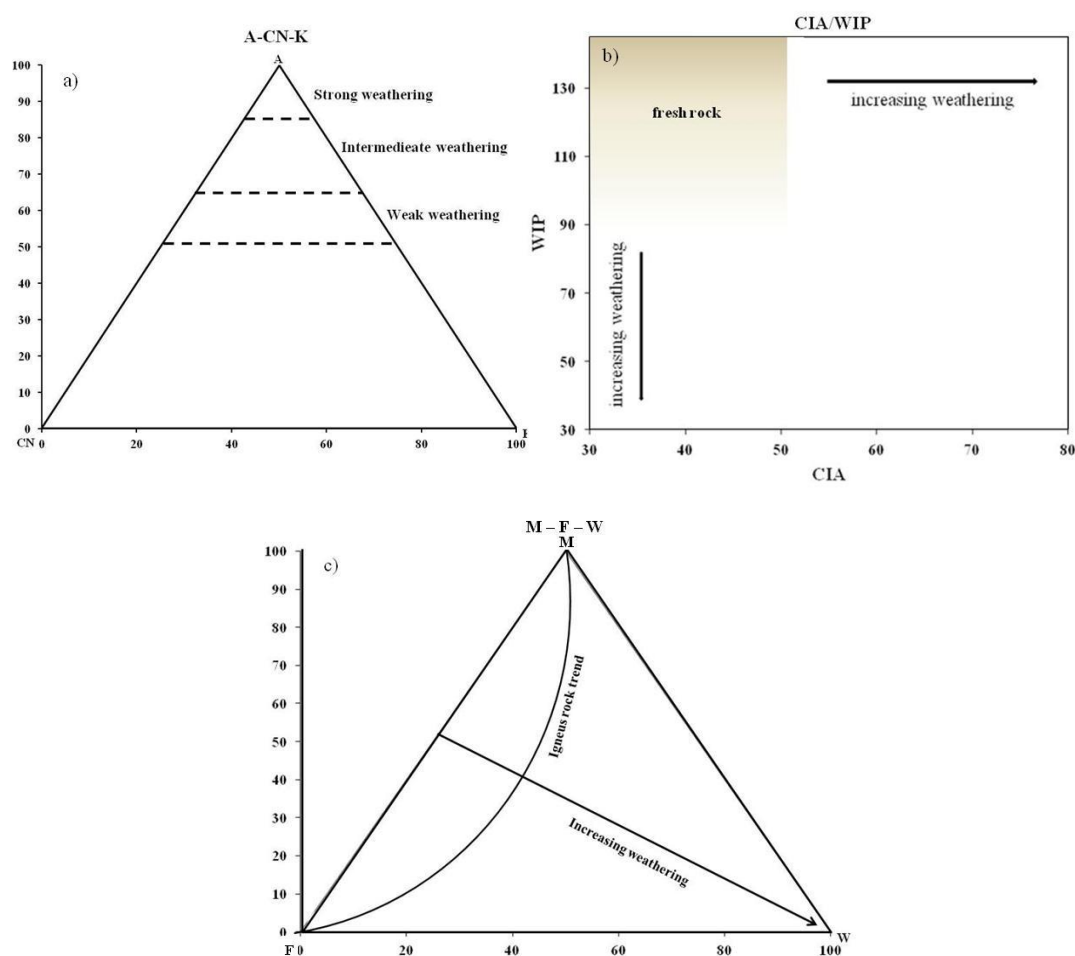


Figure 3.7: Alteration index diagram: a) A-CN-K (Al_2O_3 - $\text{CaO} + \text{Na}_2\text{O}$ - K_2O) diagram (Nesbitt and Young, 1982); b) WIP/CIA diagram (Bahlburg and Dobrzinski, 2011); c) MFW diagram (Ohta and Arai, 2007).

Analytical details

Scanning electron microscopy (SEM) observations and chemical composition of mineralogical phases on polished thin sections were determined with an Energy Dispersive Spectrometer at DiSTAR, University of Napoli Federico II (using a JEOL JSM-5310 electron microscope and an Oxford Instruments Microanalysis Unit, equipped with an INCA X-act detector and operating at 15 kV primary beam voltage, 50-100 mA filament current, variable spot size, from 30,000 to

200,000x magnification, 20 mm WD and 50 s net acquisition real time). Measurements were made with an INCA X-stream pulse processor and with INCA Energy software. Energy uses the XPP matrix correction scheme, developed by Pouchou and Pichoir (1988), and the Pulse Pile up correction. The quant optimization is carried out using cobalt (FWHM - full width at half maximum peak height- of the strobed zero = 60-65 eV). The following standards, coming from Smithsonian Institute, were used for calibration: diopside (Ca), San Carlos olivine (Mg), anorthoclase (Al, Si), albite (Na), rutile (Ti), fayalite (Fe), Cr₂O₃ (Cr), rhodonite (Mn), orthoclase (K), apatite (P), fluorite (F), barite (Ba), strontianite (Sr), zircon (Zr, Hf), synthetic Smithsonian orthophosphates (REE, Y, Sc), pure vanadium, niobium and tantalum (V, Nb, Ta), Corning glass (Th and U), sphalerite (S, Zn), sodium chloride (Cl), and pollucite (Cs). The K α , L α , L β , or M α lines were used for calibration, according to the element (Melluso et al. 2010; Guarino et al. 2016). Backscattered electron (BSE) images were obtained with the same instrument (Figure 3.8).



Figure 3.8: Scanning Electron Microscope JEOL JSM 5310 and Oxford EDS.

3.5 X-RAY Fluorescence (XRF)

General outline

The X-ray fluorescence spectroscopy (XRF) allows to determine the elemental composition of a sample through the study of the X fluorescence radiation.

This radiation is emitted by the atoms of the sample as a consequence of an excitation which is obtained typically by irradiating the sample with X-rays and Gamma-rays at high-energy. Similar effects are obtained using ion beams.

When an atom of the sample is exposed to incident radiation of suitable energy there is a certain probability that an electron, initially in a state of energy E_1 , is torn from it, producing a gap in the electronic structure of the atom. This phenomenon is known as the photoelectric effect (Franzini et al., 1975).

To restore the equilibrium conditions, an electron with higher energy $E_2 > E_1$ replaces the empty gap by releasing a photon with energy equal to $E = E_2 - E_1$. Only the transitions that respect the rules of quantum mechanics are permitted.

The term fluorescence refers to the fact that as a consequence of the irradiation a re-emission of radiation with a longer wavelength is obtained.

The fluorescence radiation emitted by a specific chemical element has a characteristic spectrum with lines at known energies, depending from the specific electronic structure of the element atoms (Leoni e Saitta, 1976).

A qualitative analysis of a sample is possible by the identification of characteristics emission lines of each chemical element.

According to the traditional notation, the energy levels are indicated by two letters. The first (K, L, M, ...) indicates the shell affected by the transition. The second ranking the energy of transition ($\alpha, \beta, \gamma, \dots$) (Figure 3.9).

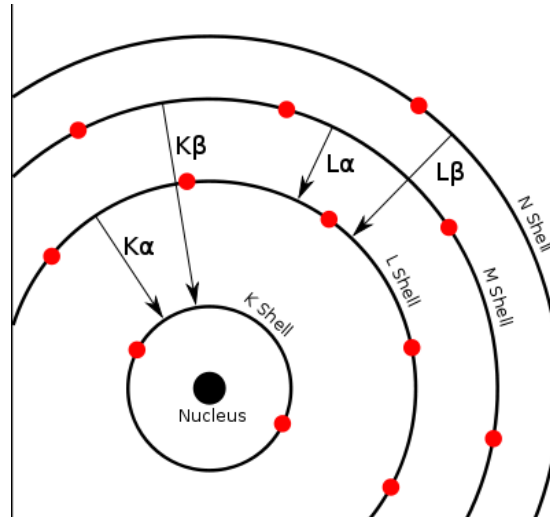


Figure 3.9: Representation of atomic energy levels.

A quantitative analysis requires a suitable processing, mainly consisting in a comparison of the intensity of X-ray lines with those of a standard samples containing known amounts of the element to be estimated.

Analytical details

The X-ray fluorescence spectrometry was performed on representative samples selected on the basis of mortars typology (bedding, coating and floor ones) at CTGA (Group Technical Centre) Italcementi.

The analysis was carried out on powder or bead (glass disk).

The latter is a glass disk result of the fusion of a sample powder with a suitable mineralizing that high temperature melts and becomes a solvent for the component oxides of the sample. This forms a homogeneous solution that under appropriate cooling conditions produces a homogeneous and amorphous glass.

- XRF spectrometer BRUKER S8 (Figure 3.10)
- Electric fusion equipment KATANAX K2 Prime (Figure 3.11)



Figure 3.10: XRF spectrometer BRUKER S8 Tiger.



Figure 3.11: Pouring of the melt sample from the crucible into the mold (KATANAX K2 Prime).

3.6 Thermal analysis

General outlines

Thermal analyses include a group of analytical procedures which provides information on the physical properties of a material subjected to a scheduled thermal treatment.

Thermal analysis can be applied to mortars using three basic techniques, Thermogravimetry (TGA), Differential Thermal Analysis (DTA) and Differential Scanning Calorimetry (DSC). Each method, though having its distinct features, gives approximately the same information being based on the physical transformations that compounds experience on being heated in controlled conditions.

Thermogravimetry (TGA) measures the weight loss in a sample as it is heated. Weight loss during heating can be related to specific physical decompositions in the materials that are due to the effects of increasing temperature. For example, gypsum can be recognized by weight loss of approximately 26.5 wt.% as a result of the transformation to anhydrite (Middendorf et al., 2005).

Differential Thermal Analysis (DTA) is the most useful, and most used methods. With DTA, a graph is continuously plotted during heating that shows the temperature difference between the sample and an inert standard (usually Al_2O_3), which is heated at the same rate and at the same time. Endothermic peaks are recorded when the standard continues to increase in temperature and the sample does not. At these times the sample is absorbing heat energy and using it to drive decomposition or a mineralogical transformation. This is usually the loss of chemically bound components, for example water from gypsum or carbon dioxide from calcite and dolomite. The endothermic or exothermic transitions are characteristic of particular minerals, which can be identified and quantified using DTA (Middendorf et al., 2005).

Differential Scanning Calorimetry (DSC) follows the same basic principle as DTA. Whereas temperature differences are measured in DTA, during heating using DSC, energy is added to maintain the sample and the reference material (Al_2O_3) at the same temperature. The amounts of energy is recorded and used as a measure of the calorific value of the thermal transitions that the sample experiences (Middendorf et al., 2005).

DTA and DSC pose another advantage over TGA in the identification of minerals in mortars, since they are capable of resolving polymorphic transformations in compounds that do not involve weight loss.

Some workers contend that it is possible to distinguish between different mortar and binder types on the basis of data derived from thermal analysis (Bakolas et al., 1995; Moropoulou et al., 1995, 1999; 2000 and 2005).

To do this they use the weight loss from a sample during thermogravimetry between 200°-600°C to represent all the structurally bound water (SBW) in hydraulic components and 600° - 850° C to represent decomposition of calcium carbonate (CaCO₃).

They plot CO₂/SBW ratio against the weight loss due to the decomposition of calcite.

CO₂/SBW ratio was calculated, shows inverse of hydraulicity in relation to the CO₂ (weight loss %). The inverse trend of hydraulicity of the mortar samples is shown to augment exponentially with CO₂.

They were able to define domains on the graphs for crushed brick mortars, cements and hot-lime mortars though the best distinction was between these hydraulic types and the non-hydraulic lime mortars.

In this research project, according with these workers, TGA-DTA analyses will be used to evaluate the mortar hydraulicity.

Analytical details

Thermal analyses were performed on powdered bulk samples and on their finer sieved fraction (<63µm), that is mostly formed by binder, by means of a Mettler Toledo TGA/SDTA 851° instrument and Mettler Toledo STAR° SW 11.0 software (Figure 3.12a) and by NETZSCH STA 449 F3 Jupiter (Figure 3.12b.) instrument in alumina crucibles, at CTGA (Group Technical Center) of Italcementi Group at Bergamo. For an effective evaluation of the aerial or hydraulic character of the analyzed mortar binders, the mass losses in the range from 40 to 1000 °C, at a heating rate of 10°C/min in nitrogen atmosphere (flow 60 mL/min).

In agreement with the literature data (Bakolas et al., 1995; 1998; Moropouloou et al., 1995, 1999; 2000 and 2005), the mass losses were attributed as follows.

- a) the mass loss up to 120° C is related to removal of adsorbed water, prevalently due to the presence of hydraulic binders, in which hygroscopic phases form during the setting and hardening processes;
- b) the loss of water in the temperature range 120-200° C is due to the crystallization water of hydrated salts, for example gypsum that may originate from the sulfation and dissolution processes of carbonates or may have been artificially added to the binder;
- c) the mass loss in the temperature range 200-600° C can be entirely attributed to the chemically bound water of hydraulic phases (C-A- S-H);
- d) the mass loss above 600° C is essentially due to the decomposition of carbonates.

Samples characterized by both high amount of structurally bound water to hydraulic compounds and low amounts of CO₂ are considered to be representative of hydraulic mortars.

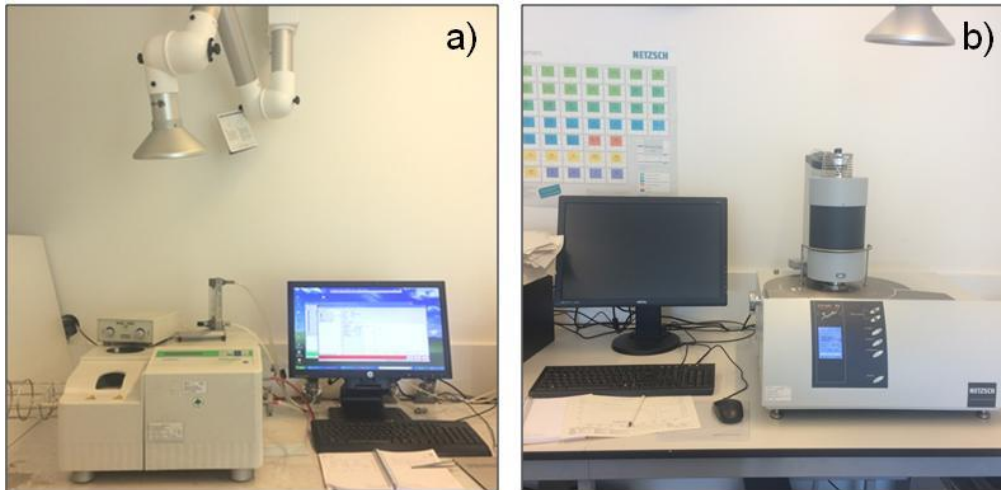


Figure 3.12: a) Mettler Toledo TGA/SDTA; b) NETZSCH STA 449 F3, at Italcementi (BG).

3.7 Mercury intrusion porosimetry (MIP)

General outline

The mercury porosimetry, developed in 1945 by Ritter and Drake allows to measure the volume and dimensions of macropores and mesopores in a porous solid (Ritter and Drake, 1945).

The technique is based on the mercury properties to be a non-wetting liquid with a great variety of solids. Thanks to this characteristic, the mercury penetrates through the open pores of a solid sample under the effect of an increasing pressure.

The radius of the penetrated pores is inversely proportional to the pressure exercised according to a given relation from Washburn (Washburn, 1921) in which a number of assumptions have to be taken into consideration:

- the surface tension of mercury and the contact angle with the solid are constant during the analysis
- the intrusion pressure should be at the equilibrium
- the pores are considered to have a cylindrical shape
- the solid does not deform under the effect of pressure

The distribution of pore volume as a function of their radius are then obtained by measuring the amount of mercury penetrated into the pores of the sample and the equilibrium pressure at which it occurs.

The determination of the pore size by the mercury penetration technique is based on the behavior of "non-wetting" liquids in the capillaries.

A liquid is "non-wetting" when its contact angle with a solid is greater than 90° .

A “non-wetting” liquid can’t be spontaneously absorbed by the solid due to the surface tension of the liquid itself. However, this penetration resistance can be overcome by applying an external pressure to the liquid.

The pressure required is a function of the inlet diameter of the pore. The relationship between the inlet diameter of the pore and the pressure exerted, in the case of pores of cylindrical geometry, it is expressed by the following function commonly known as equation of Washburn:

$$pr = -2\gamma \cos \theta$$

where:

r is the radius of the pores expressed in nm;

γ is the surface tension of mercury expressed in dynes/cm;

θ is the contact angle between mercury and the solid, expressed in °;

p is the absolute pressure expressed in Pascal.

This relationship derives from several considerations.

In a capillary of circular section, the surface tension of the liquid is exerted in the contact area for a length equal to the circumference of the pore. This force is perpendicular to the plane of the contact surface.

The force pushing the liquid out of the capillary is equal to:

$$-2 \times \pi \times r \times \gamma \times \cos \theta$$

Against this force, the external pressure exerted on the area within the circumference of contact, will be:

$$\pi \times r^2 \times p$$

At equilibrium, the two forces have the same value and the pore radius is then:

$$R = (-2 \times \gamma \times \cos \theta) / p$$

The contact angle between mercury and the sample depends on the chemical nature of the sample and varies between 125° and 160°. By convention, a value of 141.3° is commonly used to allow a comparison of results by different researchers.

Even the surface tension of mercury is variable as a function of the temperature and the most appropriate must be taken into account.

Assuming a surface tension of mercury equal to 480mN/m, a contact angle equal to 141.3° and by modeling the pores as cylindrical, the radius is obtained by the following relationship:

$$R = 75000 / p.$$

Analytical details

The mercury intrusion porosimetry analyses were performed at CTGA (Group Technical Centre) Italcementi of Bergamo on representative samples selected on the basis of typology of mortars and amount of samples.

To cover the entire range of pressures, two equipments were used:

- PASCAL 140 (up to 0,4 MPa)
- PASCAL 240 (up to 200 MPa)

The two instruments (Figure 3.13), used consecutively, allow to determine:

- total volume of pores of radius between 3,75 nm and 800 μ m (expressed in mm³/g);
- porosity (expressed in%) and bulk density (expressed in g/cm³);
- apparent density (expressed in g/cm³) and specific surface (expressed in m²/g);
- graphical and numerical representation of the distribution of pore sizes.



Figure 3.13: Porosimeters PASCAL 140 and PASCAL 240 at CTGA Italcementi (BG).

Chapter 4

Piscina Mirabilis: materials and results

4.1 Materials

Thirteen samples of mortars were collected: nine from to the pillars and the base of pillars and four belonging to the walls and the base of walls (Figure 4.1 and 4.2a-b). Nine of these are coating mortars and four are bedding mortars (Table 4.1).

For security reasons, it was possible to sample only one side of the structure.

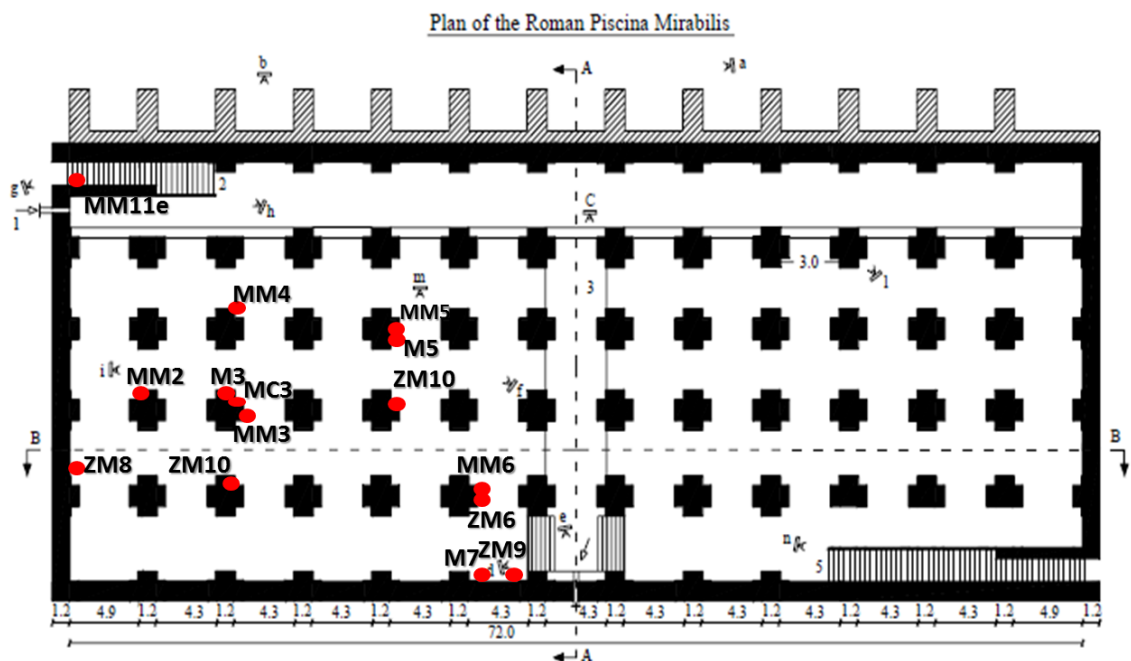


Figure 4.1 : Sketch map of the *Piscina Mirabilis* with sampling site (modified after Amalfitano et al., 1998.)

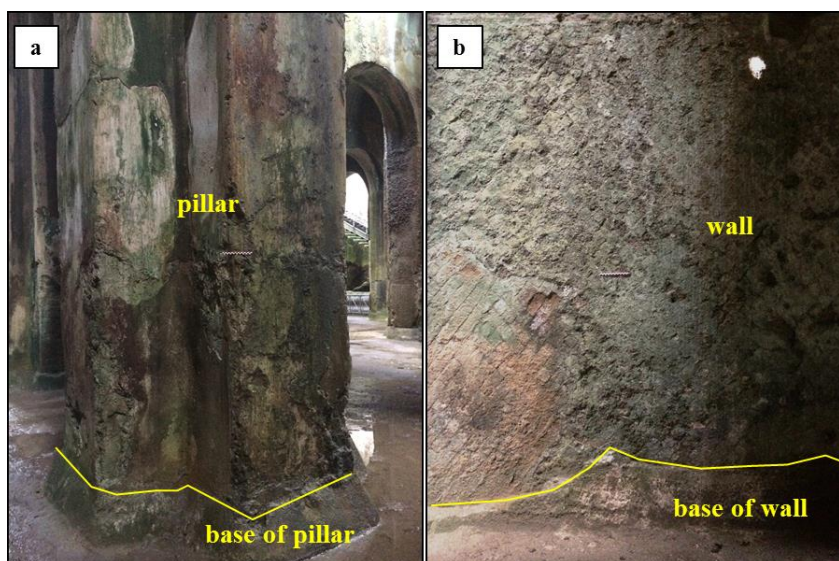


Figure 4.2: Pictures of a) pillar and base of pillar; b) wall and base of wall.

Table 4.1: samples, location and typology.

SAMPLES	LOCATION	TYOLOGY
MM2	Pillar	coating mortar
MM3	Pillar	concretion and coating mortar
M3	Pillar	bedding mortar
MM4	Pillar	concretion and coating mortar
M5	Pillar	bedding mortar
MM5	Pillar	concretion and coating mortar
MM6	Pillar	coating mortar
ZM6	Base of pillar	coating mortar
M7	Pillar	bedding mortar
ZM8	Base of wall	concretion and coating mortar
ZM9	Base of wall	concretion and coating mortar
ZM10	Base of pillar	concretion and coating mortar
M11e	Wall	bedding mortar

A photographic documentation has been produced before and after the sampling (Figure 4.3).



Figure 4.3: picture before and after sampling.

All samples underwent to a range of analytical techniques aimed at the petrographic, mineralogical, and chemical characterization of the materials.

4.2 Results

4.2.1 Macroscopic observation

Macroscopic observation was the first approach to the study of these materials, in order to identify the type of material and directing the following detail analysis.

Coating mortars show light yellow to dark brown colour. The aggregates are made of ceramic fragments, volcanic fragments and pumice variable in size from mm - to - cm (Figure 4.4).

MM3, MM4, MM5, ZM8, ZM9 and ZM10 shows a layer of concretion up to 2 cm.

MM6 samples is different from the others, since it appears greatly altered and for this reason macroscopic observations were very difficult.

Bedding mortars show light yellow to light grey colour. The aggregate consists of volcanic fragments and pumice from mm - to - cm sized (Figure 4.5).

M3 sample shows the presence of a layer of NYT (Neapolitan Yellow Tuff) thick about 1 cm, derived from the tuff block in contact with the mortar. All mortars samples show the presence of mm - to- cm lime lumps.

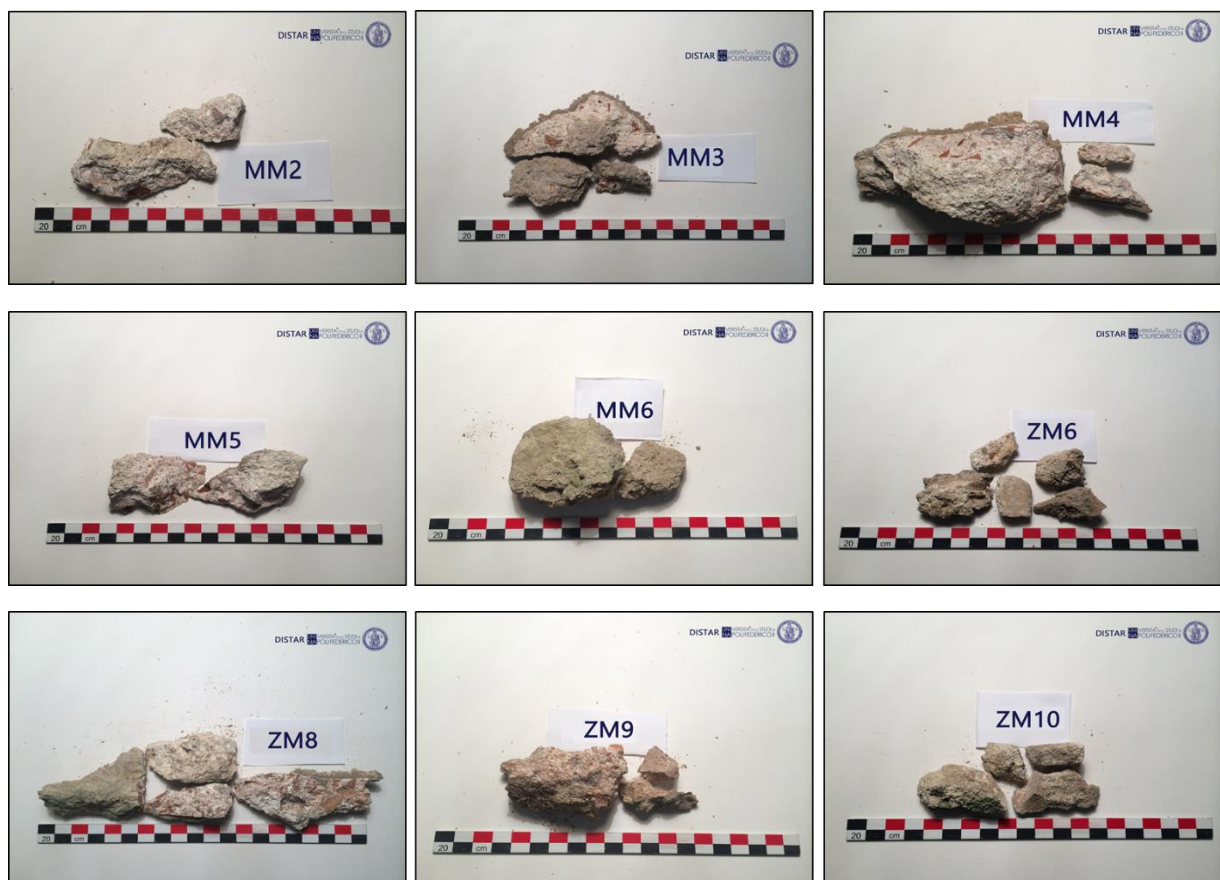


Figure 4.4: Macroscopic images of coating mortars.



Figure 4.5: Macroscopic images of bedding mortars.

4.2.2 Petrography

Thin section observations and modal analyses - performed counting 1500 points for each section (Table 4.2) - allowed to distinguish three distinct groups (A, B and C).

Coating mortar of pillars were assigned to group A, coating mortars collected from the base of pillars and walls pertain to group B and then group C is populated by bedding mortars of pillars and walls.

All mortars show presence of lime lumps (2mm – 1cm), which origin is to be sought in the properties of the slaked lime (calcium hydroxide) and in the water/quicklime ratio (Bakolas et al. 1995; Barba et al., 2009). Their formation occurred during the slaking process of the lime and it is due to an insufficient seasoning of the calcium hydroxide and a low water/lime ratio.

Therefore, the lump's compositions is mainly calcite (CaCO_3) and represents the pure lime in the mortars. Its composition is similar to the limestone used to make the lime (Elsen, 2006).

Moreover, all mortars show secondary calcite such as in the binder, on the pores rim and pumices vesicles.

The A group (MM2, MM3, MM4, MM5), is characterized by a whitish - yellowish binder with with cryptocrystalline (36.2 Vol.%) to micritic texture (7.4 Vol.%) (Figure 4.6a and 4.6b).

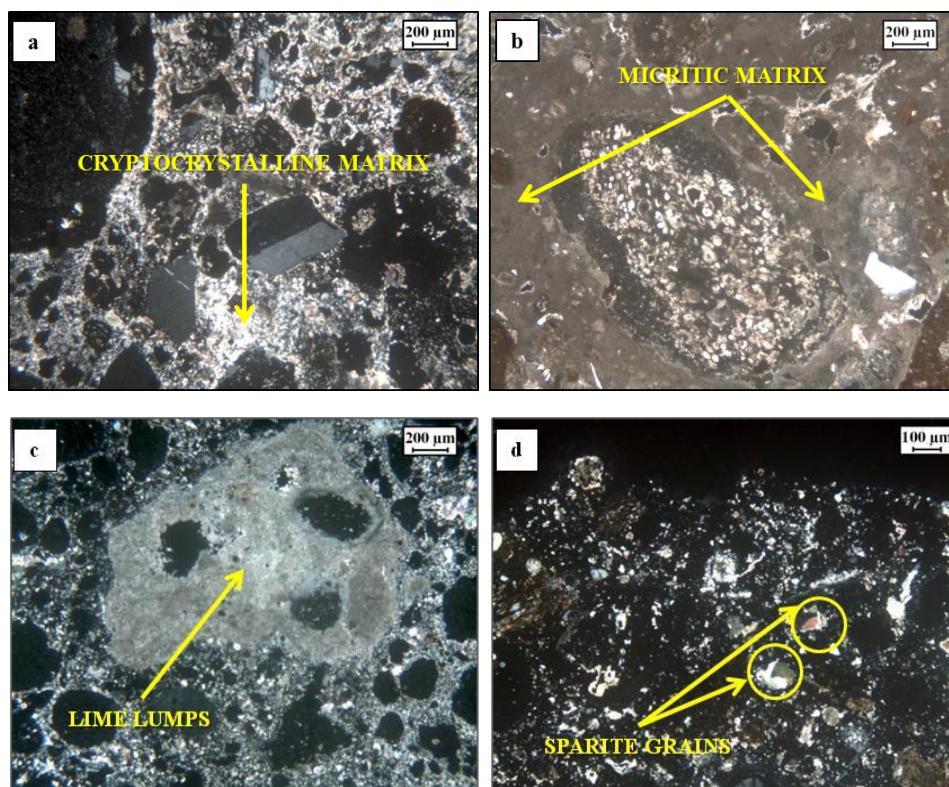
Moreover, small and fractured lumps with not well-defined edges (6.2 Vol.%, Figure 4.6c) occur in the binder along with sparite grains (2.2 Vol. %, Figure 4.6d). Sparite grains origin can be related to a residual limestone, not completely calcinated.

The aggregate fraction appears moderately sorted and composed mainly of ceramic fragments (20.4 Vol.%), volcanic fragments (4.6 Vol.%), pumice (11 Vol.%, Figure 4.6e) and scoriae with clear reaction rim (2.4 Vol.%), and crystal fragments such as sanidine (Figure 4.6f), clinopyroxene and plagioclase (5.0 Vol.%).

Ceramic fragments exhibit subangular shape and size up to 1 cm and show often mineralogical and textural differences. Some ceramic fragments, for example, show low optical activity and some high, some others, are characterized by volcanic aggregates, scoriae, volcanic glass and other only by crystal fragments (Figure 4.6g and 4.6h).

Volcanic components mainly consist of tuff fragments, characterized by pumice and obsidian fragments, lithics and crystals such as alkaline feldspar (sanidine), clinopyroxene, biotite and plagioclase set in an ashy matrix mainly constituted by volcanic glass shards affected by secondary mineralization processes (Figure 4.6i and 4.6l).

The mixture that characterizes these mortars is called *cocciopesto* (a mix of lime, powder obtained crushing shattered tiles, brick and pottery and different type of aggregates). *Cocciopesto* is a typical building material used in the ancient Rome for the waterproofing of structures such as cisterns and floors (Collepari et al., 2009)



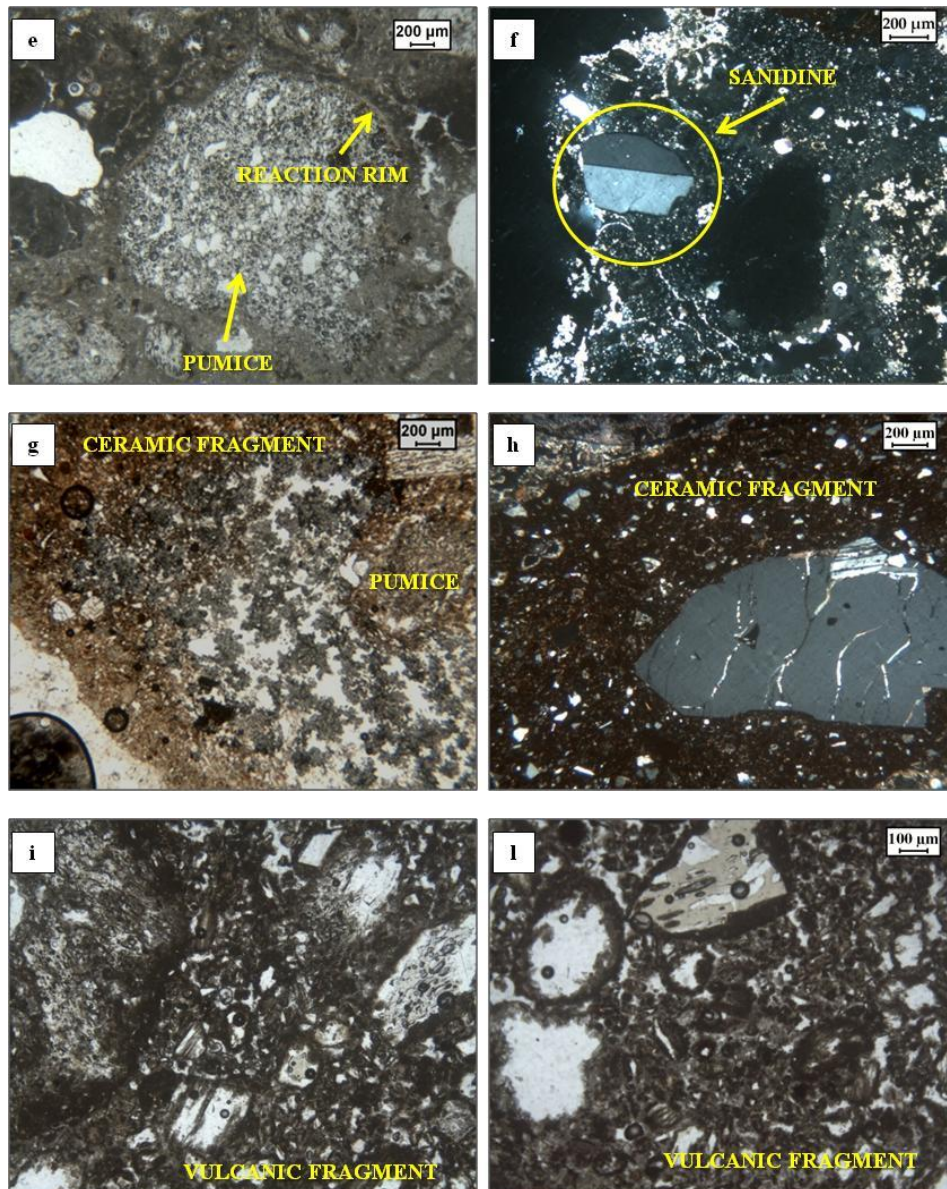


Figure 4.6: Microphotographs of mortars belonging to Group A: a) cryptocrystalline matrix (CPL) in sample MM2; b) micritic matrix (CPL) in sample MM3; c) lime lump (CPL) in sample MM3; d) sparite grains in sample MM5; e) pumice with reaction rim (PPL) in sample MM4; f) crystal fragment of sanidine (CPL) in sample MM2; g) and h) different type of ceramic fragments in sample MM4 (PPL) and (CPL); i) and h) volcanic fragments (PPL) in samples MM3 and MM5. CPL: Cross Polarized Light; PPL: Plane Polarized Light.

Moreover MM3, MM4, MM5 samples show a layer of concretion, with thickness up to 3 cm (Fig 4.7). Layers consist in couplets of alternating micrite and sparite laminae (laminae of porous, fine-grained, opaque, micritic and transparent, dense, coarse-grained, sparitic calcite).

The sparitic laminae consist in elongate, columnar and wedge-shaped crystals oriented at right angles to the lamination. The lamina couplets define the layering visible in hand specimen and thin section.



Fig 4.7: Concretion layers in sample MM4 (CPL).

The group B (ZM6, ZM8, ZM9, ZM10) is also characterized by the presence of *cocciopesto*.

The binder is characterized by beige color with cryptocrystalline (22.3 Vol.%, Figure 4.8a) to micritic texture (14.0 Vol.%, Figure 4.8b). Also, here the binder shows the presence of small and fractured lime lumps (5.7 Vol.%, Figure 4.8c) and sparite grains (0.3 Vol.%, Figure 4.8d).

The aggregates fraction is characterized mainly by ceramic fragments (34 Vol.%) that, differently from group A samples, presents a larger size (up to 2 cm), volcanic fragments (6.3 Vol.%), scoriae (3.3 Vol.%), pumices (4.3 Vol. %, Figure 4.8e), and crystal fragments such as sanidine, clinopyroxene (Figure 4.8d) and plagioclase (2.67 Vol.%).

Petrographic observations revealed also in these samples a variability among ceramic fragments (Figure 4.8f). These sometimes contain a temper of different mineralogical composition, such as quartz instead of clinopyroxene or pumice.

The samples ZM8, ZM9 and ZM10, as the other samples of A group, show the presence of a concretion layer (2 mm-1 cm) also characterized by alternating layers of micrite and sparite (Figure 4.8g and 4.8h).

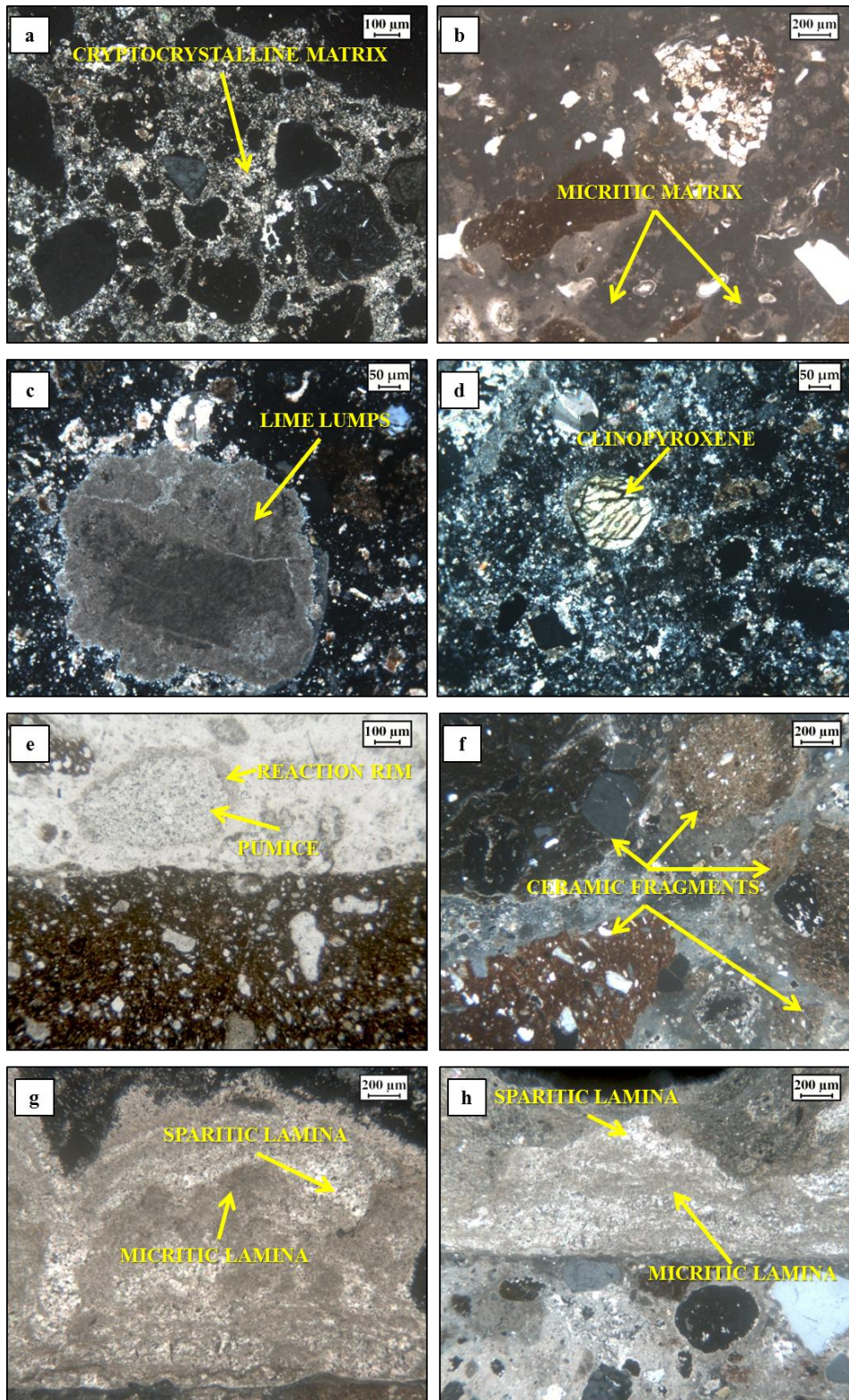


Figure 4.8: Microphotographs of mortars belonging to Group B: a) cryptocrystalline matrix (CPL) in sample ZM6; b) micritic matrix (CPL) in sample ZM8; c) lime lumps (CPL) in sample ZM6; d) sparite grains and clinopyroxene (CPL) in sample ZM9; e) pumice with reaction rim (PPL) in sample ZM10; f) different types of ceramic fragments (CPL) in sample ZM9; g) concretion layers (CPL) in sample ZM9; h) concretion layers (CPL) in sample ZM9.

Bedding mortar (M3, M5, M7) belongs to group C. These samples are characterized by a binder with brownish colour with micritic (29.3 Vol.%, Figure 4.9a) to cryptocrystalline (16.3 Vol.%,

Figure 4.9a) features. Lime lumps are present in the binder, showing undefined and irregular edges (15.0 Vol.%, Figure 4.9b). The aggregate of bedding mortars is thus poorly sorted, differently from the coating mortars, where it is well sorted. Their mineralogical composition includes volcanic fragments (1.0 Vol.%), scoriae (4.9 Vol.%) pumice (19.0 Vol.%, Figure 4.9c) and crystal fragments of clinopyroxene, sanidine and biotite (5.0 Vol.%, Figure 4.9d).

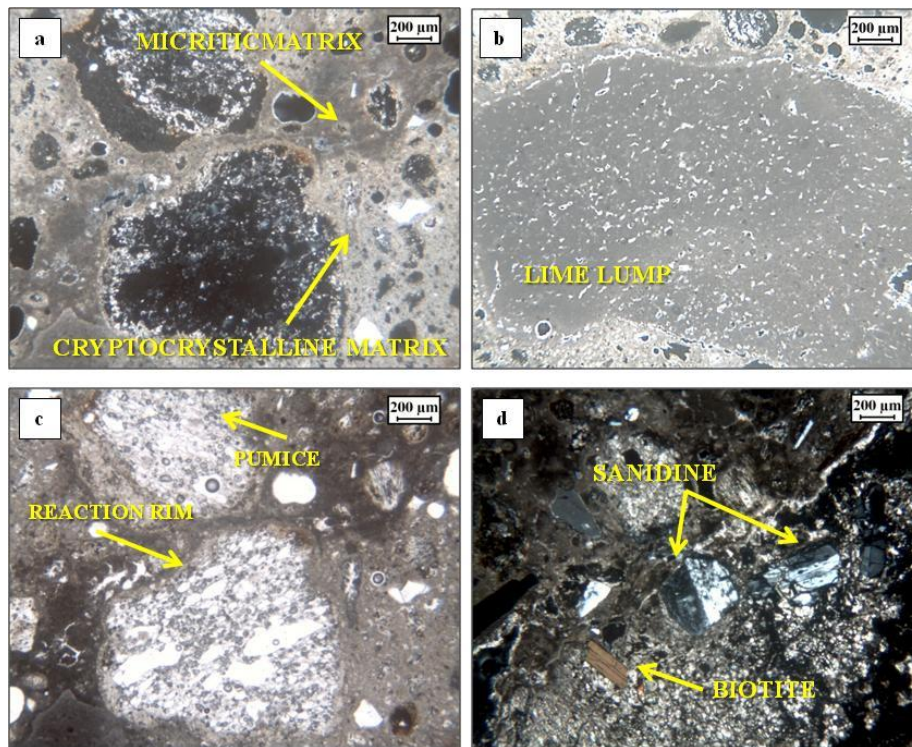


Figure 4.9: Microphotographs of mortars belonging to Group B: a) micritic matrix and sanidine (CPL) in sample M3; b) cryptocrystalline and micritic matrix (CPL) in sample M5; c) lime lumps (CPL) in sample M5; d) pumice with reaction rim (PPL) in sample M7.

Volcanic fragments can be identified as volcanic tuff, characterized by the presence of microcrystals immersed in an altered ashy matrix (Figure 4.10).

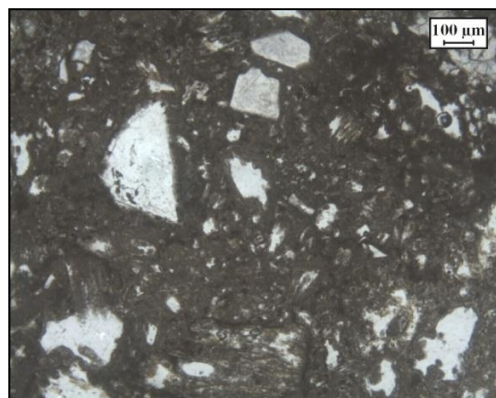


Figure 4.10: volcanic fragments (PPL) in samples M3.

M11e sample does not belong to any groups since it is a repair mortar.

A brownish colour of the binder with cryptocrystalline (49.7 Vol.%) (Figure 4.11a) to micritic aspect (12.7 Vol.%). The binder shows the presence of sparite grains (2.3 Vol.%) (Figure 4.11b) but no lime lumps. The aggregates are scarce and very poorly sorted; most of them are pumice (24.0 Vol.%) with well evident reaction rims (Figure 4.11c-d) and crystal fragments of sanidine (Figure 4.11d), clinopyroxene and plagioclase (3.7 Vol.%).

Table 4.2 reports the results of the modal analyses carried on the four selected samples.

It was evidenced that a low percentage of voids occurs in samples M11e (repair mortars) and MM5 (0.6 %), belonging to group A (coating mortars); this percentage increases in sample M3 (9.3%), a bedding mortar of group C. The modal analysis also shows that the percentage of aggregates is higher in coating mortars (MM5 and ZM8 samples) whereas in the bedding mortars (M3 and M11e sample) and in repair mortar (M11e sample) is lower (Figure 4.12).

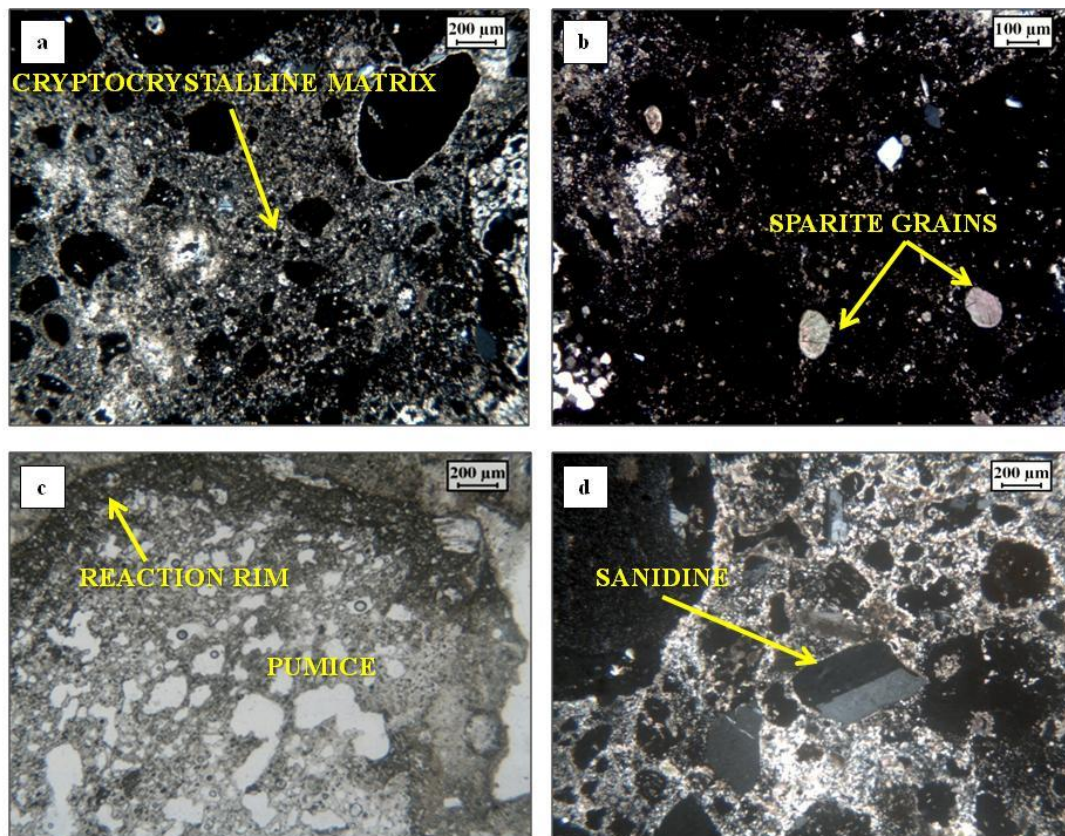


Figure 4.11: a) Cryptocrystalline matrix (CPL); b) sparite grains (CPL); c) pumice with reaction rim (PPL); d) sanidine (PPL).

Table 4.2: Modal analyses of selected mortars.

Mortars	MM5 (group A)	ZM8 (group B)	M3 (group C)	M11e (repair mortar)
Constituentes (Vol.%)				
Feldspar (Afs, Plg)	3.6	1.7	3.0	3.0
Mafic Minerals (Cpx, Am, Bt)	1.4	1.0	2.0	0.7
Volcanic fragments	4.6	6.3	1.0	0.0
Scoriae	2.4	3.3	4.7	0.0
Pumice	11.0	4.3	19.0	24.0
Ceramic fragments	20.4	34.0	-	-
Carbonate fragments	-	-	-	-
Sparite	2.2	0.3	-	2.3
Lime lumps	6.2	5.7	15.0	-
Micritic matrix	7.4	14.0	29.3	12.7
Cryptocrystalline matrix	36.2	22.3	16.7	49.7
Voids	0.6	1.7	9.3	-
Others	4.0	5.3	-	7.7
Total points	100.0	100.0	100.0	100.0
Total Binder	52.0	42.3	61.0	64.7
Total Aggregate	43.4	50.7	29.7	27.7
Binder/Aggregate ratio	1.2	0.8	2.1	2.3

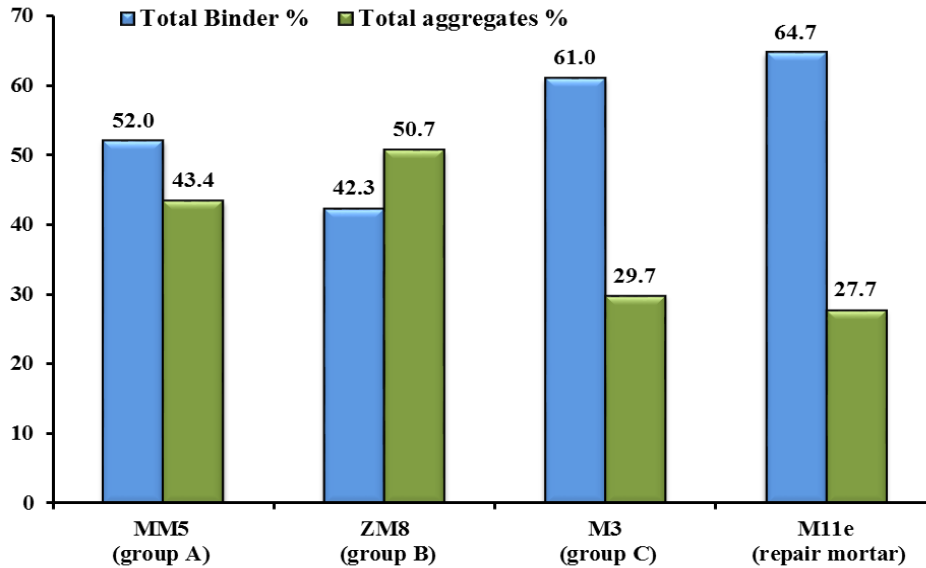


Fig 4.12: Histogram showing percentages of total binder and total aggregates in representative samples of mortars.

4.2.3 XRPD analysis

Samples were divided in binder, aggregates, and ceramic fragments, according to the UNI Normal 11305 document (mortar characterization) and then analyzed by XRPD. Results are shown in the Table 4.3, which confirmed the presence of the mineralogical phases identified in thin section (Table 4.2).

Table 4.3: Qualitative mineralogical (XRPD) composition of mortars.

Sample	Group	Main Binder Phases	Main Aggregates Phase	Main Ceramic Fragments Phases
MM2	group A	Cal, Gp, Tb	Phi, Cbz, Anl, San, Cpx, Mca	Qtz, Cal, San, Cpx, Hem, Mca
MM3	group A	Cal, Tb	Phi, Cbz, Anl, San, Cpx, Mca	Qtz, Cal, San, Hem, Mca
MM4	group A	Cal, Tb	Phi, Cbz, Anl, San, Cpx, Mca	Qtz, Cal, San, Hem, Mca
MM5	group A	Cal, Tb	Phi, San, Cpx, Mca	Qtz, Cal, San, Hem, Mca
ZM6	group B	Cal	San, Cpx, Mca	Qtz, Cal, San, Hem, Mca
ZM8	group B	Cal, Gp, Tb	Phi, Cbz, San, Cpx, Mca	Qtz, Cal, San, Cpx, Hem, Mca
ZM9	group B	Cal, Tb	Phi, Cbz, Anl, San, Cpx, Mca	Qtz, Cal, San, Cpx, Hem, Mca
ZM10	group B	Cal, Tb	Phi, Anl, San, Cpx, Mca	Qtz, Cal, San, Hem, Mca
M3	group C	Cal	Phi, Cbz, Anl, San, Cpx, Mca	
M5	group C	Cal	Phi, Cbz, Anl, San, Cpx, Mca	
M7	group C	Cal, Gp	Phi, Cbz, Anl, San, Cpx, Mca	
M11e	Repair mortar	Cal	Phi, Cbz, Anl, San, Cpx, Mca	

* Cal: calcite Tb: tobermorite; Gp: gypsum Phi: phillipsite; Cbz: chabazite; Anl: analcime; San: sanidine; Cpx: clinopyroxene; Mca: mica; Hem: hematite; Qtz: quartz.

The results of the XRPD analysis show for the binder phase mainly calcite, gypsum $\text{CaSO}_4 \cdot 2(\text{H}_2\text{O})$ and tobermorite $\{[\text{Ca}_4(\text{Si}_{5.5}\text{Al}_{0.5}\text{O}_{17}\text{H}_2)] \text{Ca}_{0.2}\text{Na}_{0.1} \cdot 4\text{H}_2\text{O}\}$ (Figure 4.13).

The presence of gypsum is due to neoformed material generated after weathering (sulphation of carbonates).

The presence of the tobermorite is very interesting, since XRPD analysis showed it in several samples. This is a low-crystallinity phase in fact, and its peaks are very difficult to detect.

Tobermorite is a rare, hydrothermal, calcium-silicate hydrate mineral with cation exchange properties (Jackson et al., 2017); it does not occur in conventional concretes, but occurs in Roman marine concrete (Stanislao et al., 2011; Jackson et al., 2013; Jackson et al., 2017) and occasionally, in hydrothermally altered volcanic rocks such as basaltic tuff (palagonite) from Surtsey volcano, Iceland (Jakobsson and Moore, 1986; Jackson et al., 2017).

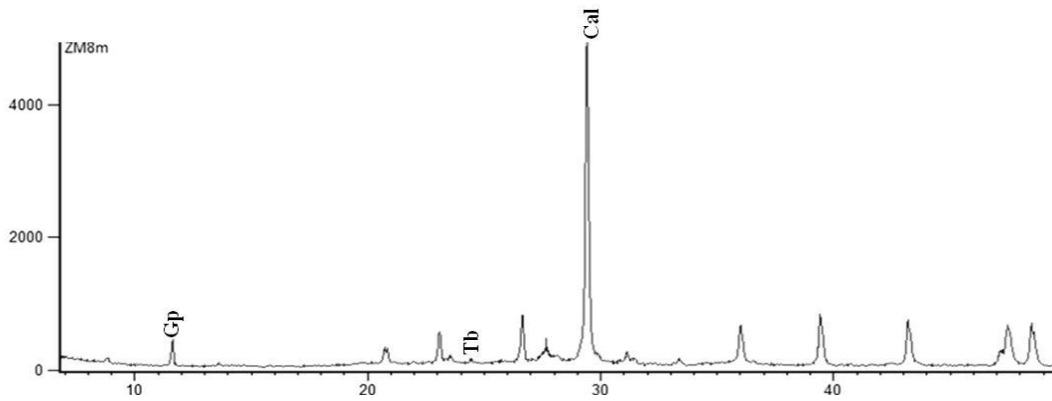


Figure 4.13: XRPD spectrum of ZM8 binder.

Referring to the aggregates, XRPD analyses suggest that they are constituted by fragments of Neapolitan Yellow Tuff (NYT), due to the presence of a typical zeolite association of this material i.e.: phillipsite, chabazite and analcime, (de Gennaro et al., 1999). Along with alkali feldspar, pyroxene and mica as a pyrogenic phases of the same formation (Figure 4.14). XRPD analysis of ceramic fragments showed calcite, quartz, mica, and hematite (Figure 4.15).

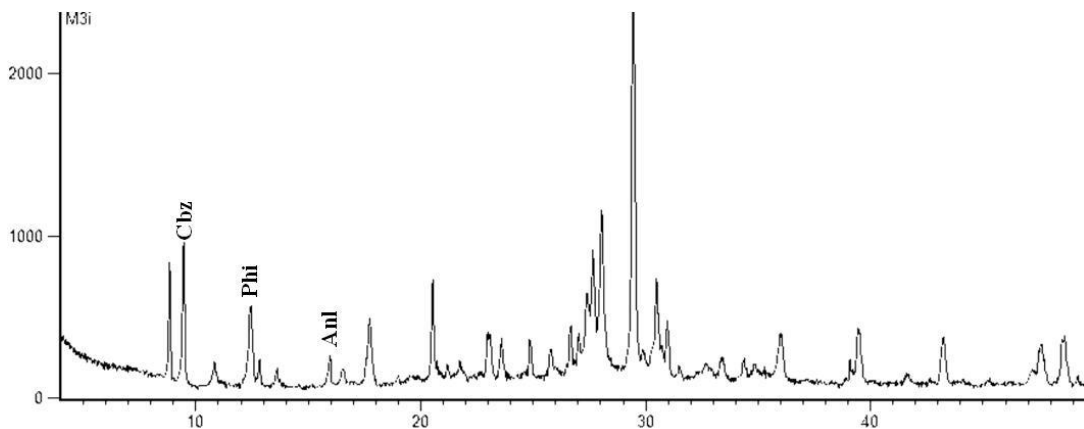


Fig 4.14: XRPD spectrum of M3 aggregates.

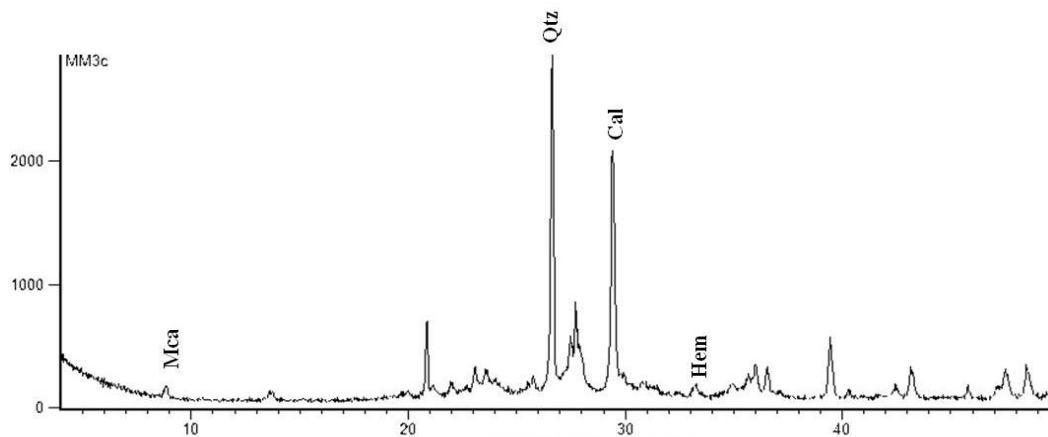


Figure 4.15: XRPD spectrum of MM3 ceramic fragments.

Moreover, XRPD analyses allowed to detect the presence of an amorphous (poorly crystalline) fraction, evidenced by the rising of the spectrum background between 18 and 40 °2 θ (Figure 4.16), probably related to the volcanic glass component and C-A-S-H phases.

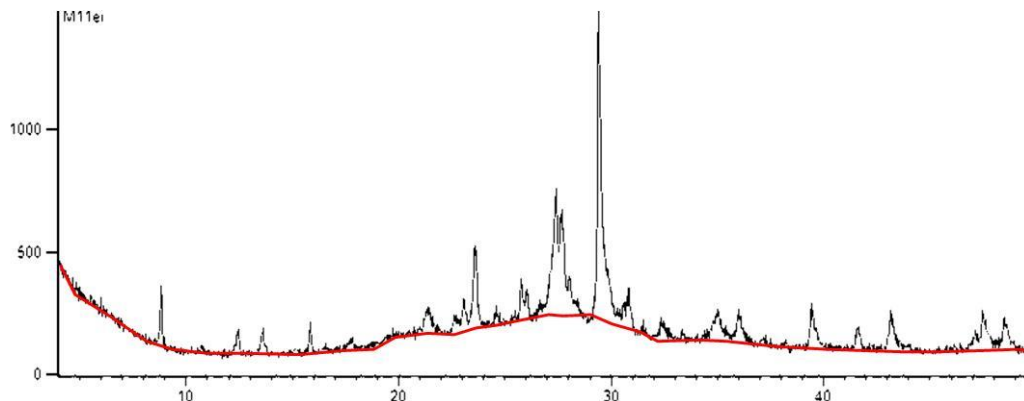
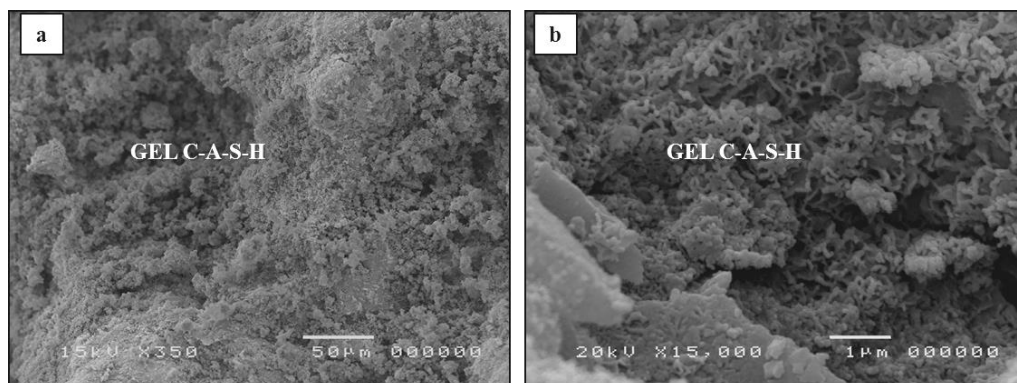


Figure 4.16: example of observed background in XRPD (sample M11e).

4.2.4 Micro-morphology and chemical analysis (SEM-EDS)

In order to support and integrate XRPD results, SEM observations were carried out on mortar fragments and polished thin sections.

As regards binder, results show the presence of newly formed hydraulic phases (C-A-S-H) (Figure 4.17a-b) and confirmed, as XRPD suggested, the presence of gypsum [$\text{CaSO}_4 \cdot 2(\text{H}_2\text{O})$] and tobermorite $\{[\text{Ca}_4(\text{Si}_{5.5}\text{Al}_{0.5}\text{O}_{17}\text{H}_2)]\text{Ca}_{0.14}\text{Na}_{0.14}\text{H}_2\text{O}\}$, that occurs in various crystal habits: "lamellar" and "acicular" (Figure 4.17c-d and Figure 4.18).



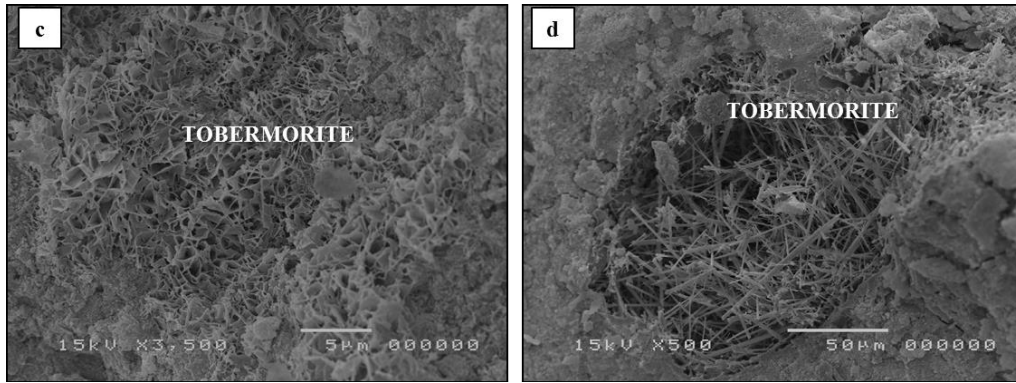


Figure 4.17: SEM images of: a) Gel C-A-S-H in sample MM2; b) Gel C-A-S-H in sample ZM8; c) tobermorite in sample MM3; d) tobermorite in sample ZM9.

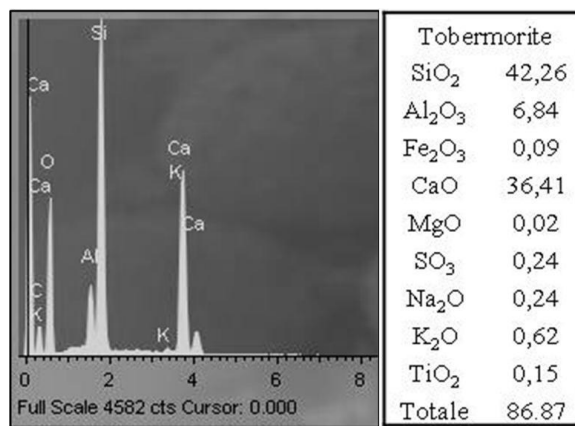


Figure 4.18: Spectrum and EDS analysis of tobermorite in sample MM3

To obtain semiquantitative information about the binder's composition and for, SEM-EDS microanalysis on polished thin section was carried out on the binder and on lime lumps (Table 4.4, Figure 4.19a-b).

Moreover SEM-EDS microanalyses allowed calculating the Hydraulicity Index (HI) according to Boynton's formula (Boynton, 1966).

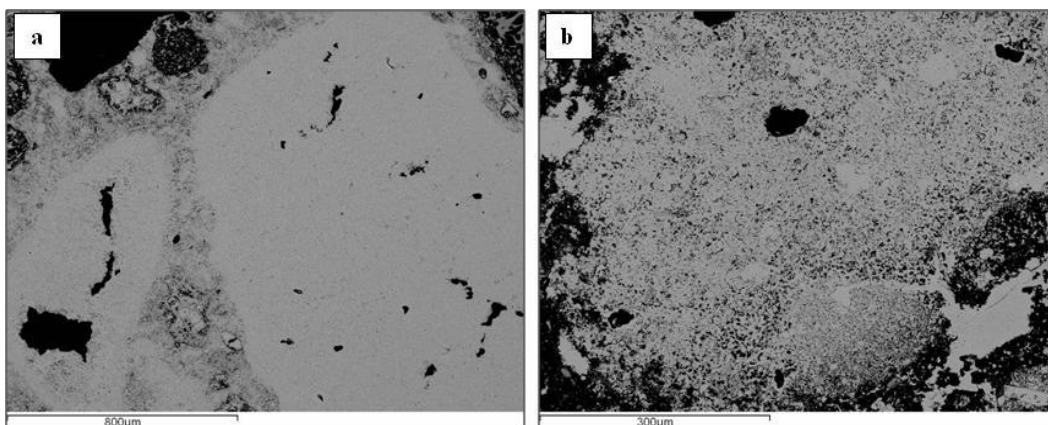


Figure 4.19: BSE-SEM images of: a) lime lumps in sample MM2; b) binder in sample M3.

The obtained chemical composition shows that studied lime lumps are composed mainly of CaO with very high values of CaO + MgO in general, between 90.67 and 96.56 % (Table 4.4, Figure 4.20). Concentrations of major elements in binder shows values of SiO₂+Al₂O₃ +Fe₂O₃ (8.48 – 17.02 %) higher than in lumps (1.79- 5.61 %) and lower contents of (CaO + MgO = 77.90 - 88.06 %; Figure 4.20).

Table 4.4 Average values of major oxides (wt.%, recalculated to 100%, EDS), lime lumps (L) and binder (B).

wt %	MM2 L	MM2 B	MM4 L	MM4 B	MM5 L	MM5 B	ZM8 L	ZM8 B	M3 L	M3 B	M7 L	M7 B
SiO ₂	2.61	12.56	0.90	5.07	4.13	14.31	1.09	11.11	1.75	4.13	3.62	6.09
TiO ₂	-	-	0.48	-	-	-	-	-	-	-	0.55	-
Al ₂ O ₃	0.94	4.40	1.18	6.72	1.48	5.44	0.70	3.27	0.49	4.18	0.78	2.91
Fe ₂ O ₃	0.48	0.06	0.15	-	-	0.23	-	-	0.39	0.17	-	-
MnO	-	-	0.18	-	-	0.14	-	-	-	-	-	-
MgO	0.16	1.67	0.61	1.33	0.09	1.63	0.29	0.71	0.68	0.43	3.80	0.68
CaO	93.15	79.47	93.14	85.16	90.58	76.28	93.66	83.54	95.89	87.63	90.44	88.41
Na ₂ O	0.07	0.55	-	0.39	0.60	0.57	0.21	0.29	-	0.50	0.03	0.51
K ₂ O	0.18	0.71	0.17	0.03	0.42	0.97	0.10	0.35	-	-	0	0.55
P ₂ O ₅	-	-	0.51	0.31	0	0	0.15	0.07	-	-	0.14	-
V ₂ O ₃	0.38	-	0.14	-	-	0.04	0.05	-	0.07	-	-	0.23
BaO	0.53	-	-	-	0.89	0	0.43	0.40	0.50	0.11	-	0.42
SO ₃	1.42	0.42	2.34	0.85	1.59	0.37	3.17	0.07	0.12	2.57	0.62	0.18
Cl-	0.09	-	-	0.14	0.23	0.02	0.14	0.05	0.13	-	-	-
F-	-	0.16	0.19	-	-	-	0.00	0.13	0.00	0.27	-	-
Total	100.00	100.00	100.00	100.00	100.00	100.00	100.00	100.00	100.00	100.00	100.00	100.00
SiO ₂ +Al ₂ O ₃ +Fe ₂ O ₃	4.04	17.02	2.23	11.79	5.61	19.98	1.79	14.38	2.62	8.48	4.40	9.01
CaO+MgO	93.31	81.14	93.75	86.49	90.67	77.90	93.95	84.25	96.56	88.06	94.25	89.10
HI	0.04	0.21	0.02	0.14	0.06	0.26	0.02	0.17	0.03	0.10	0.05	0.10

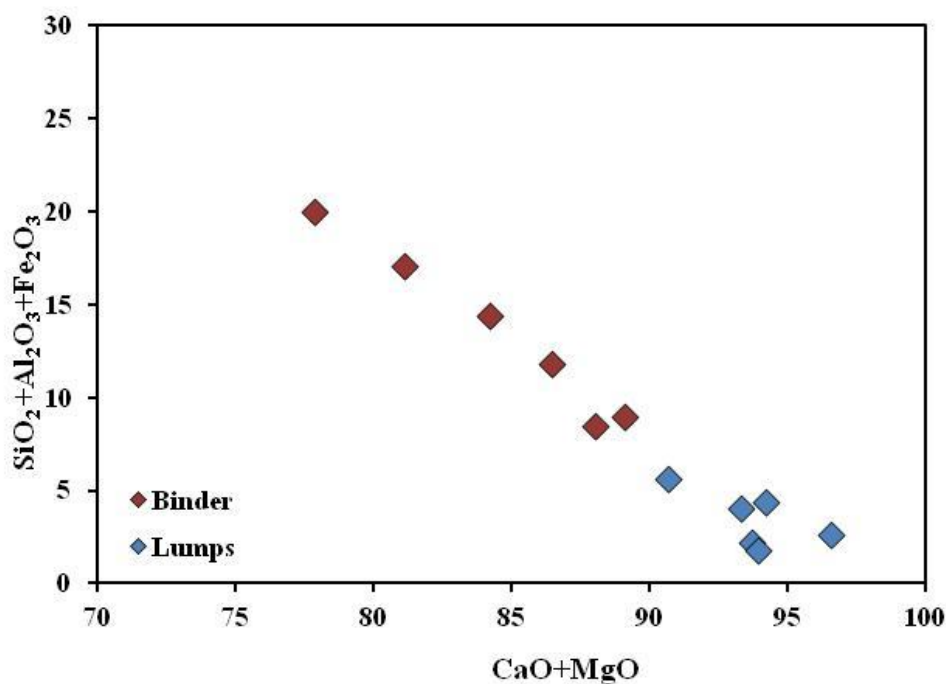


Figure 4.20: CaO + MgO vs. SiO₂ diagram (EDS), lumps and binder.

The Hydraulicity Index for lime lumps has relatively low values ($HI < 0.1$, Figure 4.21), therefore fall within the field of aerial lime (quicklime) (Zawawi, 2006).

As regards HI of binder, it shows values of 0.1 for bedding mortars (C group), and values between 0.14 – 0.26 for coating mortars (A and B groups), as observable in Figure 4.21. Thus, bedding mortars belong to the field of weakly hydraulic and coating mortars fall in the field of moderately hydraulic.

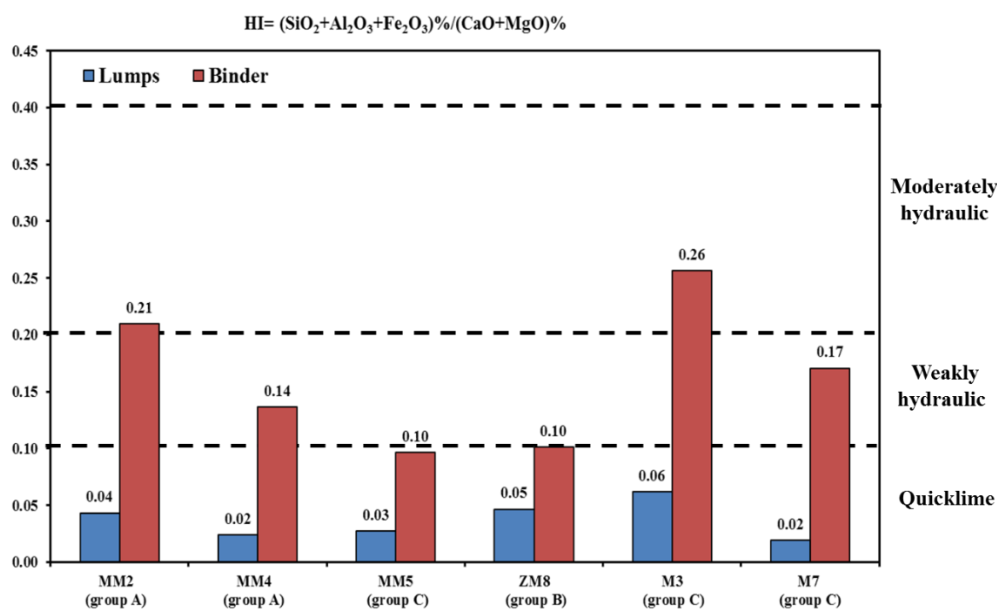


Figure 4.21: Hydraulicity Index (HI), lime lumps (blue) and binder (red) for analyzed mortars.

Higher hydraulicity values for binder are probably correlated to the abundant presence of “pozzolanic” materials (ceramic and volcanic fragments) in the samples. The presence of this material increases considerably the hydraulicity of the mixture, as the reactive silica contained in the “pozzolana” reacts with calcium hydroxide and leads to the formation of calcium silicate hydrates, the so-called C-A-S-H phases (calcium, aluminum; silicate, hydrate) (De Luca et al., 2015).

SEM EDS analysis, performed on the volcanic aggregates fraction, once again confirmed the use of Neapolitan Yellow Tuff fragments, due to the presence of phillipsite with well-defined prismatic crystal habit (Figure 4.22a-b), pseudocubic crystals of chabazite, often associated with acicular crystals of phillipsite (Figure 4.22b) (de Gennaro et al., 1999).

SEM-EDS analyses, revealed also the presence of volcanic glass (Figure 4.22c-d), mica with typical lamellar crystal habit (Figure 4.22e), along with typical "flakes" of smectite aggregates (Figure 4.22f), that are compatible with the proposed NYT origin of the aggregates.

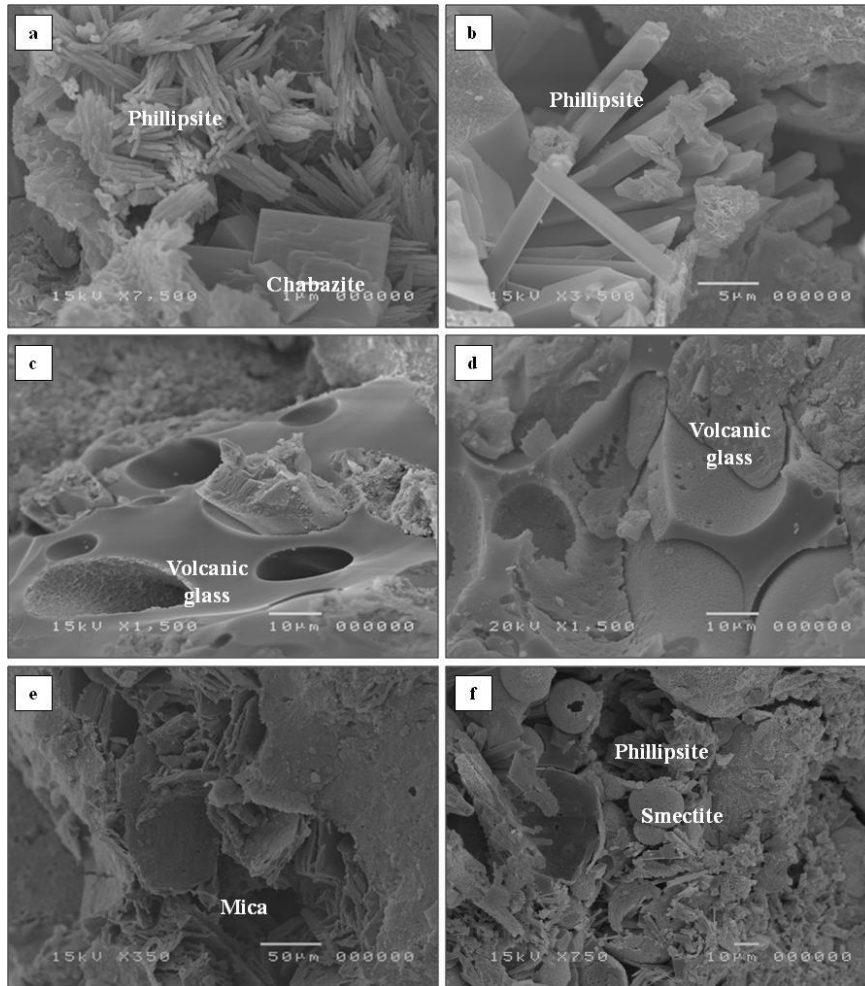


Figure 4.22: SEM images of a) chabazite and phillipsite (M7 sample); b) phillipsite (M3 sample); c) volcanic glass (MM2 sample); d) volcanic glass (MM5 sample); e) mica (MM2 sample); f) smectite e phillipsite (M7 sample).

In order to obtain further information regarding the provenance of raw materials, SEM-EDS microanalysis was carried out on pumice present in the samples (Figure 4.23, Table 4.5).

Introducing the obtained values in the Total Alkali versus Silica diagram (TAS) for the effusive volcanic rocks (Le Maitre et al., 1989) (Figure 4.24), it is possible to observe that almost all pumice fragments show trachytic compositions (Table 4.5).

The analyzed pumice follow the compositional trend of *Campi Flegrei* products, in particular they show a particular affinity with pumice belonging to NYT (Figure 4.24).

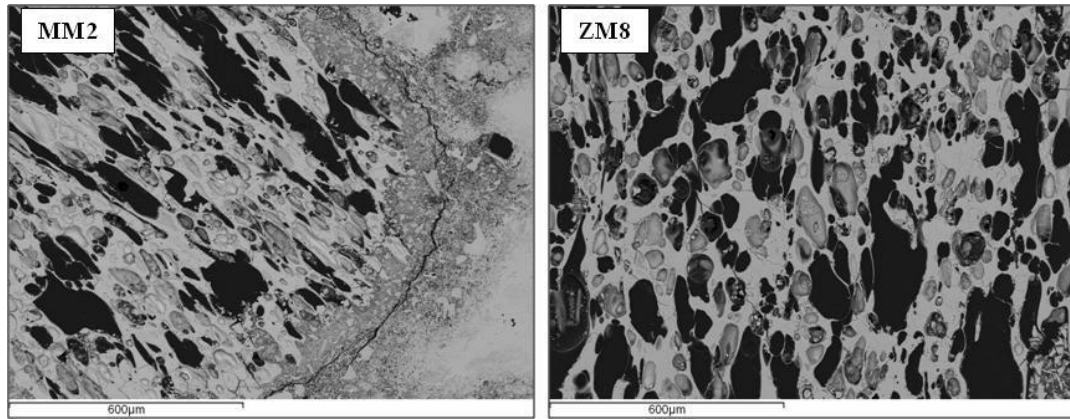


Figure 4.23: BSE-SEM image of pumice, (MM2 and ZM8 samples).

Table 4.5: Major element concentrations (wt.%, recalculated to 100%, EDS), pumice.

wt. %	MM2	MM2	MM2	MM2	MM3	M3	M3	M3	M3	M3	MM4	MM4	MM5	MM5	MM5
SiO ₂	58.59	58.94	59.27	57.68	60.57	58.14	58.99	57.91	60.95	60.73	58.41	58.40	60.40	60.48	58.45
TiO ₂	0.54	0.35	0.39	0.45	0.37	0.63	0.67	0.50	0.58	0.74	0.55	0.49	0.50	0.20	0.28
Al ₂ O ₃	18.81	19.10	18.53	19.28	18.89	18.69	18.85	18.98	18.60	18.83	18.86	19.08	18.81	18.81	18.97
Fe ₂ O ₃	3.46	3.68	3.52	3.84	2.86	3.53	2.73	4.10	2.44	3.13	4.27	4.44	3.03	2.67	3.09
MnO	0.20	-	0.32	0.19	0.14	-	0.27	0.16	0.26	0.05	0.09	-	0.15	0.09	-
MgO	0.85	0.56	0.35	0.56	0.33	0.68	0.64	0.73	0.31	0.31	0.49	0.77	0.31	0.27	0.78
CaO	3.20	2.90	2.84	2.86	2.27	3.13	2.92	2.76	2.09	1.97	2.98	2.89	2.06	2.02	2.96
Na ₂ O	3.46	3.67	3.76	4.15	4.84	3.99	3.29	3.70	4.98	5.44	3.49	4.12	5.19	4.75	3.37
K ₂ O	9.88	9.92	9.94	9.90	8.49	10.01	10.58	10.09	8.72	7.91	9.89	9.31	8.05	9.07	10.21
P ₂ O ₅	0.09	-	-	0.10	-	0.11	0.31	0.20	0.25	0.11	0.16	0.11	-	-	0.42
V ₂ O ₃	-	-	-	-	0.19	0.22	0.09	0.08	-	-	0.24	0.06	0.21	-	0.22
BaO	-	-	0.19	-	-	-	-	-	-	-	0.29	-	0.30	0.42	0.38
SO ₃	0.04	0.24	0.17	0.17	0.14	0.24	-	0.20	-	-	-	-	0.14	0.23	0.28
Cl ⁻	0.88	0.64	0.71	0.82	0.91	0.63	0.67	0.58	0.83	0.78	0.71	0.78	0.86	0.99	0.61
F ⁻	-	-	-	-	-	-	-	-	-	-	-	-	-	-	-
Total	100.00	100.00	100.00	100.00	100.00	100.00	100.00	100.00	100.00	100.00	100.00	100.00	100.00	100.00	100.00
Na ₂ O+K ₂ O	13.34	13.59	13.70	14.05	13.32	14.01	13.87	13.79	13.70	13.35	13.38	13.43	13.24	13.82	13.58

wt. %	MM5	ZM6	ZM6	M7	M7	ZM8	ZM8	ZM9	ZM9	ZM10	ZM10	M11e	M11e	M11e	M11e
SiO ₂	58.60	61.82	61.84	59.97	59.86	61.14	61.41	60.46	59.63	60.21	60.88	60.12	60.03	60.39	59.61
TiO ₂	0.17	0.46	0.40	0.28	0.12	0.70	0.44	0.22	0.44	0.36	0.21	0.71	0.50	0.15	0.31
Al ₂ O ₃	19.02	18.01	18.89	18.76	18.90	18.52	18.26	18.86	18.83	18.51	19.45	18.12	18.63	18.54	18.32
Fe ₂ O ₃	3.46	2.87	2.72	3.46	2.57	4.15	3.96	3.06	3.16	2.74	2.27	3.00	2.88	2.94	3.43
MnO	-	-	0.06	0.40	0.26	-	0.22	0.20	-	0.38	-	-	0.25	0.35	0.43
MgO	0.38	0.23	0.31	0.31	0.52	0.34	0.39	0.43	0.44	0.49	0.38	0.53	0.33	0.26	0.31
CaO	2.72	2.14	2.25	2.34	2.34	2.32	1.83	2.56	2.72	2.24	2.16	2.26	2.42	2.12	2.39
Na ₂ O	3.98	4.38	4.23	4.75	5.01	4.21	4.45	4.27	4.09	4.66	4.08	5.21	5.48	5.66	5.63
K ₂ O	10.23	9.30	8.46	8.82	9.16	8.63	8.21	9.06	9.65	9.04	9.41	9.04	8.52	8.15	8.11
P ₂ O ₅	0.25	-	0.25	-	0.03	-	-	0.09	0.22	0.22	0.30	0.20	0.26	-	0.26
V ₂ O ₃	0.20	-	-	0.12	0.04	-	-	-	-	0.15	-	-	-	0.11	0.09
BaO	0.21	-	-	-	0.18	-	0.33	0.13	-	0.20	0.04	-	-	0.43	0.11
SO ₃	-	0.20	-	-	0.19	-	-	-	0.08	0.02	0.20	-	0.03	-	-
Cl ⁻	0.78	0.57	0.60	0.80	0.82	0.41	0.88	0.65	0.73	0.77	0.63	0.81	0.70	0.90	0.99
F ⁻	-	-	-	-	-	-	-	-	-	-	-	-	-	-	-
Total	100.00	100.00	100.00	100.00	100.00	100.00	100.00	100.00	100.00	100.00	100.00	100.00	100.00	100.00	100.00
Na ₂ O+K ₂ O	14.21	13.68	12.69	13.56	14.17	12.83	12.66	13.33	13.75	13.69	13.49	14.24	13.99	13.81	13.74

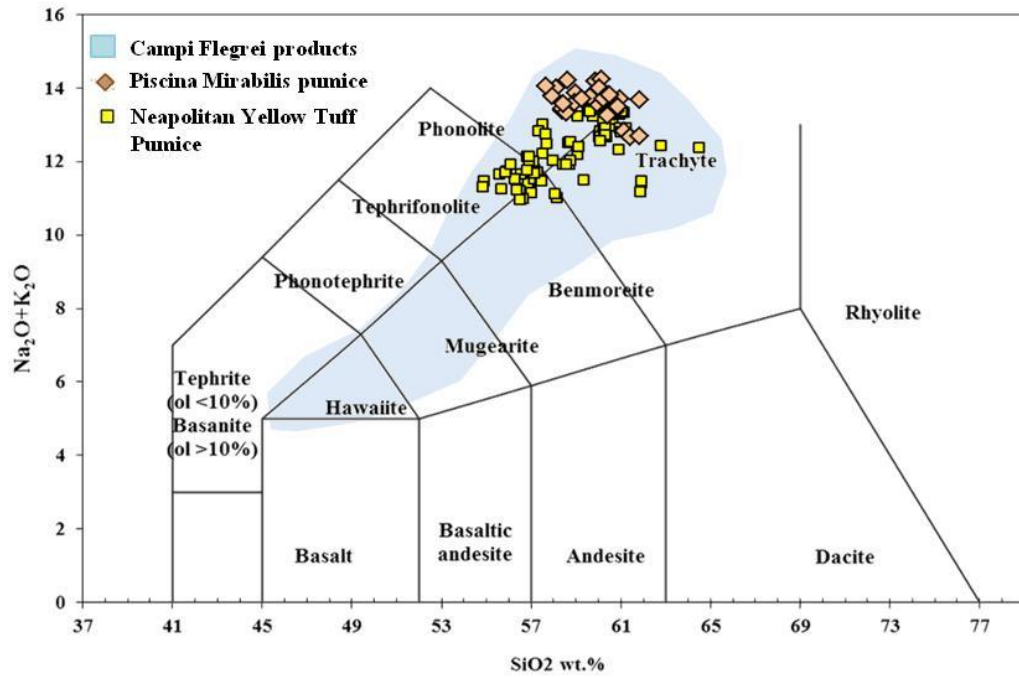


Figure 4.24: Classification of pumice fragments from investigated samples (Le Maitre et al., 1989) and geochemical comparison with Phlegrean pumice (Morra et al., 2010).

In order to exclude the possibility of analyzing altered pumice, alteration index such as CIA (Chemical Index of Alteration), WIP (Weathering Index of Parker) and W index, have been calculated.

Analyzed samples (Table 4.5) show values of CIA between 39.80 - 50.78 (Figure 4.25) , values of WIP between 103.76 - 133.44 (Figure 4.26), values of W index between 5.67 - 17.25 (Figure 4.27), (Table 4.6). These results suggesting that analyzed pumice can be considered not altered, thus allowing to use their chemical composition for the classification through TAS diagram.

A further confirmation of this assumption it is also given by the diagrams using those indexes: A – CN – K (Figure 4.25), WIP/CIA diagram (Figure 4.26) and MFW diagram (Figure 4.27).

Table 4.6 CIA, WIP and W index values for analyzed pumice

	MM2	MM2	MM2	MM2	MM3	M3	M3	M3	M3	M3	MM4	MM4	MM5	MM5	MM5
CIA	45.9	46.4	45.6	45.9	47.0	44.7	45.9	46.3	46.5	47.2	46.3	46.3	47.3	46.9	46.3
WIP	126.3	127.0	127.3	131.2	123.4	131.7	129.4	128.9	126.1	123.2	125.1	126.5	122.3	126.7	127.4
W	13.17	10.60	9.92	11.17	8.35	12.58	13.34	13.78	9.50	11.94	13.91	13.10	9.84	5.93	9.72

	MM5	ZM6	ZM6	M7	M7	ZM8	ZM8	ZM9	ZM9	ZM10	ZM10	M11e	M11e	M11e	M11e
CIA	45.8	46.0	48.3	46.5	45.8	47.5	48.3	46.8	46.0	46.2	48.3	44.7	45.2	45.8	45.0
WIP	131.5	125.5	117.4	125.5	131.4	118.9	116.5	124.0	127.9	126.7	124.1	132.0	129.9	127.5	127.8
W	6.45	9.27	9.27	7.79	4.43	14.66	12.87	7.13	10.01	8.73	6.41	11.65	8.49	4.64	7.13

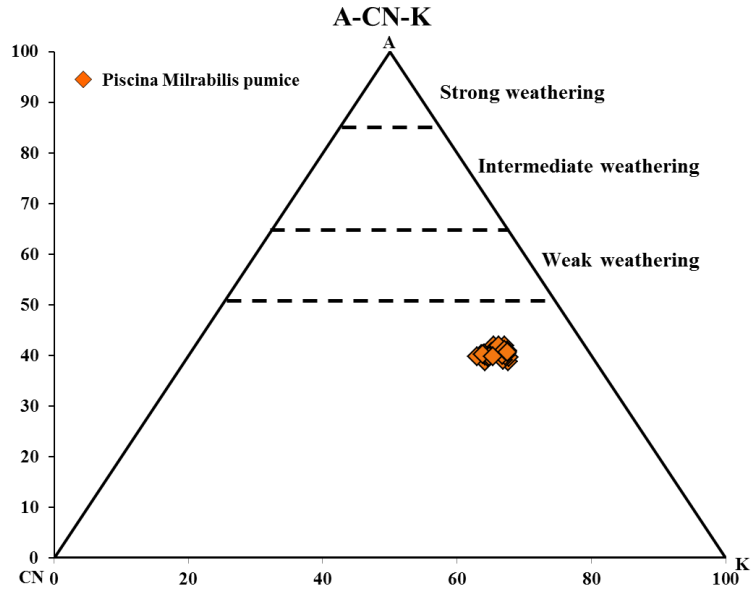


Figure 4.25: A-CN-K ($\text{Al}_2\text{O}_3 - \text{CaO} + \text{Na}_2\text{O} - \text{K}_2\text{O}$) diagram (Nesbitt and Young, 1982) for *Piscina Mirabilis* pumice.

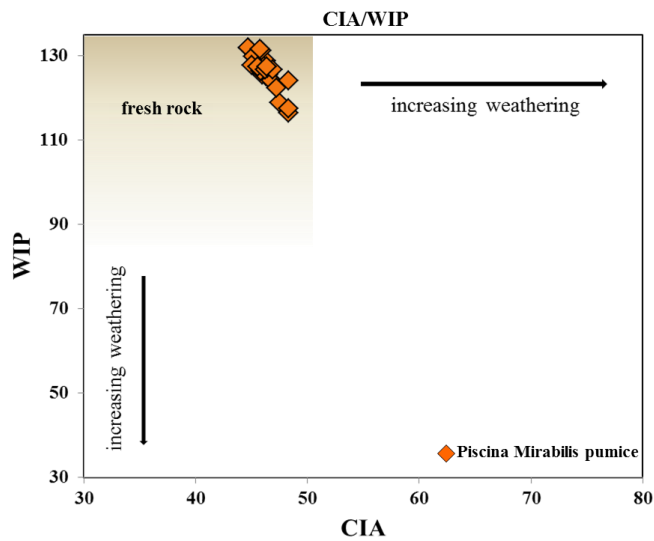


Figure 4.26: Relationship between two weathering proxies WIP and CIA (Bahlburg and Dobrzinski, 2011) for *Piscina Mirabilis* pumice.

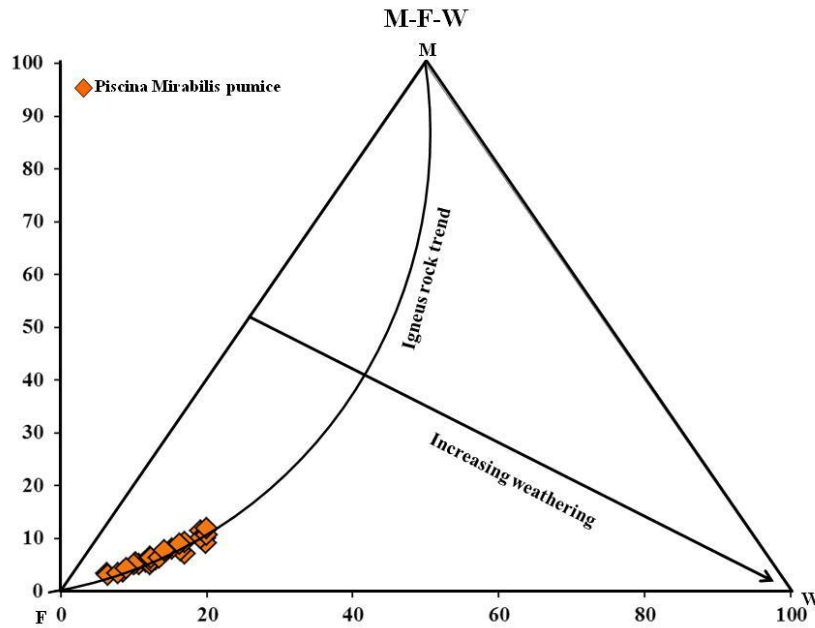


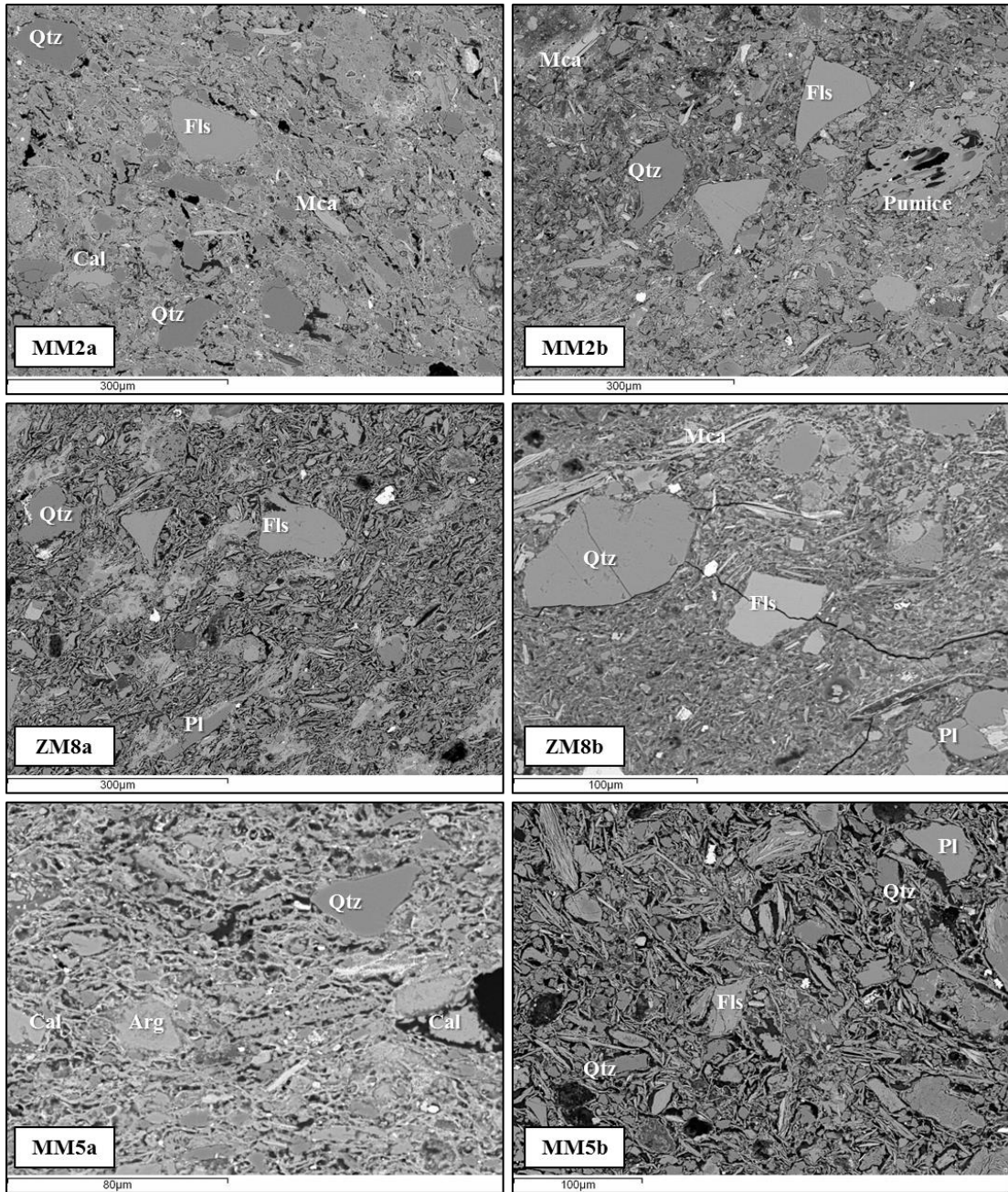
Figure 4.27: Weathering trends, MFW diagram (Ohta and Arai, 2007) for *Piscina Mirabilis pumice*.

SEM-EDS analysis of representative ceramic fragments has allowed us confirming the textural and mineralogical differences observed previously in thin section (Figure 4.28).

Furthermore, also the chemical composition on matrix of representative ceramic fragments (Table 4.7) highlight some differences because they show different concentration in CaO (3.53 – 23.56 wt.%) that can reflect different utilized raw materials.

In archaeometry the concentration of this oxide is a strong discriminant of the type of ceramic. When the percentage of this oxide is less than 6% (Maniatis and Tite, 1981) the clayey raw material used to produce ceramic fragments is defined not calcareous, otherwise it is said calcareous (>6% CaO). The better ability to resist to thermal shock makes non calcareous clays more suitable for cooking ware (Picon and Olcese, 1993; Tite et al., 2001), whereas calcareous clays are employed for the common production of common ware used as containers.

Moreover it should be remarked that also ceramic fragments from the same sample can display different CaO values (Table 4.7). This is the case of the MM5 mortar sample in which we analysed one non ceramic fragment (3.53 wt.% CaO) and another one highly (20.82 wt.% CaO), as well as in MM4 (4.17- 8.01 wt.% CaO) and ZM9 (5.60 – 15.67 wt.%).



* Cal: calcite; Qtz: quartz; Fls: feldspar; Pl: plagioclase; Arg: aragonite; Mca: mica.

Figure 4.28 Representative backscattered SEM images of different types of ceramic fragments with mineralogical composition.

Table 4.7: Chemical composition (wt.%, recalculated to 100% EDS), of matrix in the representative ceramic fragments.

wt. %	MM2	MM2	MM4	MM4	MM5	MM5	MM5	ZM8	ZM8	ZM8	ZM9	ZM9	ZM9	ZM10	ZM10
SiO ₂	52.98	58.34	59.75	60.61	45.89	51.67	58.47	62.03	61.48	56.87	48.22	55.65	55.00	56.95	47.10
TiO ₂	0.35	0.85	1.15	0.35	0.53	0.66	0.74	0.60	0.63	0.61	0.44	0.17	0.50	0.51	0.49
Al ₂ O ₃	17.28	15.18	20.08	19.52	18.55	17.49	19.67	16.30	14.10	16.07	9.44	23.07	15.83	16.63	16.00
Fe ₂ O ₃	4.33	5.37	6.61	6.58	6.90	6.11	6.38	4.48	5.01	5.34	9.21	7.00	5.35	5.87	5.83
MnO	-	0.54	0.32	0.29	0.03	0.04	-	0.73	-	-	-	0.11	-	0.32	0.05
MgO	2.14	2.21	3.89	7.32	2.11	4.90	4.94	4.50	2.41	4.71	15.52	2.41	3.25	2.26	4.26
*CaO	17.48	12.47	4.17	8.01	20.82	14.76	3.53	6.42	10.42	11.39	14.94	5.60	15.67	12.08	23.56
Na ₂ O	1.28	1.00	1.04	1.23	1.61	1.13	1.07	1.31	2.07	1.56	0.77	1.53	0.59	1.01	0.52
K ₂ O	3.78	3.44	2.80	3.87	2.14	2.27	4.66	3.02	2.61	2.66	0.53	3.05	3.10	3.08	1.72
P ₂ O ₅	-	0.43	-	0.13	-	0.41	0.11	0.05	0.49	-	0.25	-	-	0.55	-
V ₂ O ₃	-	0.06	-	-	0.23	0.11	-	0.25	0.19	-	0.37	0.60	0.18	0.20	0.33
BaO	0.22	-	0.17	-	0.57	0.06	-	-	0.13	0.33	0.11	0.77	0.42	0.31	-
SO ₃	0.09	-	-	-	0.51	0.34	0.22	0.17	0.32	0.31	0.11	0.03	-	0.13	0.12
Cl	0.07	0.12	0.02	0.11	0.12	0.04	0.21	0.16	0.11	0.16	0.09	0.00	0.11	0.10	-
F	-	-	-	-	-	-	-	-	-	-	-	-	-	-	-
Total	100.00														

4.2.5 XRF analysis

XRF analyses were conducted on representative samples of the different types of mortar (M3: bedding mortars; MM3: coating mortars; M11e: repair mortars).

Results are reported in Table 4.8.

Table 4.8. Chemical analysis (XRF), major oxides and trace elements, mortars.

wt.%	SiO ₂	TiO ₂	Al ₂ O ₃	Fe ₂ O ₃	MnO	MgO	CaO	Na ₂ O	K ₂ O	P ₂ O ₅	SO ₃	SrO	LOI
M11 e	38.14	0.28	11.07	2.36	0.10	2.99	15.29	3.05	4.62	0.06	0.11	0.108	21.50
MM3	39.57	0.30	11.67	2.74	0.10	1.46	16.40	3.14	4.79	0.07	0.13	0.116	19.18
M3	37.17	0.31	10.42	2.68	0.09	1.48	19.39	1.54	3.60	0.10	0.19	0.07	22.66

ppm	Cr	Zn	Ba	Br	Cl	Co	F	Ni	Pb	Cu	V
M11 e	58	206	527	0	1727	0	0	90	228	275	130
MM3	77	128	528	0	2122	40	0	64	209	151	0
M3	101	197	558	0	1508	0	0	109	187	170	116

Representative diagrams were selected to highlights similarities or differences between the mortars. The SiO₂/CaO diagram (Figure 4.29a) shows no differences between analyzed mortars; samples range between 37.17 and 39.57 wt.% for SiO₂ and 16.40 and 19.39 wt.% for CaO. Also, SO₃/Cl diagram (Figure 4.29b) shows a similar enrichment in chlorine between mortars.

As regards Al₂O₃/Fe₂O₃ plot (Figure 4.29c), it is possible to see that repair mortar (M11e) has similar value in Fe₂O₃ (2.36 wt.%) and different concentration in Al₂O₃ (11.07 wt%) respect to M3 and MM3 samples (2.68 - 2.74 wt.% Fe₂O₃; 10.42-11.67 wt.% Al₂O₃).

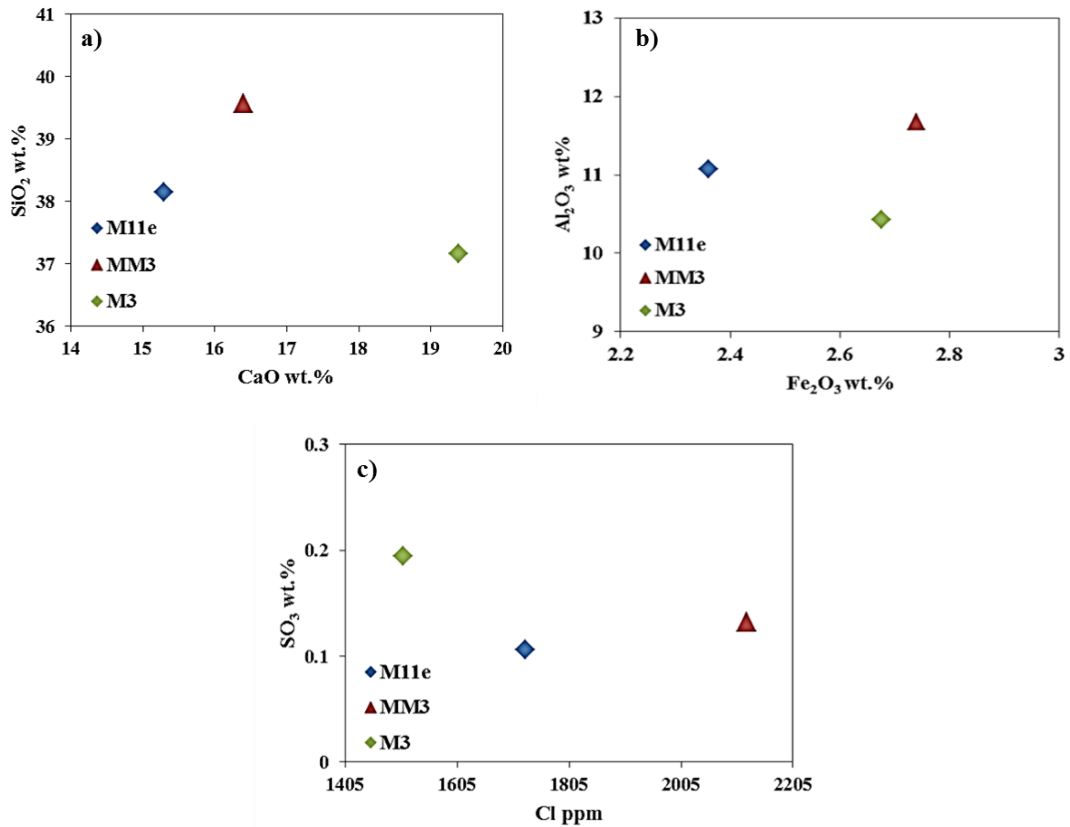


Figure 4.29: Binary diagrams representative of major oxide and trace element composition.

4.2.6 Differential and Gravimetric Thermal Analysis (DTA-TGA)

All collected sample mortars (except M7 sample) from *Piscina Mirabilis* were subjected to thermal analysis (DTA-TGA).

Thermal analysis has been used as an additional tool for the determination of the composition of this mortar throughout characterization of hygroscopic water, carbonates decomposition, $\alpha \rightarrow \beta$ phase transition of quartz and the presence of gypsum and clay minerals (Moropoulou et al., 1995).

Thermal analyses in this research project have been utilized to classify the level of hydraulicity, for this reason attention was focused on structural bound water (SBW) values, that represent the weight loss percentage of H₂O due to dehydration of calcium silicates and aluminates hydrates and occurring between approximately 200 and 600 °C, and on the weight loss percentage associated to CO₂ production related to calcite decomposition (Bonazza et al., 2013; Figure 4.30), this values are represented in Table 4.9.

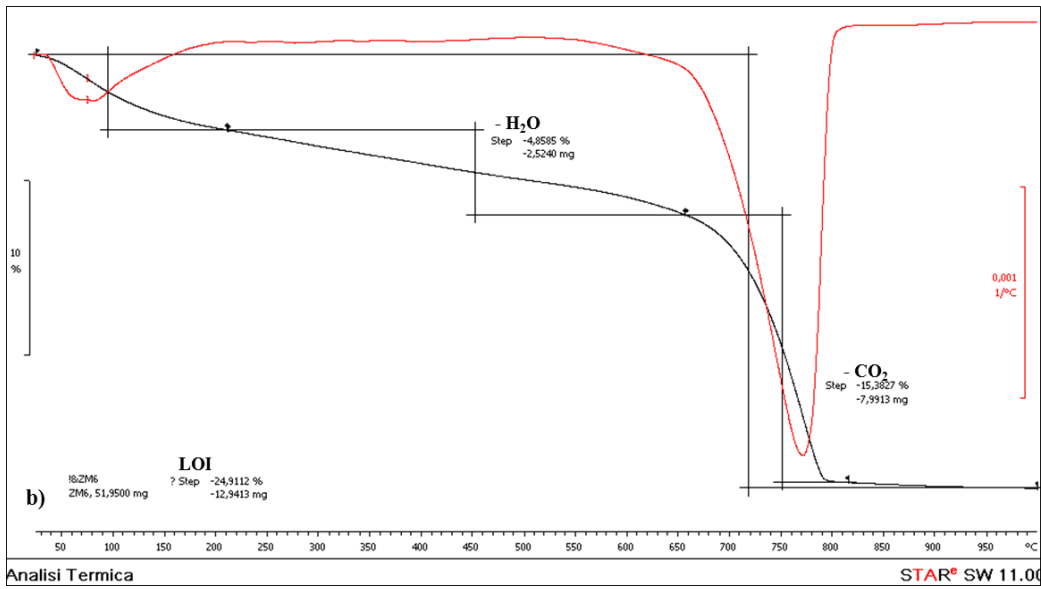
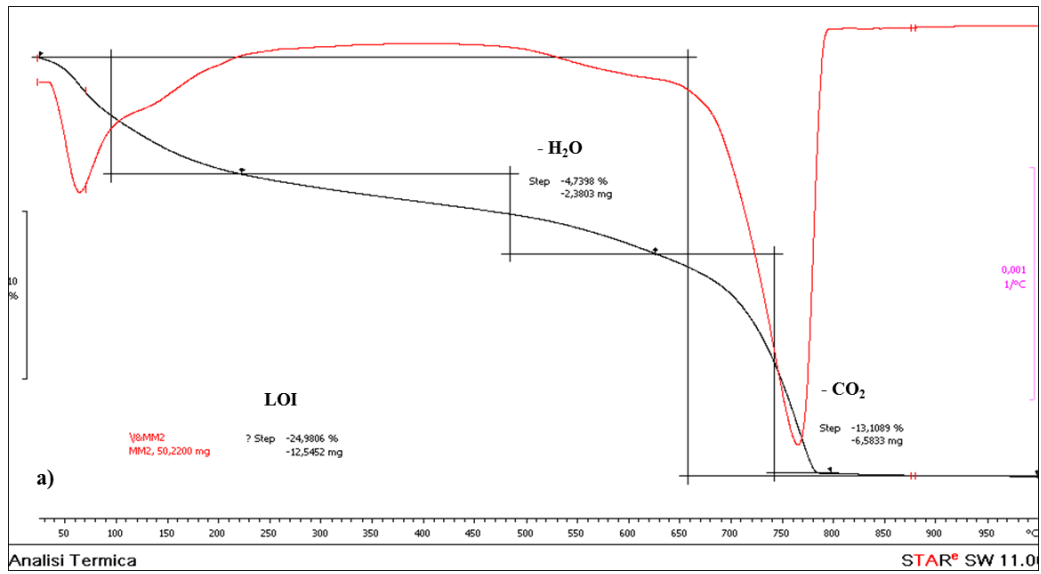


Figure 4.30: DTA-TGA plot of a) MM2 and b) ZM6 samples.

Table 4.9: Thermal analysis (DTA/DTG) features of investigated samples.

Sample	SBW %	CO₂%	CO₂/SBW	LOI
MM2	4.73	13.1		24.98
T range (°C)	220-630	630-800	2.77	25-1000
MM3	3,96	9,42		18,52
T range (°C)	223-602	602-812	2.38	25-1000
MM4	5.11	12.22		24.25
T range (°C)	220-630	630-783	2.39	25-1000
MM5	5.29	12.59		23.73
T range (°C)	210-620	620-813	2.38	25-1000
MM6	4.07	6.99		17.69
T range (°C)	210-535	535-814	1.72	25-1000
ZM6	4.85	15.38		24.91
T range (°C)	212-660	660-815	3.17	25-1000
ZM10	3.42	11.72		20.63
T range (°C)	203-623	623-801	3.43	25-1000
M3	5.02	17.77		25.21
T range (°C)	180-621	621-798	3.54	25-1000
M11e	5.87	7.01		21.43
T range (°C)	210-620	620-810	1.19	25-1000

*SBW = Structural Bound Water, LOI= Loss on Ignition

Using the obtained data by DTA-TGA the CO₂/SBW ratio was calculated, and according to Moropoulou et al. 2005 the CO₂ versus CO₂/SBW diagram allow to classify the mortars into different groups on the basis of their hydraulicity.

On this account, our mortars fall in the field of crushed brick mortars of natural pozzolanic mortars (Figure 4.31).

These results are particularly relevant because analyzed mortars in both diagrams result highly hydraulic and therefore represent a confirm of the results obtained for the the binder SEM-EDS analysis.

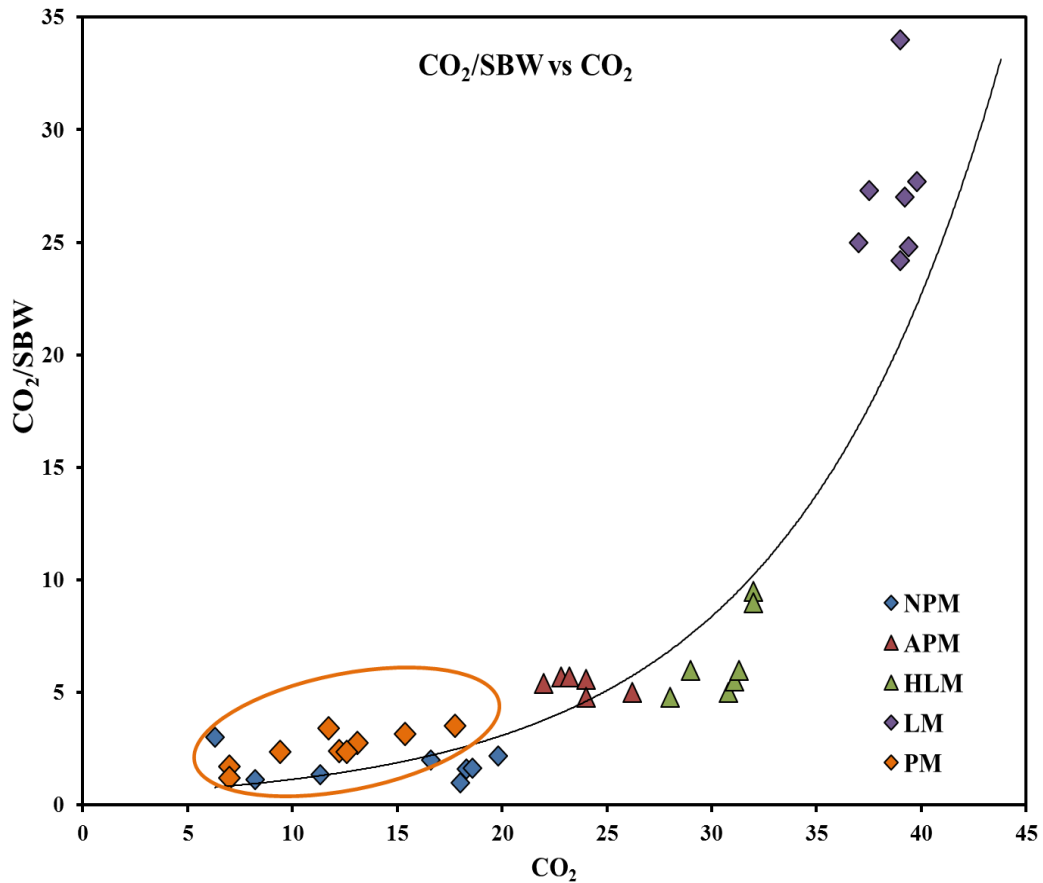


Figure 4.31: CO₂/SBW vs. CO₂ diagram, comparing mortars from *Piscina Mirabilis* (PM, orange circle) and from Moropoulou et al., 2005. (NPM: natural pozzolanic mortars; APM: artificial pozzolanic mortars; HLM: Hydraulic lime mortars; LM: lime mortars).

4.2.7 Mercury intrusion porosimetry (MIP)

Porosity of representative samples of mortars (M7, MM4, ZM8) was evaluated by mercury intrusion (MIP), according to ASTM D4404 (Determination of pore volume and pore volume distribution of soil and rock by mercury intrusion porosimetry). Analyses were performed on three fragments for each samples, and average results are reported.

Results are reported in Table 4.10 and in Figure 4.32 and Figure 4.33, where cumulative and relative pore size distributions are shown.

Table 4.10: Porosimetric features (MIP) of mortars.

Sample	M7	MM4	ZM8
Cumulative volume (mm ³ /g)	164.00	264.35	295.33
Bulk density (g/cm ³)	1.86	1.61	1.72
Total porosity (Vol. %)	30.52	39.90	52.40

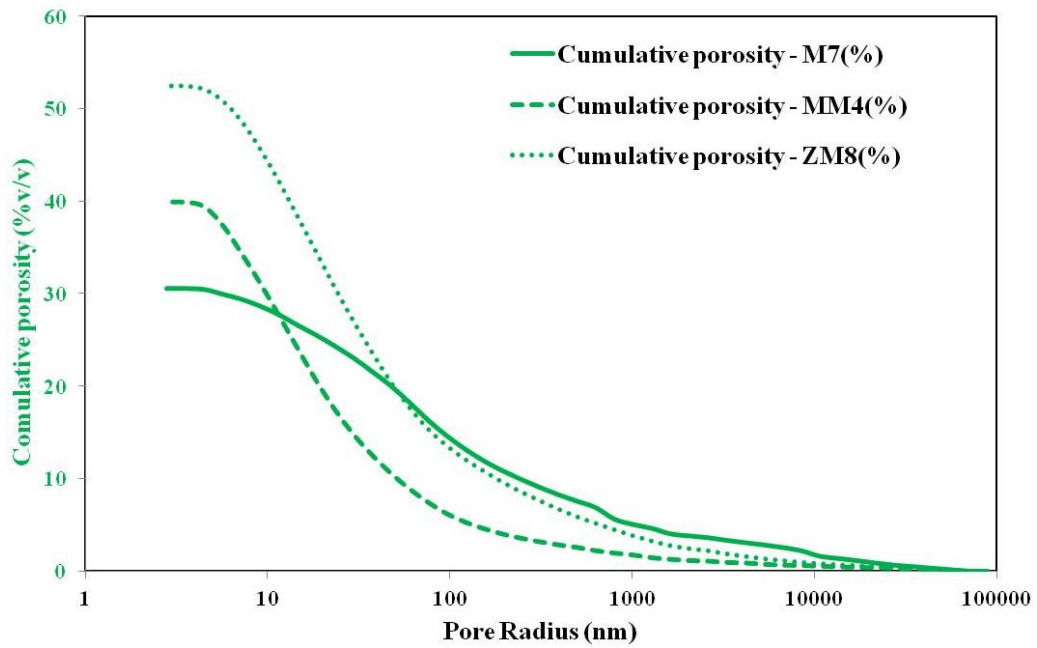


Figure 4.32: Cumulative pore size distribution for M7, MM4 and ZM8 samples.

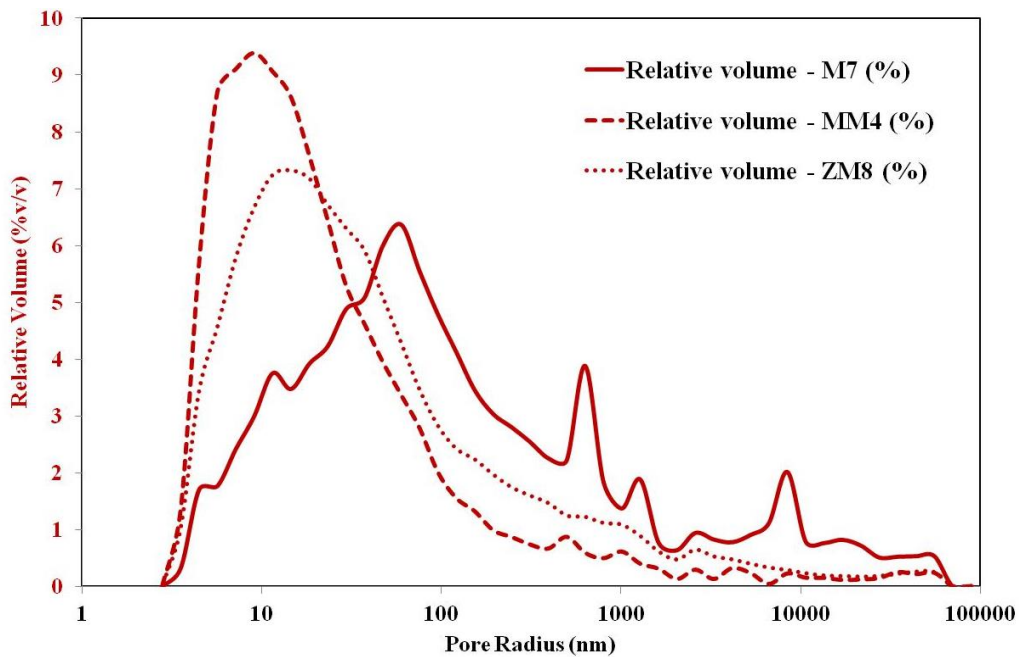


Figure 4.33: Relative pore size distribution in M7, MM4 and ZM8 samples.

Pore sizes of samples fall within the characteristic field of hydration product porosity, usually considered below 100 nm (Figure 4.33) (Metha and Monteiro, 2006; Gotti et al., 2008).

Samples show total porosity values between 30% - 54%, and MM4 and ZM8 shows unimodal and broadened shape of pore size distribution.

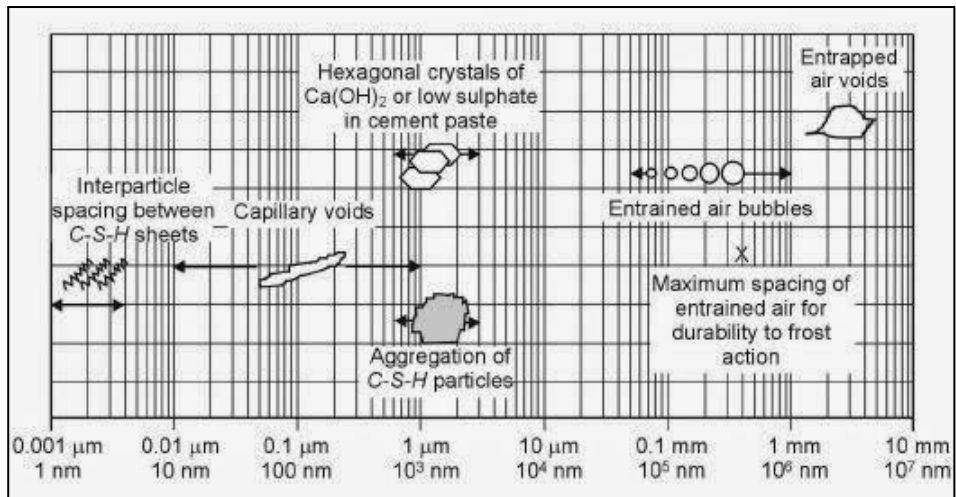


Figure 4.35: Pore sizes distribution (Metha and Monteiro, 2006)

Chapter 5

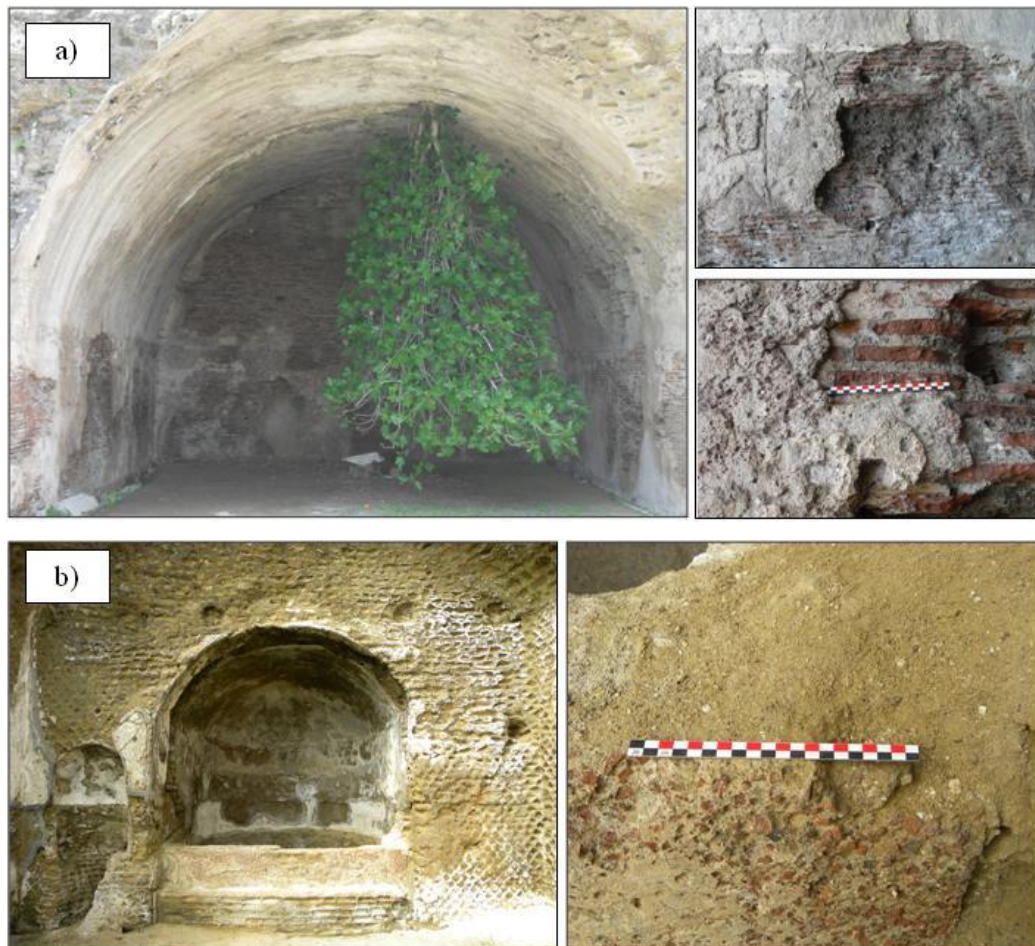
Terme di Baia: materials and results

5.1 Materials

In the area of the archaeological park of *Terme di Baia*, the sampling of 9 mortars, representing different sectors that characterizes the complex (Figure 5.1 a,b,c,d; Table 5.1), was authorized.

Sosandra area was the only area where, for safety reasons, no sampling was allowed.

Due to the complexity of the monument and the use of different materials, after detailed site inspections and a photographic campaign, it was decided to focus the study on coating mortars, since they had a longer contact with thermal water. Samples were contextualized in two planimetries (Figure 5.2 and Figure 5.3).



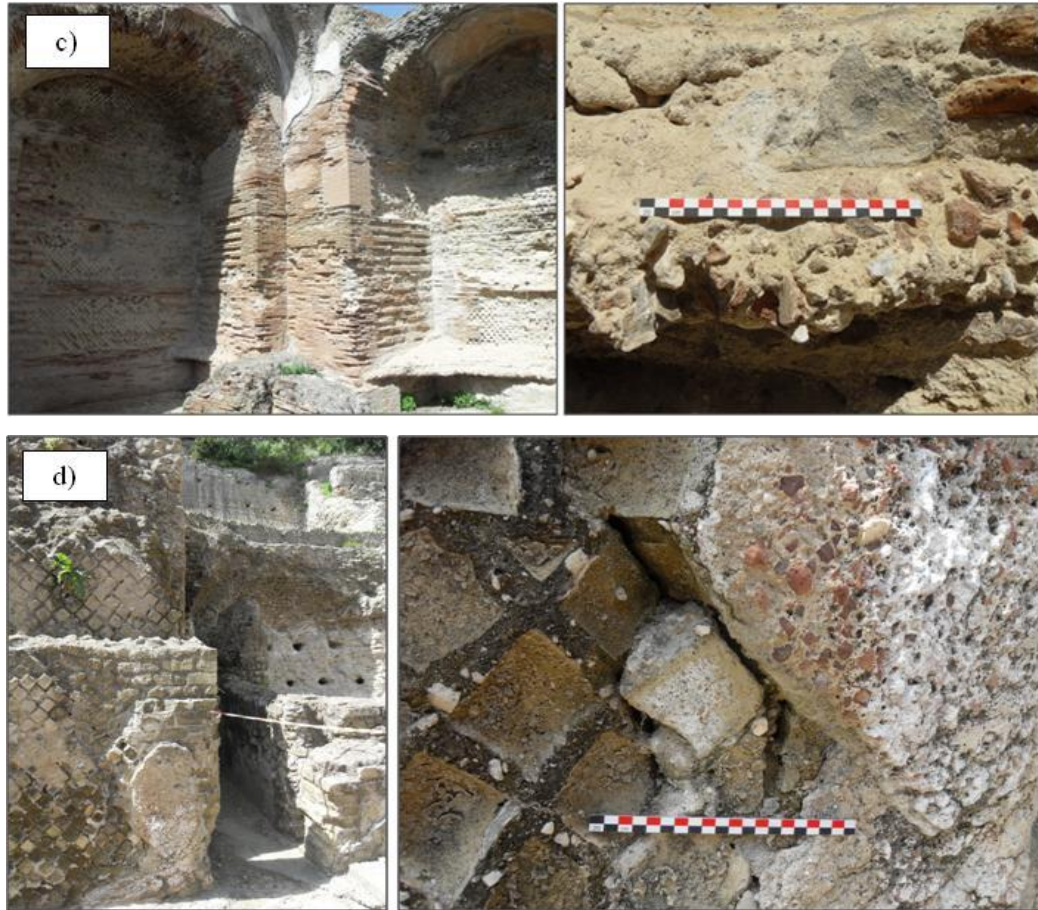


Figure 5.1: Sampling location in Terme di Baia: a) *Mercurio* area; b) *Piccole Terme* area; *Venere* area; d) *Villa of Ambulatio* area.

Table 5.1: samples, location and typology.

SAMPLE	LOCATION	TYOLOGY
PT1	Piccole Terme area	coating mortar
PT2	Piccole Terme area	coating mortar
SV1	Venere area	coating mortar
SV2	Venere area	coating mortar
TM1	Mercurio area	coating mortar
TM2	Mercurio area	coating mortar
TM3	Mercurio area	coating mortar
V1*	Mercurio area	coating mortar
VA1	Villa of Ambulatio area	coating mortar

*A suggested by archaeologists, VPI sample geographically belongs to the Mercurio area but the bathtub from which it was taken was built in successive periods

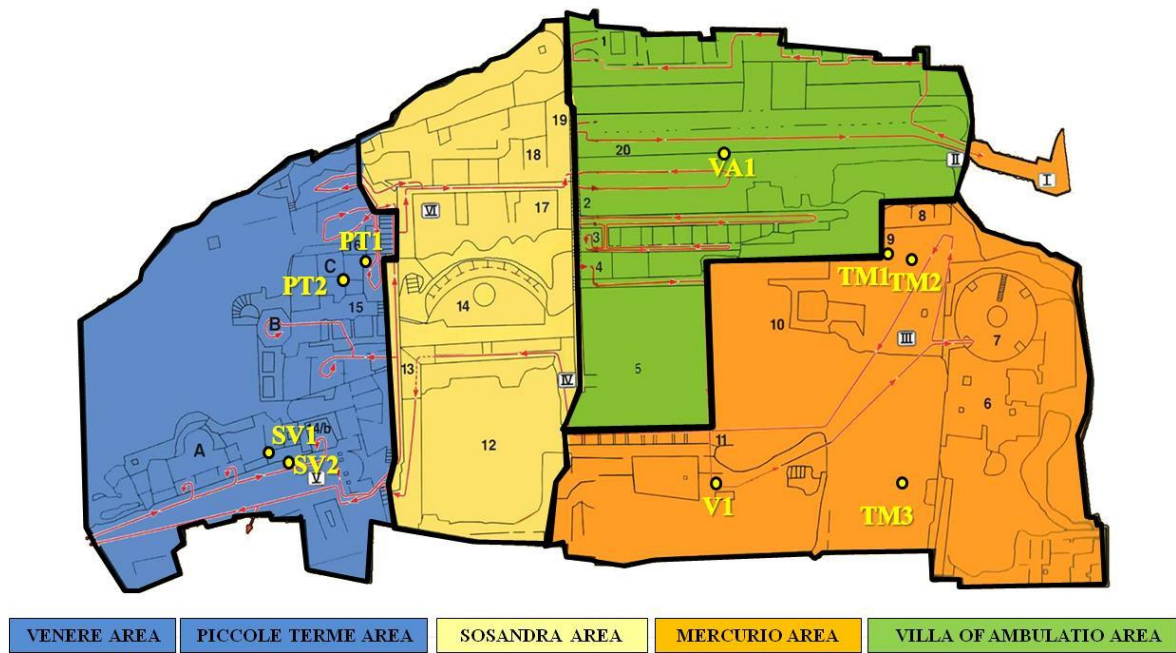


Figure 5.2: Sketch map of Terme di Baia reporting the sample location (modified after Amalfitano et al. 1998).

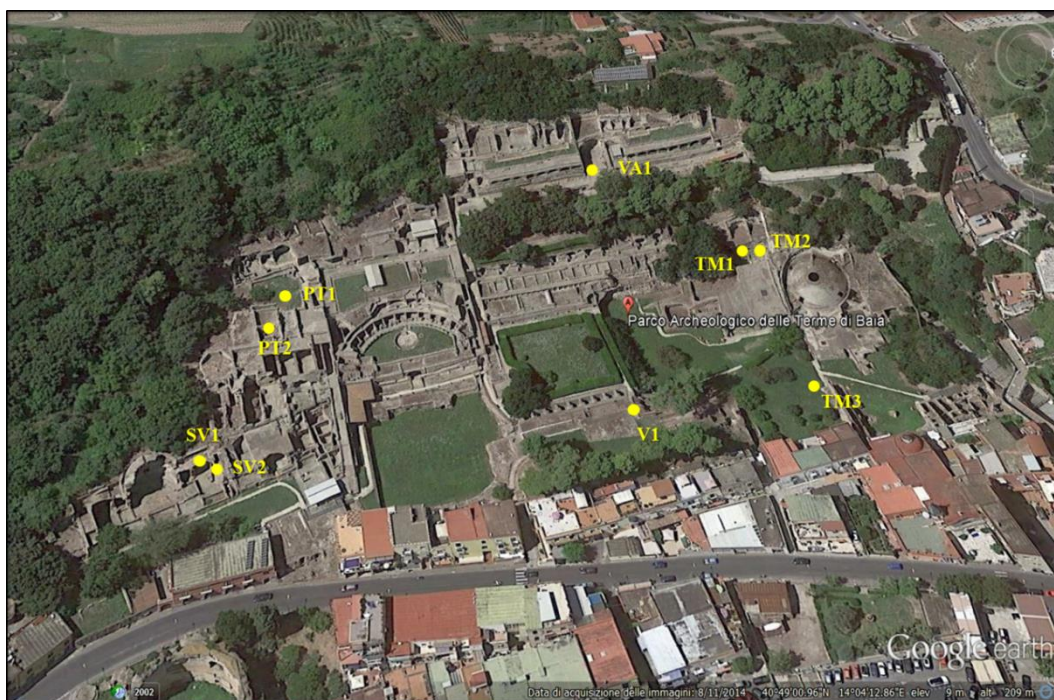


Figure 5.3: Satellite picture of Terme di Baia, along with samples location.

5.2 Results

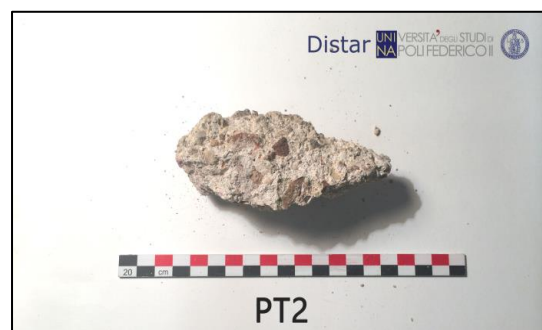
5.2.1 Macroscopic observation of samples

Macroscopic observation revealed a high similarity among the sampled coating mortars (Figure 5.4).

They have a high degree of cohesion, except for VA1 sample which is friable. The samples show a variable colour ranging from light yellow to brownish.

The aggregates are mainly made up of ceramic and volcanic fragments; in some samples carbonate fragments are also visible. The dimension size of aggregates varies from mm - to - cm.

All mortars show the presence of lime lumps, sometimes centimeter sized.



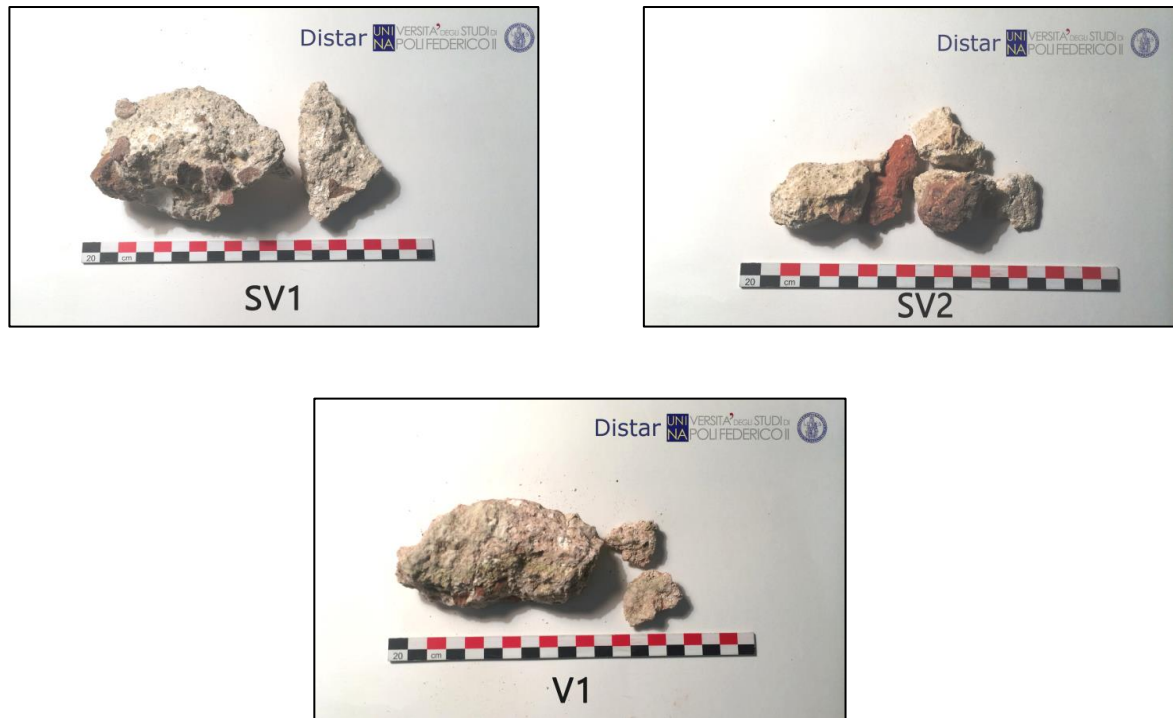


Figure 5.4: Macroscopic images of samples.

5.2.2 Petrography

Samples were prepared and studied in optical microscopy and modal analysis (Table 5.2): nine thin sections or one for each selected sample.

Petrographic analysis confirmed a high homogeneity among most of the mortars. These are characterized by a binder, with yellowish to brownish colour and cryptocrystalline (16.8 – 35.1 Vol.%, Figure 5.5a) to micritic texture (5.5 – 28.6 Vol.%, Figure 5.5b). The binder of all samples present lime lumps¹, that generally consists in unreacted lime, with undefined and irregular edges (1.3 – 4.2 Vol.%, Figure 5.5c) and sparite grains (1.1 – 3.7 Vol.%, Figure 5.5d).

Aggregates are constituted by ceramic (7.3 – 20.3 Vol.%, Figure 5.5e) and volcanic fragments (0.9 – 3.8 Vol.%, Figure 5.5f), pumice (5.5 – 15.6 Vol.%, Fig 5.5g) and scoriae with well evident reaction rims (4.1 - 16.6 Vol.%), crystal fragments of sanidine, amphibole, clinopyroxene, biotite and plagioclase (7.5 Vol.%). Some samples, among the aggregate, revealed the presence of some carbonate fragments (0.5 Vol.%) (Figure 5.5h).

¹ The origin of lime lumps is to be sought in the properties of the slaked lime (calcium hydroxide) and in the water/quicklime ratio (Bakolas et al. 1995; Barba et al., 2009). Their formation occurred during the slaking process of the lime and it is due to an insufficient seasoning of the calcium hydroxide and a low water/lime ratio.

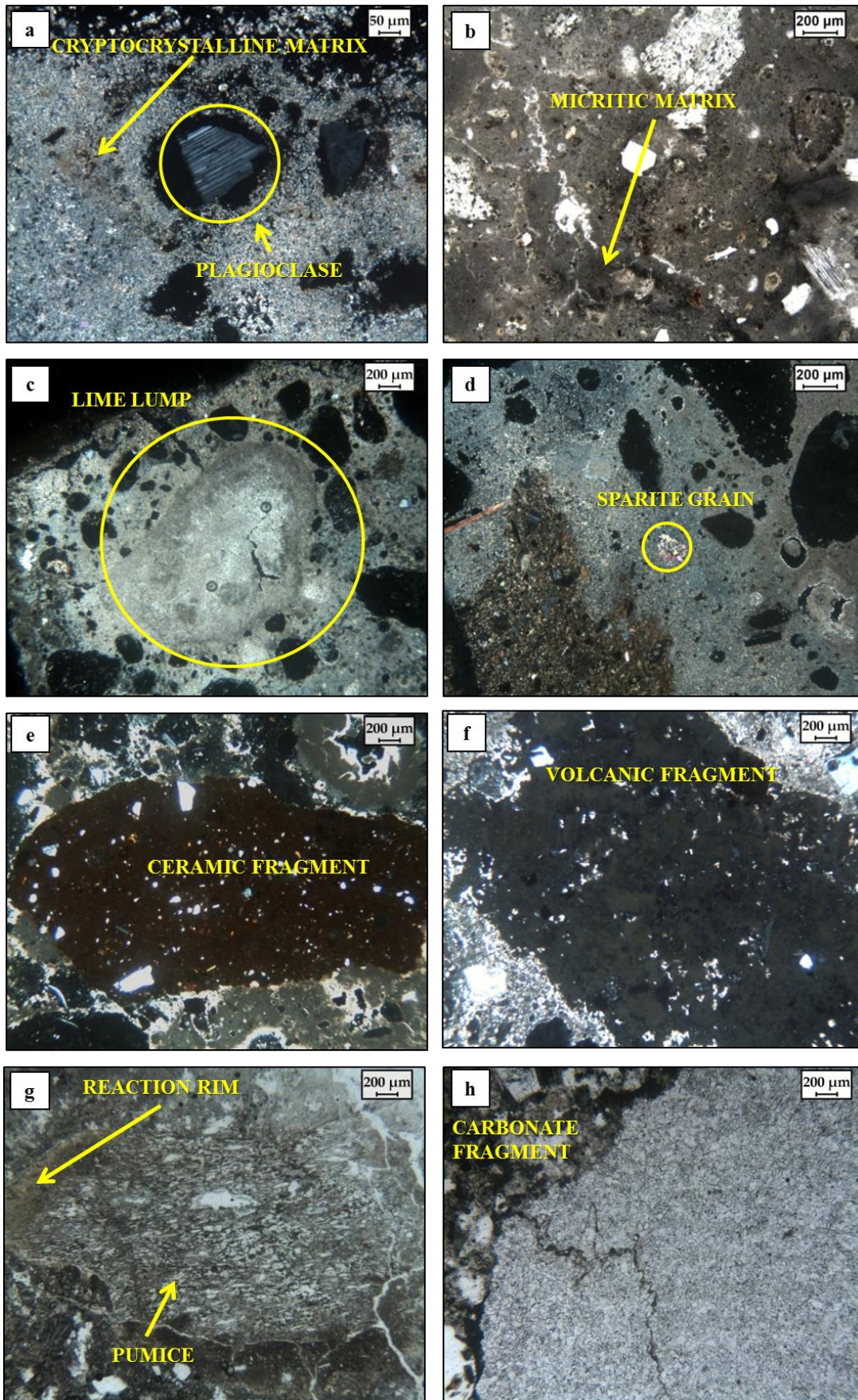


Figure 5.5: Microphotographs of mortars components: a) cryptocrystalline matrix and plagioclase (CPL) in sample PT1 b) micritic matrix (CPL) in sample TM3; c) lime lump (CPL) in sample TM2; d) sparite grains (CPL) in sample SV1; e) ceramic fragment (CPL) in sample VA1; f) volcanic fragments (PPL) in sample SV1; g) pumice with reaction rim (PPL) in sample TM3; h) carbonate fragment (PPL) in sample SV2. CPL: Cross Polarized Light; PPL: Plane Polarized Light.

Volcanic fragments can be identified as volcanic tuff, characterized by the presence of microcrystals dispersed in an ashy matrix.

Petrographic observations also revealed variability in the types of ceramic fragments texture and aggregate clasts. For example, in sample TM3 (Figure 5.6), some ceramic fragments (TM3a) shows high optical activity and contains quartz, sanidine and calcite, while others (TM3b) shows low optical activity and contain volcanic glass, pumice, scoriae and sanidine crystals fragments.

In SV1, TM3, VA1 and V1 samples, ceramic fragments display bigger size (up to 2 cm) compared to other samples.

TM1 sample is slightly different from the others, due to the presence of a layer of carbonatic “plaster” (up to 5mm in thickness), in which are clearly visible crystal fragments of calcite (Fig 5.7).

The modal analysis carried out on representative samples (PT1, PT2, TM2, SV1, VA1) highlighted that “porosity” (voids %) ranges between 1.9 – 7.0 Vol.% and the binder/aggregate ratio reaches values higher than 2 in PT2 and SV1 samples; other mortars show a value of binder/aggregate ratio equal to 1 (Table 5.2; Figure 5.8).

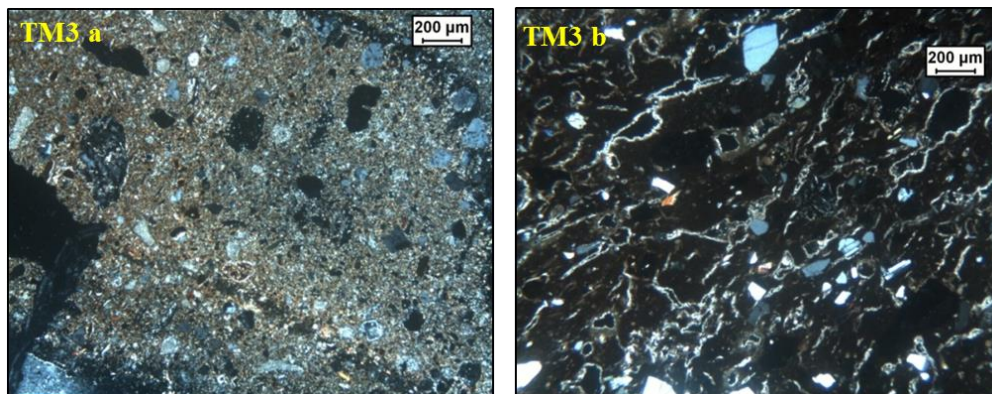


Figure 5.6: Ceramic fragmens in TM3 mortar sample (CPL).

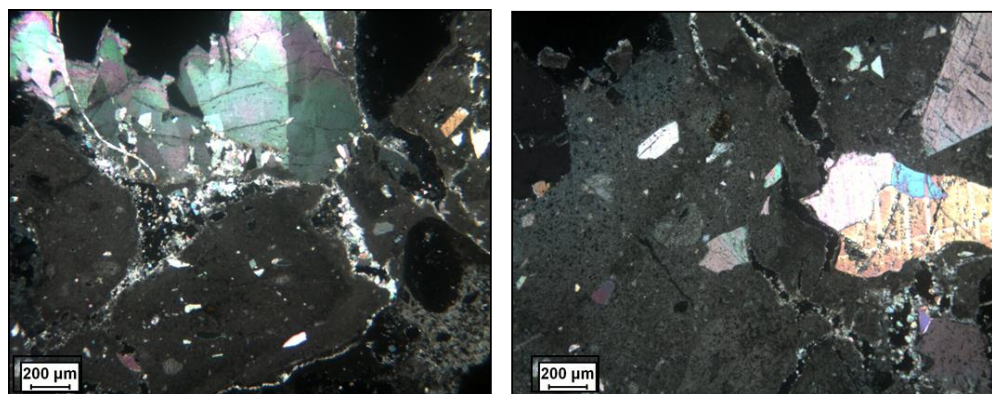


Figure 5.7: Plaster layer, TM1 mortar sample (CPL).

Table 5.2: Modal analyses of selected mortars.

Mortars	PT1	PT2	TM2	SV1	VA1
Constituents (Vol. %)					
Feldspar (Afs, Plg)	4.7	4.6	7.5	2.8	6.4
Mafic Minerals (Cpx, Am, Bt)	2.1	1.6	1.6	1.3	1.3
Volcanic fragments	0.9	3.8	1.0	1.3	1.3
Scoriae	16.6	4.2	11.5	4.1	9.5
Pumice	15.6	8.9	5.5	11.8	14.3
Ceramic fragments	9.7	7.3	20.3	6.7	11.7
Carbonate fragments	0.5	0.5	0.5	0.4	-
Sparite	1.1	3.7	1.2	1.4	1.9
Line lumps	3.3	2.5	4.2	1.5	1.3
Micritic matrix	12.3	10.6	5.5	11.0	28.6
Cryptocrystalline matrix	30.9	47.3	35.1	51.4	16.8
Voids	1.9	5.0	6.3	6.1	7.0
Others	0.5	-	-	-	-
Total points	100.0	100.0	100.0	100.0	100.0
Total Binder	47.6	64.1	46.0	65.3	48.6
Total Aggregate	50.0	30.9	47.6	28.5	44.5
Binder/Aggregate ratio	1.0	2.1	1.0	2.3	1.1

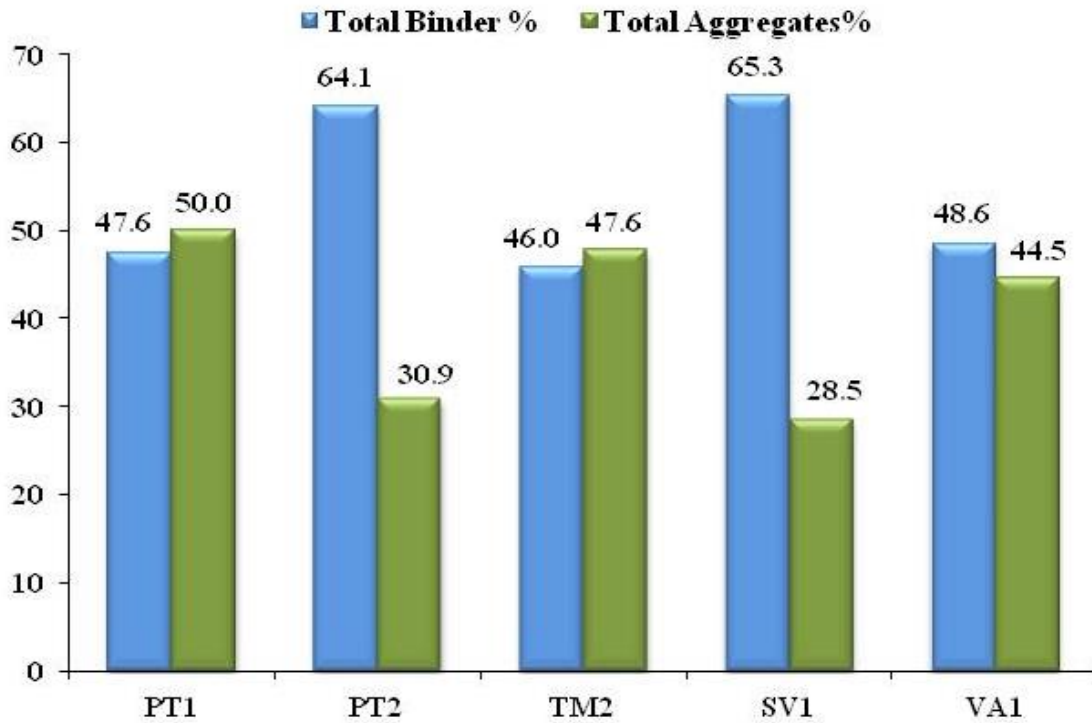


Figure 5.8: Histogram showing the percentages of total binder and total aggregates in representative samples of mortars.

5.2.3 XRPD analysis

The XRPD analysis of samples, after an appropriate separation of the different fractions (binder, aggregate and ceramic fragments, according to UNI 11305), enabled identification of mineral phases, reported in Table 5.3:

Table 5.3: Qualitative mineralogical (XRPD) composition of mortars.

Samples	Main Binder	Main Aggregates	Main Ceramic Fragments	Other
	Phases	Phases	Phases	Phases
PT1	Cal	Phi, Cbz, Anl, San, Pl, Mca	Qz, Cal, Cpx, Pl, Hem	HI
PT2	Cal	Phi, Cbz, Anl, San, Pl, Mca	Qz, Cal, Cpx, Hem	HI
SV1	Cal	Phi, Cbz, Anl, San, Pl, Mca	Qz, Cal, San, Cpx, Hem	HI
SV2	Cal, Gp	Phi, Anl, San, Pl, Cpx, Mca	Qz, Cal, Cpx, Hem	HI
TM1	Cal, Gp	Phi, Cbz, San, Pl, Cpx, Mca	Qz, Cal, Cpx, Hem	HI
TM2	Cal	Phi, Cbz, Anl, San, Pl, Cpx, Mca	Qz, Cal, San, Cpx, Hem	HI
TM3	Cal	Anl, San, Pl, Cpx, Mca	Qz, Cal, Cpx, Hem	HI
VA1	Cal	Phi, Anl, San, Pl, Mca	Qz, Cal, Pl, Cpx, Hem	HI
V1	Cal, Arg	San, Pl, Cpx, Mca	Qz, Cal, Cpx, Hem	HI

* Cal: calcite; Gp: gypsum; Arg: aragonite; Phi: phillipsite; Cbz: chabazite; Anl: analcime; San: sanidino; Cpx: clinopyroxene; Mca: mica; Hem: hematite; Qtz: quartz; HI: halite.

XRPD analyses show mainly calcite as the main binder phase, while in TM1 and SV2 samples also gypsum [CaSO₄·2(H₂O)] was detected (Figure 5.9). The presence of gypsum can be ascribed to sulphation of calcite.

In V1 sample XRPD analysis proved the presence of aragonite in binder phase; this is probably due to the fact that the bathtub from which the sample was taken, geographically belongs to the *Mercurio* area, but was likely built in a subsequent moment possibly with a different raw material limestone.

As regards aggregates, the XRPD analyses suggest that volcanic tuff fragments are aggregates of Neapolitan Yellow Tuff (NYT), due to its typical zeolitic association (i.e. phillipsite, analcime and chabazite as reported by de Gennaro et al., 2000). In addition, the presence of feldspar, pyroxene and mica also fit well with the proposed NYT provenance (Figure 5.10).

As far as ceramic fragments are concerned, the crystal phases detected are quartz, calcite and subordinately hematite, along with sanidine, clinopyroxene, plagioclase and mica (Figure 5.11).

All analyzed samples fractions show the presence of halite (NaCl), that can be probably related to marine aerosol or due to the presence of saltwater sources.

As already reported, XRPD analysis revealed also the presence of an amorphous phase (probably C-A-S-H phase or volcanic glass), recognizable by the rising of the spectrum background (Fig 5.10).

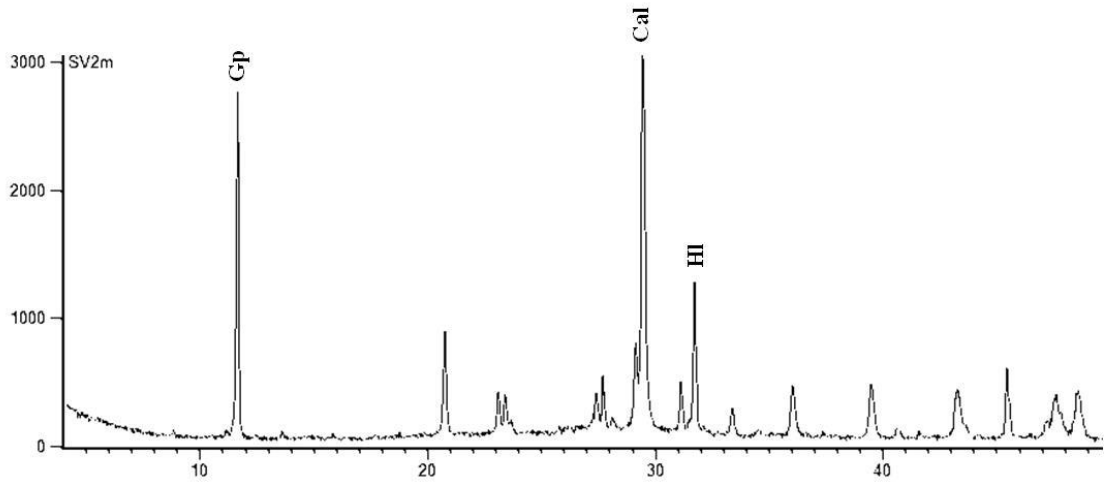


Figure 5.9: XRPD spectrum of SV2 binder.

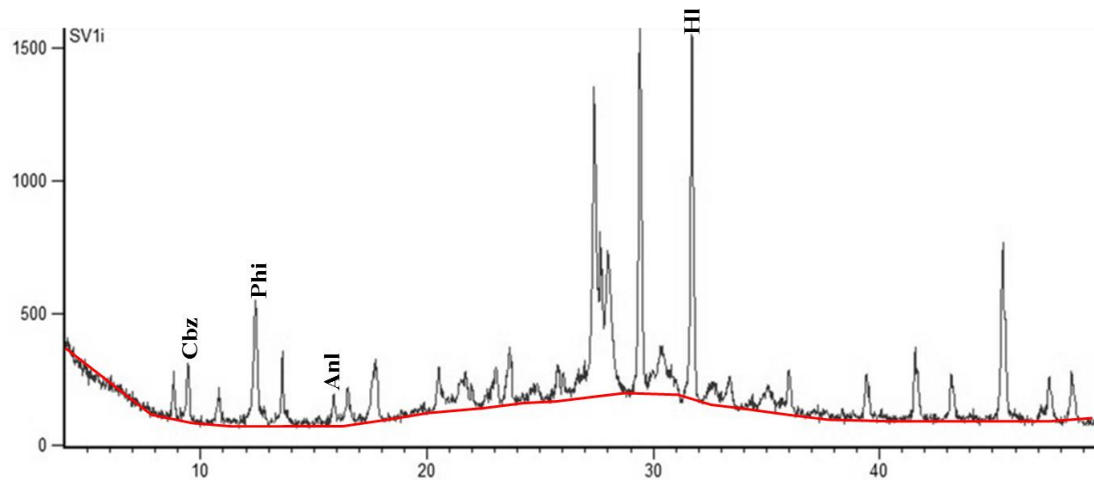


Figure 5.10: XRPD spectrum of SV1 aggregates; red line shows the rising of spectrum background.

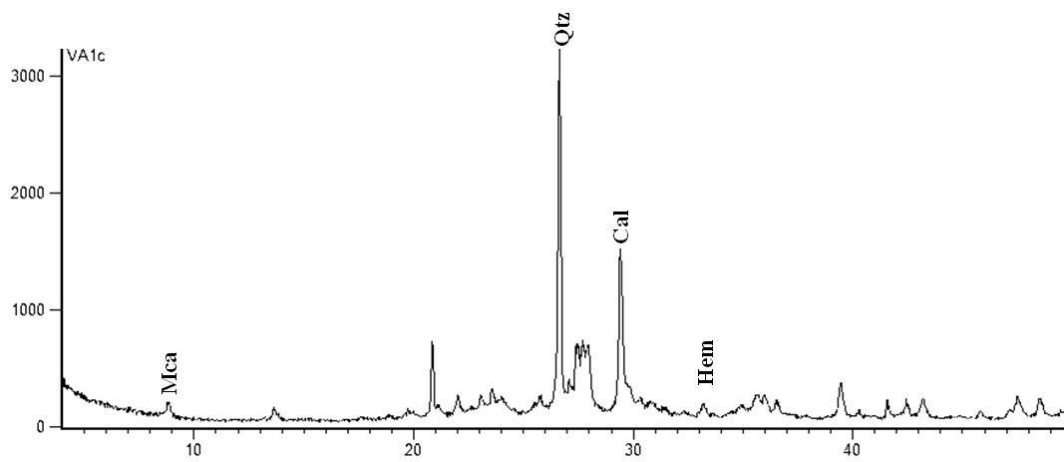


Figure 5.11: XRPD spectrum of VA1 ceramic fragments.

5.2.4 Micro-morphology and chemical analysis (SEM-EDS)

SEM-EDS analyses, performed on the binder confirmed the presence in some samples of gypsum (Figure 5.12a) and demonstrate the presence of newly-formed hydraulic phases like gel C-A-S-H (Calcium Aluminum Silicate Hydrate). Gel C-A-S-H (Figure 5.12b) is identified by the characteristic spongy morphology, formed by reaction of lime with oxides from “pozzolanic” material or ceramic fragments (Jackson et al., 2014).

As regard, volcanic aggregates, once again is confirmed the use of Neapolitan Yellow Tuff, due to: a) presence of phillipsite with prismatic crystal habit, b) pseudocubic crystals of chabazite (Figure 5.12c) (de Gennaro et al., 1999; 2000). Volcanic glass fragments (Figure 5.12d), smectite with "flakes" structure (Figure 5.12e) and mica with lamellar crystal habit (Figure 5.12f) were also observed by SEM-EDS analysis, and those phases again can be ascribed to NYT products.

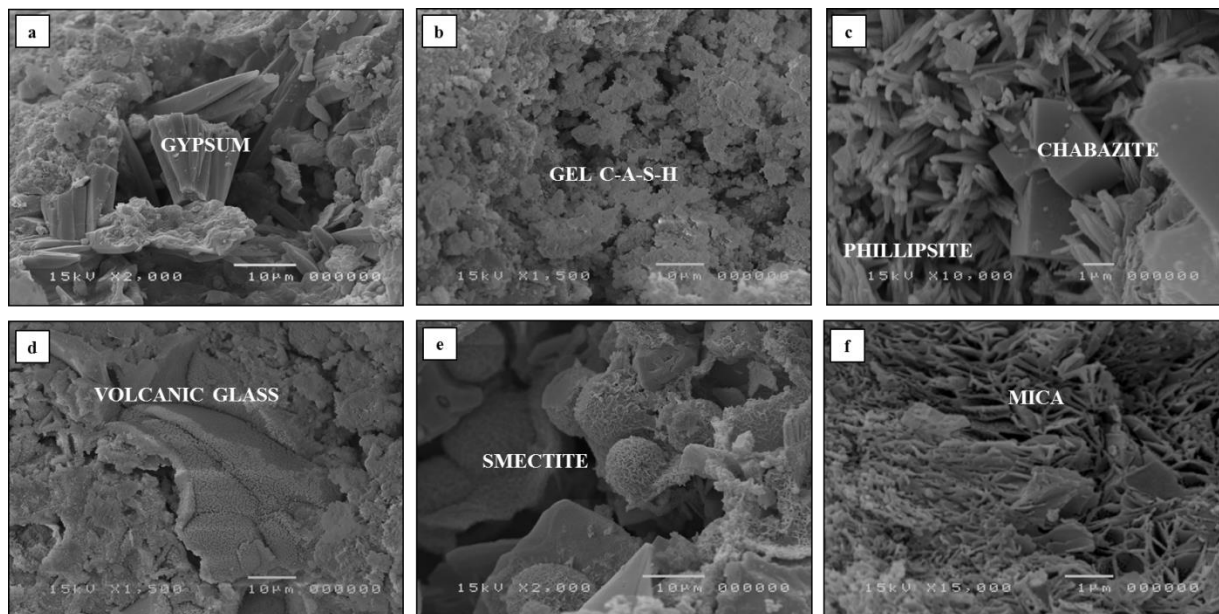


Figure 5.12: SEM image of: a) Gypsum in SV2 binder; b) Gel C-A-S-H in TM3 binder; c) Phillipsite and Chabazite in PT2 volcanic fragment; d) Volcanic glass in TM1 fragment; e) Smectite in PT1 volcanic fragment; f) mica in VA1 volcanic fragment.

To obtain further information about the binder’s composition, SEM-EDS microanalysis was also carried out on both binder and lime lumps present in the mortars (Table 5.4, Figure 5.13a-b); data were used to calculate Hydraulicity Index (HI, see chapter 3) according to Boynton’s formula (Boynton, 1966).

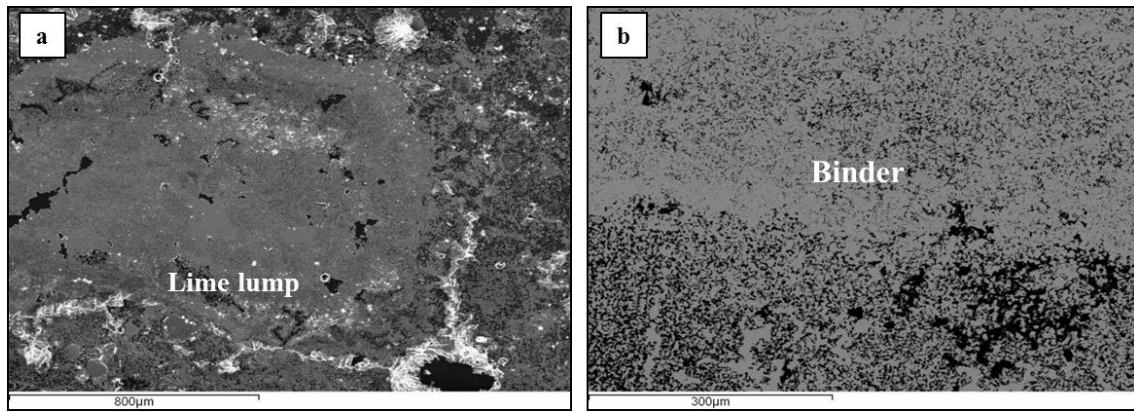


Figure 5.13: BSE-SEM images of a) example of analyzed lime lumps in sample SV2 b) e example of analyzed binder in sample TM1.

SEM-EDS microanalysis revealed that lime lumps consisted mainly of CaO, with very high values of CaO+MgO generally, between 89.02 and 96.38%, whereas binder shows concentrations of SiO₂+Al₂O₃+Fe₂O₃ (10.17 - 26.94 %), definitely higher than lumps (3.45 – 4.37 %) and lower contents of CaO+MgO (70.82 – 85.03%) (Table 5.4, Figure 5.14).

The Hydraulicity Index for lime lumps has low values (HI < 0.10, Figure 5.15), therefore those materials can be classified as aerial lime (Zawawi, 2006).

Binder show HI values between 0.12 and 0.38, thus falling in the field of weakly hydraulic and moderately hydraulic lime as reported in Figure 5.15.

HI calculation confirms the difference of V1 mortar sample compared with others, due to its high values to HI (0.38).

Low values of HI detected in lumps, as well as the considerable increase in this index for the binder, suggest that hydraulicity of examined mortars was obtained by addition of “pozzolanic” material. This information is confirmed by the presence of reaction rims around some pumice, scoriae and ceramic fragments: Si and Al migrate (by diffusion processes) from those fragments towards the binder, resulting in the formation of the so-called hydraulic phases (C–A–S–H).

Table 5.4: Average values of major oxides (wt.% recalculated to 100%, EDS), lime lumps (L) and binder (B).

wt. %	VA1 L	VA1 B	SV1 L	SV1 B	SV2 L	SV2 B	PT1 L	PT1 B	PT2 L
SiO ₂	4.87	11.19	4.78	8.59	3.34	11.18	5.16	17.42	6.07
TiO ₂	-	-	0.11	0.09	-	0.20	-	0.24	0.22
Al ₂ O ₃	1.41	3.94	0.91	3.58	0.75	2.72	1.12	4.46	1.78
Fe ₂ O ₃	-	0.71	0.05	0.50	0.35	0.52	0.20	-	0.22
MnO	0.25	-	-	-	-	0.50	-	0.19	-
MgO	0.90	1.77	-	0.68	0.28	5.16	1.05	1.28	2.32
CaO	88.52	77.16	91.52	82.37	93.41	75.17	88.36	71.18	88.67
Na ₂ O	1.15	1.62	0.67	0.72	0.42	1.63	2.35	2.95	0.49
K ₂ O	0.92	1.56	0.40	0.38	0.67	0.66	0.47	1.09	0.16
P ₂ O ₅	-	0.24	0.18	0.19	-	-	0.04	-	-
V ₂ O ₃	-	-	-	-	-	-	-	-	-
BaO	-	-	-	-	-	-	-	-	-
SO ₃	0.64	0.73	0.99	0.73	0.64	0.35	1.11	0.31	-
Cl-	-	0.10	0.06	0.80	0.14	0.26	0.14	0.12	0.07
F-	1.34	0.98	0.34	1.38	-	1.65	-	0.74	0.00
Total	100.00								
SiO₂ +Al₂O₃+Fe₂O₃	6.28	15.83	5.74	12.66	4.44	14.41	6.48	21.88	8.08
CaO+MgO	89.42	78.93	91.52	83.06	93.69	80.34	89.41	72.47	90.99
HI	0.07	0.20	0.06	0.15	0.05	0.18	0.07	0.30	0.09

wt. %	PT2 B	TM1 L	TM1 B	TM2 L	TM2 B	TM3 L	TM3 B	V1 L	V1 B
SiO ₂	10.98	5.49	8.32	6.18	14.76	1.46	12.87	1.93	17.82
TiO ₂	-	0.27	0.26	-	0.39	0.13	-	-	0.18
Al ₂ O ₃	3.93	1.09	1.85	1.24	3.02	0.93	2.85	0.78	8.04
Fe ₂ O ₃	0.06	0.11	-	0.08	0.12	-	0.75	-	1.09
MnO	0.36	-	0.16	-	-	0.13	-	0.55	-
MgO	1.29	3.07	4.52	0.91	3.40	0.52	3.62	0.26	13.29
CaO	78.69	85.95	80.51	87.77	75.87	95.56	75.39	96.10	57.53
Na ₂ O	1.47	0.41	0.61	0.42	0.16	0.13	2.21	-	0.47
K ₂ O	0.70	-	-	0.36	0.44	0.33	0.51	-	-
P ₂ O ₅	0.09	0.29	0.33	0.05	0.29	-	-	-	-
V ₂ O ₃	-	-	-	-	-	-	-	-	-
BaO	-	-	-	-	-	-	-	-	-
SO ₃	-	2.03	1.92	0.31	0.79	0.28	0.67	0.23	0.69
Cl-	0.31	0.33	0.43	0.17	0.35	-	0.20	0.16	0.02
F-	2.12	0.96	1.09	2.53	0.41	0.52	0.94	-	0.89
Total	100.00								
SiO₂ +Al₂O₃+Fe₂O₃	14.97	6.69	10.17	7.49	17.90	2.39	16.47	2.71	26.94
CaO+MgO	79.98	89.02	85.03	88.68	79.27	96.08	79.01	96.35	70.82
HI	0.19	0.08	0.12	0.08	0.23	0.02	0.21	0.03	0.38

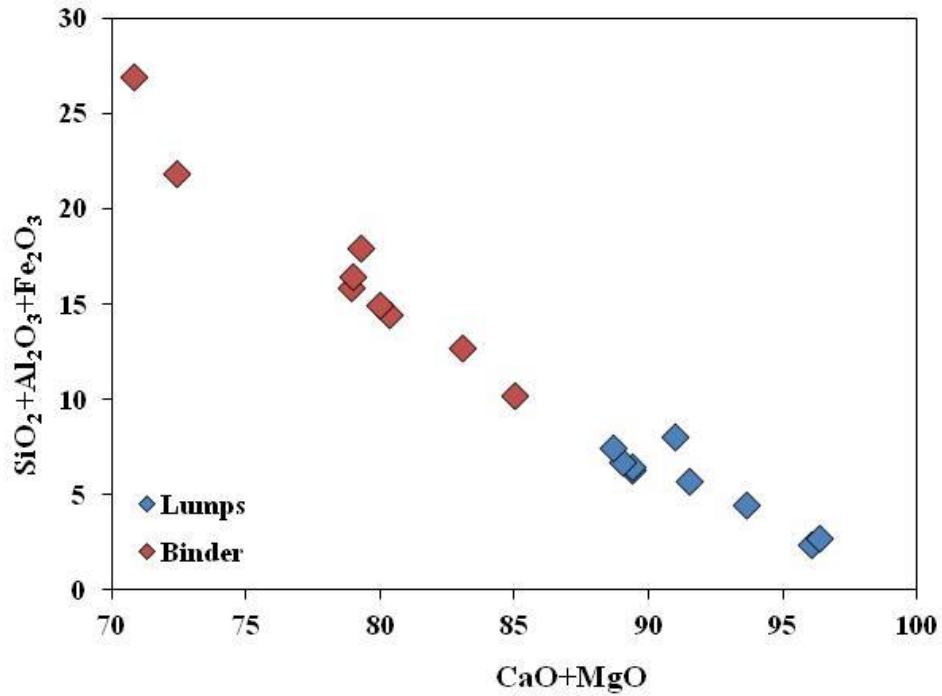


Figure 5.14: CaO + MgO vs. SiO₂ diagram (EDS), lumps and binder.

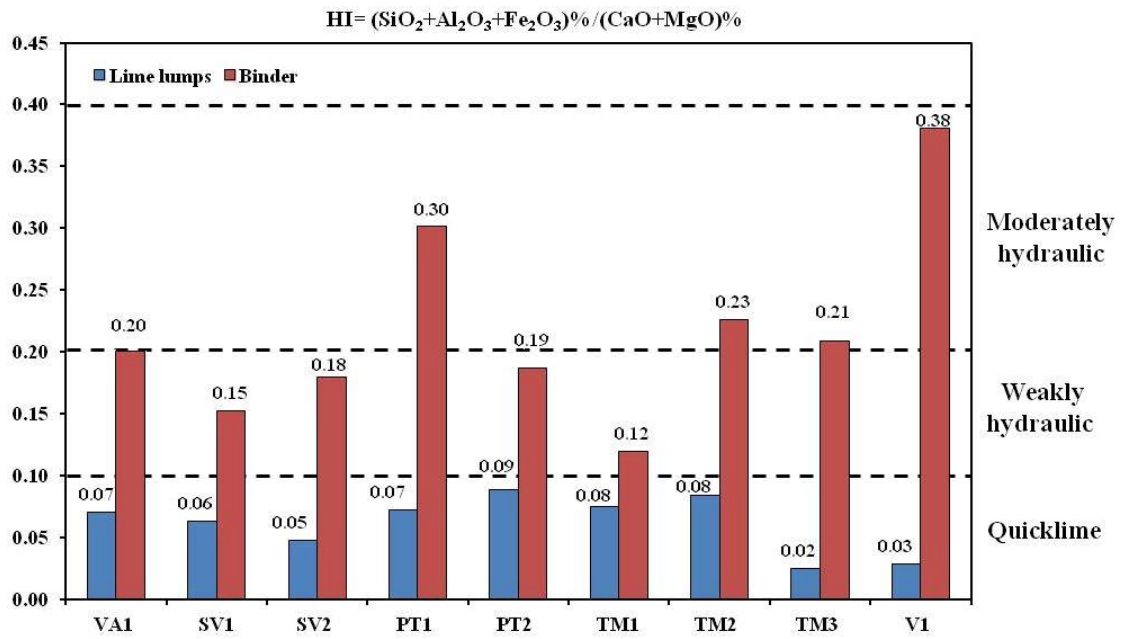


Figure 5.15: Hydraulicity Index (HI), lime lumps (blue) and binder (red) for analyzed mortars.

In order to obtain further information regarding the provenance of volcanic aggregate, SEM-EDS microanalyses were carried out on pumice present in the samples (Figure 5.16, Table 5.5).

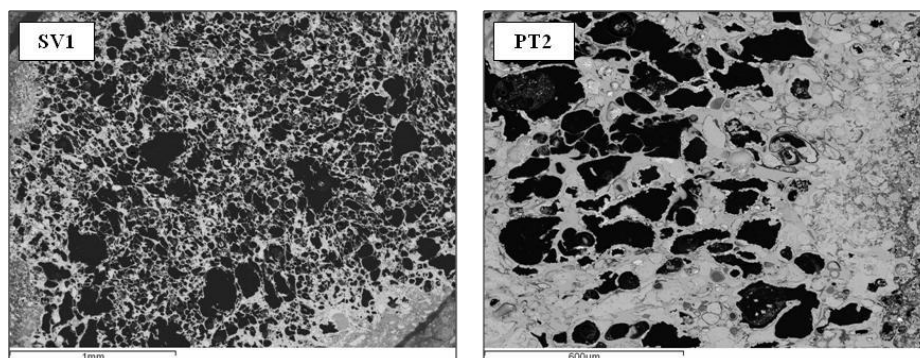


Figure 5.16: BSE-SEM image of pumice, SV1 and PT2 sample.

Table 5.5: Major element concentrations (wt.% recalculated to 100%, EDS), pumice.

wt.%	VA1	VA1	VA1	VA1	SV1	SV1	SV2	SV2	PT1	PT1	PT1	PT1	PT2	PT2
SiO ₂	63.00	60.65	61.27	61.69	56.35	61.48	61.30	61.63	61.18	61.56	61.89	61.61	61.21	61.48
TiO ₂	-	0.16	0.53	0.51	0.69	0.21	0.59	0.50	0.54	0.41	0.30	0.47	0.46	0.48
Al ₂ O ₃	19.42	18.41	18.13	18.22	18.62	17.86	17.17	18.25	17.92	18.13	17.97	16.67	17.31	17.85
Fe ₂ O ₃	1.68	3.30	3.20	2.66	5.41	3.14	4.57	3.35	3.18	3.29	3.07	4.74	4.49	2.98
MnO	-	0.39	0.12	0.21	0.27	0.28	0.11	0.36	0.32	-	-	0.17	0.20	0.45
MgO	-	0.35	0.36	0.23	1.33	0.33	0.41	0.27	0.35	0.35	0.30	0.51	0.30	0.26
CaO	2.02	2.07	1.84	1.80	4.40	2.15	1.80	1.89	1.98	1.96	1.99	1.89	2.17	2.12
Na ₂ O	5.31	6.05	5.38	5.50	3.62	5.03	5.80	5.17	5.18	5.32	5.98	5.59	5.86	5.76
K ₂ O	7.95	7.12	8.09	8.10	8.24	7.50	7.13	7.64	8.01	7.92	7.07	6.96	7.09	7.88
P ₂ O ₅	0.08	0.11	0.22	-	0.41	-	0.09	0.09	0.20	0.27	0.43	0.15	-	-
V ₂ O ₃	-	-	-	-	-	-	-	-	-	-	-	-	-	-
BaO	-	-	-	-	-	-	-	-	-	-	-	-	-	-
SO ₃	0.16	0.19	0.00	0.24	0.12	-	-	0.09	0.27	-	-	0.15	-	-
Cl ⁻	0.38	0.61	0.87	0.84	0.53	0.75	1.03	0.76	0.87	0.80	0.99	1.10	0.92	0.75
F ⁻	-	0.59	-	-	-	1.26	-	-	-	-	-	-	-	-
Total	100.00	100.00	100.00	100.00	100.00	100.00	100.00	100.00	100.00	100.00	100.00	100.00	100.00	100.00
Na ₂ O+K ₂ O	13.26	13.17	13.47	13.60	11.86	12.52	12.93	12.81	13.19	13.24	13.05	12.54	12.94	13.64

wt.%	TM1	TM1	TM1	TM1	TM1	TM1	TM2	TM2	TM3	TM3	TM3	TM3	V1	V1
SiO ₂	61.54	60.83	62.01	60.73	61.93	61.70	61.57	62.53	61.50	61.25	60.58	61.54	61.19	61.43
TiO ₂	0.03	0.37	0.42	0.67	0.41	0.45	0.30	0.71	0.43	0.29	0.54	0.54	0.27	0.20
Al ₂ O ₃	18.81	16.60	18.16	17.18	18.31	18.20	18.23	18.27	18.81	18.44	17.97	17.93	17.82	17.92
Fe ₂ O ₃	2.80	4.63	3.18	4.17	2.58	2.87	2.45	3.07	2.67	2.96	4.00	3.22	3.07	3.71
MnO	0.30	0.70	0.46	0.45	0.25	0	0.36	0.21	0.36	0.12	0.12	0.10	0.29	0.19
MgO	0.22	0.48	0.21	0.56	0.24	0.31	0.30	0.19	0.37	0.44	0.38	0.21	0.19	0.23
CaO	2.30	2.15	1.92	2.19	1.67	1.80	1.98	1.93	2.24	1.94	2.04	1.99	1.97	2.34
Na ₂ O	6.39	6.59	5.44	5.74	6.05	6.30	4.72	4.17	4.34	4.68	5.96	5.50	5.78	5.29
K ₂ O	6.91	6.52	7.11	6.94	7.19	7.26	8.97	7.94	8.36	8.79	7.38	7.72	7.81	7.58
P ₂ O ₅	-	-	0.25	0.25	-	0.22	0.36	0.16	0.12	0.27	-	0.13	-	0.20
V ₂ O ₃	-	-	-	-	-	-	-	-	-	-	-	-	-	-
BaO	-	-	-	-	-	-	-	-	-	-	-	-	-	-
SO ₃	-	-	-	-	0.27	-	-	-	-	-	-	0.08	-	0.09
Cl ⁻	0.69	0.96	0.83	1.12	0.77	0.90	0.76	0.83	0.69	0.81	1.03	1.04	0.84	0.82
F ⁻	-	0.16	-	-	0.35	-	-	-	0.12	-	-	-	0.78	-
Total	100.00	100.00	100.00	100.00	100.00	100.00	100.00	100.00	100.00	100.00	100.00	100.00	100.00	100.00
Na ₂ O+K ₂ O	13.30	13.12	12.55	12.68	13.24	13.55	13.69	12.11	12.69	13.48	13.33	13.22	13.59	12.87

Plotting the obtained values in the Total Alkali versus Silica diagram (TAS) for the effusive volcanic rocks (Le Maitre et al., 1989) (Figure 5.17), it is possible to observe that they have a trachytic compositions.

Moreover, the analyzed pumice follow the compositional trend of *Campi Flegrei* products, in particular they show affinity with pumice belonging to NYT.

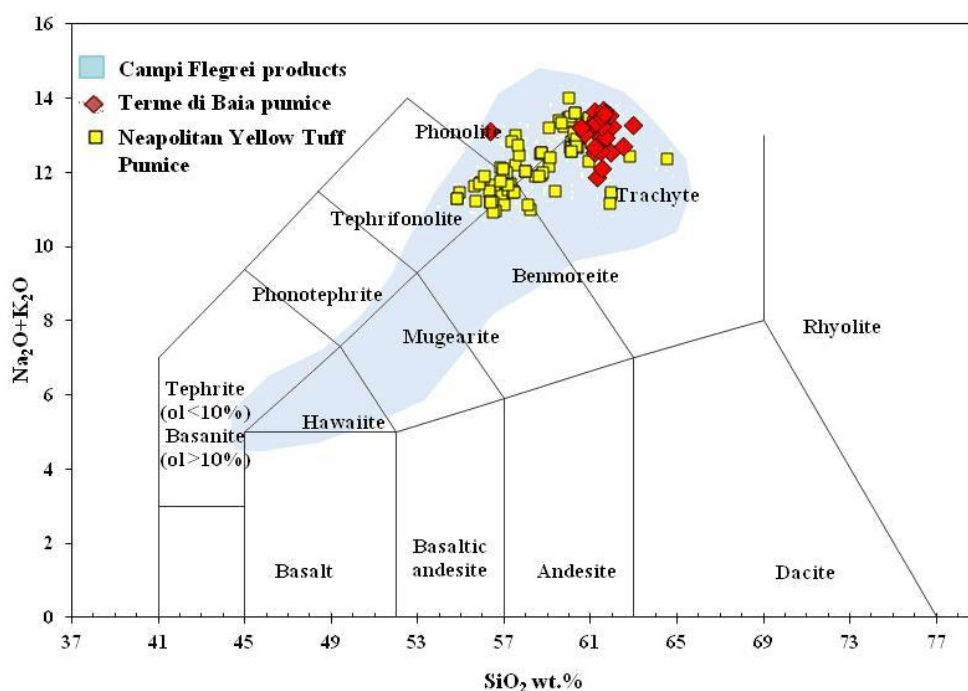


Figure 5.17: Classification of pumice fragments from investigated samples (Le Maitre et al., 1989) and geochemical comparison with Phlegrean pumice (Morra et al., 2010).

Values of alteration index such as CIA (Chemical Index of Alteration), WIP (Weathering Index of Parker) and W index and the diagram which represents various index, suggest that analyzed pumice can be considered not altered. Investigated pumice (Table 5.5) show CIA values between 42.7–49.1 (Figure 5.18), WIP values between 111.3–126.8 (Figure 5.19) and W values between 1.7–15.5 (Figure 5.20), (Table 5.6).

Table 5.6 CIA, WIP and W index values for analyzed pumice.

	VA1	VA1	VA1	VA1	SV1	SV1	SV2	SV2	PT1	PT1	PT1	PT1	PT2	PT2
CIA	46.22	46.4	46.4	46.1	46.8	46.3	44.9	42.7	46.5	46.0	45.3	46.4	44.9	45.9
WIP	122.48	124.0	124.7	122.8	116.4	121.8	120.5	126.8	122.3	121.1	116.8	125.6	126.1	124.1
W	5.32	10.9	9.0	2.2	6.7	10.8	10.3	11.3	9.6	7.2	12.9	7.2	8.3	1.7
	TM1	TM1	TM1	TM1	TM1	TM1	TM2	TM2	TM3	TM3	TM3	TM3	V1	V1
CIA	43.2	47.4	45.1	46.8	45.9	45.3	49.1	48.2	47.0	45.5	46.0	47.4	45.9	44.9
WIP	123.0	116.0	119.0	121.8	125.1	125.2	111.3	117.7	124.0	123.8	121.9	118.1	119.8	118.3
W	9.5	8.8	13.1	7.9	8.6	6.1	12.9	9.7	8.7	11.2	9.5	10.6	6.0	15.5

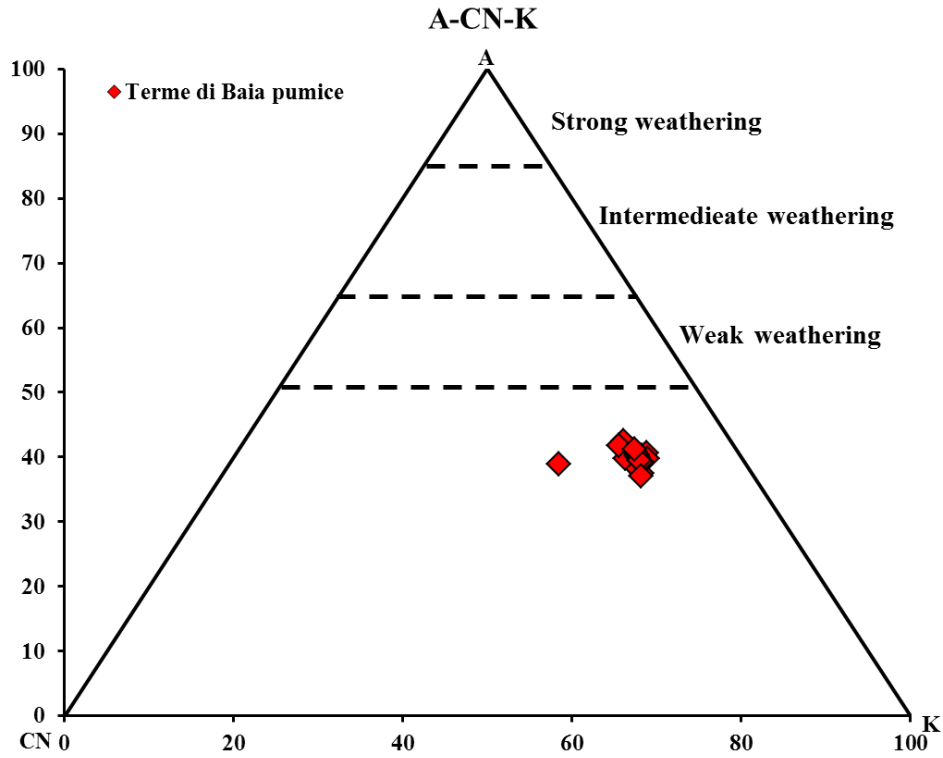


Figure 5.18: A-CN-K (Al_2O_3 — $\text{CaO}+\text{Na}_2\text{O}$ — K_2O) diagram (Nesbitt and Young, 1982) for *Terme di Baia* pumice.

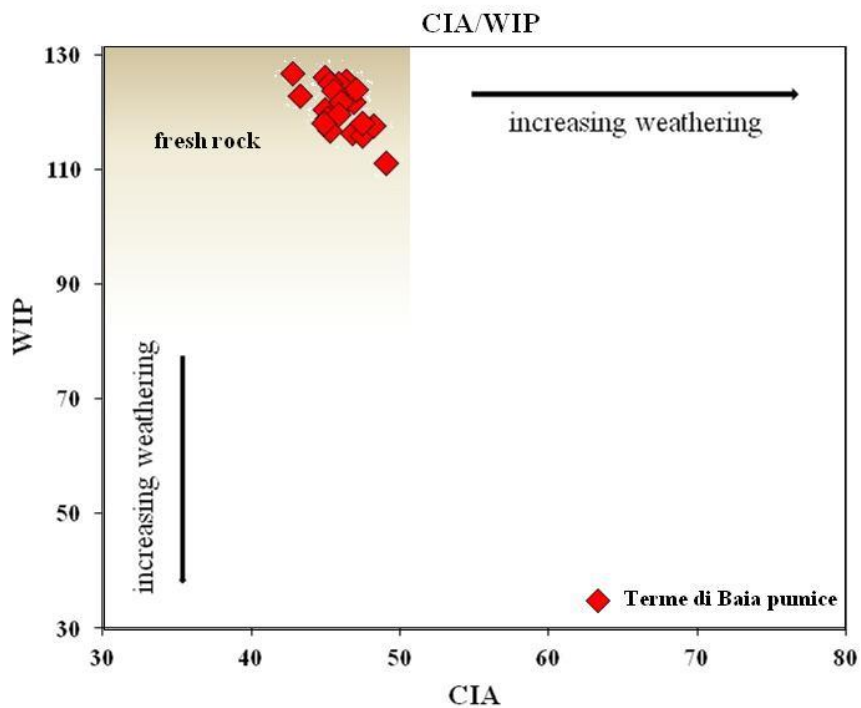


Figure 5.19: Relationship between two weathering proxies, WIP and CIA (Bahlburg and Dobrzinski, 2011), for *Terme di Baia* pumice.

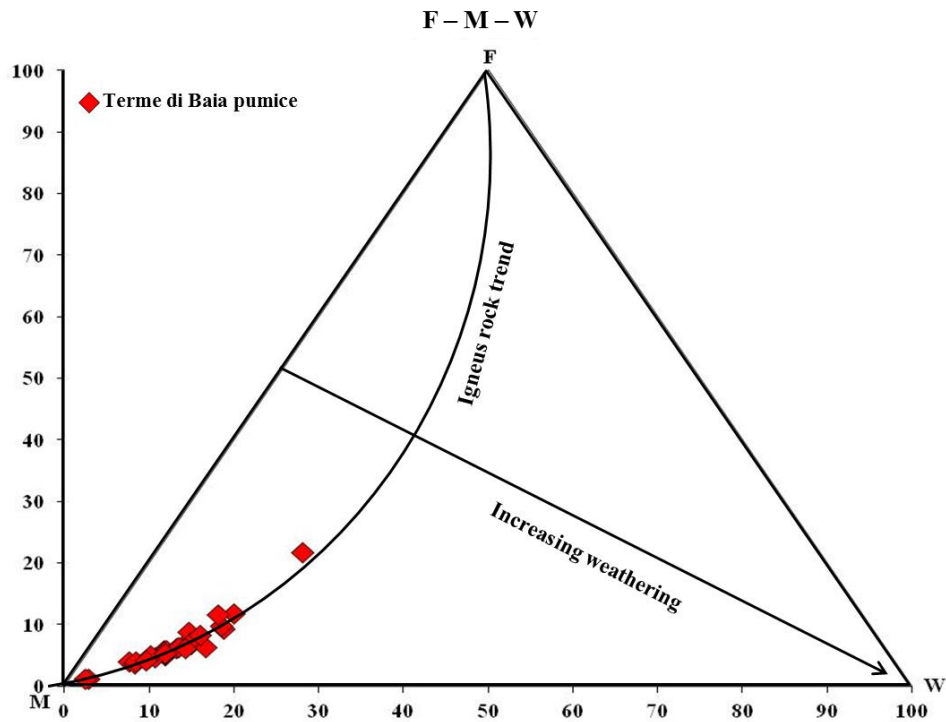


Figure 5.20: Weathering trends, MFW diagram (Ohta and Arai, 2007) for *Terme di Baia* pumice.

As regards ceramic fragments, SEM investigation confirmed presence of the phases detected with XRPD, such as: quartz (Figure 5.21a), calcite (Figure 5.21b), feldspar and mica, but EDS analysis on polished thin sections provide further interesting information (Figure 5.22). Variable concentration of CaO (3.06 – 28.17 wt.%) in the matrix have confirmed the differences among ceramic fragments (Table 5.7), highlighting the use of different clayey raw materials employed in the production of the ceramic fragments (CaO > 6 wt.% – calcareous clay; CaO < 6 wt% - non calcareous clay; Maniatis and Tite, 1981).

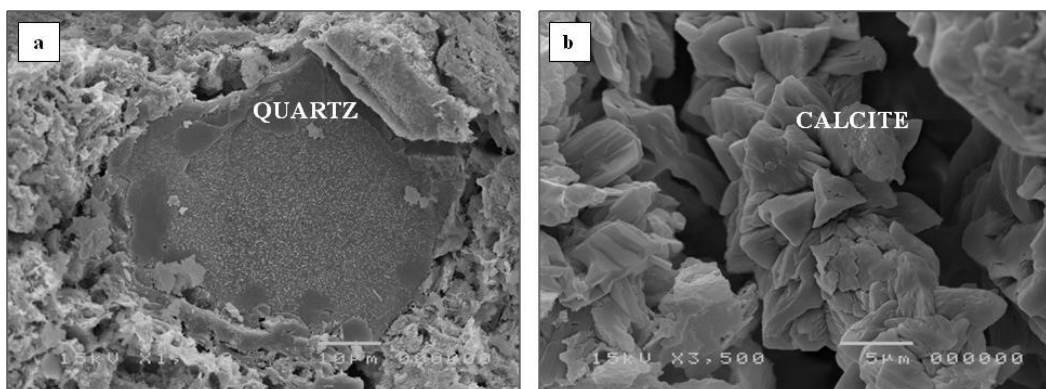
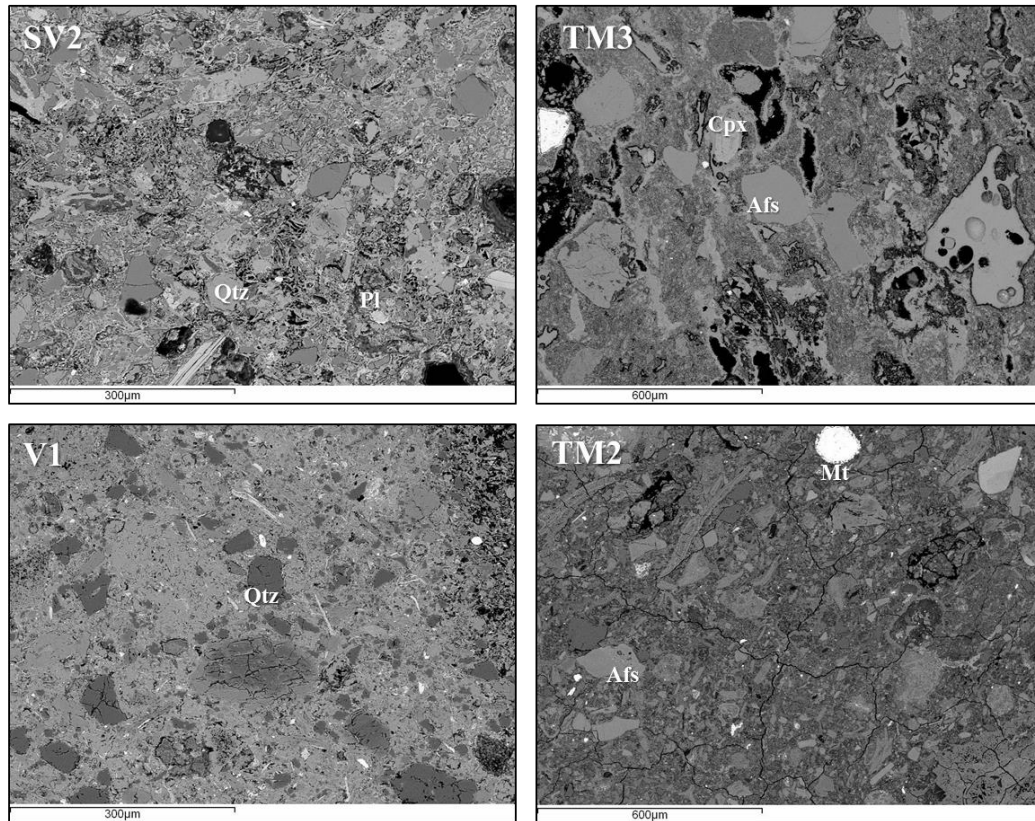


Figure 5.21: SEM image of: a) quartz in VA1 ceramic fragment; b) calcite in V1 ceramic fragment.



* Cal: calcite; Qtz: quartz; Afs: alkali feldspar; Pl: plagioclase; Mt: magnetite.

Figure 5.22: BSE SEM images of different ceramic fragments.

Table 5.7: Chemical composition (wt.% recalculated to 100%, EDS), matrix of ceramic fragments.

wt.%	SiO ₂	TiO ₂	Al ₂ O ₃	Fe ₂ O ₃	MnO	MgO	*CaO	Na ₂ O	K ₂ O	P ₂ O ₅	V ₂ O ₃	BaO	SO ₃	Cl ⁻	F ⁻	Total
SV2	52.55	0.51	19.03	6.04	0.48	2.85	12.96	1.73	3.05	0.16	-	0.19	-	0.48	-	100.00
TM3	57.69	0.77	16.73	5.75	-	2.47	10.02	1.62	4.25	0.18	-	0.42	0.08	0.03	-	100.00
TM2	49.54	0.93	29.50	5.66	0.07	1.00	3.06	3.40	6.24	0.06	-	0.19	0.05	0.30	-	100.00
V1	48.28	0.58	13.19	3.84	0.10	2.15	28.17	1.46	2.20	-	-	-	-	0.04	-	100.00

* CaO > 6 wt. – calcareous clay; CaO < 6 wt% - non calcareous clay

5.2.5 XRF analysis

XRF analyses were performed on representative samples of mortars (PT1, SV2, TM3 and V1) Results are summarized in Table 5.8.

Table 5.8: Chemical analyses (XRF), major oxides and trace elements, mortars.

wt.%	SiO ₂	TiO ₂	Al ₂ O ₃	Fe ₂ O ₃	MnO	MgO	CaO	Na ₂ O	K ₂ O	P ₂ O ₅	SO ₃	SrO	LOI
PT1	32.37	9.11	1.79	14.84	2.65	0.81	3.15	7.07	0.20	0.06	0.09	0.03	25.99
SV2	29.92	8.62	1.88	17.43	1.34	0.33	3.05	5.04	0.22	0.06	0.09	0.05	28.60
TM3	38.20	10.74	2.53	19.63	1.15	0.13	3.91	2.49	0.28	0.06	0.12	0.05	20.29
V1	25.26	6.87	2.10	26.92	6.50	0.03	1.03	0.36	0.25	0.10	0.08	0.03	30.28

ppm	Cr	Zn	Ba	Br	Cl	Co	F	Ni	Pb	Cu	V
PT1	48	164	0	0	17353	0	0	72	267	135	205
SV2	45	127	0	0	33411	0	0	85	0	146	0
TM3	114	176	0	0	3459	0	0	108	123	147	0
V1	86	152	0	0	1384	0	0	69	0	135	0

Representative diagrams were selected to highlights the similarities or differences between the mortars. The SiO₂/CaO diagram (Figure 5.23a) show the high scattering of the two oxides within the considered samples. CaO ranges between 14.58 (PT1 sample) and 26.92 wt.% (V1 sample) whereas SiO₂ shows its highest concentration in TM3 (38.20 wt. %) and the lowest in V1 (25.26 wt. %).

In the Al₂O₃/Fe₂O₃ diagram (Figure 5.23b), PT1 and SV2 mortars show chemical similarity (1.79 – 1.88 wt.% Fe₂O₃; 8.62 - 9.11wt.% Al₂O₃, respectively); quite different is the TM3 mortars (2.53 wt.% Fe₂O₃; 10.54 wt.% Al₂O₃). V1 mortar show the lowest Al₂O₃ concentration (6.87 wt.%) respect to other mortars.

The SO₃/Cl diagram (Figure 5.23c) indicate that mortars generally show different concentration of these chemical compounds, with the only exception of V1 and TM3 which plot very close each other and show the lowest concentration of SO₃ and Cl.

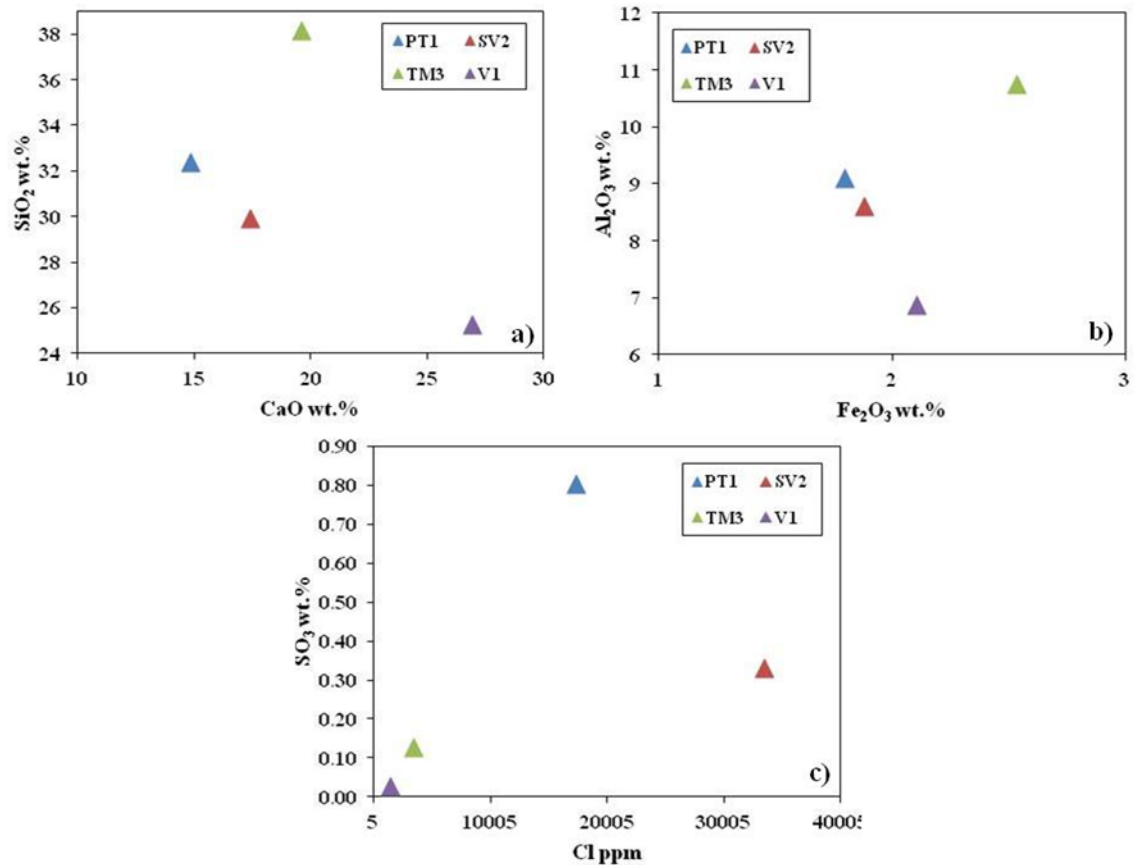


Figure 5.23: Binary diagrams representative of major oxide and trace element composition.

5.2.6 Differential and Gravimetric Thermal Analyses (DTA-TGA)

Thermal analyses (DTA-TGA) were carried out to classify the level of hydraulicity of each sample mortars. Main attention was focused on weight loss percentage of H₂O, due to dehydration of calcium silicates and aluminates hydrates, occurring between approximately 200 and 600 °C, representing structural-bound water (SBW). These values, and the weight loss percentage associated with CO₂ evolution from calcite decomposition (Bonazza et al., 2013), are represented in Table 5.9 (Figure 5.24).

CO₂/SBW vs. CO₂ (%) diagram, comparing our data with those from Moropoulou et al., 2005, (Figure 5.25), allowed to classify mortars as hydraulic, confirming what found with the SEM – EDS analysis (par. 5.2.4).

V1 mortar differs from the others since it shows the highest weight loss percentage associated to CO₂ (20.56%).

Besides, VP1 sample in CO₂/SBW vs. CO₂ (%) diagram of Moropoulou et al., (2005) fall in the field of artificial pozzolanic mortars (Figure 5.25).

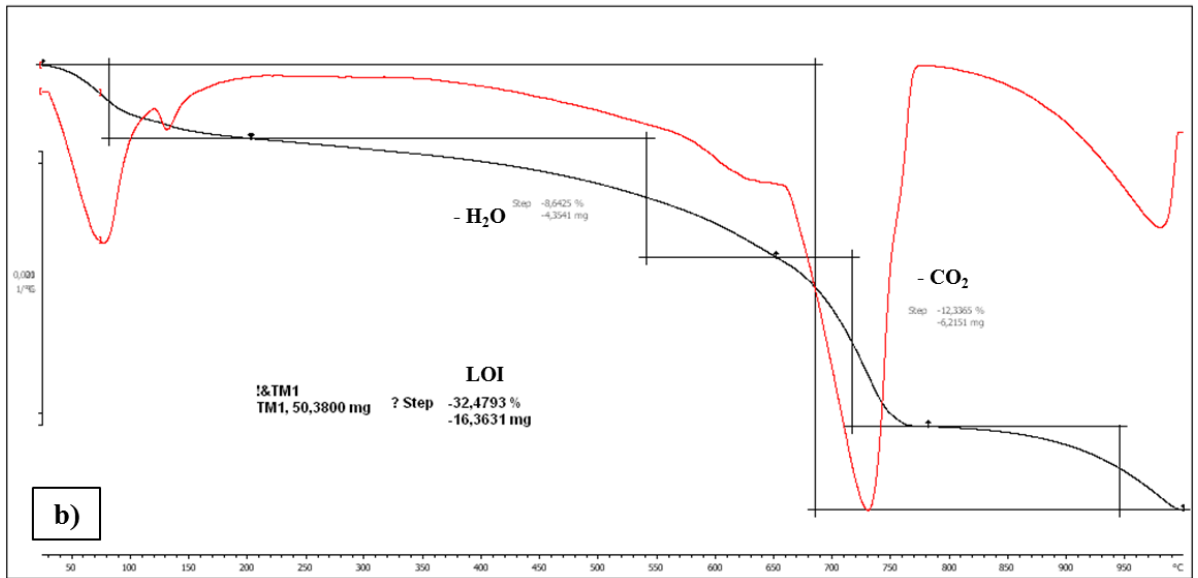
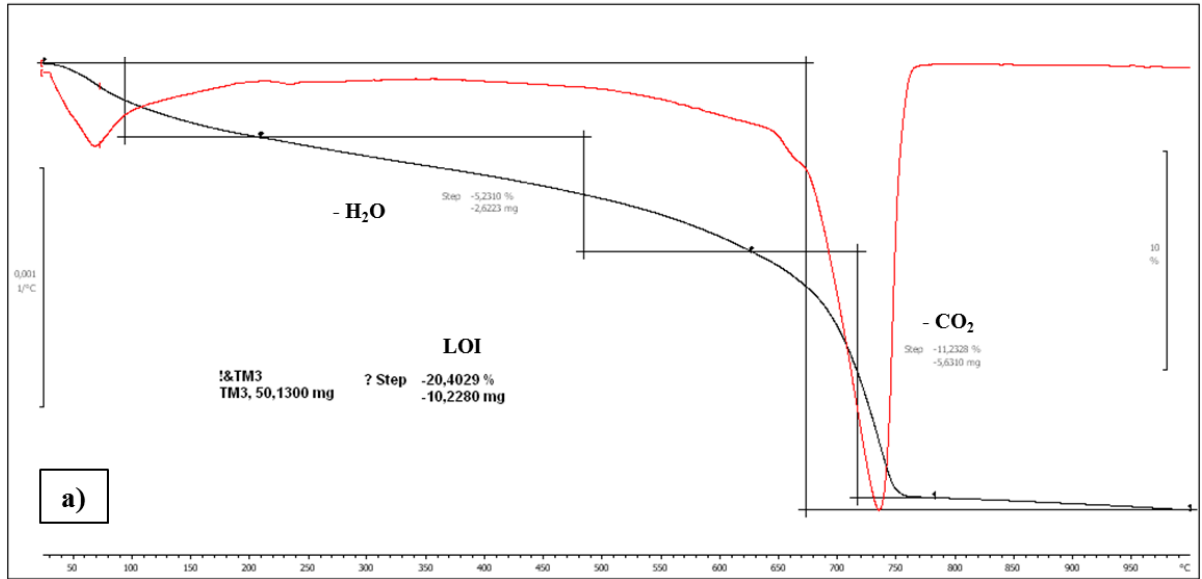


Figure 5.24: DTA-TGA plot of a)TM3 a) and b)TM1 samples.

Table 5.9: Thermal analysis (DTA/DTG) features of investigated sample.

Sample	SBW %	CO ₂ %	CO ₂ /SBW	LOI
PT1	8.54	4.79		28.32
T range (°C)	240-650	650-750	0.56	25-1000
PT2	13.63	6.24		24.49
T range (°C)	230-680	680-760	0.46	25-1000
SV1	7.12	6.34		27.45
T range (°C)	200-570	570-740	0.89	25-1000
SV2	9.42	7.11		33.17
T range (°C)	200-560	560-760	0.75	25-1000
TM1	8.64	12.33		32.47
T range (°C)	200-650	650-780	1.43	25-100
TM2	10.05	12.13		35.22
T range (°C)	210-630	630-780	1.20	25-1000
TM3	5.23	11.23		20.40
T range (°C)	200-640	640-790	2.15	25-1000
VA1	9.35	4.31		30.06
T range (°C)	240-630	630-753	6.08	25-1000
V1	3.38	20.56		25.57
T range (°C)	210-560	560-850	0.46	25-1000

*SBW = Structural Bound Water, LOI= Loss on Ignition

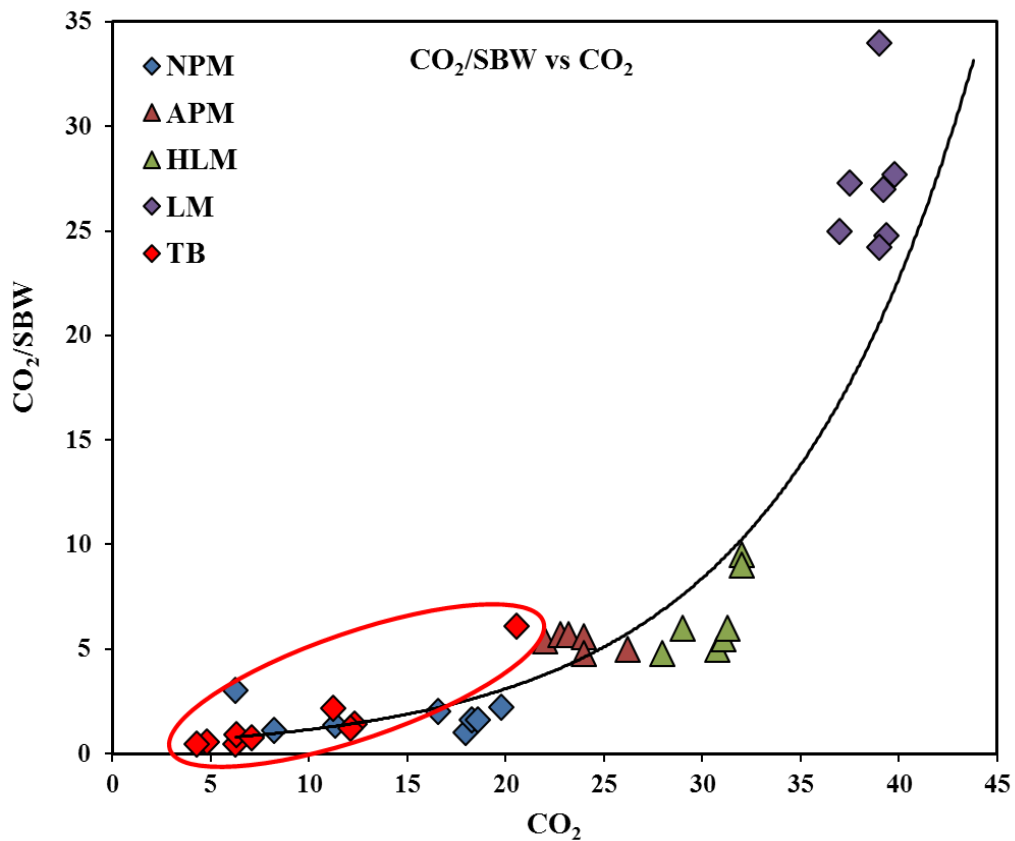


Figure 5.25: Binary CO₂/SBW vs. CO₂ diagram, comparing data from *Terme di Baia* (TB, red circle) and from Moropoulou et al., 2005. (NPM: natural pozzolanic mortars; APM: artificial pozzolanic mortars; HLM: Hydraulic lime mortars; LM: lime mortars).

Some samples show a loss of weight if exposed to temperature higher than 900° C. (Figure 5.24b). This weight loss could be ascribed to the decomposition of sulphates, or to the loss of residual water and carbon or decomposition of halite (Izzo et al., 2015).

5.2.7 Mercury intrusion porosimetry (MIP)

Two representative samples of mortars (PT2 and TM3) were analyzed by mercury intrusion (MIP) according to ASTM D4404.

The analysis was performed on three fragments for each samples, averaging the results.

Results are showed in Table 5.10, while in Figure 5.26 and Figure 5.27 diagram of cumulative porosity and relative volume distributions are reported.

Table 5.10: Porosimetric features (MIP) of mortars.

Sample	PT2	TM3
Cumulative volume (mm³/g)	370.68	244.51
Bulk density (g/cm³)	1.35	1.58
Total porosity (Vol. %)	49.91	38.17

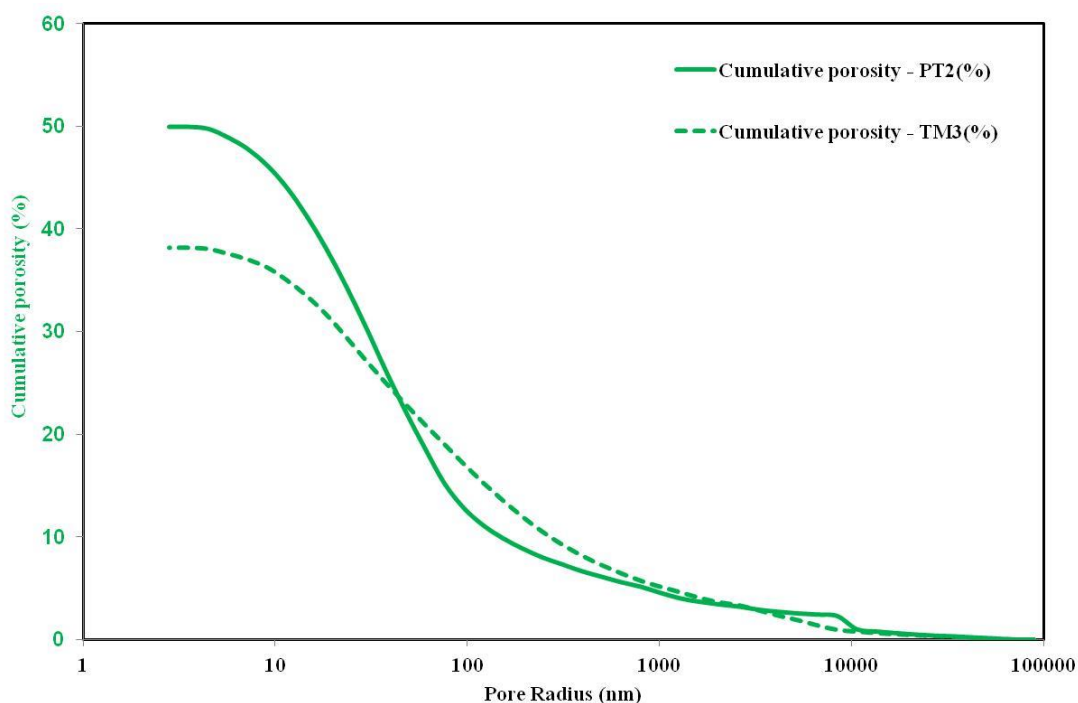


Figure 5.26: Cumulative pore size distribution for PT2 and TM3 samples.

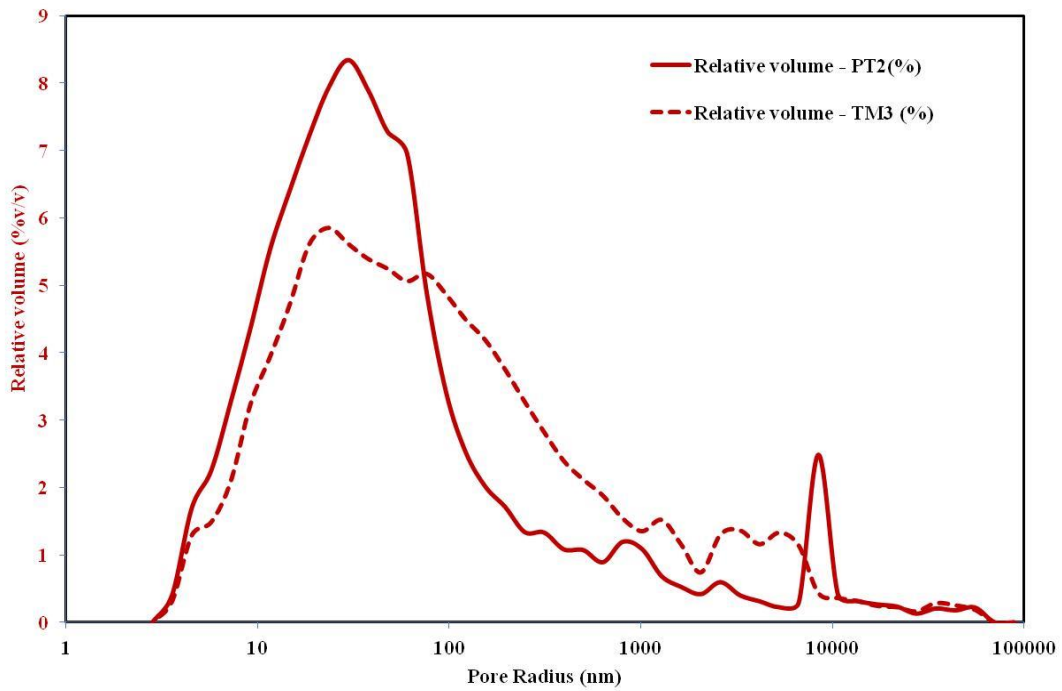


Figure 5.27: Relative pore size distribution in PT2 and TM3 samples.

Samples show values of total porosity between 38 % - 50% and shows mono-modal and broadened shape of pore size distribution.

Pore sizes of the samples fall within the characteristic field of hydration product porosity, considered considered between 10 - 100 nm (Metha et al., 2006; Gotti at al., 2008).

Chapter 6

Villa del Capo: materials and results

6.1 Materials

Thirteen mortar samples were collected from the main buildings of the *villa* (Figure 6.1; Table 6.1).

Sampled mortars were divided into three categories: coating mortars (five samples; Figure 6a) bedding mortars or wall concretes (six samples; Figure 6.2b), floor mortars (two samples; Figure 6.2c).

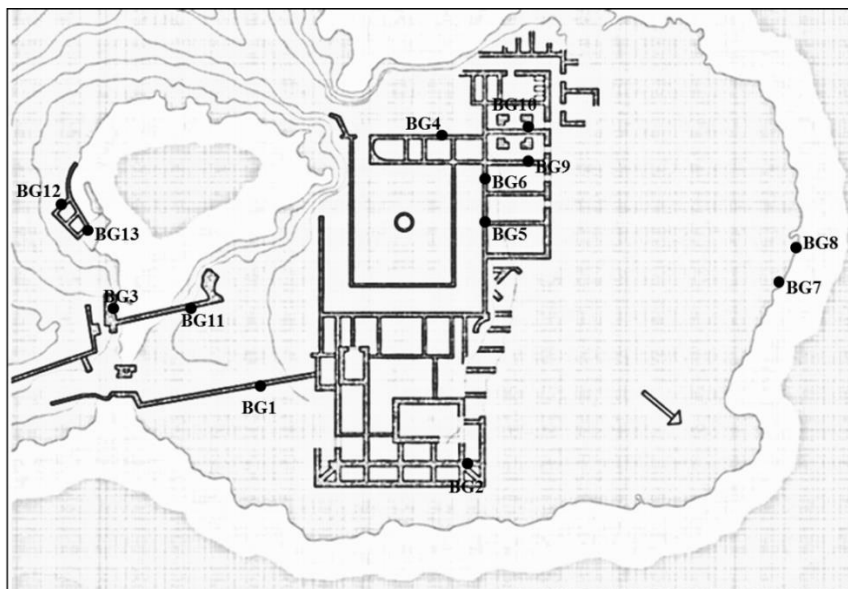


Figure 6.1: Sketch map of the *Villa del Capo* with sampling site (modified after Russo, 2006).

Table 6.1: samples, location and typology.

SAMPLE	LOCATION	TPOLOGY
BG1	external landing platform	floor mortar
BG2	noble residential area	bedding mortar
BG3	bridge and input structures of sea bath	coating mortar
BG4	"quadriportico" of sea Villa	bedding mortar
BG5	cistern of sea Villa	coating mortar
BG6	cistern of sea Villa	coating mortar
BG7	breakwater	bedding mortar
BG8	breakwater	bedding mortar
BG9	warehouses	floor mortar
BG10	warehouses	bedding mortar
BG11	bridge and input structures of sea bath	bedding mortar
BG12	cistern	coating mortar
BG13	cistern	coating mortar



Figure 6.2: Mortars categories: a) coating mortar; b) bedding mortar; c) floor mortar.

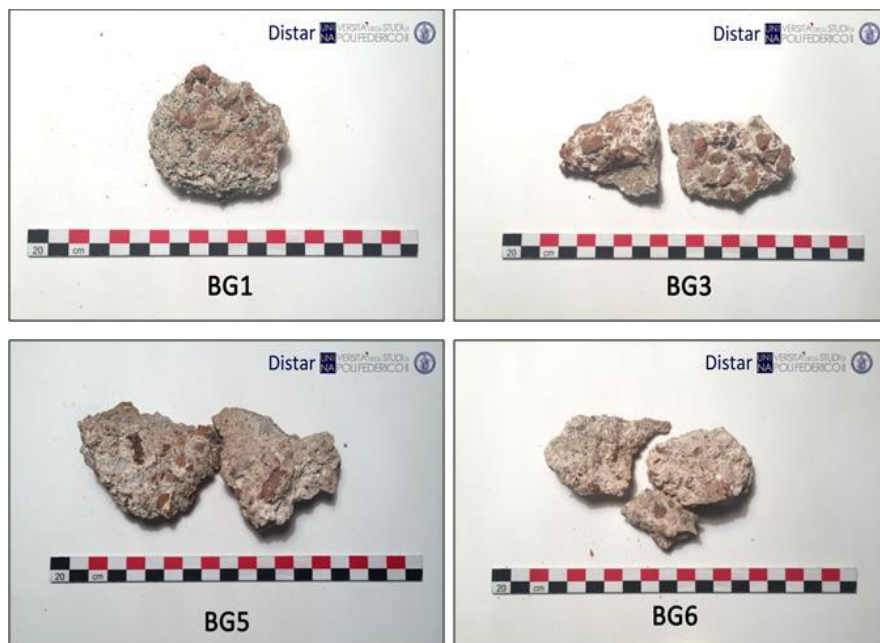
6.2 Results

6.2.1 Macroscopic observation

Mortar samples were macroscopically separated into two categories according to observation of the type of aggregate used: the first type includes coating and floor mortars or mortars with ceramic fragments (Figure 6.3); the second type includes bedding mortars (Figure 6.4) and is characterized by an aggregate only constituted by volcanic and carbonate fragments.

Bedding mortars, in most cases, display very good cohesion. A small number of samples are friable and poorly cohesive.

Coating and floor mortars contain pottery and brick fragments, volcanic fragments and lime lumps, variable in size from mm – to – cm and show very good cohesion.



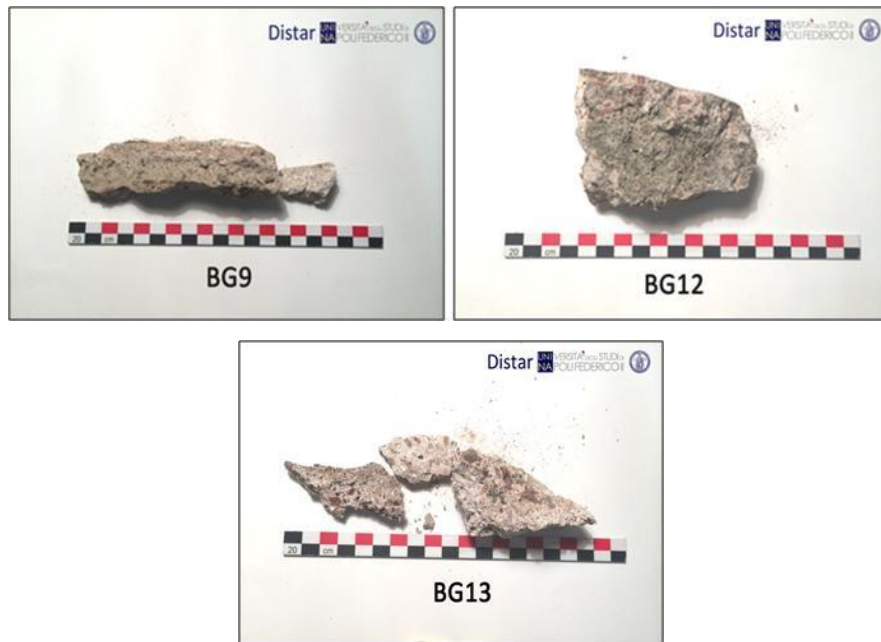


Figure 6.3: Macroscopic images of coating mortars.

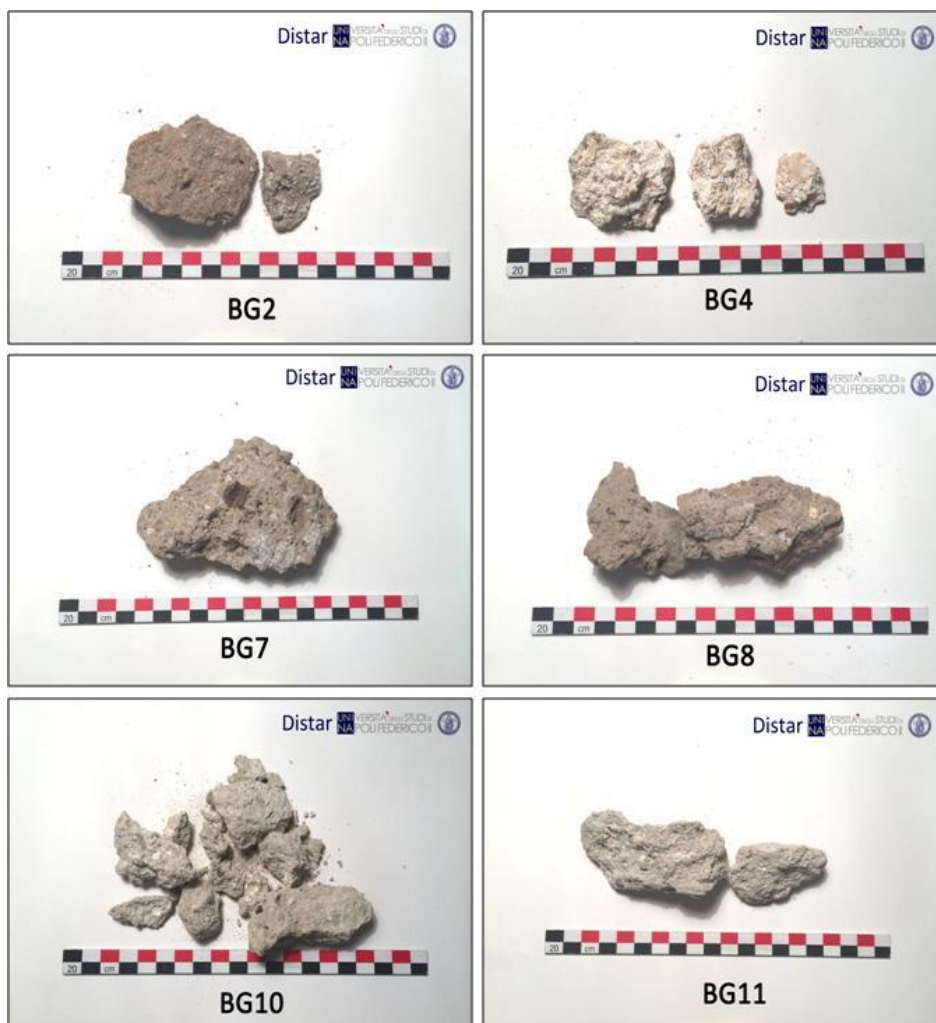


Figure 6.4: Macroscopic images of bedding mortars.

6.2.2 Petrography

Thin section observations and modal analysis - performed counting 1500 points for each section (Table 6.2) – allowed to recognize three distinct groups (A, B and C) that coincide with sampling strategy .

Coating mortar were assigned to group A, bedding mortar to group B and then group C belonging the floor mortars.

Binder phase in group A (BG3, BG5, BG6, BG12 and BG13) is characterized by homogeneous greyish-brownish colour, and shows a cryptocrystalline (31.4 Vol.%) and micritic texture (18.9 Vol.%) (Figure 6.5a). Moreover, in the binder were observed small and fractured lime lumps, that generally consist in unreacted lime, with not well-defined edges (6.3 Vol.%; Figure 6.5b) and very few percentage of sparite grains (0.4 Vol.%).

Regarding aggregates, as well as ceramic fragments (21.5 Vol.%; Figure 6.5c-d), volcanic and carbonate fragments (2.8 Vol.% - 0.5 Vol.%), pumice and scoriae with reaction rim (4.8 Vol.%; 2.2 Vol.%; Figure 6.5f), volcanic glass, and crystal fragments of plagioclase, sanidine, clinopyroxene (5.8 Vol.%) were recognized.

BG6 sample shows the presence of leucite-bearing scoriae (Figure 6.5g); in BG5 sample the presence of crystal fragments of garnet (Figure 6.5h) was also detected.

Volcanic fragments can be classified as volcanic tuff, characterized by the presence of crystals immersed in an altered ashy matrix (Figure 6.5e).

Petrographic observations also revealed a certain variability in types of ceramic fragments. These latter sometimes contain temper of different mineralogical composition: for example, in sample BG12 (Figure 6.5 c-d), we can find fragments (Figure 6.5c) containing different types of small crystals and others (Figure 6.5d) with pumices and larger crystals. Moreover, they have also different degrees of porosity: in Figure 6.5c, the porosity appears mainly sub-spherical in form, in Figure 6.5d pore shape is flattened and iso-oriented.

The binder/aggregate ratio is of about 1.4 (Table 6.2; Figure 6.10).

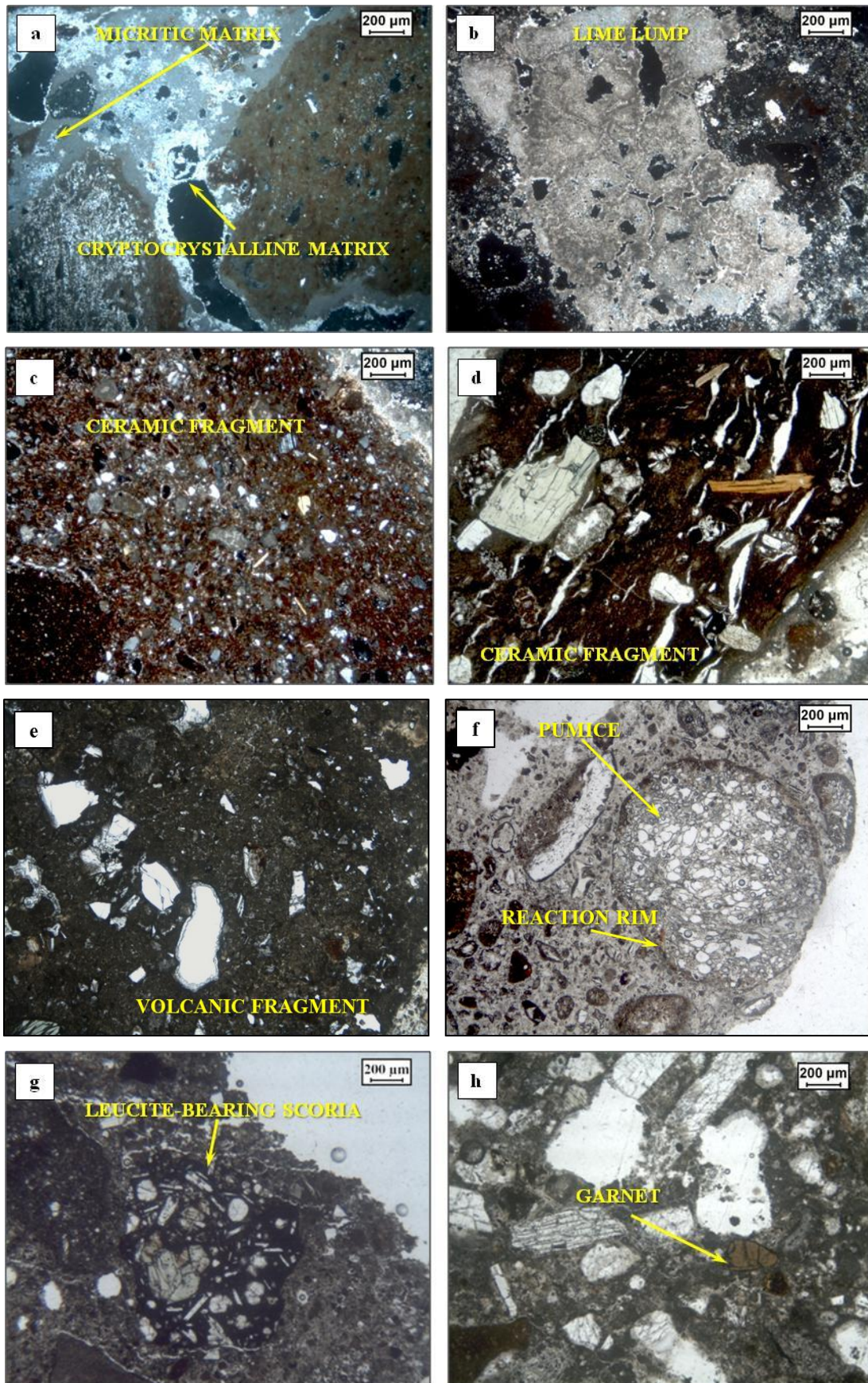


Figure 6.5: Microphotographs of mortars components: a) cryptocrystalline and micritic matrix (CPL), sample BG3; b) lime lump (CPL), sample BG12; c-d) ceramic fragments (CPL), sample BG12; e) volcanic fragment (CPL), sample BG6; f) pumice with reaction rim (PPL), sample BG13; g) leucite-bearing scoria (PPL) in sample BG6; h) garnet (PPL), sample BG5. CPL: Cross Polarized Light; PPL: Plane Polarized Light.

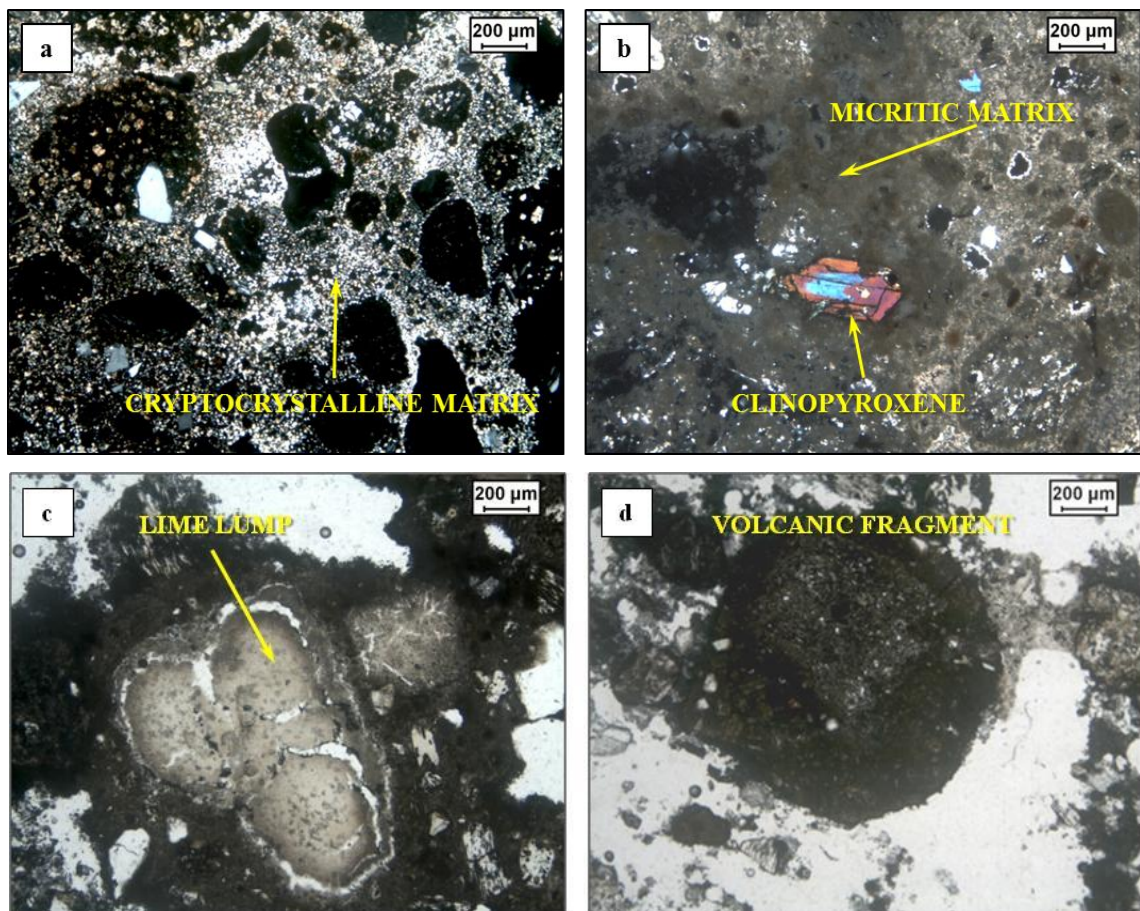
group B (BG2, BG4, BG7, BG8, BG10, BG11) is characterized by binder that varies in colour from pale brown - beige - to grey, and shows various grades of crystallinity from micritic (22.0 Vol.%; Figure 6.6a) to cryptocrystalline (36.8 Vol.%; Figure 6.6b). Also in this group the binder shows the presence of small and fractured lime lumps (5.5 Vol.%, Figure 6.6c) and a few percentage of sparite grains (0.4 Vol.%).

The aggregate is mainly composed of volcanic fragments (5.2 Vol.%; Figure 6.6d), pumice (12.0 Vol.%; Figure 6.6e), scoriae with clear reaction rim, mineral aggregates formed by clinopyroxene, sanidine, plagioclase (Figure 6.6f), biotite and, sometimes, calcite, and crystal fragments of sanidine, plagioclase, clinopyroxene (5.2 Vol.%; Figure 6.6g).

Volcanic fragments, also in this group, can be classified as volcanic tuff, characterized by the presence of microcrystals immersed in an altered ashy matrix.

In sample BG7 it was also observed the presence of acicular crystals, apparently of calcite, that fill the vugs (Figure 6.6h).

The binder/aggregate ratio was about about 2.9 (Table 6.2; Figure 6.10). Only BG11 sample shows a lower values of this ratio (1.9 Vol.%).



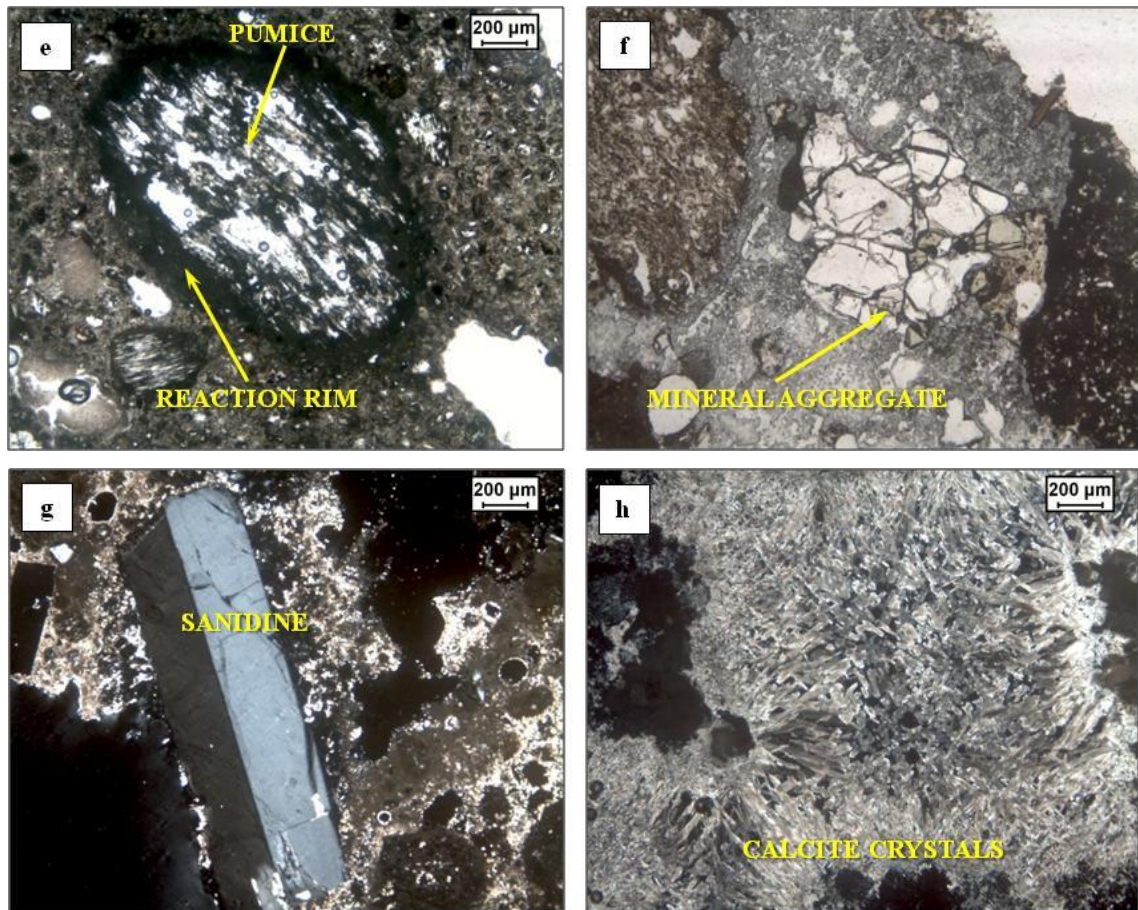


Fig 6.6: Microphotographs of mortars components: a) cryptocrystalline matrix (CPL), sample BG4; b) micritic matrix and clinopyroxene crystal fragment (CPL), sample BG2; c) lime lump (PPL), sample BG8; d) volcanic fragments (CPL), sample BG2; e) pumice with reaction rim (PPL), sample BG10; f) mineral aggregates (PPL), sample BG7; g) crystal fragment of sandidine (CPL), sample BG11; h) acicular crystals of calcite (CPL), sample (BG7).

Group C is populated by floor mortars (BG1, BG9), characterized by two layers and different between them (Figure 6.7).

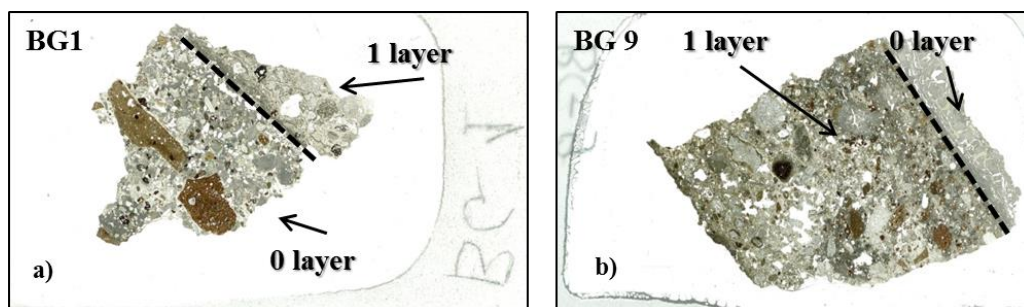


Fig 6.7: Thin sections macrographs: a) BG1 mortar; b) BG9 mortar

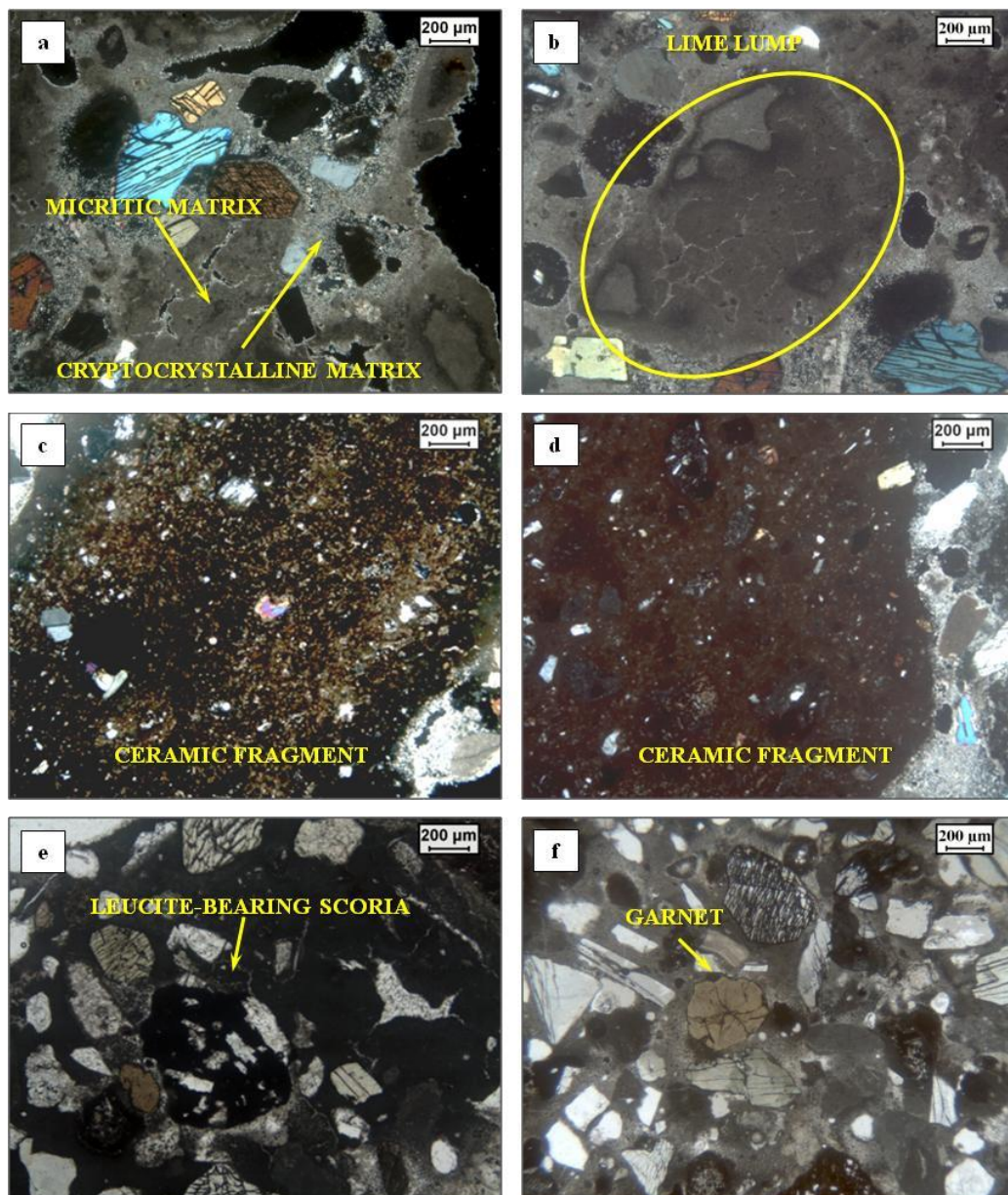
BG1 sample shows two different layers (1 and 0; Fig 6.7a). Layer 1 (external layer) is characterized by beige colour of binder, with cryptocrystalline to micritic aspect (27.5 Vol.%; 31.3 Vol.%; Figure6.8a). Binder shows also the presence of small and fractured lime lumps (5.5 Vol.%, Fig; Figure 6.8b). Aggregates are composed by different types of ceramic fragments (14.1

Vol. %; Figure 6.8c-d), scoriae (6.2 Vol.%), leucite-bearing scoriae (1.5 Vol.%; Figure 6.8e) and crystal fragments of clinopyroxene, amphibole, plagioclase, sanidine (5.9 Vol. %) and garnet (1.8 Vol.%; Figure 6.8f).

Layer 0 presents a binder grey in colour and cryptocrystalline aspect (Figure 6.8g). The aggregates are poorly sorted and composed by few leucite-bearing scoriae (Figure 6.8h), altered pumice (Figure 6.8i-l), mineral aggregates and few crystal fragments of clinopyroxene (Figure 6.8m).

Between 1 and 0 layer are evident carbonation processes (Figure 6.8o).

Modal analysis was performed only in layer 1 and the resulting the binder/aggregate ratio was about 2 (Table 6.2; Figure 6.10).



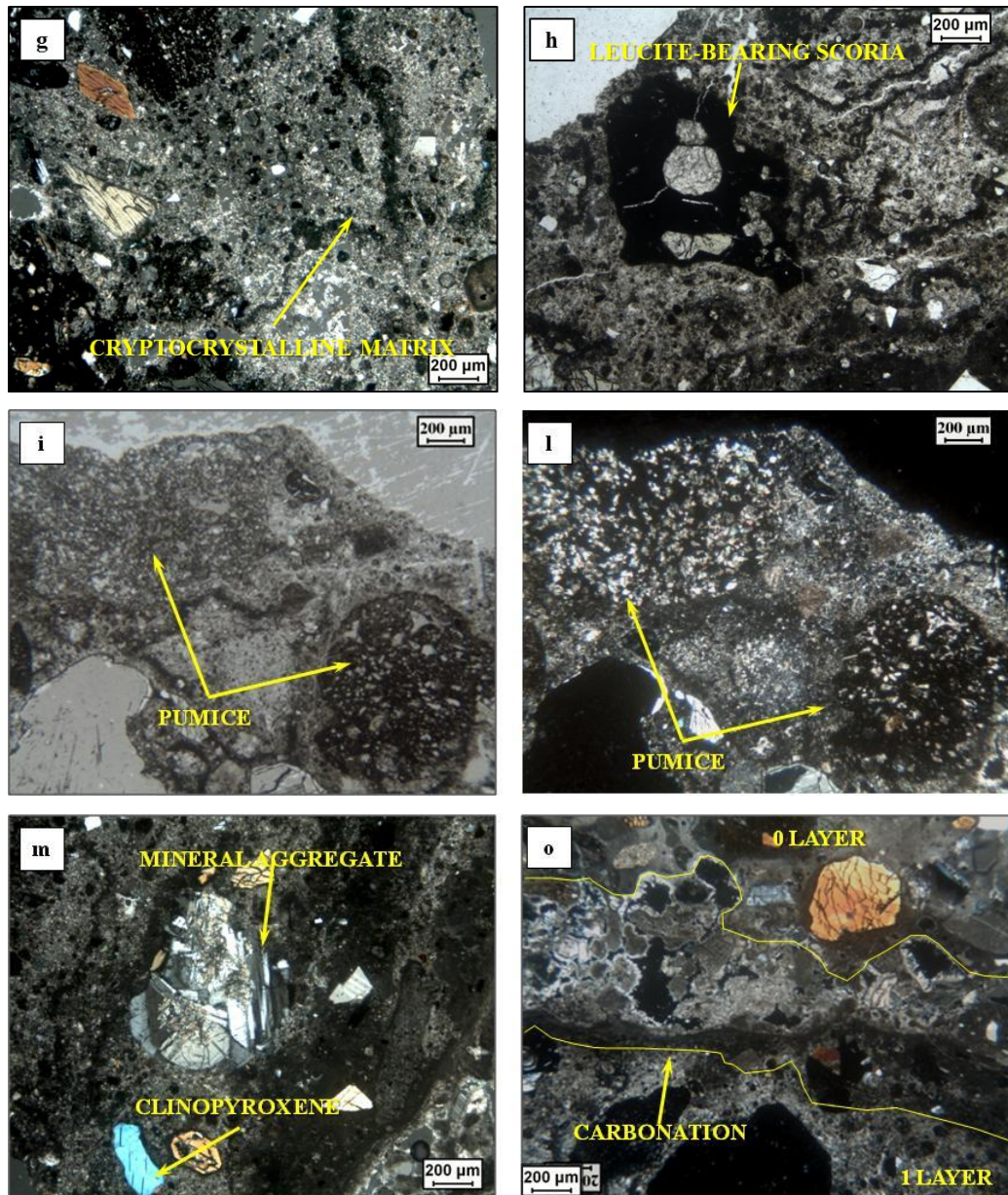


Figure 6.8: Microphotographs of BG1 mortar components: a) cryptocrystalline and micritic matrix (CPL) in layer 0; b) lime lump (CPL) layer 1; c-d) ceramic fragments (CPL) in layer 1; e) leucite-bearing scoria (PPL) in layer 1; f) garnet crystal fragment (PPL) in sample layer 0; g) cryptocrystalline matrix (CPL) in layer 0; h) leucite-bearing scoria (PPL) in layer 0; i-l) altered pumice (PPL-CPL) in layer 0; m) mineral aggregate and crystal fragment of clinopyroxene (CPL) in layer 0; o) transition between layer 1 and 0 (CPL).

Also BG9 sample shows two different layers (Figure 6.7b).

Layer 1 (external layer), is characterized by white colour of the binder, with mainly micritic aspect and it does not show any aggregates (Figure 6.9 a-b).

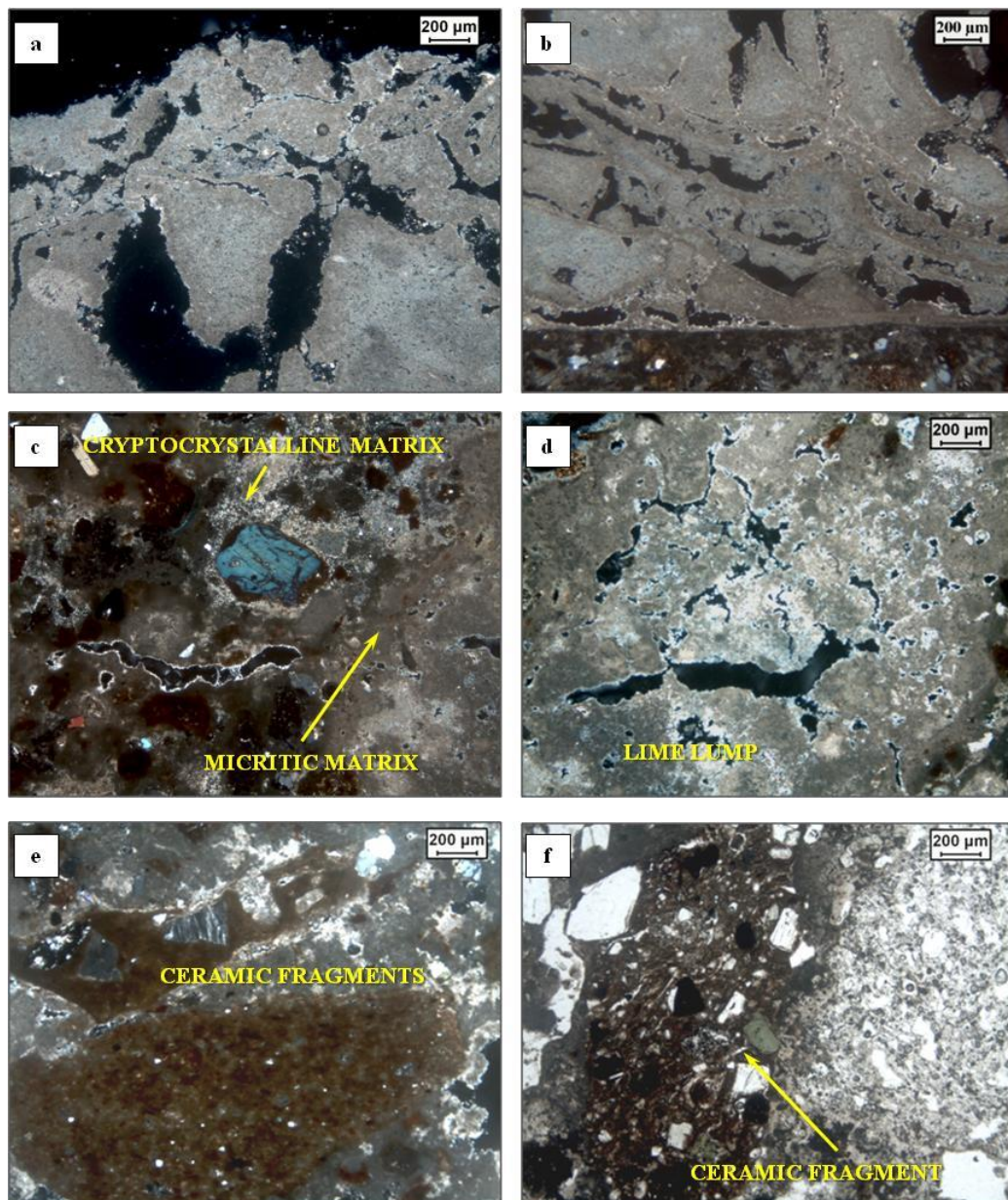
Layer 0 is characterized by a brownish colour of the binder, and shows both micritic (22.0 Vol.%) and cryptocrystalline (38.0 Vol.%; Figure 6.9c) texture. The binder phase shows also the presence of lime lumps (1.4 Vol.%, Figure 6.9d). The aggregates are composed by different types of ceramic fragments (10.3 Vol.%, Figure 6.9 e-f), pumice and scoriae with clearly evident

reaction rims (10.1 Vol.% - 2.9 Vol.%; Figure 6.9g), volcanic fragments (2.1Vol.%) and crystal fragments of clinopyroxene, sanidine (Figure 6.9h) and biotite (8.2 Vol.%).

Also in this group, as in groups A and B, volcanic fragment can be classified as volcanic tuff, characterized by the presence of microcrystals immersed in an altered ashy matrix.

The transition between 1 and 0 layer is well defined and evident (Figure 6.9b).

Modal analysis was performed on layer 0 and shows binder/aggregate ratio equal to 1.8 (Table 6.2; Figure 6.10).



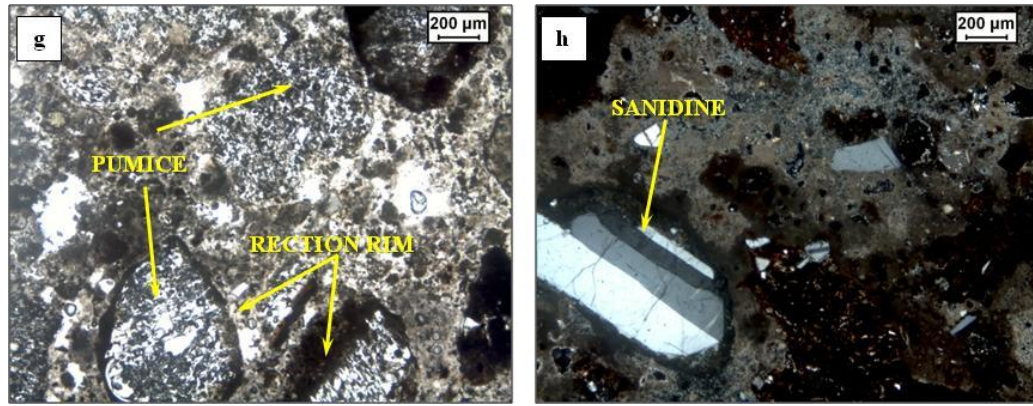


Figure 6.9: Microphotographs of BG9 mortar components: a-b) micritic aspect (CPL) of layer 1; c) cryptocrystalline and micritic matrix (CPL) in layer 0; d) lime lump (CPL) in layer 0; e-f) ceramic fragments (CPL) in layer 0; g) pumice with reaction rim (CPL) in layer 0; h) crystal fragment of sanidine (CPL) in layer 0.

Table 6.2: Modal analyses of selected mortars.

Mortars (%)	BG3	BG13	BG4	BG10	BG11	BG1	BG9
	(group A)	(group A)	(group B)	(group B)	(group B)	(group C)	(group C)
Constituents (Vol.%)							
Feldspar (Afs, Plg)	3.9	3.3	3.2	4.9	3.0	4.5	5.3
Mafic Minerals (Cpx, Am, Bt)	2.4	1.9	1.4	2.1	1.0	1.4	2.9
Garnet	-	-	-	-	-	1.8	-
Volcanic fragments	0.8	4.8	6.6	7.3	1.7	-	2.1
Scoriae	1.7	2.7	1.9	-	3.2	6.2	2.9
Leucite-bearing scoriae	-	-	-	-	-	1.5	-
Pumice	3.1	6.6	4.8	18.5	12.7	-	10.1
Ceramic fragments	25.1	18.0	-	-	-	14.1	10.3
Carbonate fragments	0.6	0.4	-	-	-	1.9	-
Sparite	0.3	0.5	0.9	0.3	0.1	0.1	-
Lime lumps	4.9	7.7	7.0	3.5	6.0	3.9	1.4
Micritic matrix	22.4	15.5	35.1	20.9	9.9	31.3	22.0
Cryptocrystalline matrix	30.1	32.7	26.3	28.3	55.6	27.5	38.0
Voids	4.7	0.1	12.8	14.1	6.8	4.7	4.7
Others	0.1	5.7	-	-	-	1.0	0.3
Total points %	100.0	100.0	100.0	100.0	100.0	100.0	100.0
Total Binder %	57.7	56.4	69.3	53.1	71.6	62.9	61.4
Total Aggregate%	37.5	37.8	17.9	32.9	21.6	31.4	33.7
Binder/Aggregate ratio	1.5	1.5	3.9	1.6	3.3	2.0	1.8

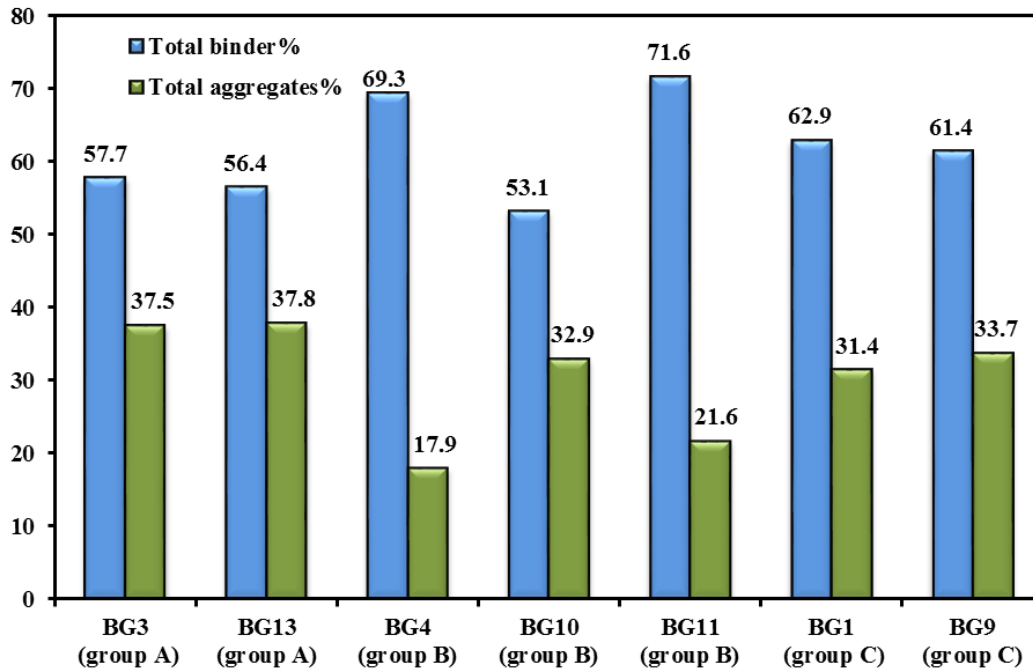


Figure 6.10: Histogram with percentages of total binder and total aggregates in selected samples of mortars from *Villa del Capo*.

6.2.3 XRPD analysis

Samples were separated in binder, aggregates and ceramic fragments, according to the UNI Normal 11305 document (mortar characterization) and then analyzed by XRPD. Results are reported in Table 6.3.

Table 6.3: Qualitative mineralogical (XRPD) composition of mortars.

Samples	Group	Main Binder Phases	Main Aggregates Phases	Main Ceramic Fragments Phases	Other Phases
BG1	group C	Cal, Hc	Anl, San, Pl, Mca	Cal, San, Pl, Hem	HI
BG2	group B	Cal, Gp	Anl, San, Pl, Mca, HI		HI
BG3	group A	Cal	Phi, Anl, San, Pl, Mca		HI
BG4	group B	Cal, Hc	Phi, Anl, San, Pl, Mca, HI		HI
BG5	group A	Cal, Hc	Phi, Pl, Mca, HI	Cal, San, Pl, Hem, HI	HI
BG6	group A	Cal, Gp, Hc	Phi, Anl, San, Pl, Mca, HI	Cal, San, Pl, Hem, HI	HI
BG7	group B	Cal, Gp, Hc	Phi, Cbz, Anl, San, Pl, Mca, HI		HI
BG8	group B	Cal, Gp	Phi, Cbz, Anl, San, Pl, Mca, HI		HI
BG9	group C	Cal,	Phi, Anl, San, Pl, Mca, HI	Cal, San, Pl, Cpx, Hem, HI	HI
BG10	group B	Cal, Hc	Phi, Anl, San, Pl, Mca, HI		HI
BG11	group B	Cal	Anl, San, Pl, Mca, HI		HI
BG12	group A	Cal, Gp	Anl, San, Pl, Mca,	Cal, San, Pl, Cpx, Hem,	HI
BG13	group A	Cal	Phi, Cbz, Anl, San, Pl, Mca	Cal, San, Pl, Cpx, Hem,	HI

*Cal: calcite, Hc: hydrocalumite; Gp: gypsum; Phi: phillipsite; Cbz: chabazite; Anl: analcime; San: sanidine; Cpx: clinopyroxene; Pl: plagioclase; Mca: mica; Hem: hematite; Qtz: quartz.; HI: halite

Results of XRPD analyses show that calcite is the main phase of the binder; in some samples gypsum $[\text{CaSO}_4 \cdot 2(\text{H}_2\text{O})]$ and hydrocalumite $\text{Ca}_2\text{Al}(\text{OH})_6[\text{Cl}_{1-x}(\text{OH})_x] \cdot 3(\text{H}_2\text{O})$ (Figure 6.11) were also detected.

Gypsum could be ascribed to sulphation processes of calcite. Hydrocalumite, also known as Friedel's salt or AFm phase in cement science, belongs to the family of layered double hydroxides (LDHs) (Tian and Guo, 2014).

Generally, hydrocalumite-like structures represent the predominant mineral species that concentrate chloride in the ancient sea-water mortars (Jackson et al., 2013), and may be the result of migration of Cl^- anions from the sea-water saturated portlandite to aluminium-rich sites along the perimeters of the relict lime clasts or voids of mortars (Jackson et al., 2013).

As far as aggregates fraction is concerned, XRPD analyses suggest that volcanic tuff fragments can be associated to Neapolitan Yellow Tuff (NYT), due to the presence of typical zeolitic association of this material i.e.: phillipsite, chabazite, and analcime (de Gennaro et al., 1999) (Figure 6.12). In addition to this, the presence of alkalifeldspar, pyroxene and mica could be also associated to the NYT formation.

XRPD analysis of ceramic fragments showed mainly quartz, calcite, mica, and hematite (Figure 6.13).

All samples show the presence of halite.

XRPD analysis allowed to detect the presence of an amorphous fraction (poorly crystalline), recognized by the rising of the spectrum background (Figure 6.14) related to volcanic glass components and C-A-S-H (calcium, aluminum, silicate, hydrate) phases.

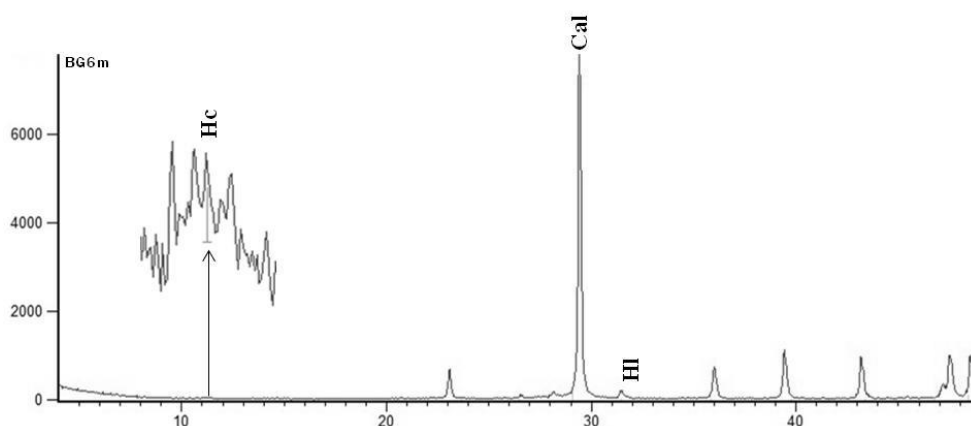


Figure 6.11: XRPD spectrum of BG6 binder ; Hc= Hydrocalumite

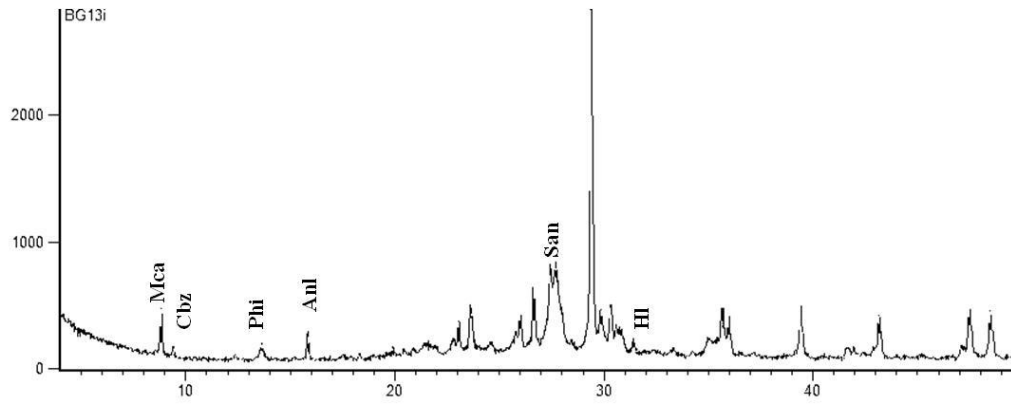


Figure 6.12: XRPD spectrum of BG13 aggregates.

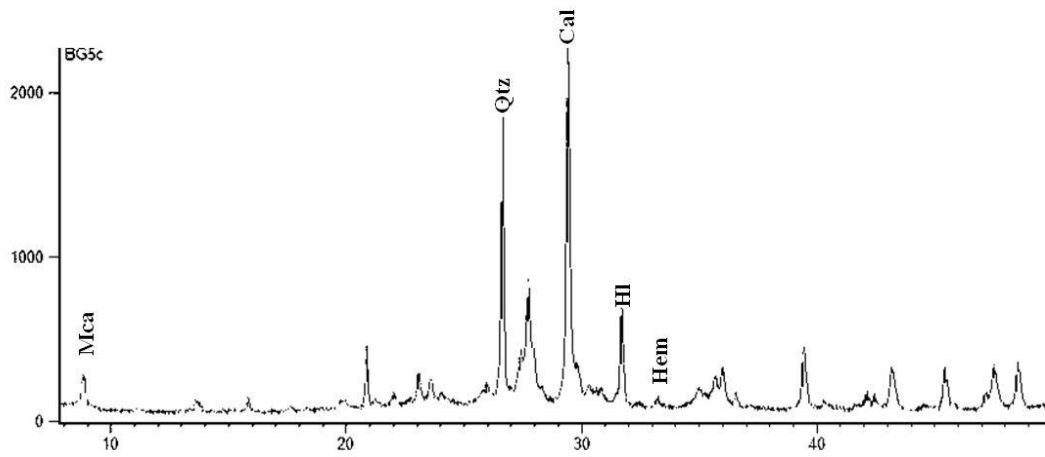


Figure 6.13: XRPD spectrum of BG5 ceramic fragments.

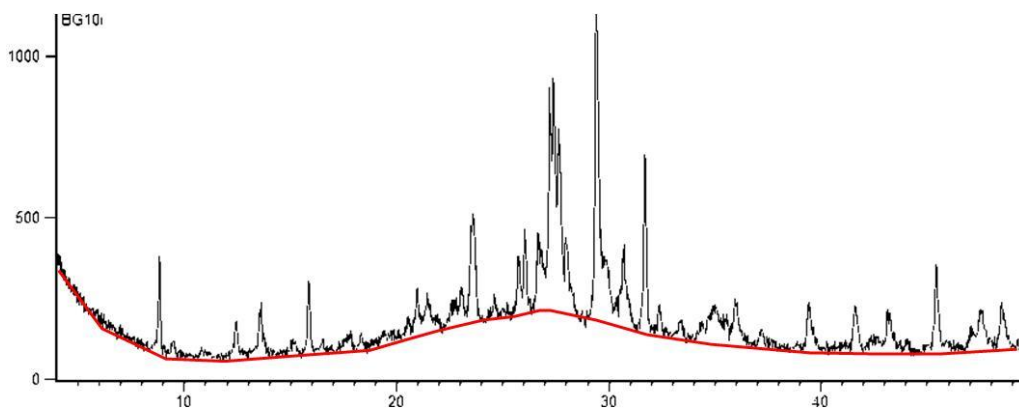


Figure 6.14: Observed background (red line) in BG10 aggregates XRPD spectrum.

6.2.4 Micro-morphology and chemical analysis (SEM-EDS)

SEM-EDS analyses were performed to obtain information on the microstructure and major element composition of both binder and aggregates.

Results for binder show the presence of newly formed hydraulic phases (C-A-S-H) (Figure 6.15a), and confirmed, as XRPD suggested, presence of halite (NaCl) (Figure 6.15b) and hydrocalumite $\text{Ca}_2\text{Al}(\text{OH})_6[\text{Cl}_{1-x}(\text{OH})_x] \cdot 3(\text{H}_2\text{O})$ (Figure 6.15c-d).

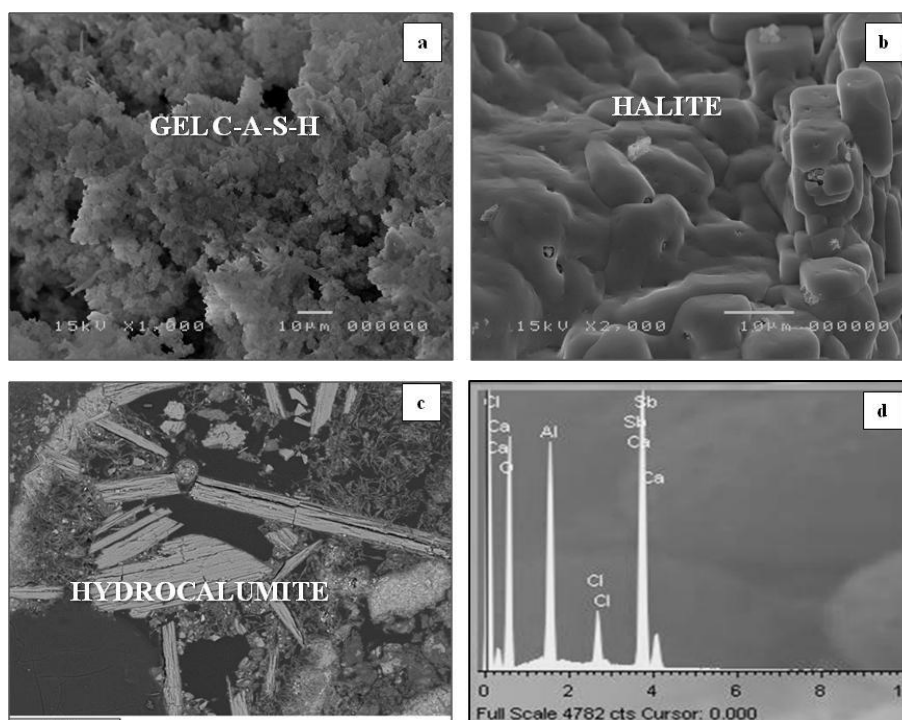


Figure 6.15: SEM images of a) Gel C-A-S-H, BG12 binder sample; b) halite crystals, BG10 binder sample; c) BSE-SEM image of hydrocalumite, BG6 sample; d) EDS spectrum of hydrocalumite, BG6 sample.

SEM EDS analyses were carried out on both lime lumps and binder (Figure 6.16a-b), in order to obtain information about: a) type of used lime for the production of mortars, b) define the Hydraulicity Index (HI) and the degree of hydraulicity of the binder.

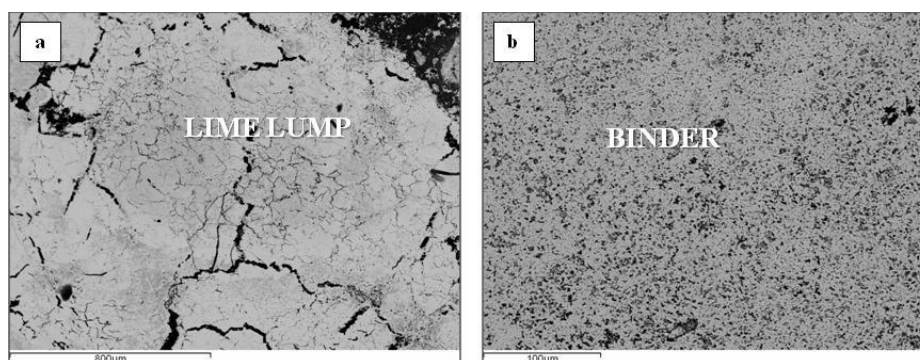


Figure 6.16: BSE-SEM images of a) example of analyzed lime lumps sample BG12 b) e example of analyzed binder sample BG 10

Obtained chemical composition of lime lumps shows that they are composed mainly of CaO with very high values of CaO + MgO in general, between 90.56 and 95.56 % (Table 6.4 , Figure 6.17). Chemical composition of binder shows values of SiO₂+Al₂O₃+Fe₂O₃ (8.48 – 18.71 %) higher than in lumps (2.70 – 4.09 %) and lower contents of CaO + MgO (79.52 – 87.62%; Table 6.4 Figure 6.17).

Hydraulicity Index, calculated according to Boynton’s formula (Boynton, 1966), for lime lumps has low values (HI < 0.1, Figure 6.18), and therefore can be classified as quicklime (Zawawi, 2006).

As regards HI of binder, it shows values between 0.10 – 0.24, which refer to a weak to moderate hydraulicity (Figure 6.16).

For this reason, is it possible to infer that mortars became hydraulic by the addition of aggregates (volcanic materials and ceramic fragments) with peculiar features. These aggregates produce a “pozzolanic reaction”, due to their silica and alumina content, that reacted with calcium hydroxide leading to the formation of calcium aluminum silicate hydrates, the so-called C-A-S-H phases (De Luca et al., 2015), furtherly testified and confirmed by reaction rims around pumice, scoriae and ceramic fragments.

Table 6.4: Average values of major oxides (wt.% recalculated to 100%, EDS), lime lumps (L) and binder (B).

wt. %	BG1 L	BG1 B	BG3 L	BG3 B	BG4 L	BG4 B	BG5 L	BG5 B	BG9 L
SiO₂	2.34	7.94	3.73	9.82	1.74	6.80	0.52	7.76	2.21
TiO₂	-	-	0.88	-	-	0.59	-	-	0.37
Al₂O₃	1.32	2.24	0.82	3.19	0.96	1.68	2.43	3.07	1.21
Fe₂O₃	-	0.21	-	0.70	-	-	0.50	0.28	-
MnO	-	0.24	0.15	0.09	0.08	0.60	0.42	0.15	0.19
MgO	1.87	0.71	1.28	5.19	0.10	0.31	0.55	3.34	2.19
CaO	93.68	85.67	91.09	78.61	95.85	87.31	93.11	82.56	88.38
Na₂O	0.16	1.20	0.90	0.60	0.60	1.06	0.42	0.91	0.69
K₂O	-	0.35	0.13	0.13	0.17	0.34	-	0.22	0.03
P₂O₅	-	0.30	-	0.09	0.12	0.56	-	0	0.48
V₂O₃	-	-	-	-	-	-	-	-	-
BaO	0.49	0.27	-	-	-	-	-	0.22	-
SO₃	0.13	0.61	0.29	0.52	0.04	0.48	0.40	0.62	0.30
Cl	-	0.26	0.30	0.80	0.35	0.27	1.16	0.24	3.70
F	-	-	0.42	-	-	-	0.47	0.63	0.25
Total	100.00	100.00	100.00	100.00	100.00	100.00	100.00	100.00	100.00
SiO₂ + Al₂O₃ + Fe₂O₃	3.67	10.39	4.54	13.71	2.70	8.48	3.46	11.11	3.42
CaO + MgO	95.56	86.38	92.37	83.80	95.95	87.62	93.66	85.89	90.56
HI	0.04	0.12	0.05	0.16	0.03	0.10	0.04	0.13	0.04

wt. %	BG9 B	BG10 L	BG10 B	BG11 L	BG11 B	BG12 L	BG12 B	BG13 L	BG13 B
SiO ₂	8.85	2.87	8.04	1.52	6.79	1.72	14.11	2.88	12.90
TiO ₂	0.40	-	0.33	-	-	0.34	0.26	-	0.24
Al ₂ O ₃	2.65	0.86	2.34	1.43	3.77	2.10	3.70	1.08	3.82
Fe ₂ O ₃	-	0.37	0.18	0.50	0.19	-	0.90	0.41	1.27
MnO	0.48	-	0.17	0.42	-	0.41	0.32	0.20	-
MgO	0.74	2.48	4.04	0.55	1.42	2.13	0.67	0.26	7.78
CaO	85.58	91.12	82.02	93.11	84.83	92.07	77.64	93.36	71.74
Na ₂ O	1.37	0.45	0.71	0.42	0.89	0.18	1.07	0.59	0.53
K ₂ O	0.94	-	0.19	-	0.43	0.09	0.74	0.55	0.30
P ₂ O ₅	0.30	-	0.04	-	-	-	-	-	-
V ₂ O ₃	-	-	-	-	-	-	-	-	-
BaO	0.20	-	0.08	-	1.01	-	0.10	-	-
SO ₃	-	0.87	0.58	0.40	0.56	0.20	0.23	0.43	0.60
Cl ⁻	0.50	0.99	0.28	1.16	0.10	0.02	0.26	0.24	0.83
F ⁻	-	-	-	0.47	-	0.75	0.00	-	-
Total	100.00	100.00	100.00	100.00	100.00	100.00	100.00	100.00	100.00
SiO ₂ + Al ₂ O ₃ + Fe ₂ O ₃	11.49	4.09	10.57	3.46	10.76	3.82	18.71	4.37	17.99
CaO + MgO	86.32	93.60	86.06	93.66	86.25	94.20	78.31	93.62	79.52
HI	0.13	0.04	0.12	0.04	0.12	0.04	0.24	0.05	0.23

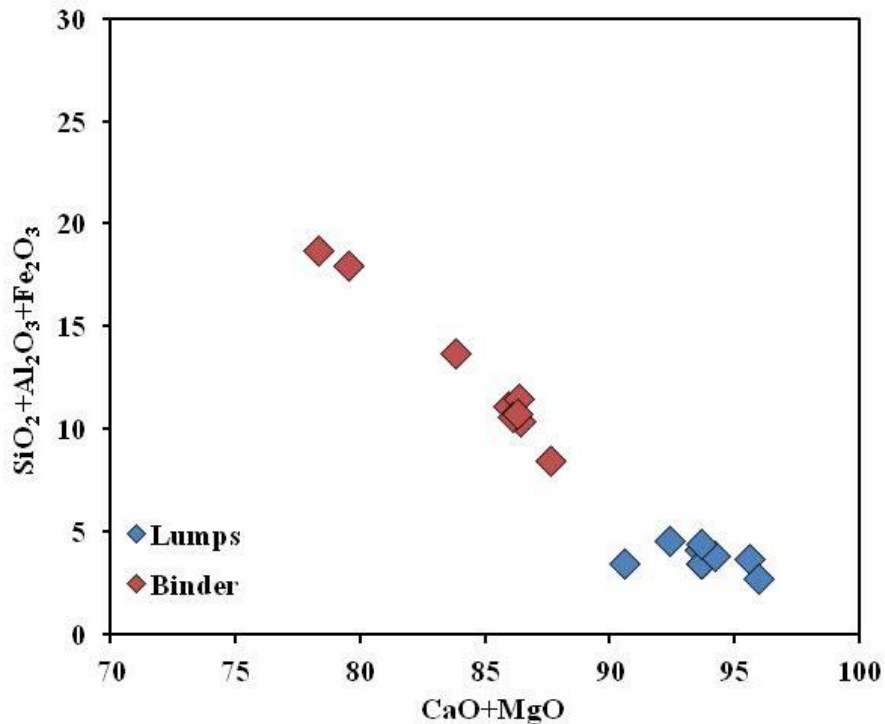


Figure 6.17: CaO + MgO vs. SiO₂ diagram (EDS), lumps and binder.

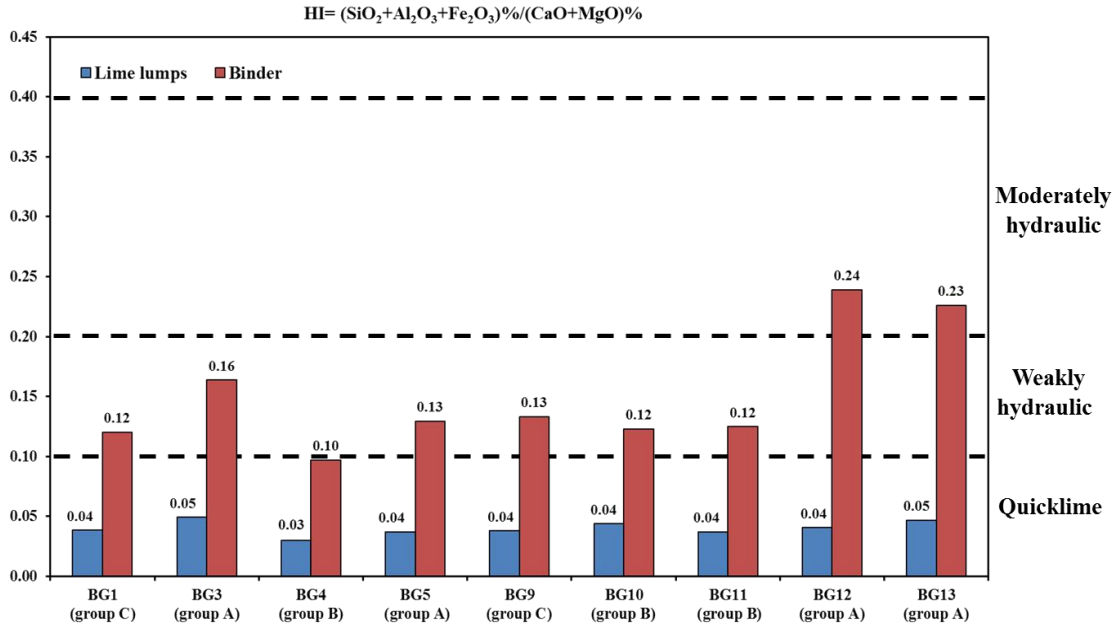


Figure 6.18: Hydraulicity Index (HI), lime lumps (blue) and binder (red) for analyzed mortars.

Referring to the volcanic aggregates, SEM EDS analysis furtherly confirmed the above mentioned hypothesis of the employment of aggregate of Neapolitan Yellow Tuff, due to the presence of phillipsite with well-defined prismatic crystal habit and pseudocubic crystals of chabazite, along with roundish crystals of analcime (Figure 6.19a-b-c), (de Gennaro et al., 1999).

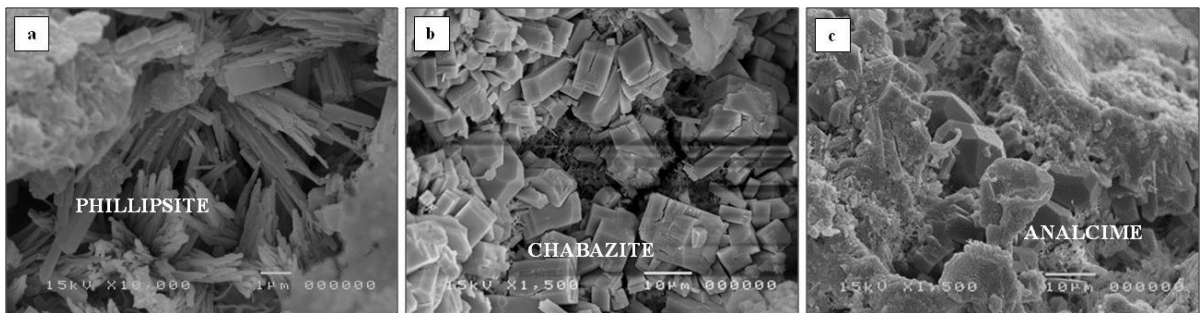


Figure 6.19: SEM image of: a) phillipsite clusters, BG8 volcanic fragment; b) chabazite crystals, BG8 volcanic fragment; c) analcime crystals, BG2 volcanic fragment.

In order to obtain further information, SEM-EDS microanalysis was carried out also on pumice from different samples (Figure 6.20; Table 6.5).

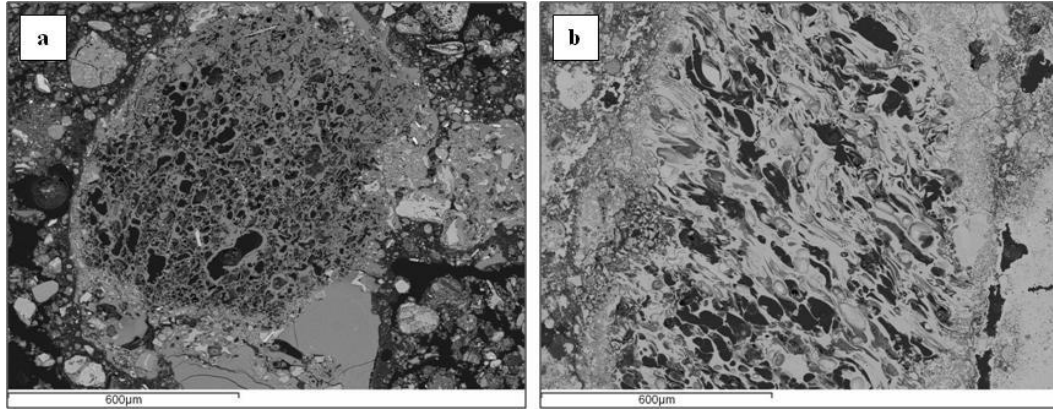


Figure 6.20: BSE-SEM image of pumice, BG10 (left) and BG13 (right) samples.

Table 6.5: Major element concentrations (wt.% recalculated to 100%, EDS), pumice.

wt.%	BG2	BG2	BG2	BG2	BG3	BG3	BG3	BG3	BG4	BG4	BG4	BG4	BG5	BG5	BG5	BG5	BG7	BG7	BG7	BG7
SiO ₂	60.29	60.68	62.34	63.27	61.28	60.78	61.61	62.63	59.20	56.38	58.31	57.50	60.99	61.35	52.38	53.22	56.03	56.65	62.11	61.86
TiO ₂	0.28	0.32	0.34	0.25	0.48	0.54	0.33	0.56	0.62	0.58	0.23	0.29	0.34	0.67	1.21	0.57	0.27	0.50	0.38	0.32
Al ₂ O ₃	18.78	18.71	18.28	18.69	18.45	18.75	18.19	17.70	18.82	18.26	19.12	19.15	17.82	18.24	18.95	19.06	18.47	18.59	18.07	17.91
Fe ₂ O ₃	3.64	3.26	3.04	1.97	3.42	3.99	3.35	4.15	4.07	5.57	4.85	5.05	2.95	2.88	7.43	6.82	4.14	3.60	2.12	2.25
MnO	0.27	-	0.09	0.36	0.18	0.37	0.54	0.02	0.10	-	-	0.21	0.44	0.14	0.12	0.17	0.13	0.11	0.15	0.22
MgO	0.63	0.74	0.55	0.39	0.25	0.36	0.17	0.35	0.87	1.23	1.18	0.74	0.34	0.27	2.11	2.27	1.17	1.13	0.29	0.15
CaO	2.66	2.61	1.30	1.46	1.52	1.71	1.73	1.80	2.72	4.45	3.43	3.26	1.11	0.88	5.26	5.67	3.31	4.07	1.38	1.51
Na ₂ O	3.69	4.67	6.08	5.58	6.65	6.83	6.18	5.01	3.62	3.26	3.82	3.21	6.91	6.92	4.14	4.00	3.86	4.55	4.38	4.76
K ₂ O	9.55	8.52	7.56	7.40	7.27	6.64	7.06	6.77	9.62	9.55	8.19	9.14	6.33	6.92	6.76	6.80	7.54	7.50	6.85	7.66
P ₂ O ₅	-	0.18	0.05	0.12	0.21	0.04	-	0.29	-	0.28	0.03	0.36	0.30	0.04	0.48	0.44	0.15	0.09	0.23	-
SO ₃	-	-	-	0.20	-	-	-	-	0.39	0.36	0.04	0.10	-	-	0.18	0.19	0.10	0.36	-	0.14
BaO	-	0.09	0.18	0.27	0.10	-	0.23	0.17	0.00	0.27	0.68	0.53	0.05	0.16	-	0.34	0.52	0.76	0.19	-
Cl ⁻	0.58	0.56	0.48	0.25	0.53	0.37	0.96	0.95	0.38	0.36	0.59	0.61	0.60	0.68	0.32	0.37	0.31	0.24	0.41	0.73
F ⁻	-	-	-	-	-	-	-	-	-	-	-	-	2.08	1.14	1.40	0.68	3.85	1.81	3.65	2.72
Total	100.00	100.00	100.00	100.00	100.00	100.00	100.00	100.00	100.00	100.00	100.00	100.00	100.00	100.00	100.00	100.00	100.00	100.00	100.00	100.00
Na ₂ O+K ₂ O	13.24	13.18	13.64	12.98	13.92	13.48	13.24	11.78	13.24	12.81	12.02	12.35	13.25	13.84	10.90	10.80	11.40	12.05	11.23	12.42

wt.%	BG9	BG9	BG9	BG9	BG10	BG10	BG10	BG10	BG11	BG11	BG11	BG11	BG12	BG12	BG12	BG12	BG13	BG13	BG13	BG13
SiO ₂	59.21	58.71	60.09	59.55	63.29	62.14	60.11	61.33	56.99	57.53	59.37	59.06	61.97	62.41	61.48	61.42	57.51	56.41	58.22	57.48
TiO ₂	0.31	0.32	0.93	0.47	0.30	0.52	0.59	0.62	0.65	0.64	0.34	0.40	0.68	0.60	0.41	0.28	0.35	0.58	0.26	0.26
Al ₂ O ₃	18.61	17.93	18.31	17.76	18.65	18.32	18.36	17.79	18.81	18.93	18.82	18.68	18.20	18.06	18.87	18.63	19.36	19.47	19.29	19.72
Fe ₂ O ₃	3.67	3.11	3.29	3.31	2.43	3.51	4.05	4.17	5.12	3.87	4.08	3.98	2.88	3.15	3.18	4.24	4.78	3.61	3.49	3.49
MnO	0.00	0.21	0.37	0.31	0.18	0.10	0.00	0.32	0.41	0.45	0.24	0.00	0.06	0.10	0.35	0.05	0.25	0.05	0.00	0.35
MgO	0.39	0.51	0.54	0.41	0.19	0.30	0.63	0.30	0.82	0.83	0.54	0.69	0.32	0.19	0.34	0.26	0.94	0.86	0.80	0.67
CaO	2.31	2.55	1.80	2.00	2.19	2.13	1.80	1.62	3.49	3.06	2.40	2.55	1.00	1.02	2.29	2.15	3.53	3.66	3.07	3.07
Na ₂ O	4.61	4.35	4.55	5.20	3.93	4.71	4.90	5.93	3.44	3.41	4.50	4.26	7.97	7.87	3.77	4.40	4.09	4.35	4.61	4.10
K ₂ O	8.97	8.79	7.92	7.81	8.41	7.56	8.67	7.24	9.89	10.31	9.17	9.33	6.22	6.03	8.56	8.91	9.35	9.61	9.47	9.81
P ₂ O ₅	0.03	0.13	0.03	0.20	0.04	0.10	-	0.18	-	-	0.02	0.31	0.04	0.07	0.14	0.20	-	-	0.13	-
SO ₃	-	0.25	-	0.13	0.13	-	0.27	-	0.25	0.58	0.19	0.06	0.15	-	0.29	0.21	-	-	0.05	0.11
BaO	0.05	0.07	-	-	0.07	-	0.00	-	-	-	-	-	-	0.10	0.04	-	0.17	-	0.14	0.60
Cl ⁻	0.76	0.86	0.83	0.67	0.43	0.96	1.03	0.91	0.64	0.59	0.74	0.69	0.79	0.69	0.61	0.62	0.63	0.70	0.70	0.68
F ⁻	1.32	1.50	1.66	2.49	-	-	-	-	-	0.18	-	0.39	-	-	-	-	-	-	-	-
Total	100.00	100.00	100.00	100.00	100.00	100.00	100.00	100.00	100.00	100.00	100.00	100.00	100.00	100.00	100.00	100.00	100.00	100.00	100.00	100.00
Na ₂ O+K ₂ O	13.59	13.14	12.47	13.01	12.34	12.28	13.56	13.17	13.33	13.72	13.67	13.58	14.19	13.91	12.33	13.31	13.43	13.96	14.08	13.91

Using Total Alkali versus Silica diagram (TAS) for the effusive volcanic rocks (Le Maitre et al., 1989) for the investigated samples, it is possible to observe that pumice fragments show trachytic compositions; their classification follows the compositional trend of *Campi Flegrei* products, in particular with pumice belonging to NYT (Figure 6.22).

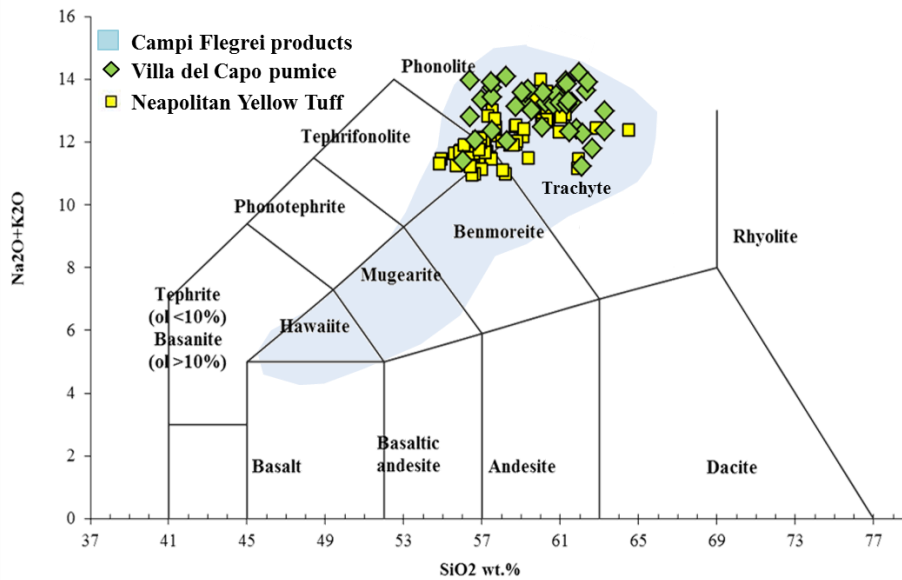


Figure 6.22: Classification of pumice fragments from *Villa del Capo* (Le Maitre et al., 1989) and geochemical comparison with Phlegrean pumice (Morra et al., 2010).

Moreover SEM-EDS investigation suggested also the possible use of geomaterials from Somma-Vesuvius complex, due to the presence of volcanic scoriae containing analcime (typical product of leucite alteration) and garnet fragments (Figure 6.23) (Santacroce et al., 2003) typical of this materials.

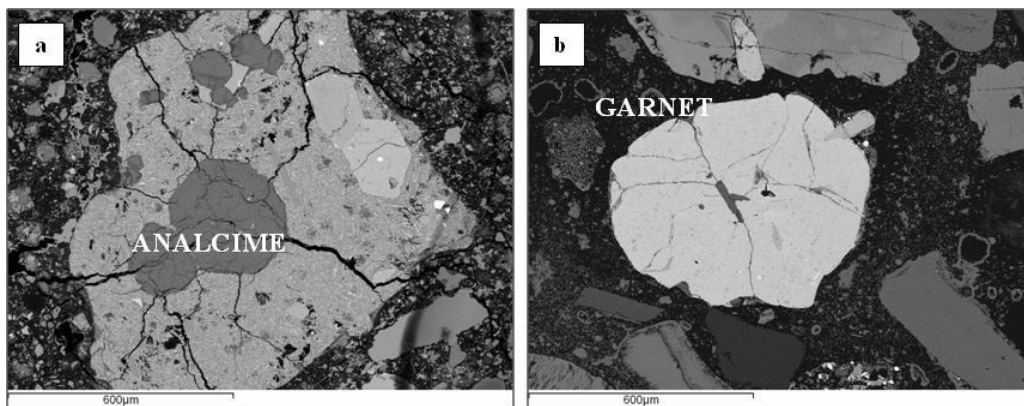


Figure 6.23: BSE- SEM images of: a) analcime bearing scoria, BG1 sample; b) garnet crystal, BG5 sample.

In addition to what previously reported, also chemical composition of analyzed garnet (calculated following Locock, 2008; Table 6.7) shows its similarity with garnets of Somma-Vesuvio (andradite 46-70 mol% and grossularia 16-45 mol%; taken by Scheibner et al., 2007; unpublished data on garnets from intrusive Somma-Vesuvius rocks. L. Melluso, personal communication).

Table 6.7: Chemical composition of garnet (wt.%, EDS).

Analysis (wt%)	BG1 garnet	BG1 garnet	BG5 garnet
SiO ₂	35.27	35.40	34.61
TiO ₂	3.75	2.88	3.55
Al ₂ O ₃	8.26	8.77	8.97
FeO _{tot}	18.63	18.41	17.16
MnO	0.68	1.39	0.98
MgO	0.13	0.41	0.23
CaO	32.16	32.02	31.59
Na ₂ O	0.40	0.28	0.22
Total (calc)	99.26	99.56	97.31
Recalculated (wt%)			
final FeO	1.60	0.46	1.69
final Fe ₂ O ₃	18.92	19.95	17.19
Total	101.16	101.56	99.02
End-members			
Schorlomite-Al	8.04%	8.33%	8.22%
Morimotoite	0.46%	-	1.98%
NaTi garnet	3.08%	0.35%	1.74%
Spessartine	1.54%	3.15%	2.27%
Pyrope	0.50%	1.64%	0.94%
Almandine	3.45%	1.02%	3.21%
Grossular	25.64%	27.21%	28.65%
Andradite	57.29%	55.90%	52.99%
Remainder	0.00%	2.39%	0.00%
Total	100.00%	99.99%	100.00%
Quality Index	Superior	Good	Superior

* Quality Index represents quality of a garnet analysis, calculated according to Locock (2008)

Analyzed, alteration index such as CIA (Chemical Index of Alteration), WIP (Weathering Index of Parker) and W index were calculated to verify the representativeness of the chemical analyses on pumice.

Analyzed samples (Table 6.5) show values of CIA between 43.43 – 51.36, values of WIP between 102.83 – 133.44, values of W index between 6.76 - 17.25 (Table 6.8).

These results suggest that analyzed pumice can be considered not altered, thus allowing to use their chemical composition for the classification through TAS diagram.

A further confirmation of this result is also given by A – CN – K (Figure 6.24), WIP/CIA (Figure 6.25) and MFW diagrams (Figure 6.26).

Table 6.8: CIA, WIP and W index values for analyzed pumice.

	BG2	BG2	BG2	BG2	BG3	BG3	BG3	BG3	BG4	BG4	BG4	BG4	BG5	BG5	BG5	BG7	BG7	BG7	BG7	
CIA	46.92	46.36	47.07	48.51	46.10	46.55	46.48	48.42	46.91	43.43	47.20	47.57	46.82	47.12	44.43	44.01	47.37	44.69	51.36	48.71
WIP	123.63	124.05	125.10	119.08	127.59	124.76	121.78	109.28	124.37	125.87	116.81	117.57	121.27	125.54	114.78	115.30	111.27	119.14	102.83	113.16
W	10.10	9.05	10.24	6.76	9.76	11.27	7.35	13.89	15.88	15.22	10.47	12.48	9.39	13.59	17.25	13.56	10.54	10.25	10.17	7.39

	BG9	BG9	BG9	BG9	BG10	BG10	BG10	BG10	BG11	BG11	BG11	BG11	BG12	BG12	BG12	BG12	BG13	BG13	BG13	BG13
CIA	46.40	45.70	48.64	46.23	48.82	48.04	47.00	46.41	45.30	45.88	46.47	46.23	45.66	45.84	49.00	47.26	45.43	44.56	45.18	46.22
WIP	125.70	122.67	115.27	120.54	113.75	113.94	125.05	121.14	126.86	129.11	126.94	126.84	129.70	126.94	114.27	122.41	128.63	133.44	132.98	130.77
W	9.03	8.73	17.31	10.58	7.37	11.38	14.92	13.08	16.10	15.18	10.51	11.70	12.33	11.05	11.03	7.96	10.51	12.66	8.02	8.40

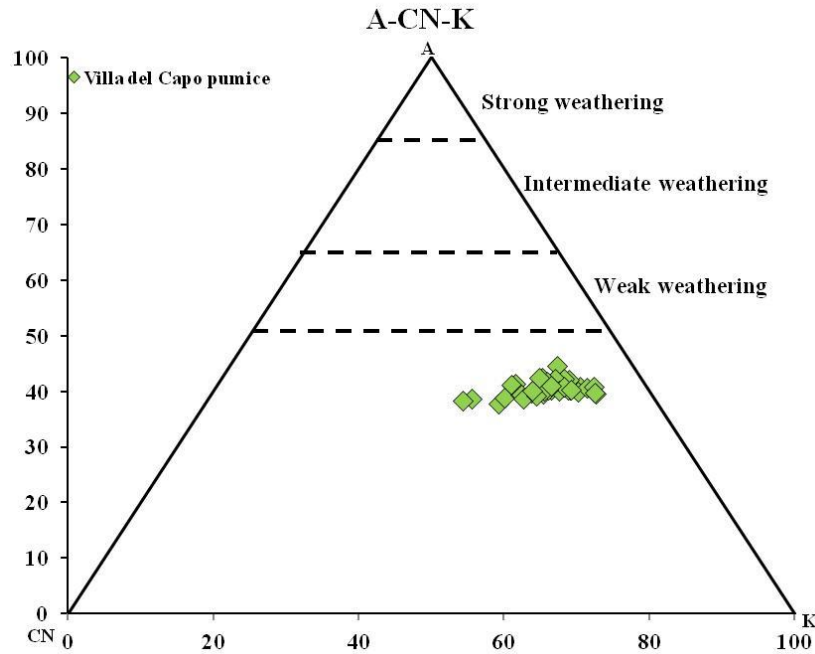


Figure 6.24: A-CN-K (Al_2O_3 — $\text{CaO}+\text{Na}_2\text{O}$ — K_2O) diagram (Nesbitt and Young, 1982) for *Villa del Capo* pumice.

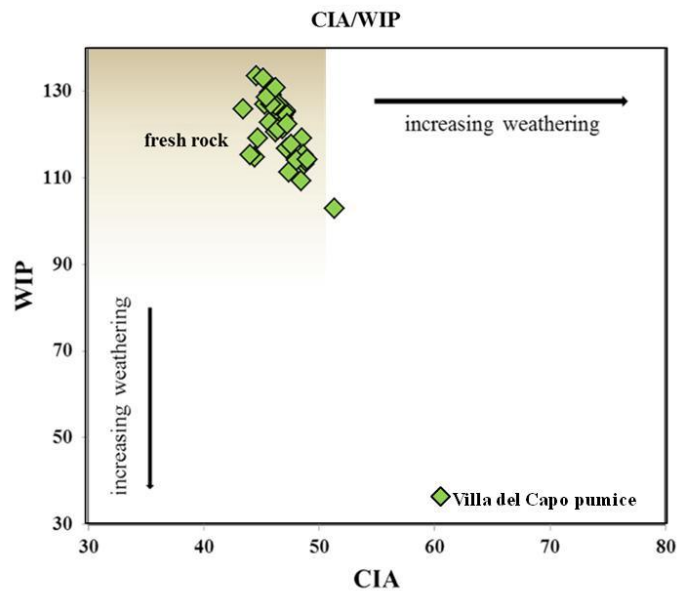


Figure 6.25: Relationship between two weathering proxies, WIP and CIA (Bahlburg and Dobrzinski, 2011), for *Villa del Capo* pumice.

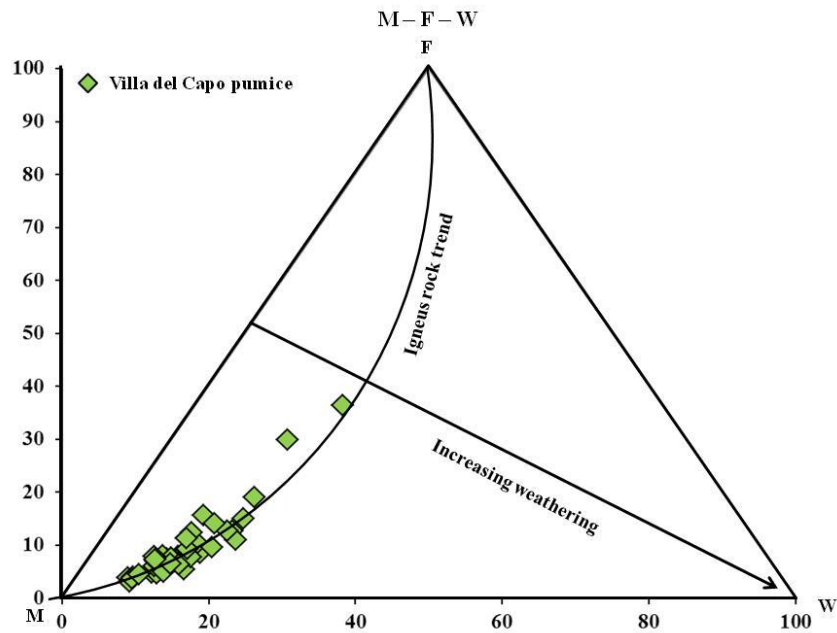
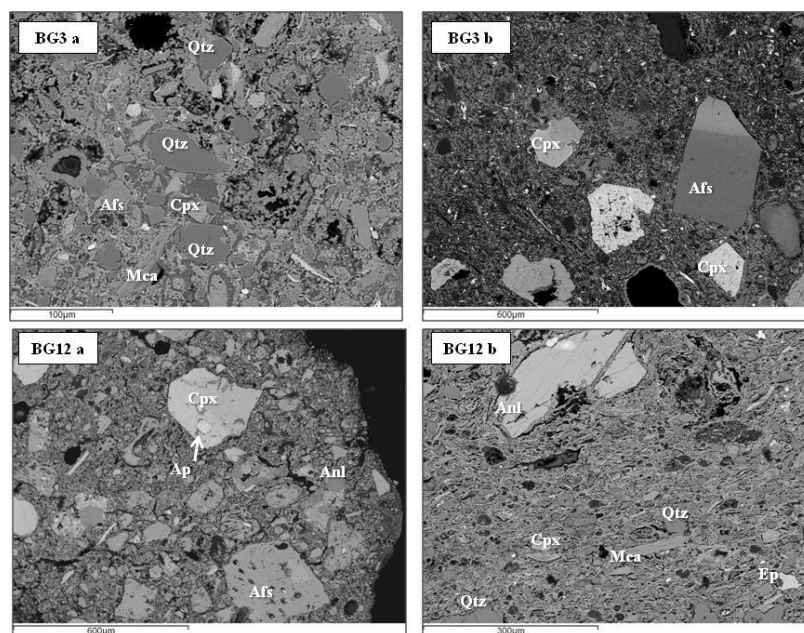


Figure 6.26: Weathering trends, MFW diagram (Ohta and Arai, 2007) for *Villa del Capo* pumice.

Regarding ceramic fragments, as for the previous sites, SEM-EDS analysis allowed to confirm textural and mineralogical differences, previously observed in thin section (Figure 6.27). This differences are testified also by use of different clayey raw materials, utilized for the production of ceramic fragments, as inferred by different CaO content in matrix (4.30 – 32.42 wt.%; Table 6.9) (CaO > 6 wt.% – calcareous clay; CaO < 6 wt% - non calcareous clay; Maniatis and Tite, 1981) (see chapter 4 par. 4.2.4).



* Cal: calcite; Qtz: quartz; Afs: alkalifeldspar; Cpx: clinopyroxene; Anl: analcime; Mca: mica; Ap: apatite; Ep: epidote.

Figure 6.27: BSE SEM images of different ceramic fragments.

Table 6.9: Chemical composition (wt.% recalculated to 100%, EDS), matrix of ceramic fragments.

wt.%	BG1	BG1	BG3	BG3	BG5	BG5	BG5	BG6	BG6
SiO ₂	55.68	35.52	54.18	51.00	50.00	54.07	54.07	55.58	53.90
TiO ₂	0.99	3.65	0.34	0.34	1.23	0.90	0.90	0.47	0.64
Al ₂ O ₃	17.77	9.20	13.72	15.13	13.88	17.23	17.23	15.47	18.70
Fe ₂ O ₃	6.31	17.61	4.51	4.90	-	6.11	6.11	4.64	4.79
MnO	-	1.01	-	0.18	-	0.29	0.29	0.22	-
MgO	3.25	0.24	5.13	3.21	2.73	3.51	3.51	2.55	2.23
*CaO	10.27	32.42	17.43	19.08	19.04	12.83	12.83	11.78	9.98
Na ₂ O	0.18	-	0.45	0.66	0.12	-	-	0.14	-
K ₂ O	2.79	0.22	1.04	1.65	1.91	1.22	1.22	1.95	3.06
P ₂ O ₅	2.17	-	2.48	2.95	3.43	2.18	2.18	3.72	2.95
V ₂ O ₃	0.13	-	0.05	0.73	0.82	1.26	1.26	0.75	0.42
BaO	-	0.13	0.29	0.00	0.11	0.39	0.39	0.20	0.61
SO ₃	-	-	0.00	0.00	2.96	-	-	2.55	2.74
Cl ⁻	0.45	-	0.38	0.16	3.62	-	-	0.00	-
F ⁻	-	-	-	-	-	-	-	-	-
Total	100.00								

wt.%	BG6	BG7	BG9	BG12	BG12	BG12	BG13	BG13	BG13
SiO ₂	53.84	50.94	51.36	53.31	58.63	54.94	60.57	52.53	56.77
TiO ₂	0.67	0.57	0.55	1.10	0.53	0.87	1.14	0.56	0.69
Al ₂ O ₃	15.27	21.72	14.56	22.37	19.42	21.41	15.98	17.64	19.54
Fe ₂ O ₃	4.43	6.09	5.11	7.08	3.90	7.57	6.32	4.29	5.49
MnO	0.10	0.20	0.11	0.17	0.58	0.03	-	0.30	0.30
MgO	2.59	10.32	3.17	4.73	2.45	4.12	3.29	3.23	2.05
*CaO	16.96	2.87	17.47	7.04	7.98	5.65	4.30	13.46	5.93
Na ₂ O	-	-	-	0.07	0.14	-	-	0.09	0.23
K ₂ O	1.58	1.32	1.80	1.23	2.76	1.21	2.00	3.50	3.50
P ₂ O ₅	2.46	2.62	2.52	2.54	3.42	3.58	4.55	3.20	4.42
V ₂ O ₃	0.76	0.19	0.35	0.02	-	0.11	0.63	0.66	0.95
BaO	0.20	0.00	0.16	0.33	-	0.41	0.11	0.38	0.13
SO ₃	1.14	3.10	2.84	-	-	-	0.97	-	-
Cl ⁻	-	0.07	-	-	0.19	0.11	0.15	0.16	-
F ⁻	-	-	-	-	-	-	-	-	-
Total	100.00								

*CaO > 6 wt.% – calcareous clay; CaO < 6 wt% - non calcareous clay

6.2.5 XRF analysis

Representative samples of different types of mortar (BG1- BG9: floor mortars; BG3-BG12: coating mortars; BG7-BG9: bedding mortars), were also studied by XRF (X-ray fluorescence) to determine their chemical composition in terms of major and trace elements.

Results are reported in Table 6.10. Representative diagrams were selected to highlights similarities or differences between the mortars.

The SiO₂/CaO diagram (Figure 6.28a) shows that bedding mortars (BG7-BG10) have a similar SiO₂ and CaO composition (40.63 – 46.25 wt.% SiO₂; 3.01 – 8.96 wt.% CaO). Floor mortars instead have highest CaO and lowest SiO₂ concentration than others *Villa del Capo* mortars. The coating mortars show values in SiO₂ and CaO if compared to bedding and floor mortars.

The Al₂O₃/Fe₂O₃ (Figure 6.28b) diagram shows that floor mortars have again similar composition in Al₂O₃ and Fe₂O₃ (5.96 – 7.92 wt.% Al₂O₃; 2.51 – 2.27 wt.% Fe₂O₃), while the other mortars of the same site are quite different.

In SO₃/Cl diagram (Figure 6.28c) show that the floor mortars have a high and wide variation in Cl (2222 – 15635 ppm and 999 - 6395 ppm, respectively) as in coating mortars (999 - 6395). Such variation is much lower in bedding mortars (12770 – 13632 ppm).

Table 6.10: Chemical analysis (XRF), major oxides and trace elements, mortars

wt.%	BG1	BG3	BG7	BG9	BG10	BG12
SiO ₂	26.37	35.05	40.63	27.01	46.25	36.73
TiO ₂	0.29	0.26	0.52	0.26	0.32	0.46
Al ₂ O ₃	5.96	8.39	13.96	7.92	13.31	10.65
Fe ₂ O ₃	2.51	2.50	4.06	2.27	2.57	3.89
MnO	0.07	0.08	0.13	0.07	0.14	0.10
MgO	5.00	4.61	7.23	2.76	1.67	7.41
CaO	30.74	20.73	3.01	25.67	8.96	15.89
Na ₂ O	1.42	1.75	5.78	2.39	4.80	1.08
K ₂ O	1.32	2.12	2.92	2.01	4.99	1.92
P ₂ O ₅	0.16	0.07	0.09	0.09	0.05	0.15
SO ₃	0.22	0.18	0.40	0.20	0.09	0.20
SrO	0.06	0.05	0.07	0.12	0.03	0.05
LOI	25.51	23.45	19.72	27.64	15.46	21.25
ppm	BG1	BG3	BG7	BG9	BG10	BG12
Cr	220	137	126	84	121	138
Zn	109	149	120	136	181	158
Ba	656	492	612	-	-	437
Br	-	-	-	-	-	-
Cl	2222	6395	13632	15635	12770	999
Co	-	34	13	-	-	30
F	-	-	-	-	-	-
Ni	127	91	73	83	91	98
Pb	-	-	-	-	202	-
Cu	157	206	133	175	141	228
V	210	234	177	-	163	199

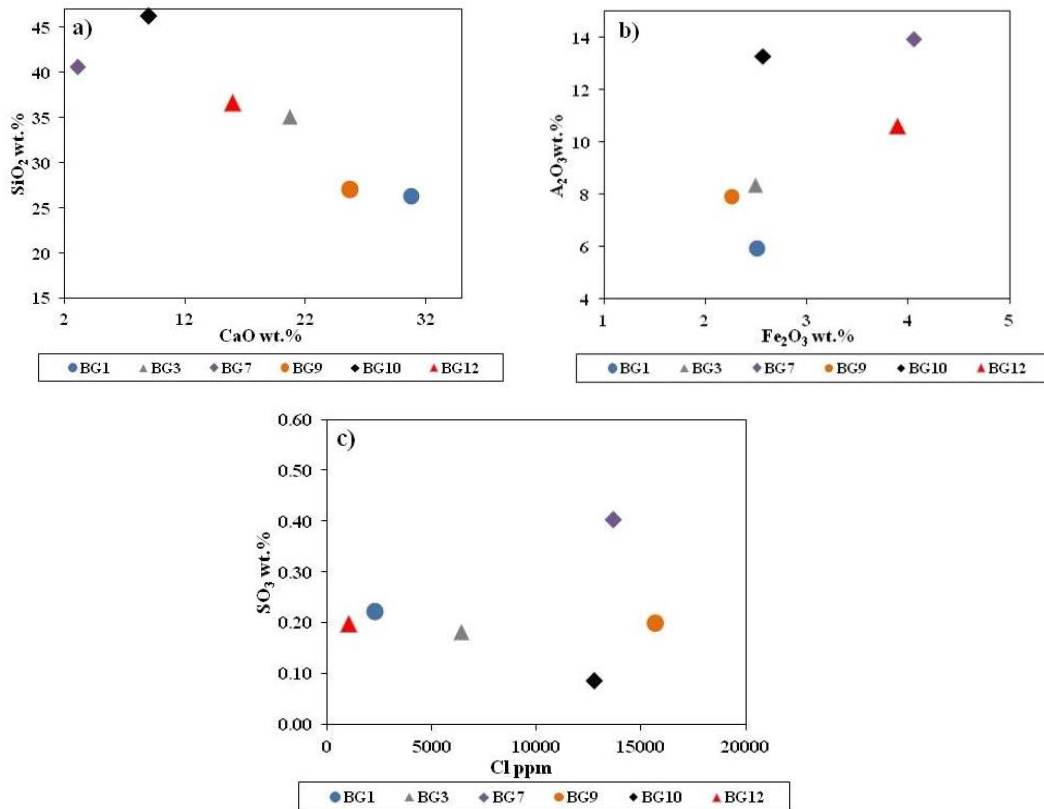


Figure 6.28: Binary diagrams representative of major oxide and trace element composition

6.2.6 Differential and Gravimetric Thermal Analysis (DTA-TGA)

In order to obtain further information regarding hydraulicity features of mortar samples from *Villa del Capo*, thermal analyses (DTA-TGA) were carried out.

In the temperature range between 200 and 600 °C the estimated weight loss is due to structurally bound water (SBW) from the hydraulic compounds, while at temperature range between 600 and 850 °C the weight loss is due to CO₂ evolution as a consequence of the decomposition of calcium carbonate (CaCO₃) (Figure 6.29). Table 6.11 reports results for this specific technique.

CO₂/SBW ratio was calculated and, according to Moropoulou et al. (1995, 2005), mortars were classified into different groups on the basis of their hydraulicity.

According to data of Moropoulou et al. (2005), *Villa del Capo* mortars fall in the field of natural pozzolanic mortars (Figure 6.30), confirming the results obtained by SEM-EDS analyses (see par. 6.2.4).

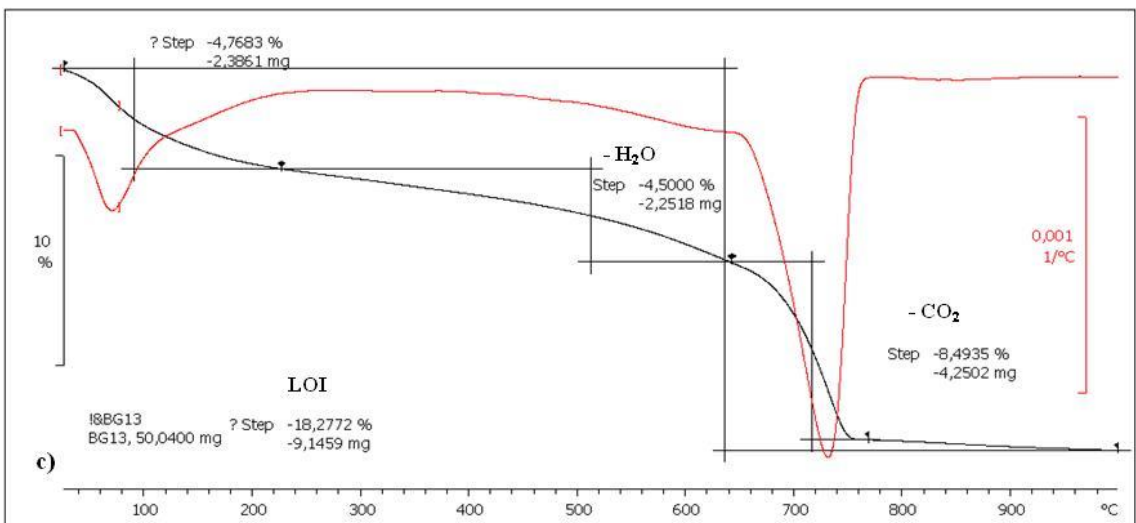
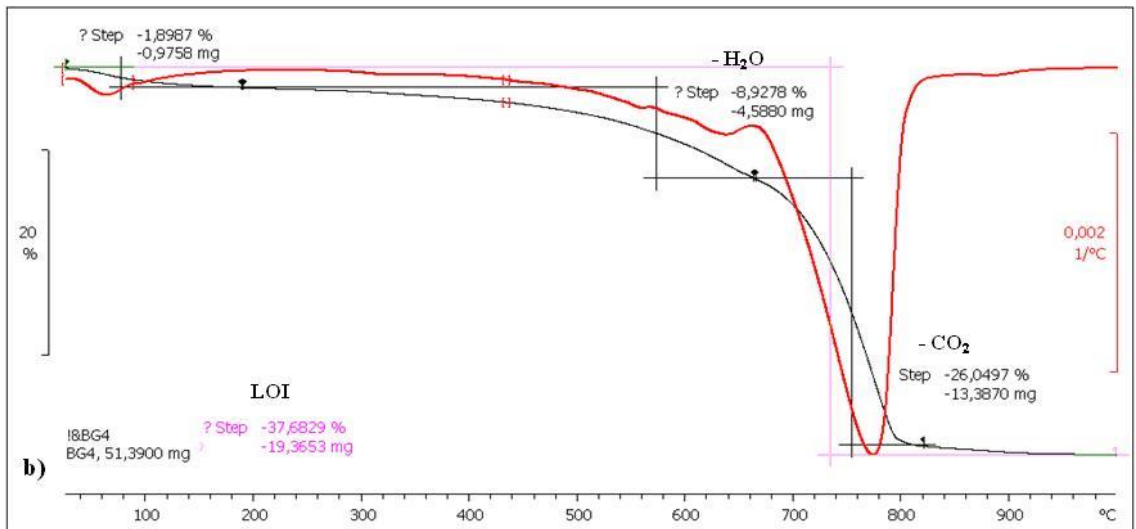
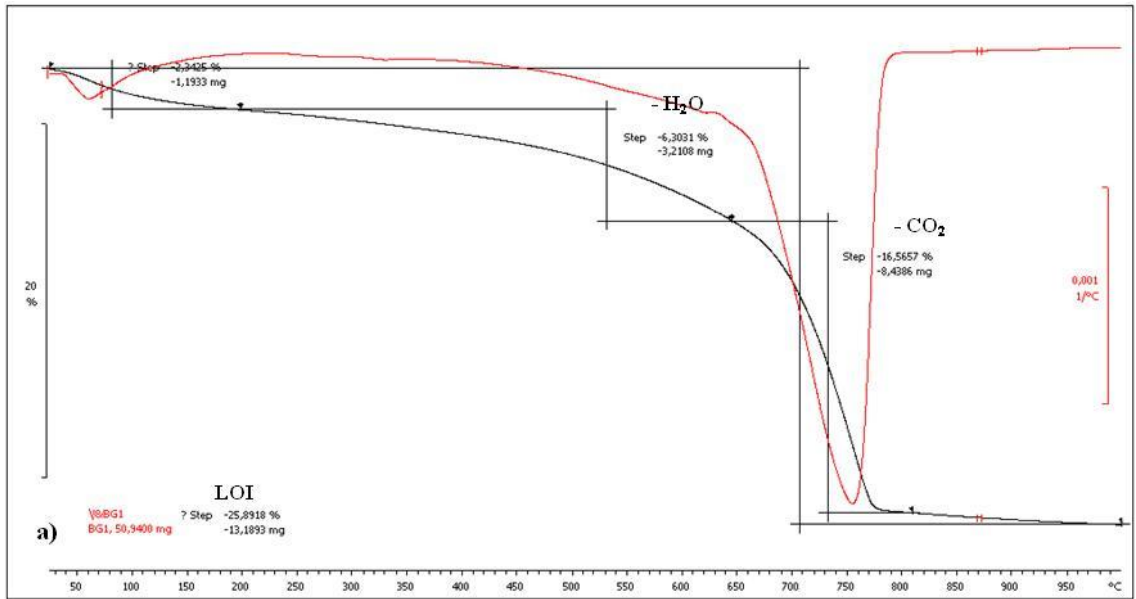


Figure 6.29: DTA-TGA plot of a)BG1 b) BG4 and c)BG13 samples.

Table 6.11: Thermal analysis (DTA/DTG) features *Villa del Capo* samples.

Sample	SBW %	CO ₂ %	CO ₂ /SBW	LOI %
BG1	6.3	8.43		
T range (°C)	203-640	640-810	1.34	25.89
BG3	9.6	8.43		
T range (°C)	200-623	623-780	0.88	23.69
BG4	8.42	13.38		
T range (°C)	180-642	642-820	1.59	37.68
BG5	12.21	4.08		
T range (°C)	220-642	642-740	0.33	31
BG6	7.81	9.78		
T range (°C)	200-640	640-812	1.25	37.03
BG9	10.13	10.12		
T range (°C)	210-641	641-780	1.00	29.33
BG10	4.92	3.03		
T range (°C)	200-562	562-740	0.62	17.51
BG11	4.75	5.64		
T range (°C)	208-542	542-684	1.19	22.06
BG12	4.62	8.06		
T range (°C)	200-640	640-780	1.74	20.67
BG13	4.5	8.49		
T range (°C)	220-640	640-775	1.89	18.27

*SBW = Structural Bound Water, LOI= Loss on Ignition

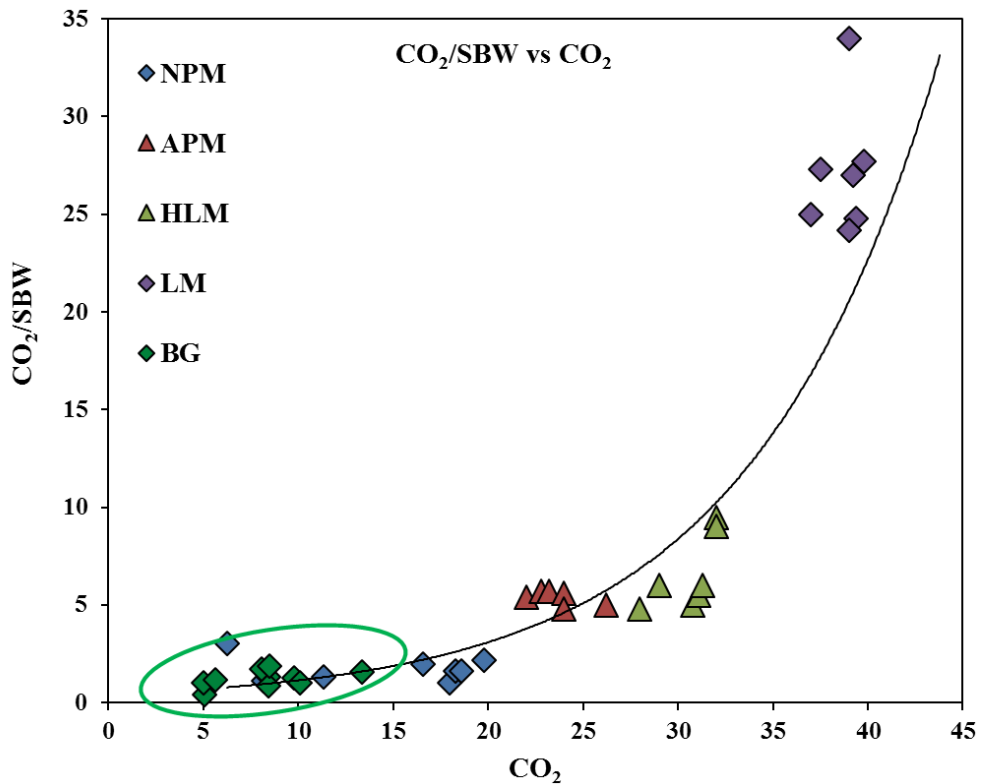


Figure 6.30: Binary CO₂/SBW vs. CO₂ diagram, comparing data from *Villa del Capo* (BG, green circle) and from Moropoulou et al., 2005. (NPM: natural pozzolanic mortars; APM: artificial pozzolanic mortars; HLM: Hydraulic lime mortars; LM: lime mortars).

6.2.7 Mercury intrusion porosimetry (MIP)

Porosity of representative samples of mortars (BG4 and BG12) was evaluated by mercury intrusion porosimetry (MIP), according to ASTM D4404 (Determination of pore volume and pore volume distribution of soil and rock by mercury intrusion porosimetry). Analyses were performed on three fragments for each samples, and average results are reported.

Results are shown in Table 6.12 and Figure 6.31 and Figure 6.32, where cumulative and relative pore size distributions are reported.

Pore sizes of samples is between 10 - 100 nm, falling within the characteristic field of hydration product porosity, usually considered below 100 nm (Metha et al., 2006; Gotti at al., 2008).

Samples show total porosity values between 40% - 43%, and unimodal and broadened shape of pore size distribution.

Table 6.12: Porosimetric features (MIP) of mortars.

Sample	BG4	BG12
Cumulative volume (mm³/g)	295.86	295.33
Bulk density (g/cm³)	1.47	1.43
Total porosity (Vol. %)	42.47	39.82

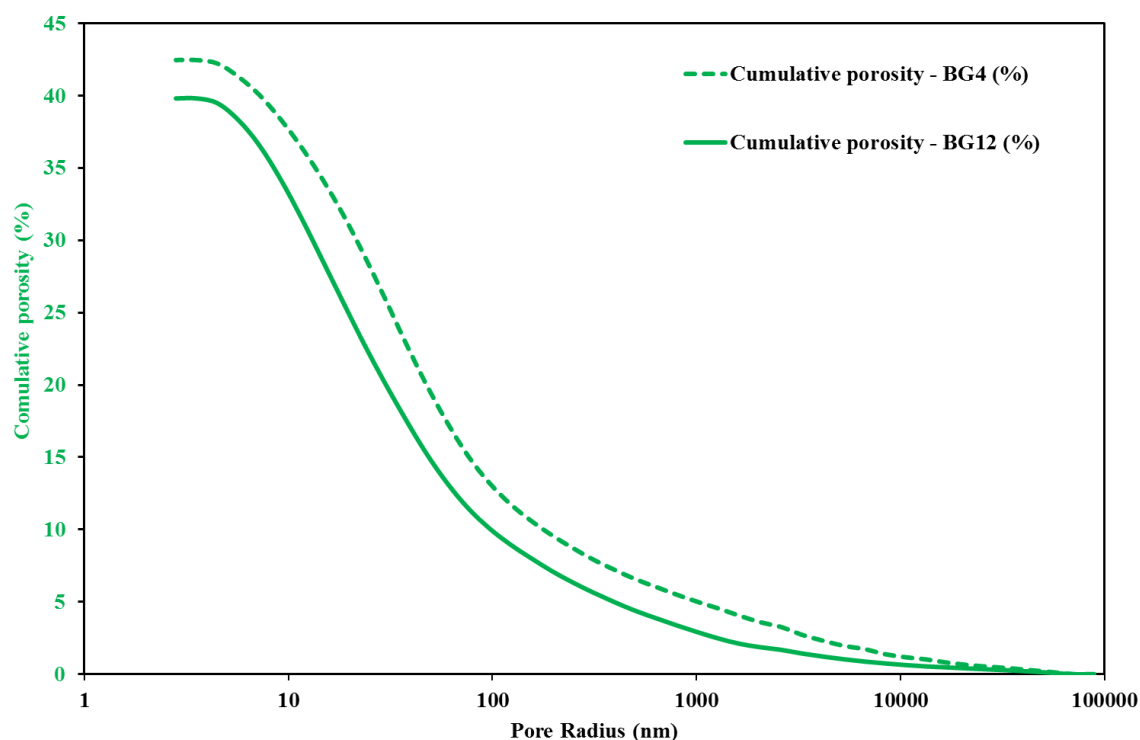


Figure 6.31: Cumulative pore size distribution for BG4 and BG12 samples.

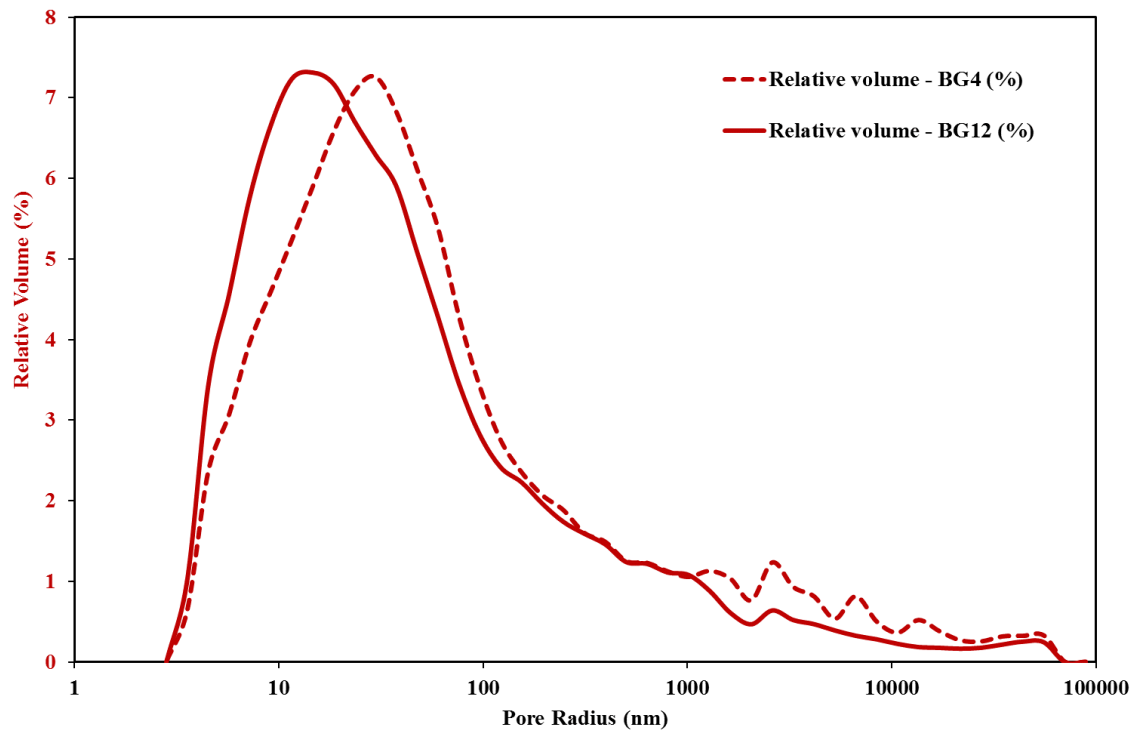


Figure 6.32: Relative pore size distribution in for BG4 and BG12 samples.

Chapter 7

Villa del Pezzolo: materials and results

7.1 Materials

Ten different samples were collected on several walls from the archaeological site (Figure 7.1), supervised by the archaeologists and the Superintendence of Archeological Heritage of Campania in order to collect representative materials of the building.

Nine bedding mortars and one floor mortar were collected: three corresponding to the first building phase, three to the second one and four to the third (Table 7.1; Figure 7.1)

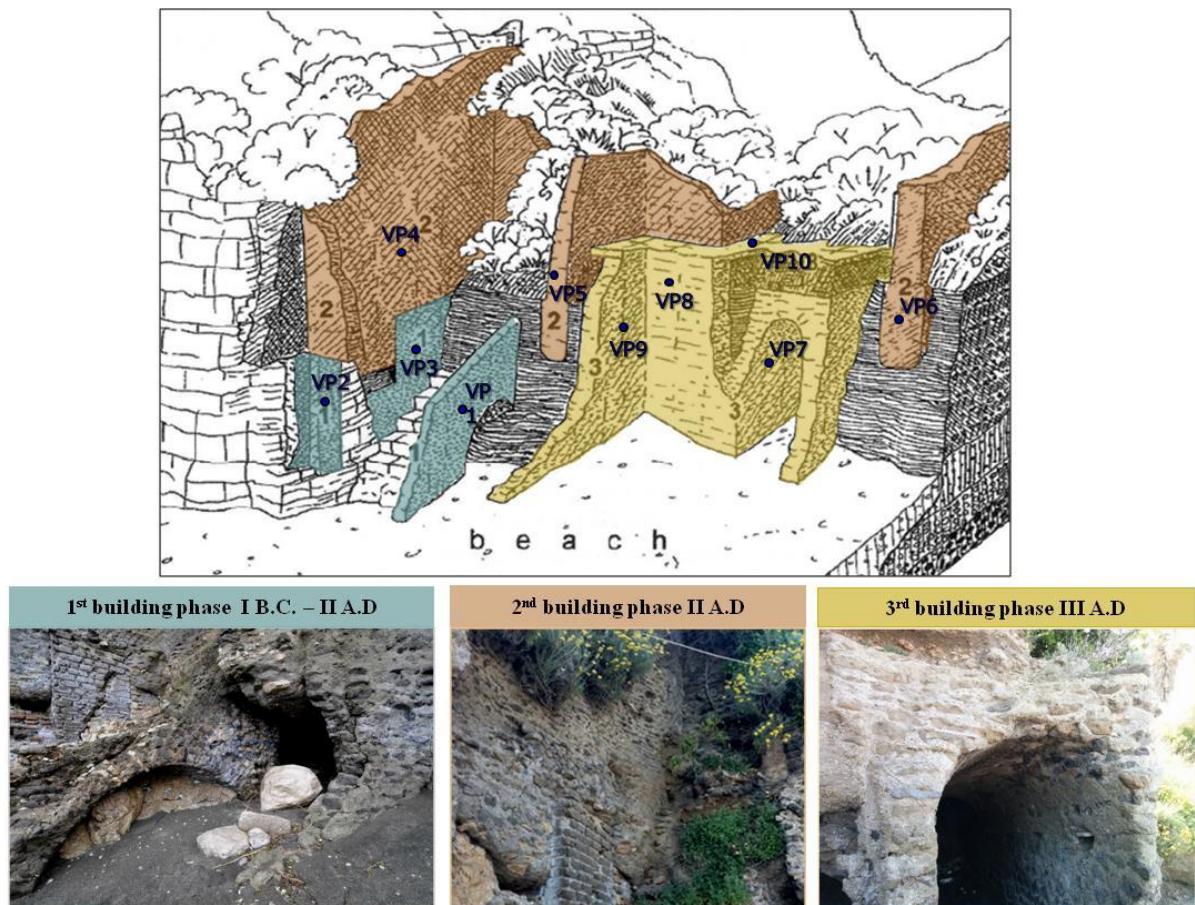


Figure 7.1 Sketch map of the *Villa del Pezzolo* with sampling site and details of building phases (modified after Aucelli et al., 2016).

Table 7.1: samples, location and typology.

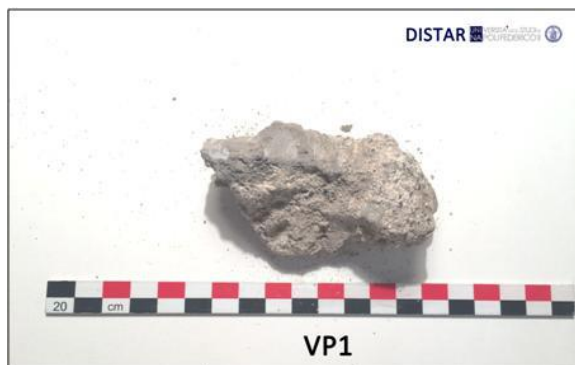
SAMPLES	LOCATION	TYPOLGY
VP1	1 st building phase	bedding mortar
VP2	1 st building phase	bedding mortar
VP3	1 st building phase	bedding mortar
VP4	2 nd building phase	bedding mortar
VP5	2 nd building phase	bedding mortar
VP6	2 nd building phase	bedding mortar
VP7	3 rd building phase	bedding mortar
VP8	3 rd building phase	bedding mortar
VP9	3 rd building phase	bedding mortar
VP10	3 rd building phase	floor mortar

7.2 Results

7.2.1 Macroscopic observation

Macroscopic observations of the samples show light yellow to dark brown colours, with coarse aggregates ranging in diameter from 3 mm up to 3 cm (Fig 7.2). Aggregates are made of volcanic and carbonatic fragments along with, in some samples, few ceramic fragments.

Mortars show lumps (2-4 mm) that generally consists in no reacted lime, which origin is to be researched in the properties of the slaked lime (calcium hydroxide) and in the water/quicklime ratio (Bakolas et al. 1995; Barba et al., 2009). They formed during the slaking process of the lime an insufficient seasoning of the calcium hydroxide and a low water/ lime ratio.



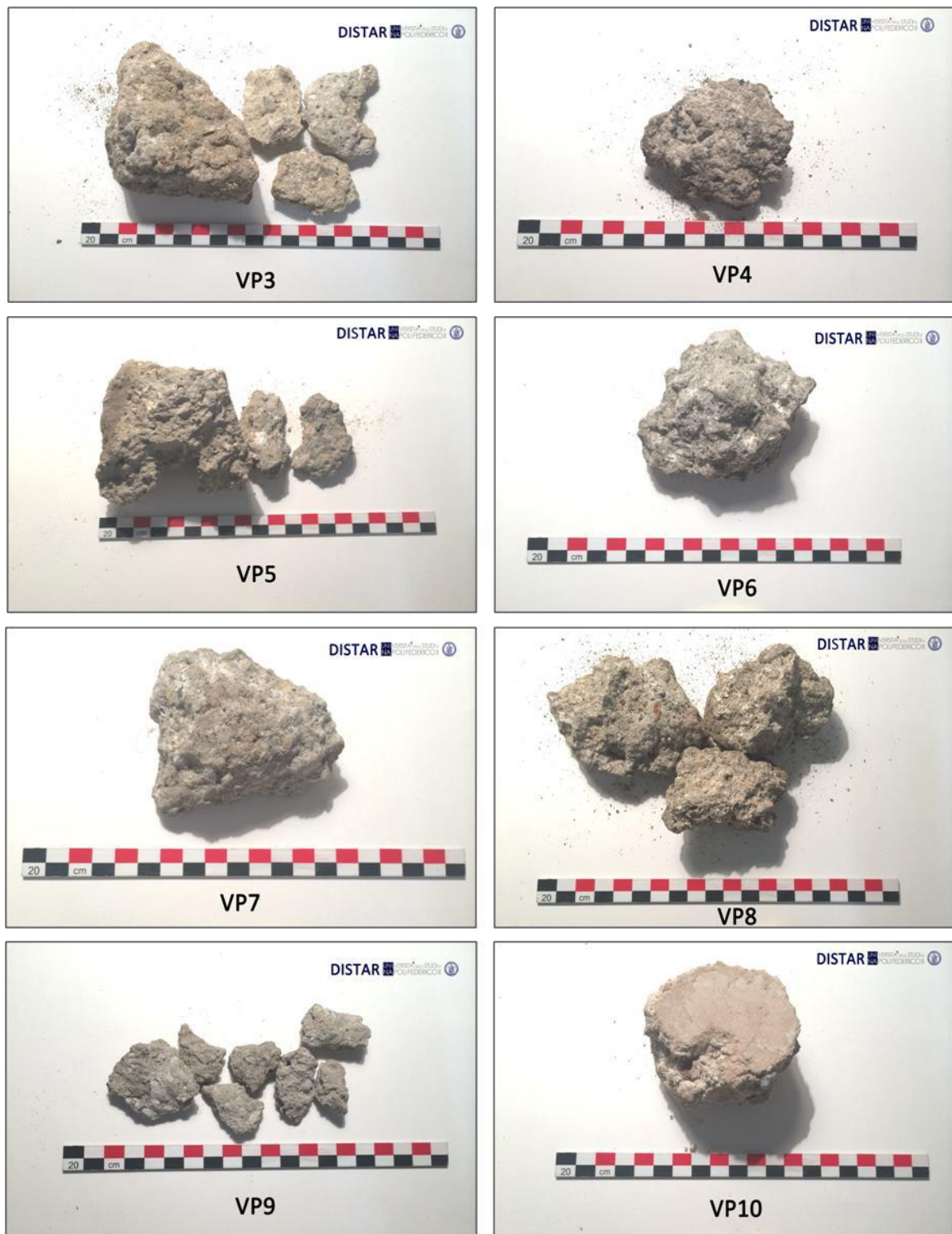


Figure 7.2: Macroscopic images of bedding mortars.

7.2.2 Petrography

Thin section observations and modal analysis, performed counting 1500 points for each representative section (Table 7.2), allowed to identify three (A, B and C) groups of samples (Figure 7.3).

To the group A belong samples of the first building phase, to group B belong samples of the second building phase and finally to group C the samples of the third building phase, that match with the sampling category.

All mortars show poor homogeneity and compactness of the binder.

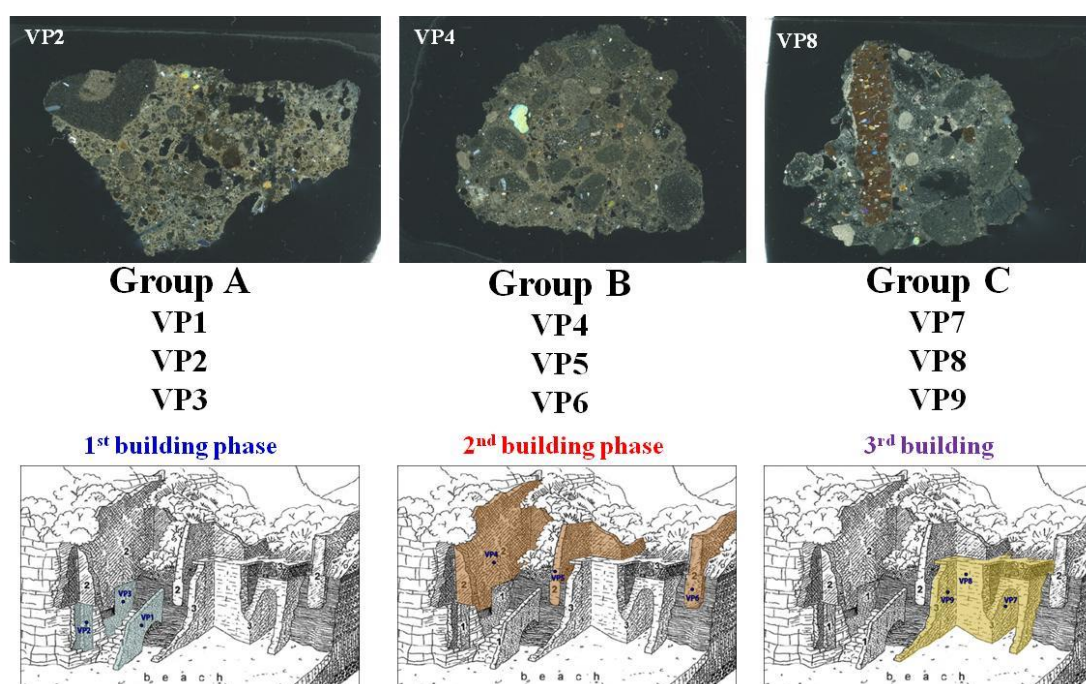


Figure 7.3: identified groups of mortars.

Moreover, secondary calcite was observed in all samples, such as in the binder, on the pore rims and in the pumice vesicles.

The Group A (VP1, VP2, VP3, first building phase) is characterized by a yellowish-light brown cryptocrystalline and micritic binder (35.4 Vol.%; 12.6 Vol.%; Figure 7.4a-b). Small and fractured lime lumps were also observed (3.0 Vol.%; Figure 7.4c).

The aggregates are constituted mainly by pumice (15.7 Vol.%; Figure 7.4d), volcanic and carbonate fragments (10.6 Vol.%; 2.1 Vol.%; Figure 7.4a-e), scoriae (3.7 Vol.%), and crystal fragments of plagioclase, clinopyroxene and sanidine (6.5 Vol.%; Figure 7.4f).

In particular, volcanic fragments are characterized by glassy shards partially devitrified.

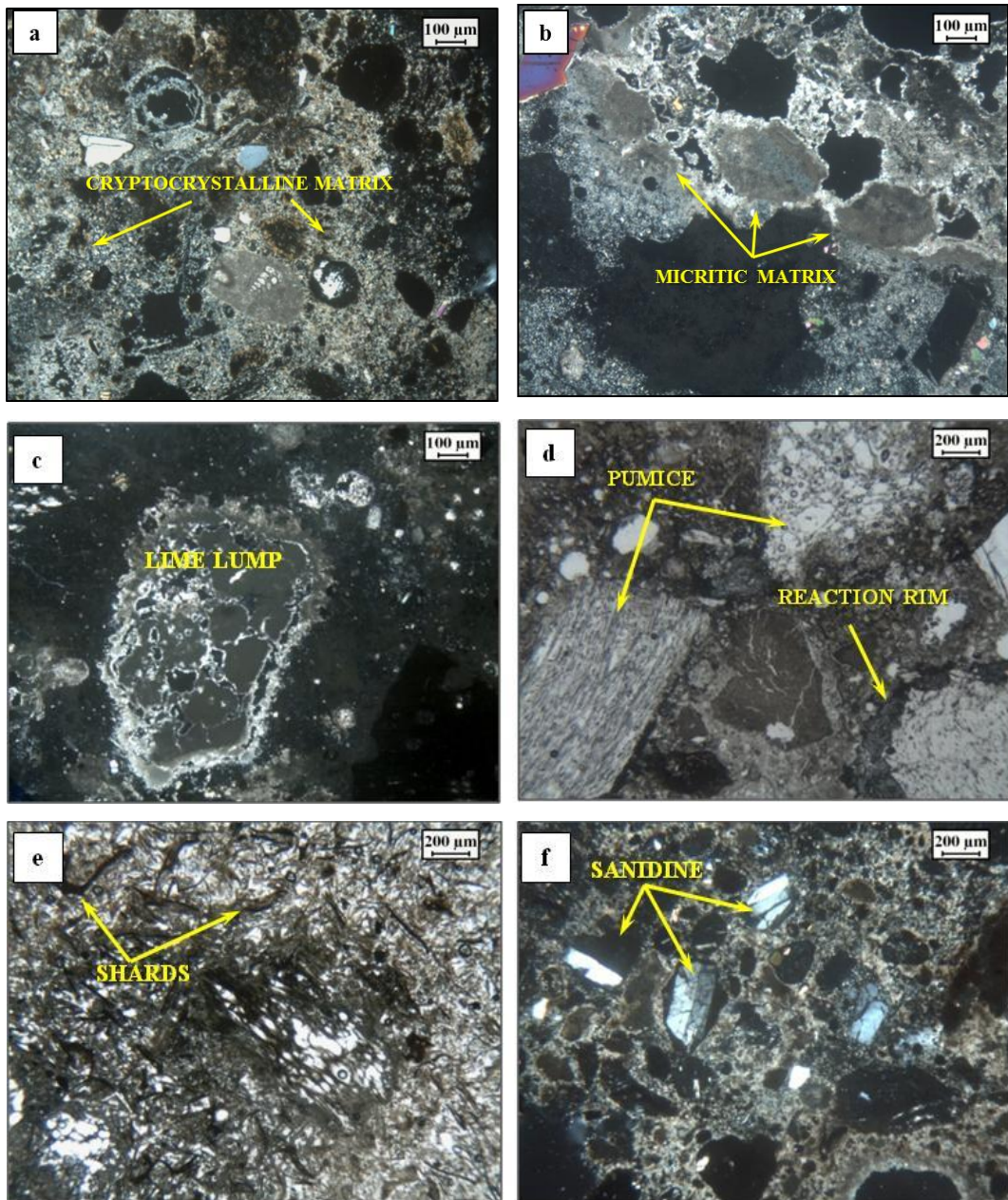


Figure 7.4: Microphotographs of mortars belonging to Group A: a) cryptocrystalline matrix and carbonate fragment (CPL) in VP2 sample; b) micritic matrix (CPL) in VP3 sample; c) lime lump (CPL) in VP2 sample; d) pumice with reaction rim (PPL) in VP1 sample; e) glassy shards (PPL) in VP3 sample; f) crystal fragments of sanidine (CPL) in VP1 sample. CPL: Cross Polarized Light; PPL: Plane Polarized Light.

Group B (VP4, VP5, VP6, second building phase) includes mortars with binder variable in colour from light grey to brown. The binder phase is mainly characterized by cryptocrystalline matrix (43.8 Vol.%) and a low percentage of micritic matrix (4.9 Vol.%) (Figure 7.5a).

Lime lumps are present only in VP4 and VP5 sample (1.8 Vol.%); they are small, fractured, and poorly compacted with not well defined edges. In VP5 sample lumps are present as relicts (Figure 7.5b).

Shape of aggregate varies from sub-angular to sub-rounded and their size distribution is moderately sorted.

The aggregate fraction is characterized by volcanic fragments (0.9 Vol.%), carbonate and marble fragment (5.3 Vol.%; Figure 7.5c), scoriae (1.2 Vol.%), deeply altered pumice (with garnet and leucite fragments) (12.1 Vol.%; Figure 7.5d), leucite-bearing scoriae (13.3 Vol.%; Figure 7.5e), and crystal fragments of plagioclase, clinopyroxene, sanidine, garnet and leucite (8.6 Vol.%; Fig 7.5f).

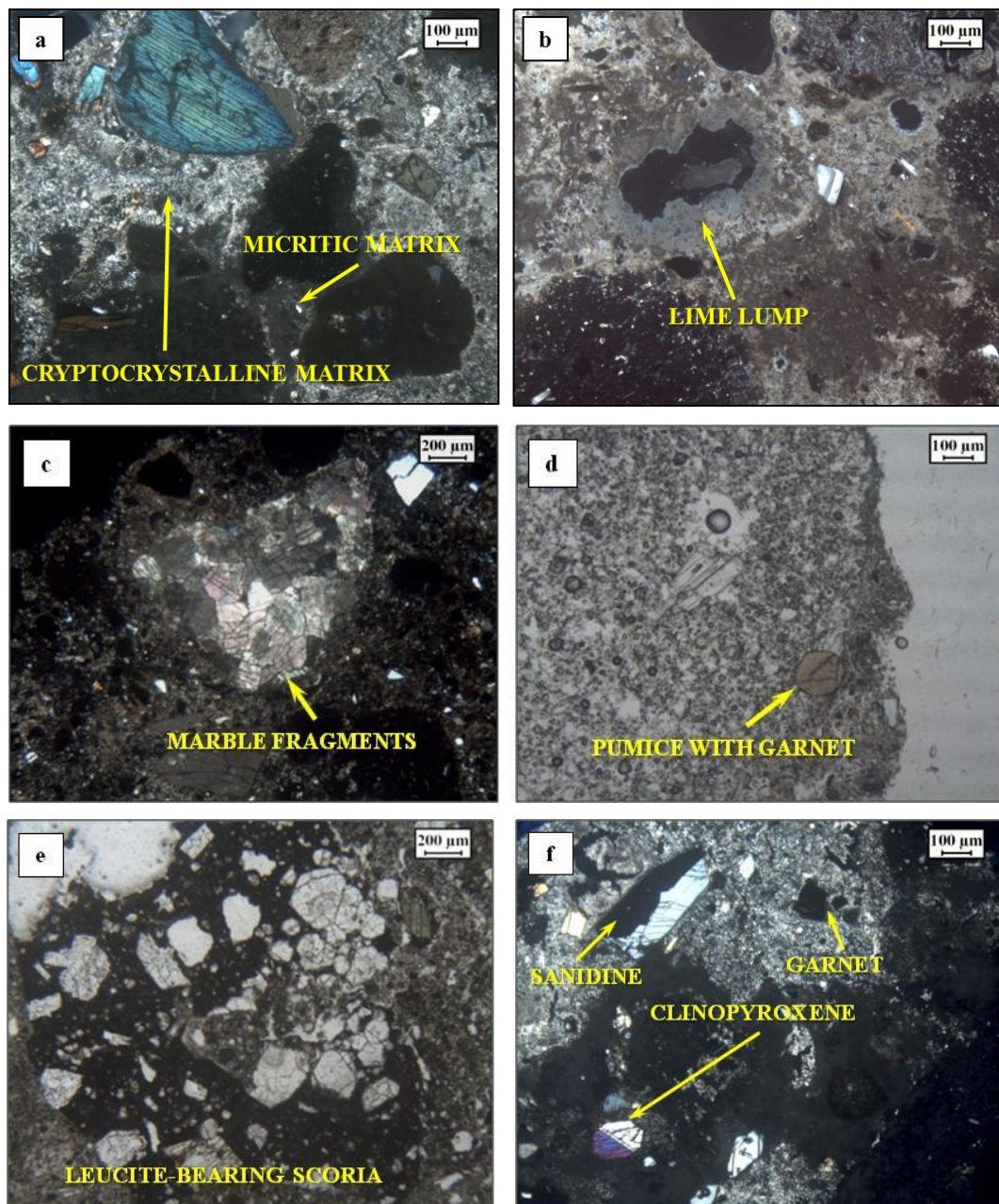


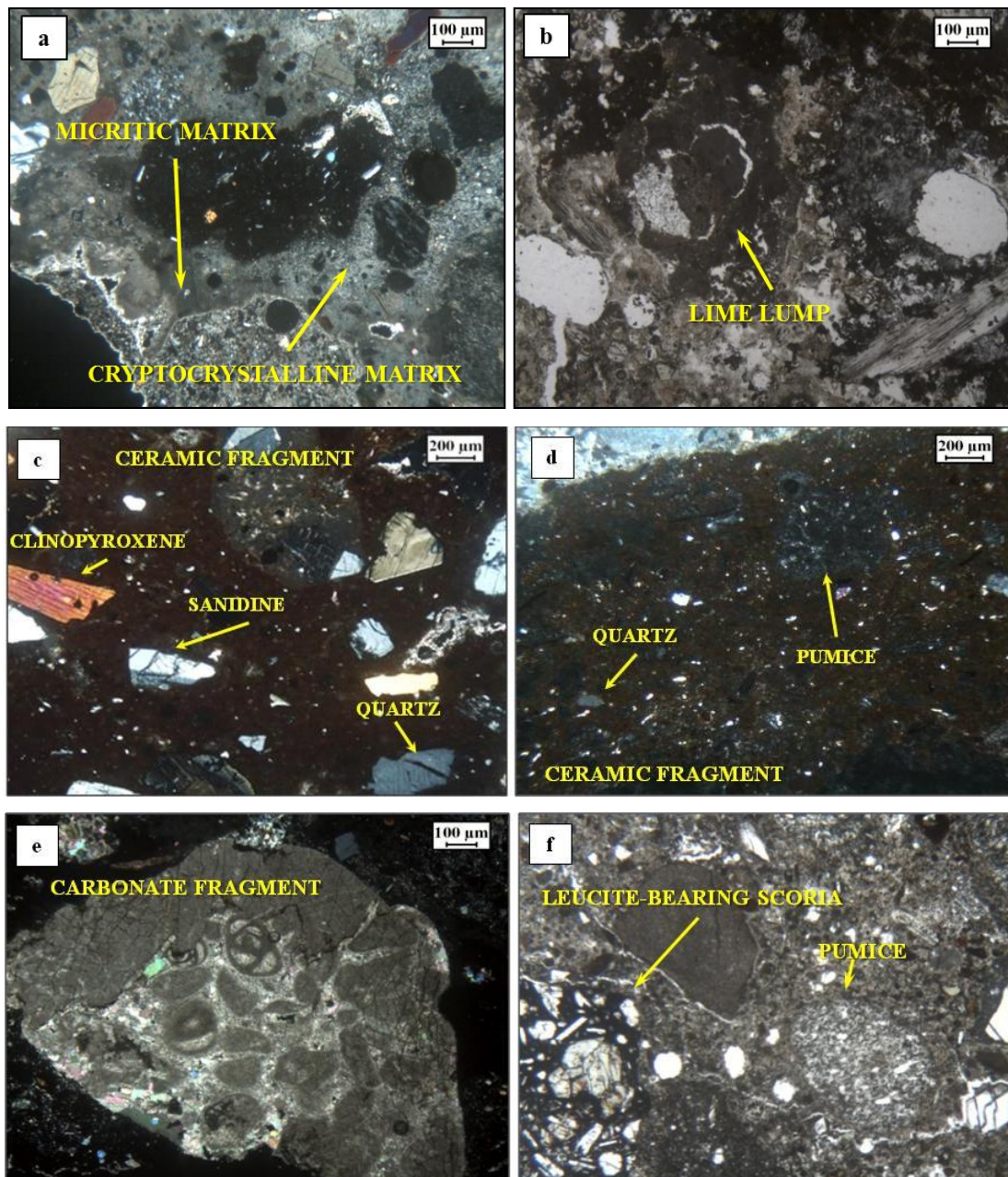
Figure 7.5: Microphotographs of mortars belonging to Group B: a) cryptocrystalline and micritic matrix (CPL) in VP4 sample; b) relict of lime lump (CPL) in VP5 sample; c) marble fragment (CPL) in VP4 sample; d) pumice with garnet (PPL) in VP6 sample; e) leucite – bearing scoria (PPL) in VP4 sample; f) crystal fragments of sanidine, garnet and clinopyroxene (CPL) in VP6 sample.

The binder phase of samples from C group (VP7, VP8, VP9, third building phase) is composed again of cryptocrystalline matrix (37.3 Vol%), micritic matrix (3.6 Vol.%) (Figure 7.6a) and a

few percentage of lime lumps (1.8 %; Figure 7.6b). The colour varies between grey and dark-brownish.

The aggregate fraction appears moderately sorted and sub-rounded, composed by ceramic (VP8 and VP9, 15.5 Vol.%; Figure 7.6c-d), volcanic and carbonate fragments (0.5 Vol.%; 15.5 Vol.%; Figure 7.6e), pumice (16.3 Vol.%; Figure 7.6f), leucite-bearing scoriae (2.6 Vol.%; Figure 7.6f), amphibole, garnet and leucite as crystal fragments (7.8 Vol.%; Figure 7.6g). In these samples, mineral aggregates formed by clinopyroxene, leucite, analcime and, sometimes, calcite was also detected.

VP9 sample is slightly different from other samples, due to the presence of sparite grains in the binder (Figure 7.6h). Its origin can be related to a residual limestone, not completely calcinated.



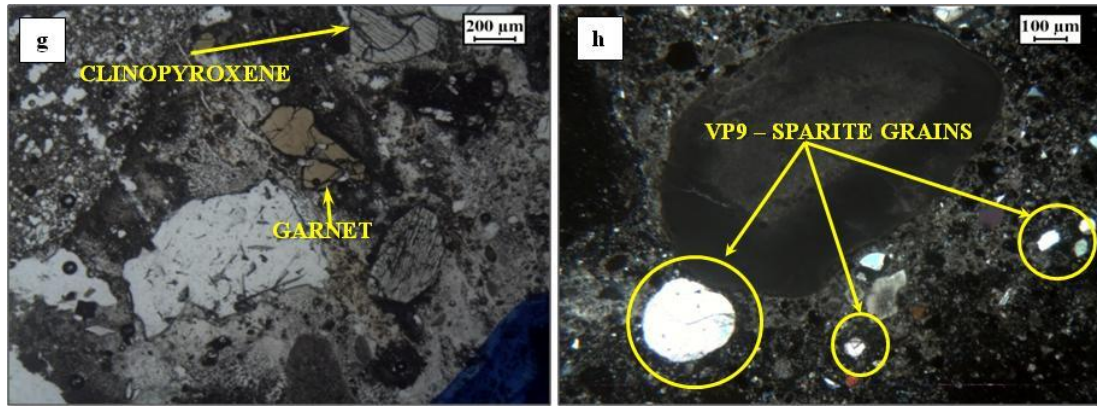


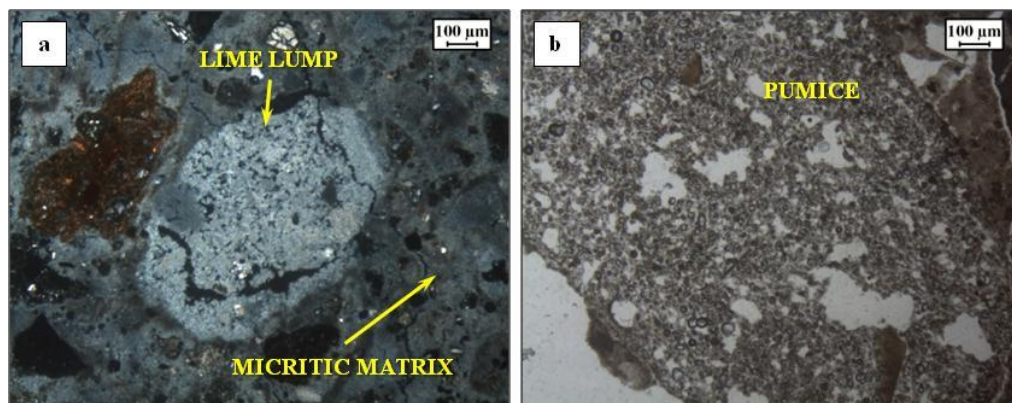
Figure 7.6: Microphotographs of mortars belonging to Group C; a) cryptocrystalline and micritic matrix (CPL) in VP8 sample; b) lime lump (CPL) in VP7 sample; c) and d): mineralogical phases in different ceramic fragments (CPL) of VP9 sample; e) carbonate fragment (CPL) in VP8 sample; f) leucite – bearing scoria and pumice (PPL) in VP7 sample; g) crystal fragments of garnet and clinopyroxene (CPL) in VP8 sample; h) sparite grains (CPL) in VP9 sample.

VP10 sample is a floor mortar, and here the use of *cocciopesto*, also called *Opus signinum*, a typical building techniques used in ancient Rome for making floor and waterproofing cistern, was identified. *Cocciopesto* is composed by a) a mixture of lime, b) powders obtained crushing shattered tiles, bricks and pottery and c) different type of aggregates e.g., pumice (Figure 7.7b). The binder phase is composed mainly by micritic matrix (25.4 Vol.%;) and also shows the presence of lime lumps (2.2 Vol.%; Figure 7.7a).

Ceramic fragments, both from samples of group C and VP10 sample (Figure 7.6c-d; Fig 7.7c-d), often show mineralogical and textural differences. Some of them show low optical activity and some high, some others show volcanic aggregates, scoriae, volcanic glass and others only crystal fragments.

The modal analysis (Table 7.2), performed on representative samples, highlighted differences in the aggregate/binder ratio.

VP10 sample (floor mortar) and bedding mortars belonging to group C, show a binder/aggregate ratio lower than 1, that is to say that the percentage of the aggregate is higher than that of the binder phase (Figure 7.8).



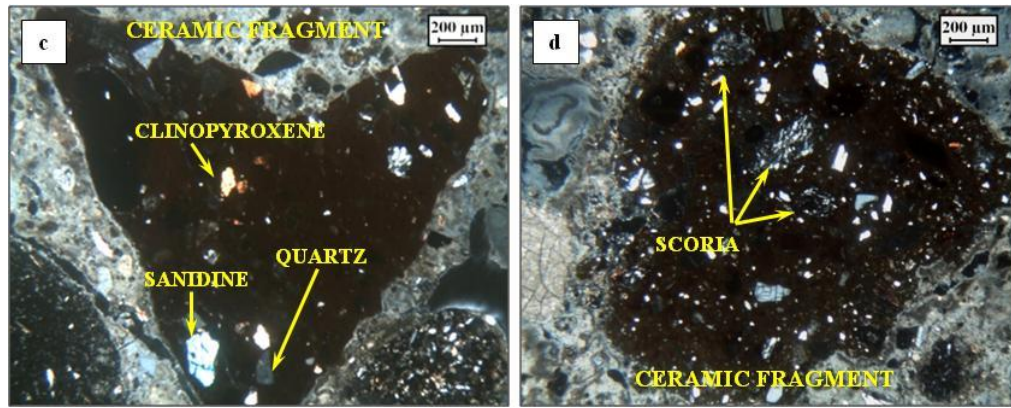


Figure 7.7: Microphotographs of VP10 mortar sample: a) micritic matrix and lime lump (CPL); b) pumice (PPL); c) and d) mineralogical phases in different ceramic fragments (CPL).

Table 7.2: Modal analyses of selected mortars.

Mortars	VP2 (A group)	VP5 (B group)	VP8 (C group)	VP10 (floor mortar)
Constituentes (Vol.%)				
Feldspar (Afs, Plg)	3.4	2.6	2.3	3.1
Mafic Minerals (Cpx, Am, Bt)	3.1	6.0	4.8	5.9
Garnet	0.6	0.3	1.6	1.2
Volcanic fragments	10.6	0.9	0.5	0.8
Scoriae	3.7	1.2	1.3	0.7
Leucite-bearing scoriae	-	13.3	4.6	3.7
Pumice	15.7	12.1	15.0	17.3
Ceramic fragments	-	-	15.5	16.2
Carbonate fragments	2.1	5.3	6.9	4.5
Line lumps	3.0	1.8	1.8	2.2
Micritic matrix	12.6	4.9	10.6	25.4
Cryptocrystalline matrix	35.4	43.8	28.3	11.3
Voids	12.1	7.3	6.4	7.0
Others	0.6	0.6	0.6	0.7
Total points %	100.0	100.0	100.0	100.0
Total Binder %	51.0	50.6	42.6	38.9
Total Aggregate%	39.3	41.6	50.4	53.4
Binder/Aggregate ratio	1.3	1.2	0.8	0.7

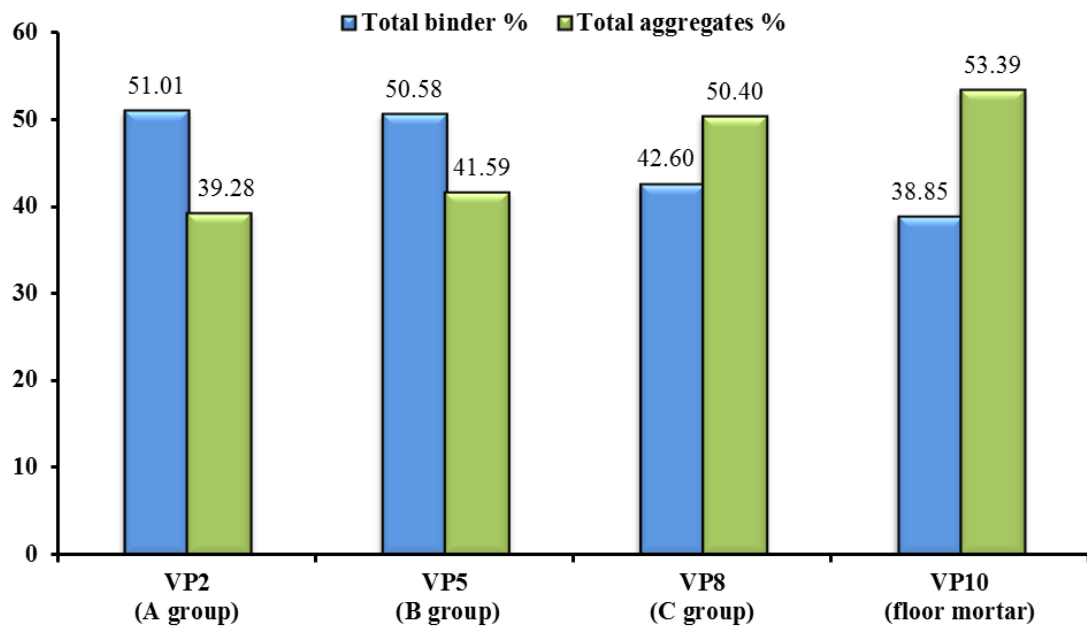


Figure 7.8: Histogram showing percentages of total binder and total aggregates in representative samples of mortars.

5.2.3 XRPD analysis

Samples were divided into binder, aggregates, and ceramic fragments, according to the UNI Normal 11305 document (mortar characterization) and then analyzed by XRPD. Results are showed in Table 7.3.

The XRPD results show calcite as the main mineral in mortar-based materials along with gypsum (Figure 7.9; Table 7.3), alkali feldspar (sanidine), plagioclase, analcime, mica clinopyroxene as mineral phases of the aggregate; low amounts of leucite, and chabazite are also present (Figure 7.10; Figure 7.11; Table 7.3).

In ceramic fragments, occurrences of calcite, quartz, mica and hematite were observed (Table 7.12; Table 7.3).

XRPD analyses allowed to reveal also the presence of an amorphous fraction (Figure 7.13), probably related to a) volcanic glass component (pumice and scoriae) and b) C-A-S-H phases; the latter formed after that pozzolanic reactions between lime and volcanic glasses or ceramic fragments took place. All analyzed samples show the presence of halite.

Table 7.3: Qualitative mineralogical (XRPD) composition of mortars.

Samples	Group	Main Binder Phases	Main Aggregates Phases	Main Ceramic Fragments Phases	Other Phases
VP1	group A	Cal	Cbz, Lct, San, Pl, Cpx, Mca		HI
VP2	group A	Cal, Gp	Cbz, Anl, San, Pl, Cpx, Mca		HI
VP3	group A	Cal, Gp	Anl, San, Pl, Cpx, Mca		HI
VP4	group B	Cal	Anl, Lct, San, Pl, Cpx, Mca		HI
VP5	group B	Cal	Anl, Lct, San, Pl, Cpx, Mca		HI
VP6	group B	Cal	Anl, San, Pl, Cpx, Mca		HI
VP7	group C	Cal	Anl, Lct, San, Pl, Cpx, Mca		HI
VP8	group C	Cal	Anl, San, Pl, Cpx, Mca	Qz, Hem, Cpx, Pl	HI
VP9	group C	Cal, Gp	Anl, Lct, San, Pl, Cpx, Mca	Qz, Hem, Cpx	HI
VP10	Floor mortar	Cal, Gp	Anl, San, Pl, Cpx, Mca	Qz, Hem, Cpx, Pl	HI

* Cal: calcite; Gp: gypsum; Cbz: chabazite; Anl: analcime; San: sanidine; Cpx:clinopyroxene;Lct: leucite; Mca: mica; Hem: hematite; Qtz: quartz; HI: halite.

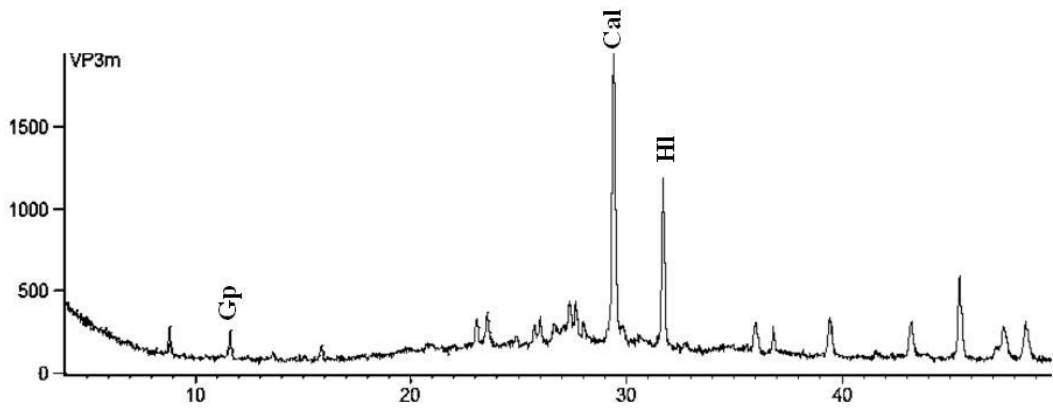


Figure 7.9: XRPD spectrum of VP3 binder.

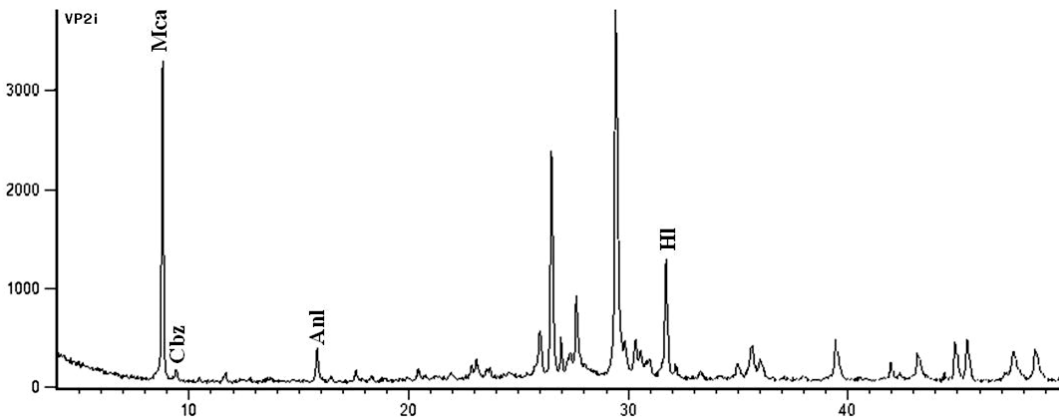


Figure 7.10: XRPD spectrum of VP2 aggregate.

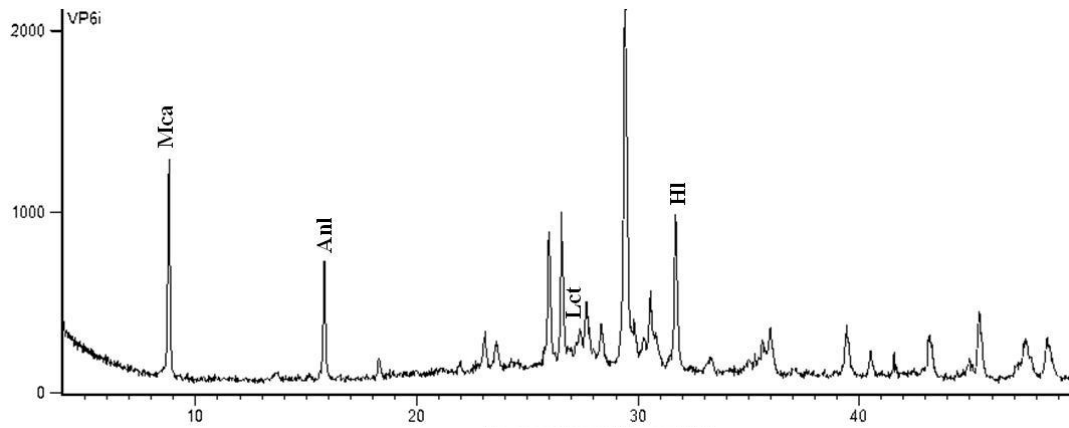


Figure 7.11: XRPD spectrum of VP6 aggregate.

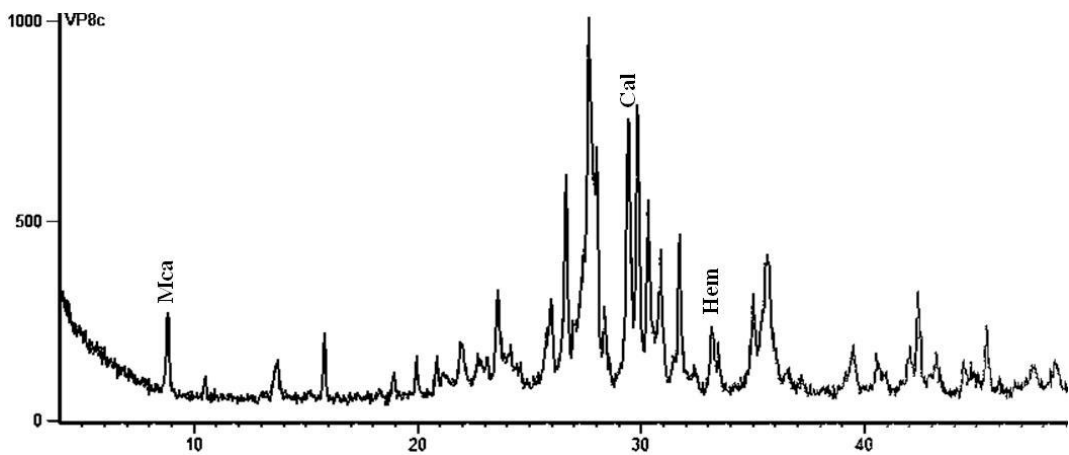


Figure 7.12: XRPD spectrum of VP8 ceramic fragment.

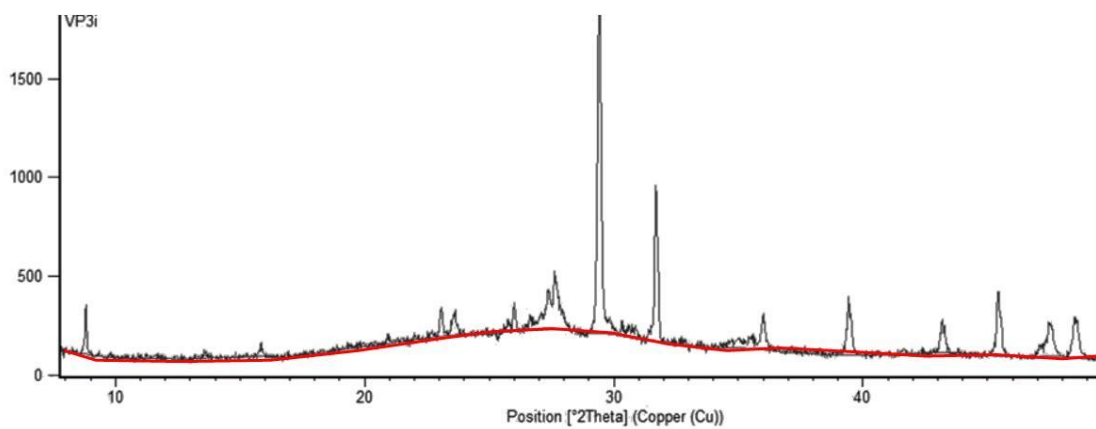


Figure 7.13: example of observed background in XRPD (sample VP3 aggregates).

7.2.4 Micro-morphology and chemical analysis (SEM-EDS)

SEM-EDS analyses were performed in order to support and integrate XRPD results.

As regards binder, results show presence of hydraulic phases called Gel C-A-S-H; (calcium, aluminum, silicate, hydrate), and confirmed gypsum [$\text{CaSO}_4 \cdot 2(\text{H}_2\text{O})$] presence, as XRPD suggested (Figure 7.14).

The Gel C-A-S-H is a result of the reaction between silica and aluminum contained in the “pozzolanic” material (volcanic and ceramic fragments), and calcium hydroxide.

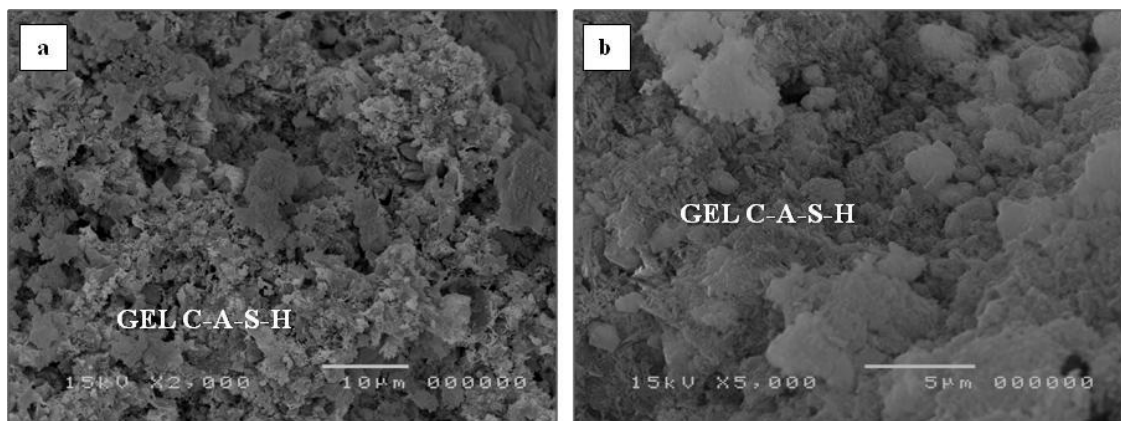


Figure 7.14: SEM images of Gel C-A-S-H: a) sample VP3; b) sample VP5.

In order to obtain major information about the binder’s composition, SEM-EDS microanalysis was carried out on polished thin section on binder and lime lumps present in the mortars (Table 7.4; Figure 7.15). Moreover, Hydraulicity Index (HI), according to Boynton’s formula (Boynton, 1966), was calculated to achieve information on the level of hydraulicity reached by the mortars.

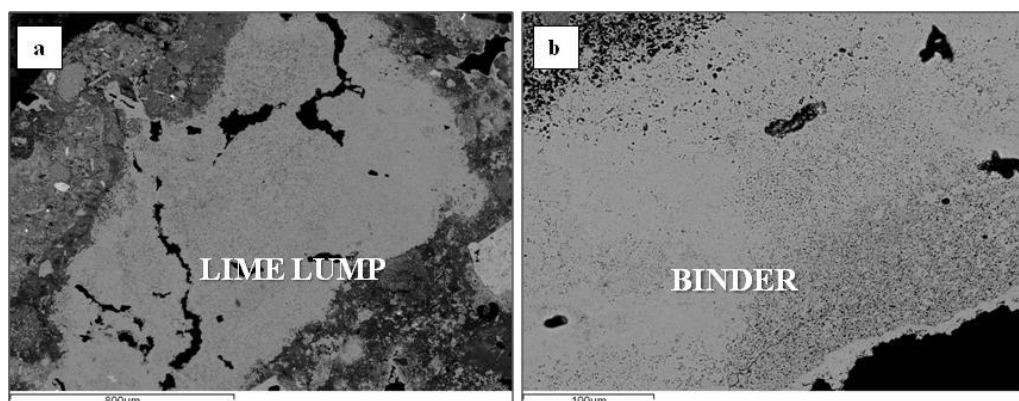


Figure 7.15: BSE-SEM images of a) example of analyzed lime lumps in sample VP9; b) example of analyzed binder in sample VP4.

Lime lumps results composed mainly of CaO with very high values of CaO + MgO in general, between 94.31 and 97.06 % (Table 7.4). Chemical composition of binder shows values of

SiO₂+Al₂O₃ +Fe₂O₃ (9.06 – 19.54 %) higher than in lumps (1.90 – 3.65%) and lower contents of CaO + MgO (78.50 –89.09 %; Figure 7.16).

Table 7.4: Average values of major oxides (wt.%, recalculated to 100%, EDS), lime lumps (L) and binder (B).

wt. %	VP1 L	VP1 B	VP2 L	VP2 B	VP3 L	VP3 B	VP4 L	VP4 B
SiO ₂	1.59	9.56	1.89	9.52	2.42	7.60	1.42	5.84
TiO ₂	0.24	0.41	-	-	-	-	0.35	0.40
Al ₂ O ₃	0.22	5.65	0.95	3.13	0.95	3.95	0.26	3.16
Fe ₂ O ₃	0.80	-	0.65	0.33	0.07	0.70	0.16	0.54
MnO	0.22	-	-	0.11	-	-	-	-
MgO	0.68	7.01	0.26	1.51	2.15	3.08	0.87	1.17
CaO	93.83	75.95	94.65	79.38	92.16	80.25	95.32	86.49
Na ₂ O	0.52	0.23	0.59	0.88	0.56	0.56	0.14	0.41
K ₂ O	0.54	-	0.12	1.25	-	0.49	-	0.45
P ₂ O ₅	-	-	-	0.14	-	-	-	-
V ₂ O ₃	-	-	0.45	-	-	0.44	-	-
BaO	-	-	0.15	-	0.26	0.53	-	-
Cl	0.18	0.37	0.12	0.22	0.52	0.46	0.81	1.41
F	-	-	-	-	-	-	-	-
SO ₃	1.18	0.82	0.18	3.52	0.91	1.96	0.67	0.12
Total	100.00							
SiO₂ +Al₂O₃+Fe₂O₃	2.61	15.21	3.49	12.98	3.45	12.24	2.61	9.54
CaO+MgO	94.51	82.96	94.91	80.89	94.31	83.33	94.51	87.66
HI	0.03	0.18	0.04	0.16	0.04	0.15	0.03	0.11

wt. %	VP5 L	VP5 B	VP7 L	VP7 B	VP9 L	VP9 B	VP10 L	VP10 B
SiO ₂	1.11	5.72	1.16	3.36	1.58	9.59	3.02	13.81
TiO ₂	-	-	0.80	-	0.35	-	0.11	0.42
Al ₂ O ₃	0.62	3.20	0.88	5.58	0.20	6.01	0.63	5.73
Fe ₂ O ₃	0.18	0.23	0.52	0.12	0.37	0.31	-	-
MnO	0.23	-	0.16	-	0.31	-	-	-
MgO	12.98	6.57	0.70	0.21	3.30	11.42	9.35	12.86
CaO	84.07	82.70	95.10	88.86	93.34	70.97	85.70	65.64
Na ₂ O	0.33	0.24	0.23	0.23	-	0.17	0.31	0.19
K ₂ O	0.11	-	-	-	-	-	-	-
P ₂ O ₅	0.18	-	0.25	-	0.27	-	0.23	-
V ₂ O ₃	-	0.23	-	0.29	0.06	0.07	0.39	-
BaO	0.20	-	-	-	-	0.33	-	-
Cl	-	0.78	-	0.05	0.23	0.23	-	0.31
F	-	-	-	-	-	-	-	-
SO ₃	-	0.34	0.22	0.30	-	0.89	0.27	1.04
Total	100.00							
SiO₂ +Al₂O₃+Fe₂O₃	1.90	9.15	2.55	9.06	2.15	15.92	3.65	19.54
CaO+MgO	97.06	89.27	95.79	89.08	96.64	82.39	95.05	78.50
HI	0.02	0.10	0.03	0.10	0.02	0.19	0.04	0.25

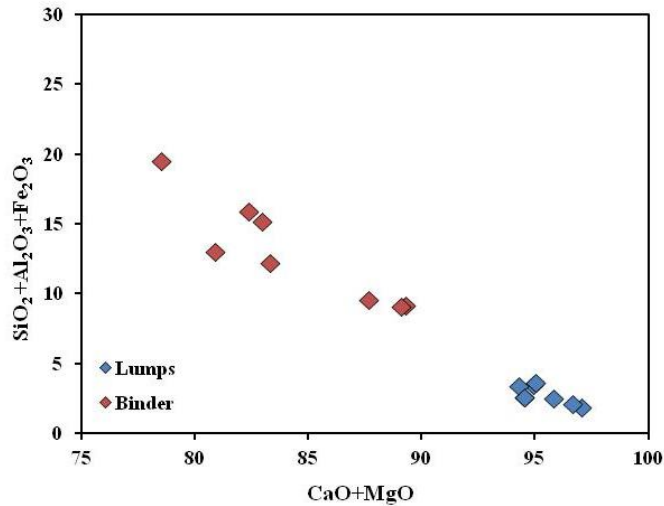


Figure 7.16: CaO + MgO vs. SiO₂ diagram (EDS), lumps and binder.

Hydraulicity Index for lime lumps of mortars shows low values (HI < 0.1, Figure 7.16; Table 7.4), therefore these materials can be considered aerial lime (quicklime) (Zawawi, 2006).

HI of binder between 0.10 – 0.19, thus falling in the field of weakly hydraulic lime (Figure 7.16; Table 7.4).

Mortars from the first and the third building phase (group A and group C) result more hydraulic than mortars of the second building phase (group B).

V10 mortar sample, as already mentioned, is different from the others since it is a floor mortar, showing an high HI value (0.25) and therefore can be considered a moderately hydraulic lime (Table 7.4; Figure 7.17). The differences of HI values can be related to the use of different types of aggregate in the three different building phases.

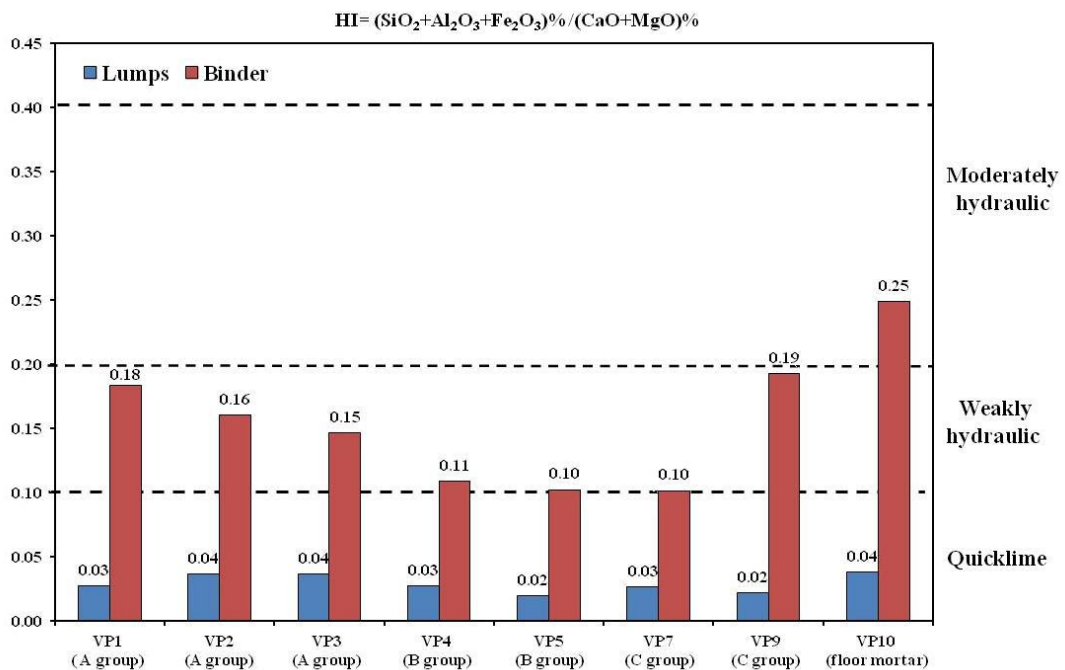


Figure 7.17: Hydraulicity Index (HI), lime lumps (blue) and binder (red) for analyzed mortars.

Regarding volcanic aggregates found in the sample of the first building phase, SEM EDS analyses pointed out the use of the Campania Ignimbrite (CI-WGI, Langella et al., 2013) testified by the peculiar presence of glassy shards, partially devitrified and partially coated by micrometric feldspar crystals (Figure 7.18; Langella et al., 2013).

Moreover, chemical composition of glassy shards (Table 7.5) and pumice (Table 7.6) from aggregate, classified in the TAS diagram, follow the compositional trend of CI (Figure 7.19).

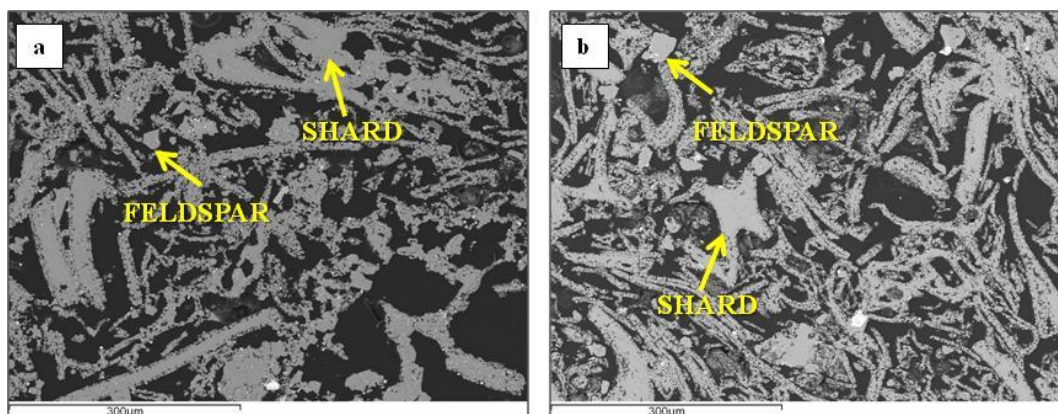


Figure 7.18: BSE-SEM images of glassy shards partially coated by a thin layer of micrometric feldspars a) in sample VP2; b) in sample VP3.

Table 7.5: Major element concentrations (wt.% recalculated to 100%, EDS), glassy shards.

wt.%	VP1	VP2	VP2	VP3
SiO ₂	62.24	62.35	61.59	62.14
TiO ₂	0.64	0.43	0.30	0.55
Al ₂ O ₃	18.95	18.74	18.91	18.53
Fe ₂ O ₃	2.68	2.24	2.61	2.99
MnO	0.22	0.38	0.00	0.24
MgO	0.23	0.19	0.31	0.20
BaO	-	-	-	0.57
CaO	2.24	1.41	1.86	1.40
Na ₂ O	7.47	5.74	5.85	5.83
K ₂ O	4.75	7.55	6.65	7.51
P ₂ O ₅	0.00	0.14	0.20	0.05
V ₂ O ₃	-	-	-	-
BaO	-	-	-	-
SO ₃	0.19	0.12	0.12	0.02
Cl ⁻	0.34	0.70	0.46	0.50
F	-	-	-	-
Total	100.00	100.00	100.00	100.00
Na₂O+K₂O	12.22	13.29	12.51	13.34

Table 7.6: Major element concentrations (wt.% recalculated to 100%, EDS), pumice.

wt. %	VP1	VP1	VP2	VP2	VP3	VP3
SiO ₂	57.10	60.20	61.69	61.66	58.05	58.21
TiO ₂	0.49	0.75	0.88	0.37	0.48	0.12
Al ₂ O ₃	18.50	18.51	18.81	18.61	18.80	18.85
Fe ₂ O ₃	-	0.13	0.41	0.21	-	-
MnO	-	0.04	0.00	0.00	0.23	0.18
MgO	1.56	1.54	0.26	0.31	1.07	0.67
BaO	5.07	6.01	2.76	3.17	4.76	4.16
CaO	4.13	6.62	1.81	1.95	3.51	3.32
Na ₂ O	3.73	3.44	5.18	6.03	3.21	3.63
K ₂ O	8.23	9.87	7.52	7.12	9.54	9.86
P ₂ O ₅	0.35	0.37	-	-	0.30	0.03
V ₂ O ₃	-	-	-	-	-	-
BaO	-	-	-	-	-	-
SO ₃	0.30	0.08	0.13	-	-	-
Cl ⁻	0.46	0.44	0.83	0.82	0.51	0.65
F ⁻	-	-	-	-	-	-
Total	100.00	100.00	100.00	100.00	100.00	100.00
Na₂O+K₂O	11.96	13.30	12.70	13.14	12.75	13.49

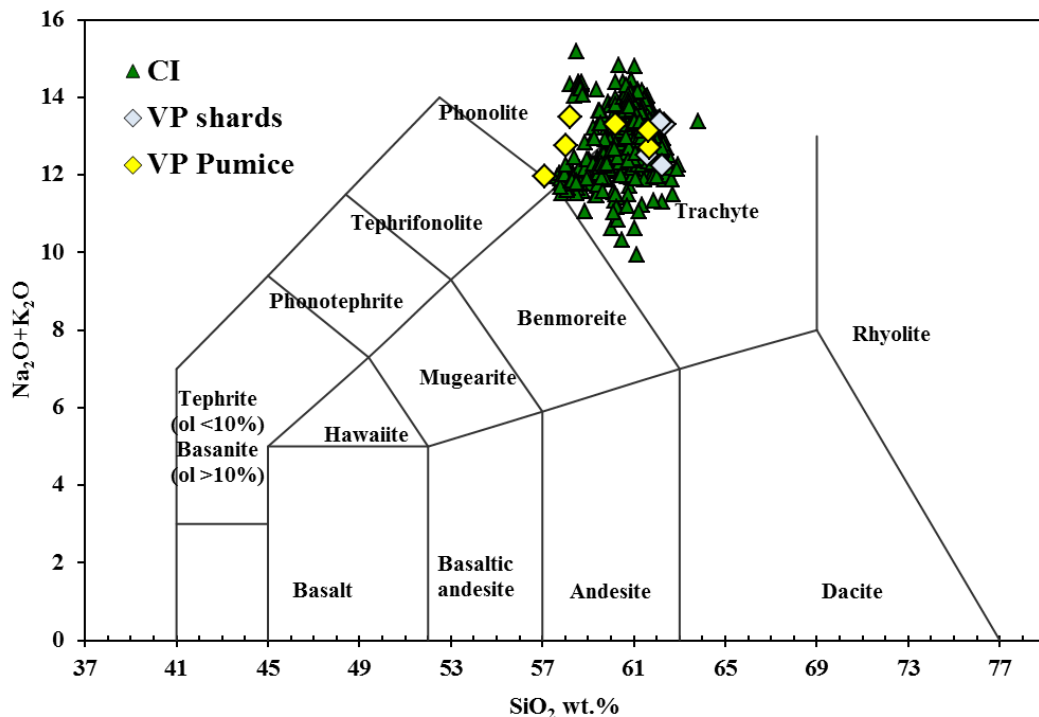


Figure 7.19: Classification of pumice from investigated samples (Le Maitre et al., 1989) and geochemical comparison with Phlegrean (CI) pumice (Morra et al., 2010).

SEM EDS analyses, performed on the volcanic aggregates of the second and third building phase (both dated after AD 79 eruption of Vesuvius), revealed the use of materials from Somma-Vesuvius volcanic complex, as confirmed by the presence of volcanic scoriae containing abundant leucite and garnet fragments (Figure 7.20a-b), both in pumice and binder, typical of these volcanic products (Santacroce et al., 2003).

Moreover, chemical composition of pumice (Table 7.7) from these two building phases, classified in the TAS diagram (Figure 7.21), follow the compositional trend of pumice ascribed to the 79 Vesuvius' eruption.

In addition, also chemical composition of analyzed garnet (calculated following Locock, 2008; Table 7.8), a solid solution between andradite (48.98 - 58.38 mol%) and grossular (25.91- 30.46 mol%), indicated that those minerals are definitely similar to those from Somma-Vesuvio (andradite 46-70 mol% and grossularia 16-45 mol%; Scheibner et al., 2007 and data on garnets from intrusive Somma-Vesuvius rocks. L. Melluso, personal communication).

Moreover, the chemical compositions of glassy shards and pumice, plotted in the TAS diagram, follow the compositional trend of the CI.

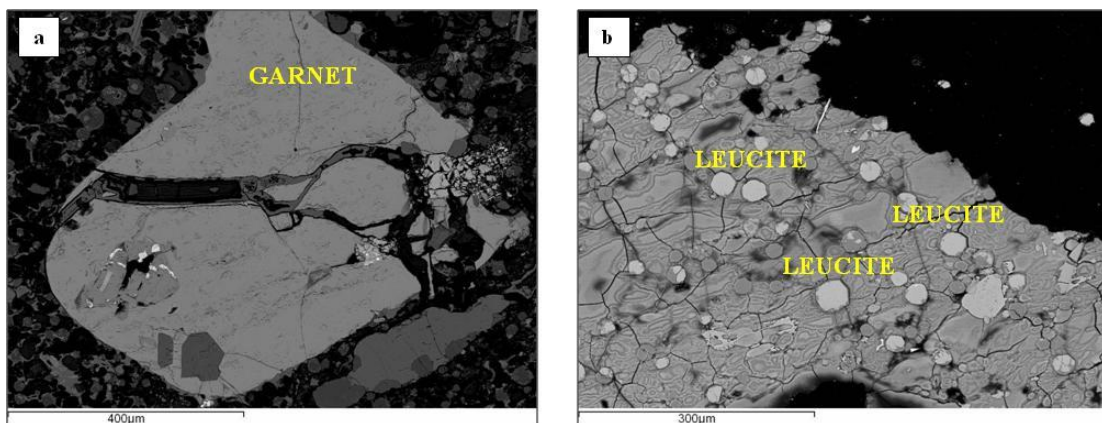


Figure 7.20: BSE-SEM images, a) garnet in VP7 sample; b) leucite bearing scoria in VP4 sample.

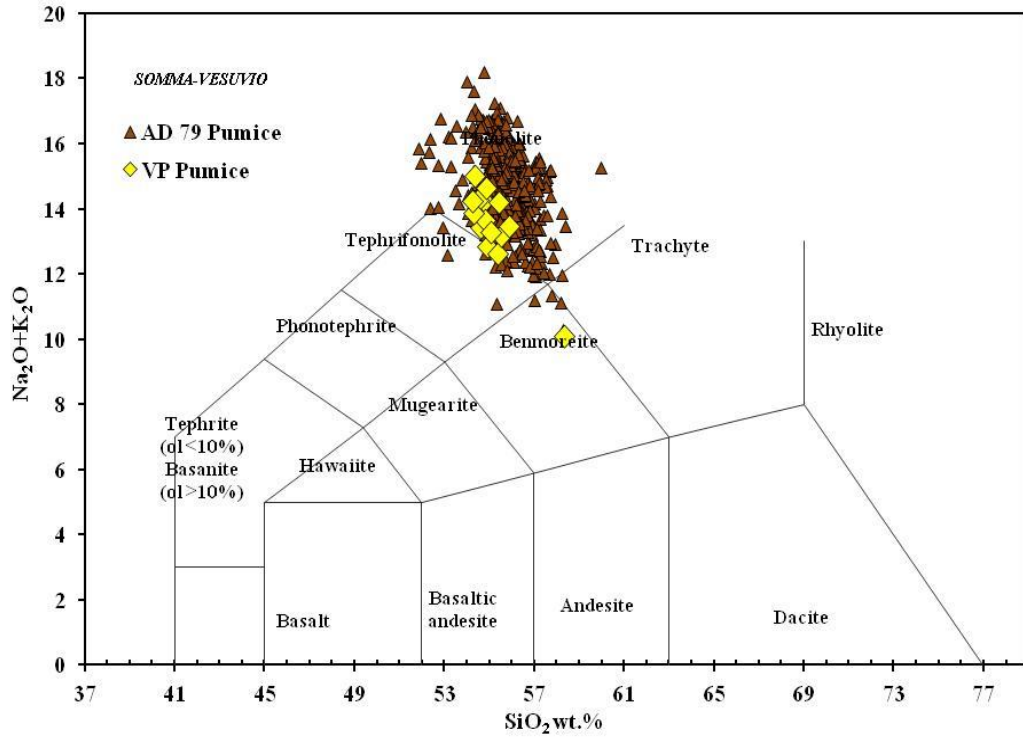


Figure 7.21: Classification of pumice from investigated samples (Le Maitre et al., 1989) and geochemical comparison with Somma-Vesuvius (AD 79) pumice (Morra et al., 2010).

Table 7.7: Major element concentrations (wt.% recalculated to 100%, EDS), pumice.

wt. %	VP4	VP4	VP5	VP5	VP6	VP6	VP7	VP7
SiO ₂	54.93	54.60	54.79	54.53	55.38	58.35	54.88	55.43
TiO ₂	0.29	0.71	0.16	0.38	0.46	0.33	0.04	0.34
Al ₂ O ₃	20.63	20.47	20.55	20.31	21.13	22.97	20.98	20.45
Fe ₂ O ₃	0.18	0.36	0.02	-	0.23	-	-	0.34
MnO	-	-	0.17	0.27	-	0.03	0.06	0.13
MgO	0.38	0.44	0.60	0.50	0.66	0.10	0.34	0.44
BaO	3.64	3.09	3.39	3.48	4.21	1.72	4.06	3.48
CaO	5.22	5.32	4.76	4.88	4.75	5.52	4.14	4.29
Na ₂ O	6.06	6.45	5.12	5.01	6.10	4.99	6.21	5.86
K ₂ O	6.77	6.98	9.11	9.26	6.50	5.09	8.43	8.32
P ₂ O ₅	0.28	0.24	-	0.18	0.18	-	0.18	0.15
V ₂ O ₃	-	-	-	-	-	-	-	-
BaO	-	-	-	-	-	-	-	-
SO ₃	0.14	0.46	-	0.10	0.11	0.07	-	0.05
Cl ⁻	0.92	0.58	0.62	0.66	0.71	0.30	0.75	0.70
F ⁻	-	-	-	-	-	-	-	-
Total	100.00	100.00	100.00	100.00	100.00	100.00	100.00	100.00
Na ₂ O+K ₂ O	12.83	13.43	14.23	14.27	12.60	10.09	14.65	14.18

wt. %	VP8	VP8	VP9	VP9	VP10	VP10	VP10	VP10
SiO ₂	55.63	54.85	55.54	54.32	54.37	54.25	55.09	55.91
TiO ₂	0.50	0.45	0.52	0.35	0.48	0.53	0.59	0.21
Al ₂ O ₃	21.02	21.01	20.47	20.53	21.00	20.02	20.56	20.40
Fe ₂ O ₃	-	0.47	0.17	0.24	0.04	0.18	0.26	0.07
MnO	0.14	-	-	0.17	0.22	-	-	-
MgO	0.34	0.43	0.67	0.56	0.51	0.64	0.40	0.49
BaO	3.28	3.68	3.37	3.85	3.46	4.03	3.56	3.56
CaO	4.70	4.29	4.79	4.92	3.92	4.87	5.29	4.87
Na ₂ O	6.00	6.15	6.68	6.73	5.80	5.35	6.55	6.87
K ₂ O	7.23	7.50	6.47	7.14	9.19	8.88	6.73	6.60
P ₂ O ₅	-	0.15	0.15	0.27	0.04	0.10	0.02	-
V ₂ O ₃	-	-	-	-	-	-	-	-
BaO	-	-	-	-	-	-	-	-
SO ₃	0.22	0.16	0.22	0.04	0.21	0.18	0.13	0.07
Cl ⁻	0.89	0.86	0.91	0.68	0.62	0.90	0.75	0.65
F	-	-	-	-	-	-	-	-
Total	100.00							
Na₂O+K₂O	13.23	13.65	13.15	13.87	14.99	14.23	13.28	13.47

Table 7.8: chemical composition (wt.%, EDS) of garnets.

	VP6 garnet	VP6 garnet	VP8 garnet	VP9 garnet	VP5 garnet	VP5 garnet
SiO ₂	35.64	34.99	35.41	35.80	35.22	34.39
TiO ₂	2.97	2.93	2.60	2.54	3.02	2.17
Al ₂ O ₃	8.53	8.49	9.02	8.97	8.99	8.54
Cr ₂ O ₃	-	-	-	-	0.15	-
V ₂ O ₃	-	0.19	0.28	0.55	-	0.16
FeO / FeO _{tot}	17.81	18.59	17.16	18.13	17.81	18.11
MnO	1.38	1.08	1.30	1.34	1.06	1.45
MgO	0.20	0.20	0.23	0.17	0.23	0.36
CaO	31.19	31.10	31.55	32.60	31.23	31.54
Na ₂ O	0.02	0.17				
Total (calc)	97.74	97.74	97.54	100.09	97.72	96.71
Recalculated (wt%)						
final FeO	3.50	2.42	2.56	1.65	3.34	0.56
final Fe ₂ O ₃	15.90	17.98	16.23	18.31	16.09	19.50
final MnO	1.38	1.08	1.30	1.34	1.06	1.45
final Mn ₂ O ₃	0.00	0.00	0.00	0.00	0.00	0.00
Total	99.33	99.55	99.18	101.92	99.34	98.66
End-members						
<i>Schorlomite-Al</i>	4.14%	6.82%	5.17%	7.10%	5.96%	6.73%
Morimotoite	9.71%	1.74%	5.68%	1.04%	6.68%	-
NaTi garnet	0.16%	1.33%	-	-	-	-
Goldmanite	-	0.63%	0.91%	1.76%	-	0.52%
Uvarovite	-	-	-	-	0.47%	-
Spessartine	3.18%	2.50%	2.99%	3.02%	2.45%	3.38%
Pyrope	0.80%	0.80%	0.91%	0.69%	0.93%	1.47%
Almandine	4.75%	4.93%	3.93%	3.32%	5.39%	1.30%
Grossular	28.28%	25.91%	30.46%	28.05%	28.60%	27.37%
Andradite	48.98%	55.35%	49.94%	55.02%	49.50%	58.38%
Remainder	0.00%	0.00%	0.00%	0.00%	0.00%	0.87%
Total	100.00%	100.01%	99.99%	100.00%	99.98%	100.02%
Quality Index	Superior	Superior	Superior	Superior	Superior	Excellent

*The quality index represents the quality of a garnet analysis, calculated with Locock file (Locock, 2008)

In order to confirm the representativeness of the analyses carried out on pumice and glassy shards for the investigation, alteration indexes such as: CIA (Chemical Index of Alteration), WIP (Weathering Index of Parker) and W were calculated.

Pumice show values of CIA between 42.34 – 49.16, values of WIP between 103.62– 142.87, values of W index between 1.89 – 15.61 (Table 7.9).

Glassy shards were found only in volcanic aggregates of the first building phase and these materials show values of CIA between 46.84 – 48.33, values of WIP between 115.58 – 121.67, values of W index between 7.11 – 10.71 (Table 7.10).

These results confirmed that analyzed glassy shards and pumice are to be considered not altered, so the performed analysis and subsequent classification through TAS diagram could be considered accurate.

Another confirmation of this hypothesis is provided also by the diagrams using such indexes: A – CN – K (Figure 7.22), WIP/ CIA (Figure 7.23) and MFW (Figure 7.24).

Table 7.9: CIA, WIP and W index values for analyzed pumice.

	VP1	VP1	VP2	VP2	VP3	VP3	VP4	VP4	VP5	VP5	VP6
CIA	45.06	43.89	48.53	46.78	46.10	45.39	43.49	42.38	43.27	42.81	45.12
WIP	119.10	123.01	116.94	121.83	122.50	127.50	127.74	133.48	138.39	138.62	125.32
W	13.70	15.61	12.90	8.21	15.00	6.50	5.04	6.84	4.40	6.56	7.86
	VP6	VP7	VP7	VP8	VP8	VP9	VP9	VP10	VP10	VP10	VP10
CIA	49.16	43.83	43.60	44.49	44.66	43.38	42.52	44.11	42.34	42.62	42.76
WIP	103.62	140.40	136.85	129.63	132.53	130.61	136.79	142.87	138.89	132.10	133.18
W	3.52	1.89	5.94	6.45	6.87	6.88	5.72	7.43	8.20	6.61	4.21

Table 7.10: CIA, WIP and W index values for analyzed glassy shards.

	VP1	VP2	VP2	VP3
CIA	46.84	48.14	48.33	47.76
WIP	115.58	121.20	116.09	121.67
W	8.25	8.07	7.11	10.71

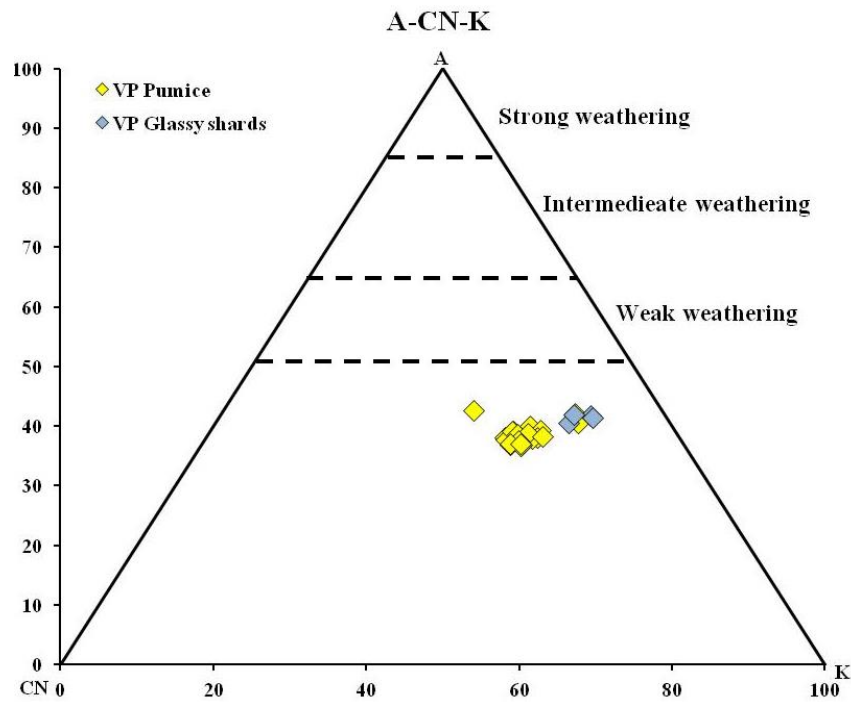


Figure 7.22: A-CN-K (Al_2O_3 — $\text{CaO}+\text{Na}_2\text{O}$ — K_2O) diagram (Nesbitt and Young, 1982) for *Villa del Pezzolo* pumice and glassy shards. The left side of the diagram shows the range of CIA values of pumice.

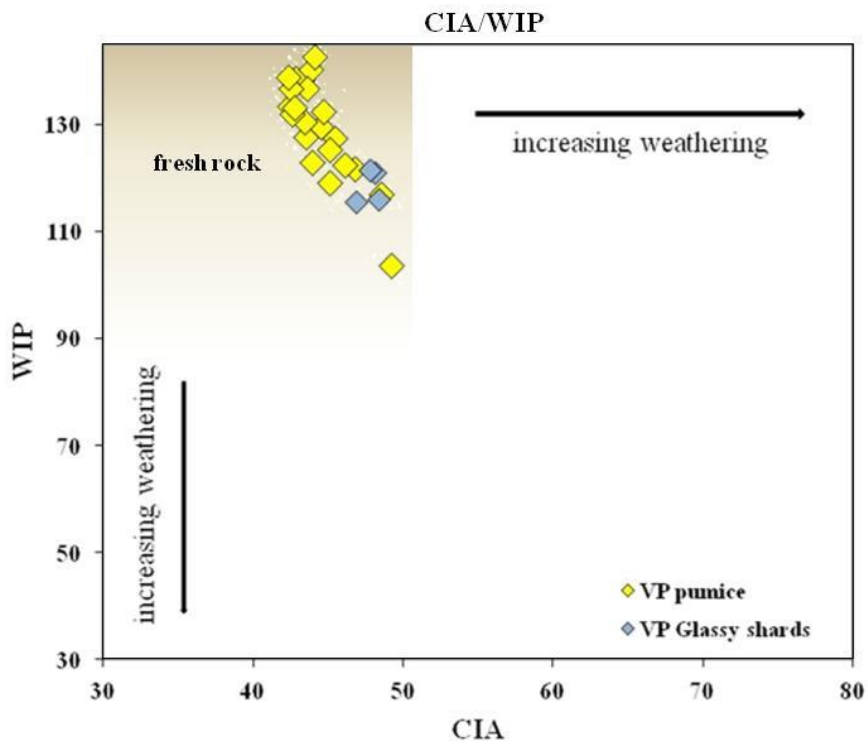


Figure 7.23: Relationship between two weathering proxies WIP and CIA (Bahlburg and Dobrzinski, 2011) for *Villa del Pezzolo* pumice and glassy shards.

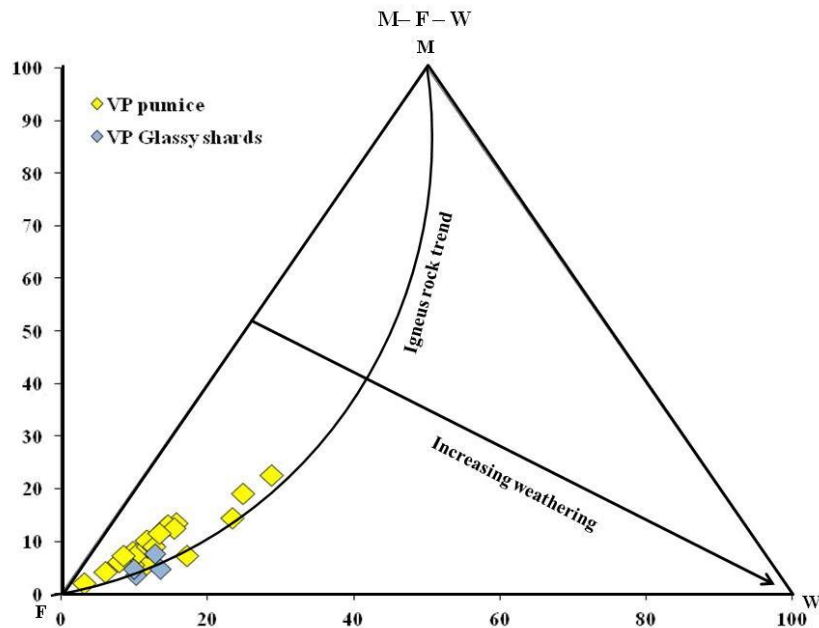
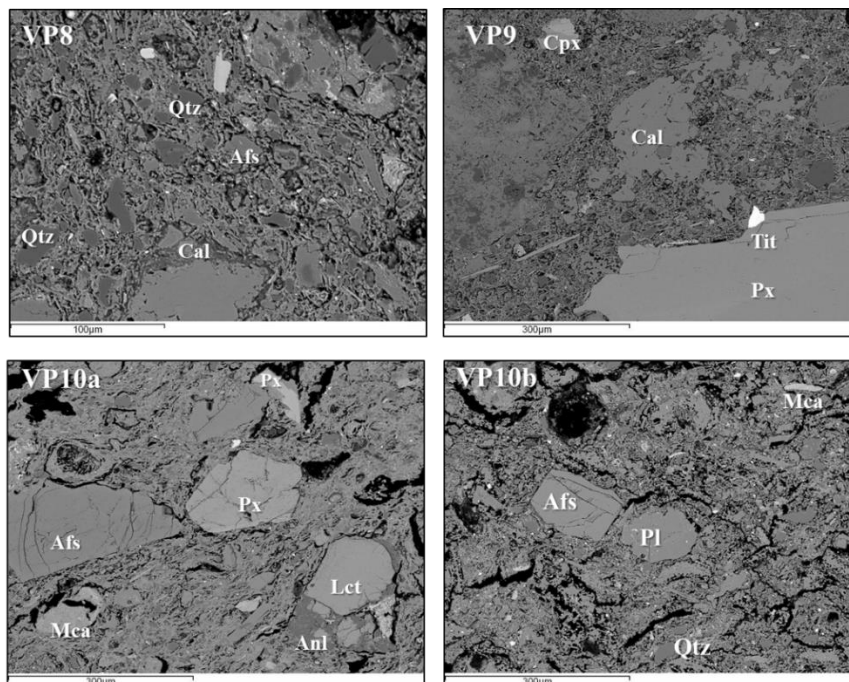


Figure 7.24: Weathering trends, MFW diagram (Ohta and Arai, 2007) for Villa del Pezzolo pumice and glassy shards.

As regard ceramic fragments found in the samples of third building phase, they show often mineralogical and textural differences as suggest by thin section observation. SEM EDS microanalysis confirmed these differences (Figure 7.25), testified also by different CaO concentration in clayey raw material (CaO > 6 wt% - calcareous clay; CaO < 6 wt% - non calcareous clay; Maniatis and Tite, 1981; Table 7.11).



* Cal: calcite; Qtz: quartz; Afs: alkalifeldspar; Pl: plagioclase; Lct: leucite; Anl: analcime; Tit: titanite; Cpx: clinopyroxene; Mca: mica.

Figure 7.25: BSE-SEM images of different types of ceramic fragments with mineralogical composition.

Table 7.11: Chemical composition (wt. % recalculated to 100%, EDS), of matrix in the representative ceramic fragments.

wt. %	SiO ₂	TiO ₂	Al ₂ O ₃	Fe ₂ O ₃	MnO	MgO	*CaO	Na ₂ O	K ₂ O	P ₂ O ₅	V ₂ O ₃	BaO	SO ₃	Cl ⁻	F ⁻	Total
VP8	49.59	0.37	18.09	6.82	0.19	5.04	14.68	1.03	2.60	0.17	0.16	0.57	-	0.09	-	100.00
VP9	56.35	0.76	18.30	2.39	0.10	1.14	10.50	3.50	7.09	0.08	0.13	-	0.17	0.07	-	100.00
VP10	60.42	1.06	20.43	4.94	-	2.16	8.13	2.39	4.86	0.12	-	0.12	0.03	0.82	-	100.00
VP10	57.16	0.49	18.78	5.73	0.18	2.82	4.37	1.09	3.44	0.24	0.13	-	-	0.10	-	100.00

*CaO > 6 wt. – calcareous clay; CaO < 6 wt% - non calcareous clay

7.2.5 XRF analysis

XRF analyses were conducted on representative samples of the different building phase (VP2, VP5, VP8, VP9), and results are reported in Table 7.12.

Representative diagrams were selected to highlights the similarities or differences between the investigated mortars.

All mortars in the SiO₂/CaO diagram (Figure 7.26a) show wide variation in the CaO and SiO₂ oxides. The samples VP2 and VP5 show the lowest CaO (11.24 – 12.04 wt.%) and the highest SiO₂ (34.25 – 34.64 wt.%) content. The VP8 sample has the highest CaO and the lowest and SiO₂ (19.08 wt.% and 26.59 wt.%, respectively).

Al₂O₃/Fe₂O₃ diagram (Figure 7.26b) for VP2 and VP5 mortars shows chemical similarity (2.62 – 3.34 wt.% Fe₂O₃; 8.63 – 12.05 wt.% Al₂O₃); VP8 mortars is the most different (2.62 wt.% Fe₂O₃; 8.63 wt.% Al₂O₃).

The SO₃/Cl diagram (Figure 7.26c) shows that the mortars have generally similar concentration of SO₃ (0.10 – 1.56 wt%), but different concentration of Cl.

VP9 sample is different compared to others mortars due to its higher SO₃ (1.56 wt.%) and lowest Cl (43218 ppm) content.

Table 7.12: Chemical analysis (XRF), major oxides and trace elements, mortars.

wt. %	SiO ₂	TiO ₂	Al ₂ O ₃	Fe ₂ O ₃	MnO	MgO	CaO	Na ₂ O	K ₂ O	P ₂ O ₅	SO ₃	SrO	LOI
VP2	34.64	0.38	11.61	3.34	0.11	2.48	11.24	6.67	3.93	0.08	0.39	0.07	19.25
VP5	34.25	0.33	12.05	3.04	0.10	2.91	12.04	5.05	5.55	0.15	0.10	0.11	19.81
VP8	26.59	0.31	8.63	2.62	0.08	3.68	19.08	4.26	2.90	0.15	0.23	0.08	26.29
VP9	30.51	0.34	10.24	2.95	0.10	4.12	14.62	5.17	2.97	0.16	1.56	0.10	22.67

ppm	Cr	Zn	Ba	Br	Cl	Co	F	Ni	Pb	Cu	V
VP2	96	146	476	155	56952	52	-	95	-	316	0
VP5	101	144	1124	97	42930	55	-	103	-	255	120
VP8	126	165	768	101	49335	54	-	96	-	147	197
VP9	107	152	947	-	43218	-	-	75	-	212	193

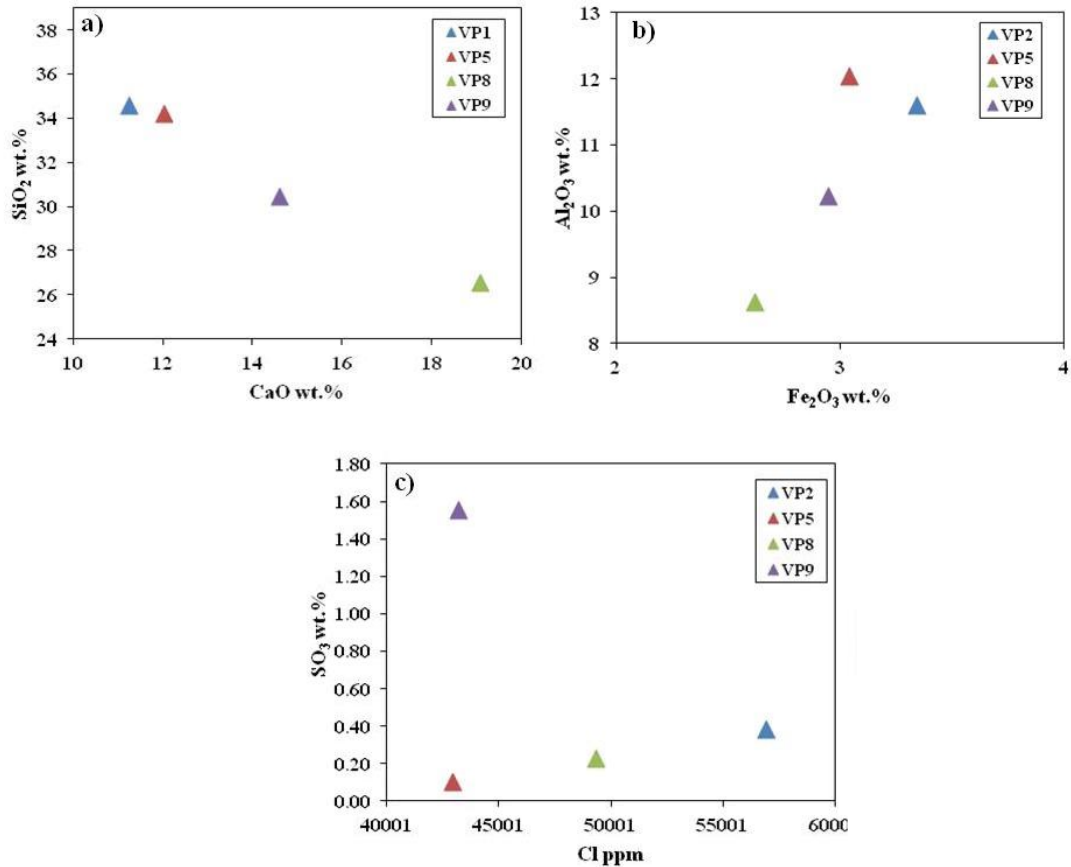


Figure 7.26: Binary diagrams representative of major oxide and trace element composition.

7.2.6 Differential and Gravimetric Thermal Analysis (DTA-TGA)

Thermal analysis is used as a useful tool to characterize hydraulicity of samples mortars, since it easily detects the presence of compounds with hydraulic features and provides fundamental information which allows the identification of the type of mortar.

Table 7.13 reports the percentage of weight loss estimated from the TG–DTG curves within the selected temperature ranges. In the temperature range between 200 and 600 °C the weight loss is due to structurally bound water (SBW) from the hydraulic compounds and, finally, the loss of CO₂ as a consequence of the decomposition of calcium carbonate (CaCO₃), taking place at temperature range between 600 and 850° C (Figure 7.27).

The CO₂ to structurally bound water ratio in relation to CO₂ percentage (% weight loss in the temperature range of 600–850 °C) is shown in Figure 7.28.

From the observation of this plots and comparing our data with data of Moropoulou et al., 2005, mortars can be defined as hydraulic.

Some sample mortars show also the weight loss around 950 °C, and this weight loss above 900 °C could derive from decomposition of sulphates, or to loss of residual water and carbon and/or decomposition of halite (Izzo et al., 2015).

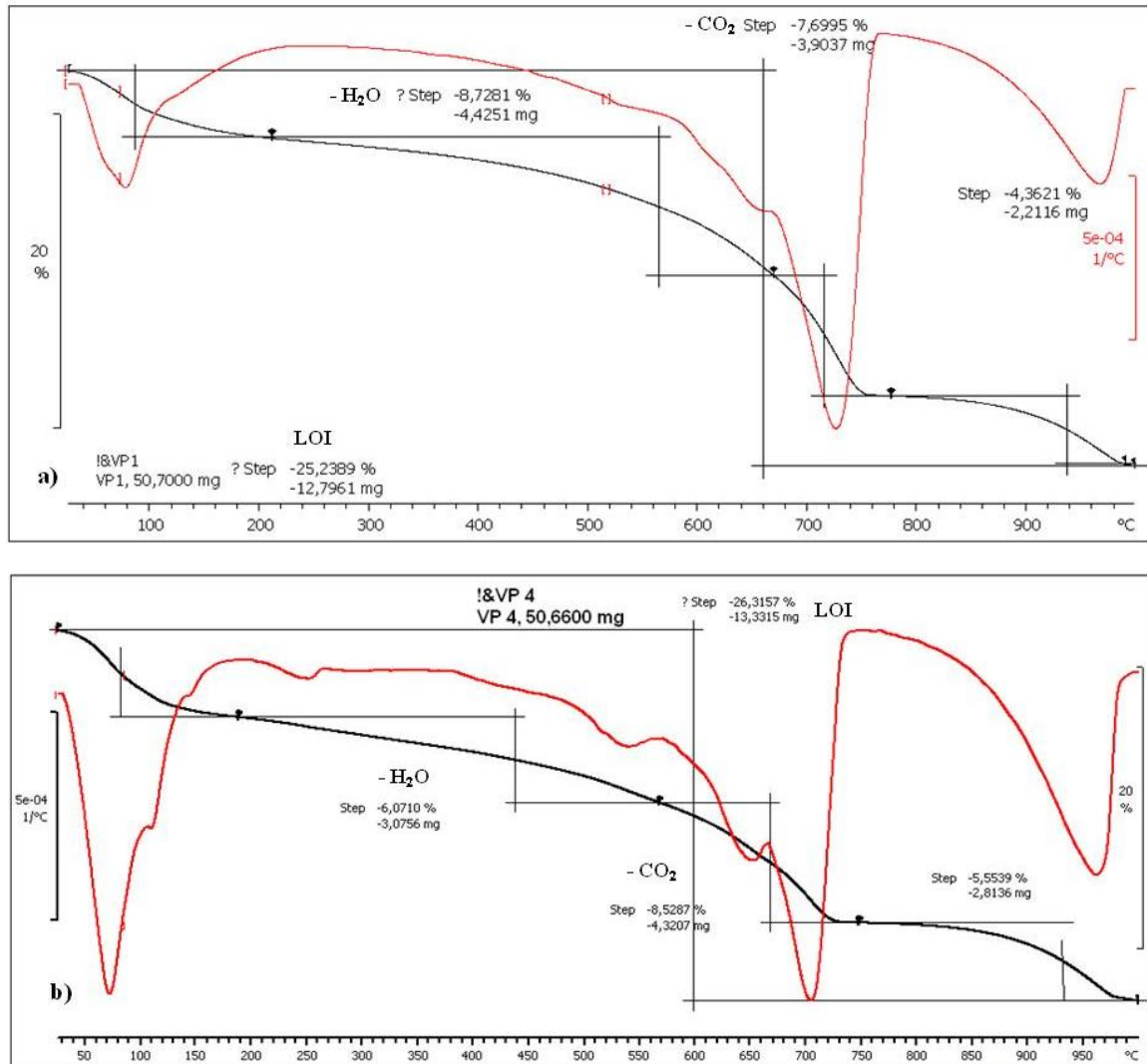


Figure 7.27: DTA-TGA plot of a) VP1 and b)VP4 samples

Table 7.13: Thermal analysis (DTA/DTG) features of investigated sample.

Sample	SBW %	CO ₂ %	CO ₂ /SBW	LOI
VP1	8.72	7.69		25.23
T range (°C)	200-675	675-780	0.88	25-1000
VP2	8.07	3.93		26.39
T range (°C)	200-540	540-740	0.49	25-1000
VP3	10.38	3.10		28.39
T range (°C)	180-660	660-740	0.33	25-1000
VP4	6.07	8.52		26.31
T range (°C)	165-540	540-780	1.40	25-1000
VP5	7.49	2.13		27.25
T range (°C)	200-640	640-745	0.28	25-100
VP7	7.33	3.15		28.10
T range (°C)	180-620	620-760	0.70	25-1000
VP8	9.77	4.33		30.21
T range (°C)	180-630	630-740	0.44	25-1000
VP9	8.98	4.02		26.76
T range (°C)	220-580	580-740	0.45	25-1000
VP10	3.45	15.82		23.78
T range (°C)	160-530	530-780	4.59	25-1000

*SBW = Structural Bound Water, LOI= Loss on Ignition

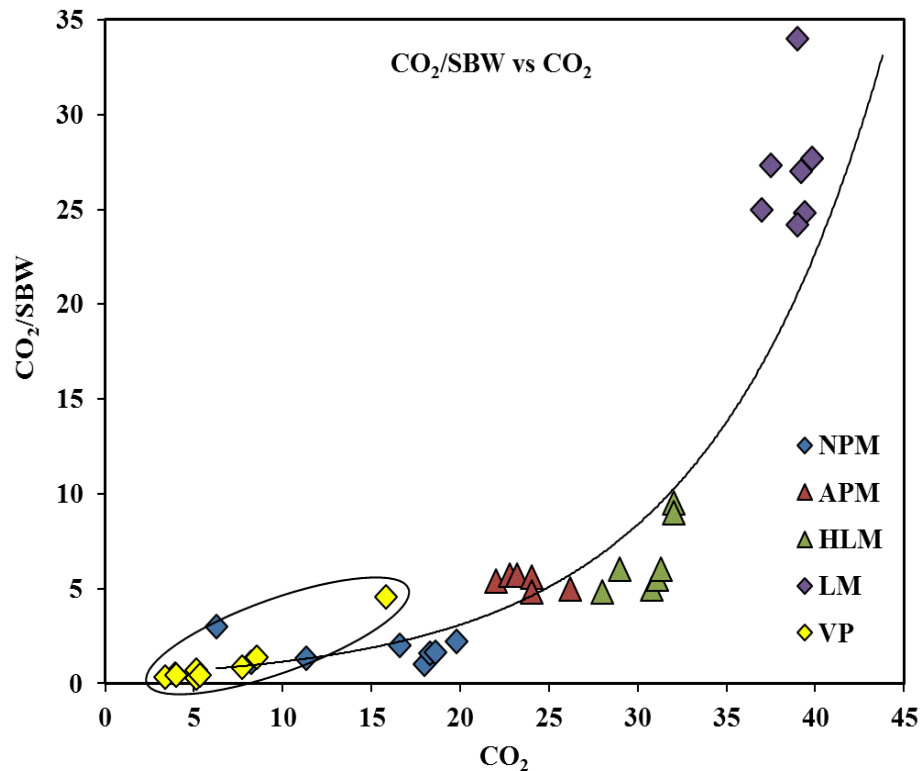


Figure 7.28: CO₂/SBW vs. CO₂ diagram, comparing mortars from Villa del Pezzolo (VP, black circle) and from Moropoulou et al., 2005. (NPM: natural pozzolanic mortars; APM: artificial pozzolanic mortars; HLM: Hydraulic lime mortars; LM: lime mortars).

7.2.7 Mercury intrusion porosimetry (MIP)

Mercury Intrusion Porosimetry (MIP) was employed for the determination of pore size distribution and pore volume, according to ASTM D4404, of representative mortars of the three building phases (VP1, VP5, VP8).

Analyses were performed on three fragments for each samples, and average results are reported in Table 7.14 and in Figure 7.29 and 7.30, where cumulative and relative pore size distributions are shown.

Table 7.14: Porosimetric features (MIP) of mortars.

Sample	VP1	VP5	VP8
Cumulative volume (mm³/g)	262.11	284.97	307.29
Bulk density (g/cm³)	1.64	1.52	1.46
Total porosity (Vol. %)	40.42	42.96	44.65

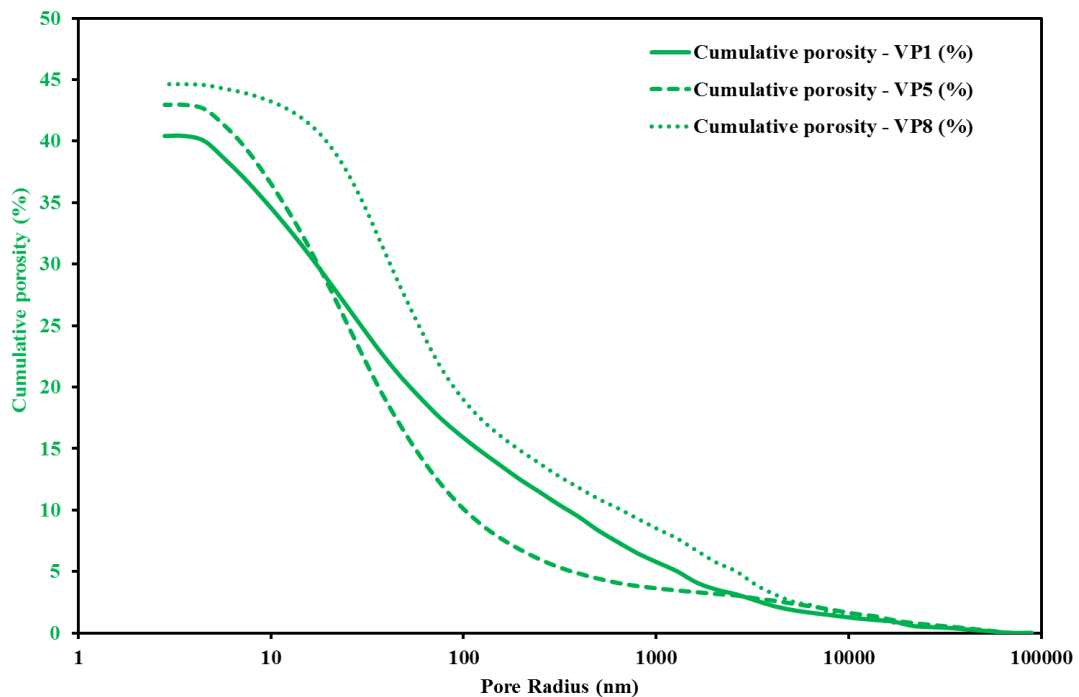


Figure 7.29: Cumulative pore size distribution for VP1, VP5 and VP8 samples.

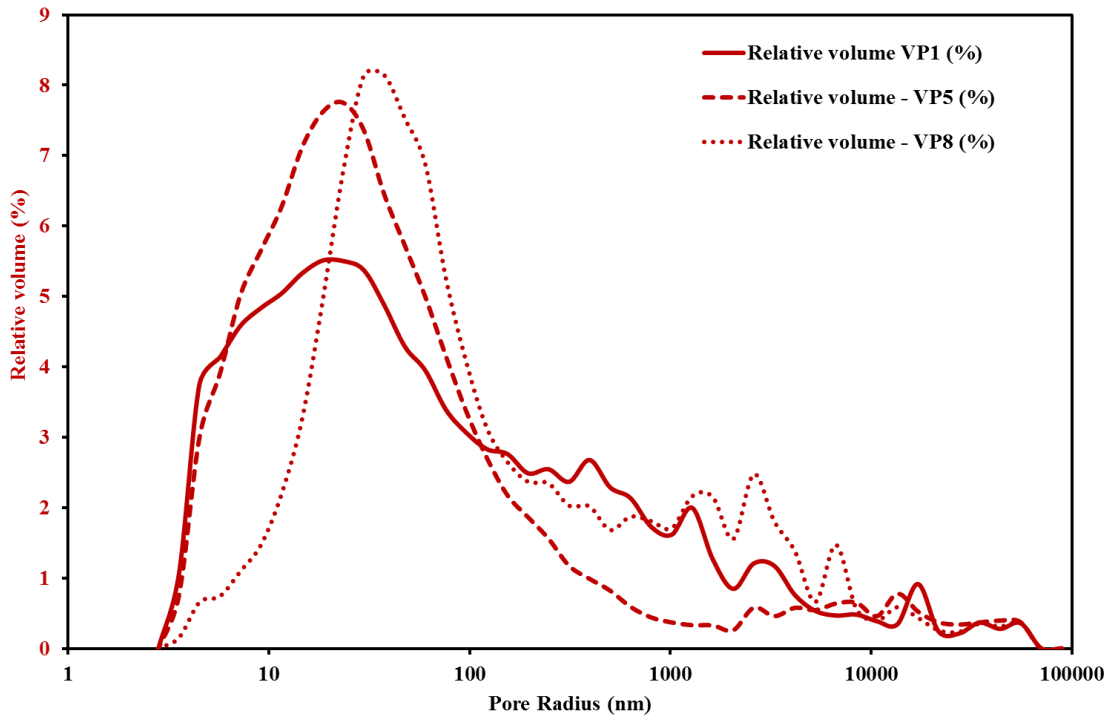


Figure 7.30: Relative pore size distribution in VP1, VP5 and VP8 samples.

Pore sizes of samples fall within the characteristic field of hydration product porosity, usually considered below 100 nm (Figure 4.33) (Metha et al., 2006; Gotti et al., 2008).

Samples show total porosity values between 40% - 43%, unimodal and broadened shape of pore size distribution.

Chapter 8

Standard hydraulic mortar

8.1 Production

Modern hydraulic mortars are artificial products, consisting of a mixture of binder (such as cement and / or lime), water, fine aggregate (e.g. sand) and any additives, that have the property of setting and hardening and/or under water.

The mix proportion has to ensure workability to fresh mortar and mechanical strength after the setting and curing.

A standard hydraulic mortar (according to EN 196-1:2005) is a special type of mortar used to determine the conformity of a cement to a specific class of resistance according to EN 197-1. This is essentially determined by the compressive strength values obtained on mortar specimens mould and stored in accordance with the procedures of standard EN 196-1. The method comprises the determination of the compressive strength of prismatic test specimens (40 mm × 40 mm × 160 mm in size).

In this study the same method of preparation was used. The mix design of realized standard hydraulic mortar (SHM) is: one part of natural hydraulic lime, three parts by mass of CEN Standard sand and one half part of water (water/cement ratio 0.50).

The used natural hydraulic lime, according to UNI EN 459-1, is a lime with hydraulic properties produced by burning more or less argillaceous or siliceous limestones (including chalk), with reduction to powder by slaking with or without grinding. This material has the property of setting and hardening when mixed with water and by reaction with carbon dioxide from the air (carbonation). Hydraulic properties exclusively result from special chemical composition of the natural raw material. Grinding agents up to 0,1% are allowed. Natural hydraulic lime does not contain any other additions.

CEN Standard sand (ISO standard sand) is a natural sand, which is siliceous particularly in its finest fractions. The particles are generally isometric and rounded in shape.

The mortar is prepared by mechanical mixing and is compacted in a mould using a jolting apparatus. The specimens are stored in the mould in a moist atmosphere (**T: 20±1 °C; RH > 90%**) for 24h. After the demoulding, specimens are stored under water until the required age.

The realized SHM was studied after 40 days of curing, while time required to determine the soundness are 28 days (Figure 8.1).



Figure 8.1: Production of standard hydraulic mortar

8.2 Results

Standard hydraulic mortar after reaching the soundness was subjected to thermal analyses (DTA- TGA) and Mercury intrusion porosimetry (MIP).

8.2.1 Differential and Gravimetric Thermal Analysis (DTA-TGA)

Thermal analyses (DTA-TGA) were carried out to classify the level of hydraulicity. The attention, as in the analyzed Roman mortars, was focused on weight loss percentage of H₂O, due to dehydration of calcium silicates and aluminates hydrates, occurring between 200 and 600 °C, representing structural-bound water (SBW) and on decomposition of calcium carbonate (CaCO₃) between 600° and 800° (Figure 8.2).

These percentage and the CO₂/SBW ratio are reported in Table 8.1.

Comparing the obtained data with those from Moropoulou et al. (2005, Figure 8.3), as in analyzed Roman mortars, allowed to classify the SHM as hydraulic. SHM show also a weight loss at about 400 °C, probably related to phyllosilicates decomposition due to the argillaceous nature of the starting limestone.

Table 8.1: Thermal analysis (DTA/DTG) features of SHM mortar

Sample	SBW %	CO ₂ %	CO ₂ /SBW	LOI
SHM	1.69	2.54	2.77	6.53
T range (°C)	200-530	530-770		25-1000

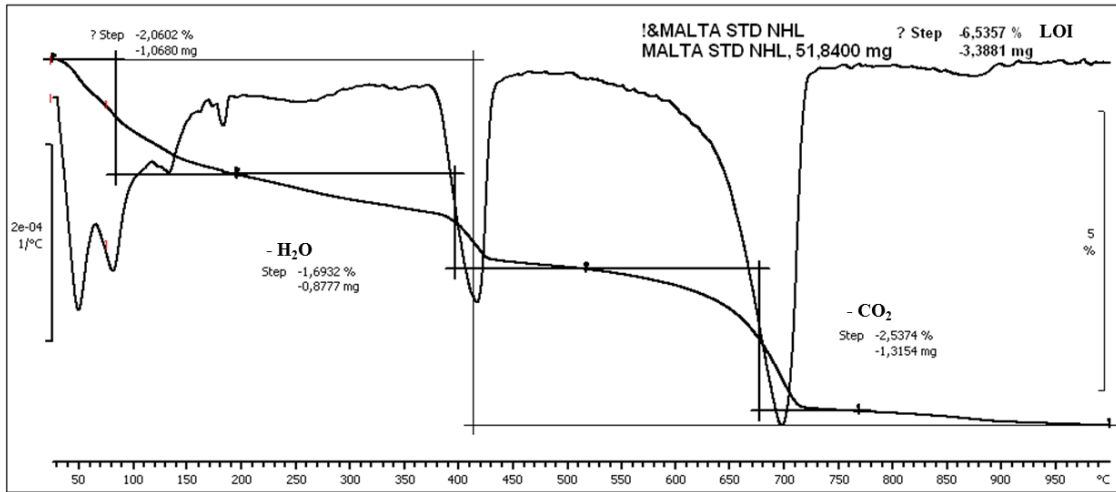


Figure 8.2: DTA-TGA plot of SHM mortar

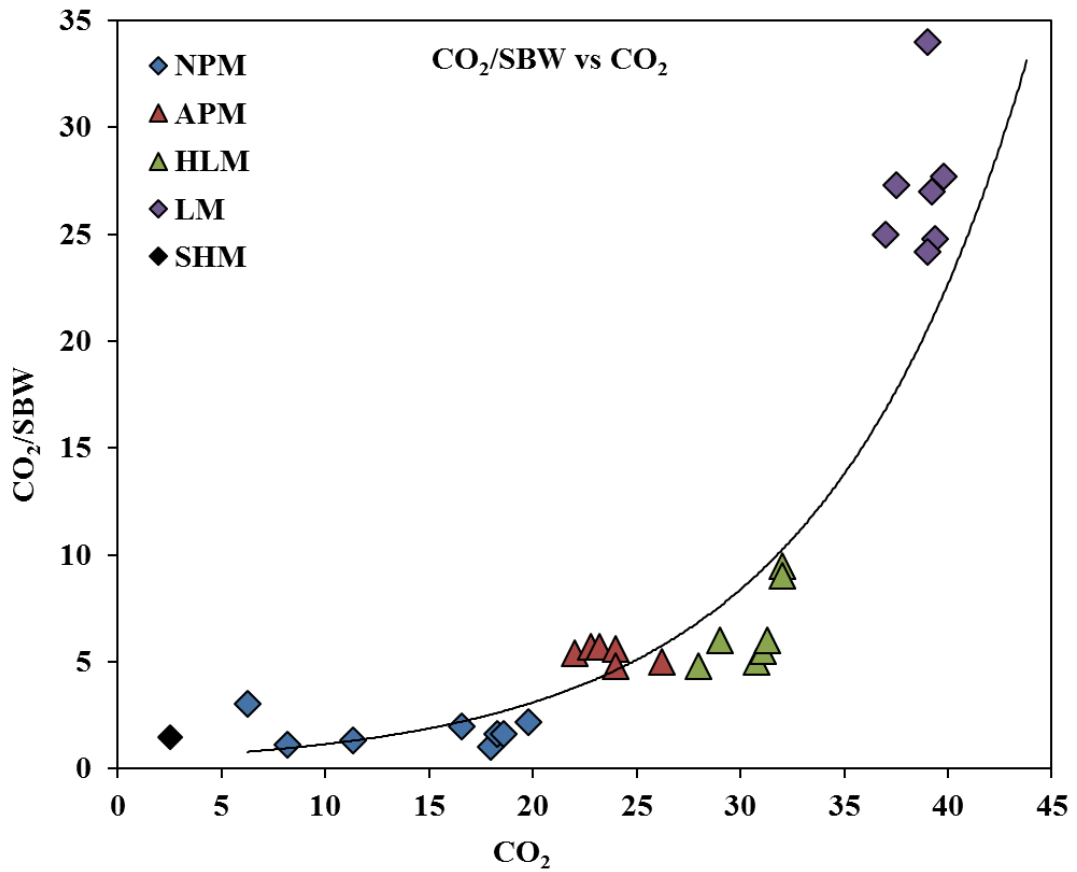


Figure 8.3: Binary CO₂/SBW vs. CO₂ diagram, comparing data from SHM mortar sample and from Moropoulou et al., 2005. (NPM: natural pozzolanic mortars; APM: artificial pozzolanic mortars; HLM: Hydraulic lime mortars; LM: lime mortars; SHM: standard hydraulic mortar)

8.2.2 Mercury intrusion porosimetry (MIP)

Porosity of SHM was evaluated by mercury intrusion porosimetry (MIP), according to ASTM D4404 (Determination of pore volume and pore volume distribution of soil and rock by mercury intrusion porosimetry). Analyses were performed on three fragments, and average results are reported in Table 8.2 and Figure 8.4 and 8.5, where cumulative and relative pore size distributions are shown.

SHM shows values of total porosity equal to 23.88 Vol.% and shows bi-modal and broadened shape of pore size distribution.

Capillary porosity, defined by pores with radii from 10 to 1000 nm, is between 100 and 1000 nm, and represents residual space between cement and aggregate grains that was originally filled with interstitial water; large pores (greater than 1000 nm) generally represent air entrapment (Taylor, 1997).

Table 8.2: Porosimetric features (MIP) of SHM.

Sample	SHM
Cumulative volume (mm ³ /g)	111.05
Bulk density (g/cm ³)	2.16
Total porosity (Vol. %)	23.88

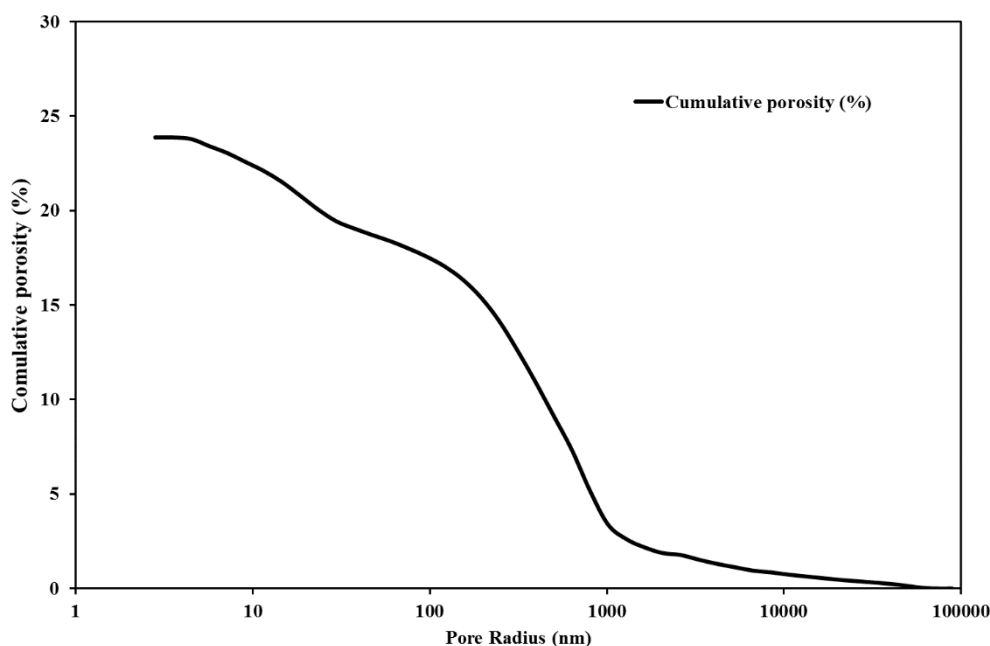


Figure 8.4: Cumulative pore size distribution for SHM mortar

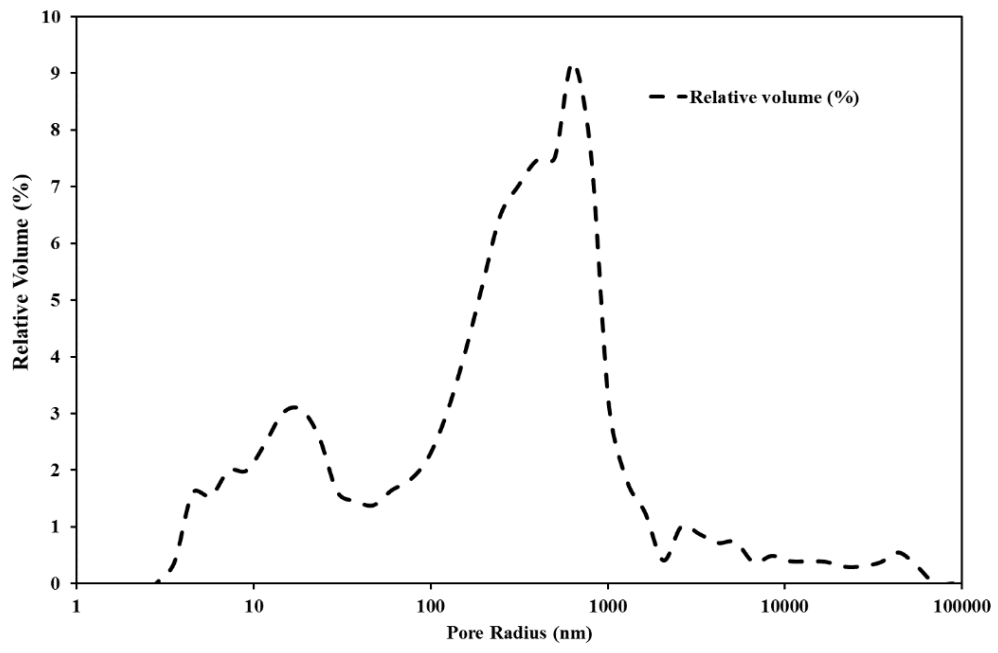


Figure 8.5: Relative pore size distribution in SHM mortar

Chapter 9

Discussions

Mineralogical, petrographical, chemical and physical-mechanical analyses performed on mortars samples showed different mix design.

Bedding mortars result from a mixture of slaked lime, water, fine grained volcanic materials and aggregates of volcanic and carbonate rocks origin (Figure 9.1), whereas, coating and floor mortars, may be considered as a mixture of slaked lime, water, fine grained volcanic and ceramic materials with volcanic, ceramic and carbonatic aggregates (Figure 9.2).

The mix-design of coating and floor mortars is also called *Cocciopesto* or *Opus signinum*. Vitruvius in *De architectura (Liber VIII)*, in fact, describes this mix design, calling it "signinum", as the mix used to waterproof the tanks containing water, the thermal pools and the caverns of aqueducts ².

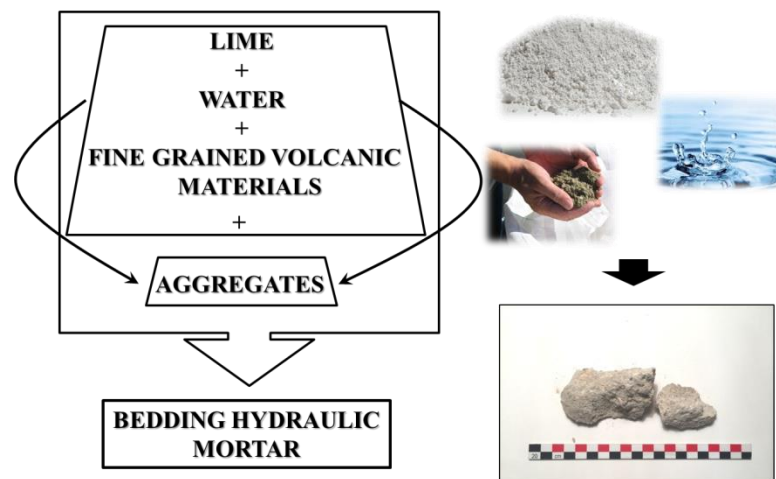


Figure 9.1: Bedding mortars mix-design.

² *Sin autem loca dura erunt aut nimium venae penitus fuerint, tunc signinis operibus ex tectis aut superioribus locis excipiendae sunt copiae. In signinis autem operibus haec sunt facienda. Uti harena primum purissima asperrimaque paretur, caementum de silice frangatur ne gravius quam librarium, calx quam vehementissima mortario mixta, ita ut quinque partes harenae ad duas respondeant. Eorum fossa ad libramentum altitudinis, quod est futurum, calcetur vectibus ligneis ferratis.* (De Architectura, Liber VIII)

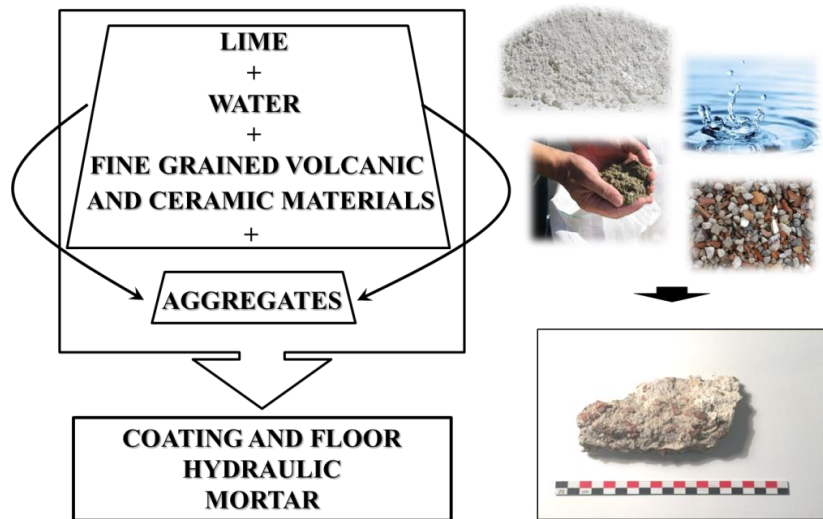


Figure 9.2: Coating and floor mortars mix design.

The hydraulicity of examined mortars was proved by SEM-EDS and thermal analyses.

EDS microanalyses were performed on binder and on lime lumps, which, as specified previously, consist of unreacted lime (Bakolas et al. 1995; Barba et al., 2009). The results show that lime lumps, of all analyzed mortars, are composed mainly of CaO with very high values of CaO + MgO, between 89% and 96%, whereas higher concentrations of $\text{SiO}_2 + \text{Al}_2\text{O}_3 + \text{Fe}_2\text{O}_3$ (9% - 20%) were retrieved in the binder, with respect to the lime lumps (1% - 6%), and lower contents of CaO + MgO (75-86%) (Figure 9.3).

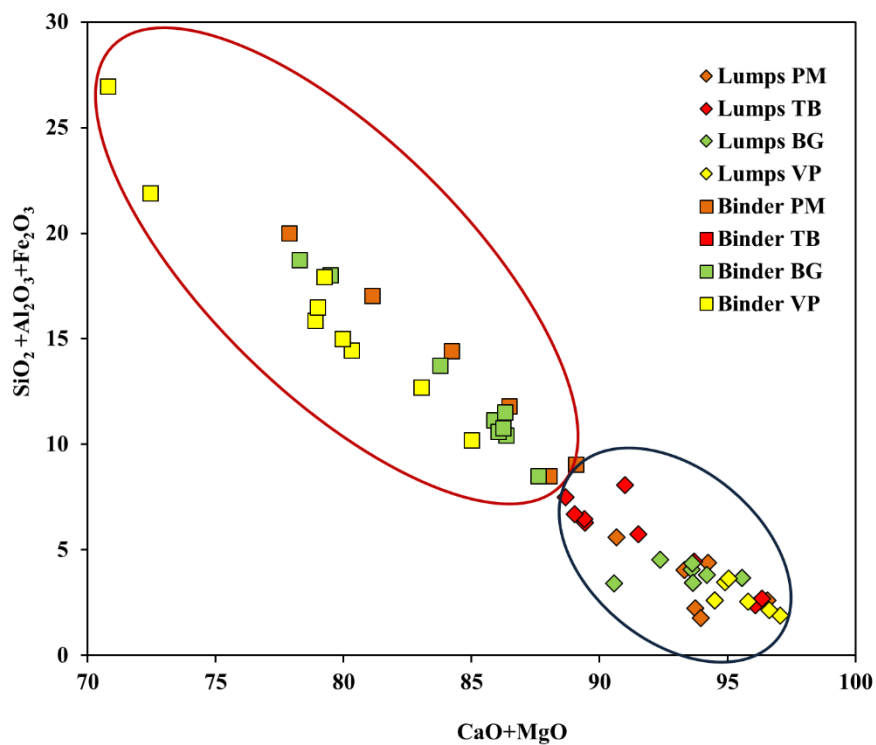


Figure 9.3: CaO + MgO vs. SiO_2 diagram (EDS), lumps (blu circle) and binder (red circle).

As regard the evaluation of Hydraulicity Index (HI), according to Boynton's formula (Boynton, 1980), the lime lumps of the mortars show very low values ($HI < 0.10$), belonging to the field of quicklime (Zawawi, 2006; Figure 9.4), while the binders' HI ranges between 0.10 and 0.38, falling into the fields of weakly-moderately hydraulic (Figure 9.4).

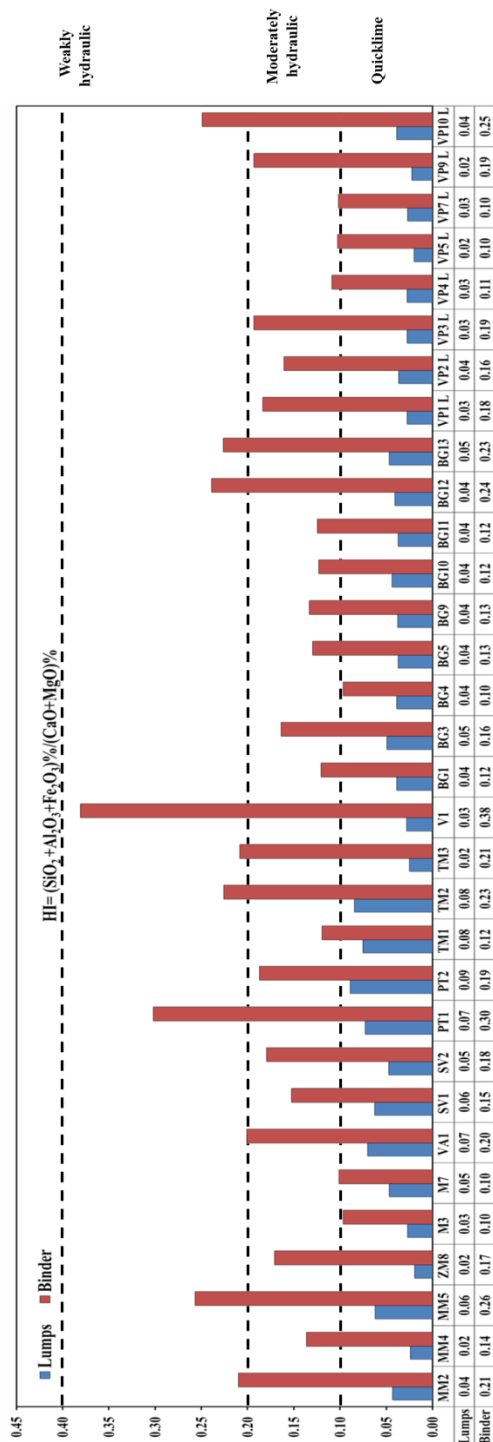


Figure: 9.4: Hydraulicity Index (HI), lime lumps (blue) and binder (red) for all analyzed mortars.

Thus, the results of the HI analysis allowed to consider that hydraulicity of mortars is associated to the abundant presence of materials with “pozzolanic” activity (ceramic and volcanic fragments), which

increases considerably since the reactive silica contained in the “*pozzolana*” reacts with calcium hydroxide, leading to the formation of calcium silicate hydrates: the so-called C-A-S-H phases (calcium, aluminum; silicate, hydrate) (De Luca et al., 2015).

Furthermore, coating and floor mortars ($0.12 \leq HI \leq 0.38$) are more hydraulic than bedding mortars (M3; M5; M7; BG4; BG10; BG11; $0.10 \leq HI \leq 0.12$) due to the presence of ceramic fragments.

In addition, the composition of the lime lumps confirms, once again, what stated in the ancient texts: Pliny the Elder, in *Historia Naturalis*, commented on the risk of skimping on lime in a mortar, specifying that lime made from white limestone is preferable. In particular, lime deriving from hard limestones (non-porous, and free from cracks; Aucelli et al., 2016) turned to be more useful to produce concrete works (*structurae*), while, those deriving from porous stone is better for wall plaster. Therefore, he disapproved the use of lime made from **silex** for both purposes. Moreover, he suggested that it is more useful to produce lime from quarried stone rather than using stones taken from riverbanks³.

Thermal analyses were also performed to evaluate the total (binder plus aggregates) hydraulic features of these materials. This technique was used by many authors to study and classify ancient and modern mortars on the basis of their relative contents of gypsum, carbonates and hydraulic compounds analyses (Moropoulou et al. 1995; 2005; Bonazza et al., 2013). The investigated mortars (fraction <63 μm) show a progressive loss of mass in the range 20–1000°C. In agreement with literature data, particular attention was paid in the 200–600°C range of temperature, where the percentage of mass losses may be entirely attributed to the water fraction chemically bound to hydraulic phases (C–A–S–H), whereas at temperature higher than 600°C, the percentage of mass loss is essentially due to the decomposition of carbonates.

Using the obtained data CO_2/SBW ratio was calculated, and according to Moropoulou et al. 2005 all analyzed mortars can be classified as highly hydraulic.

In particular examined mortars fall in the field of of natural pozzolanic mortars (Figure 9.5).

³ *Calcem e vario lapide Cato censorius inprobat; ex albo melior. quae ex duro, structurae utilior; quae ex fistuloso, tectoriis; ad utrumque damnatur ex silice. utilior eadem effosso lapide quam ex ripis fluminum collecto, utilior e molari, quia est quaedam pinguior natura eius.* (Historia naturalis, 36)

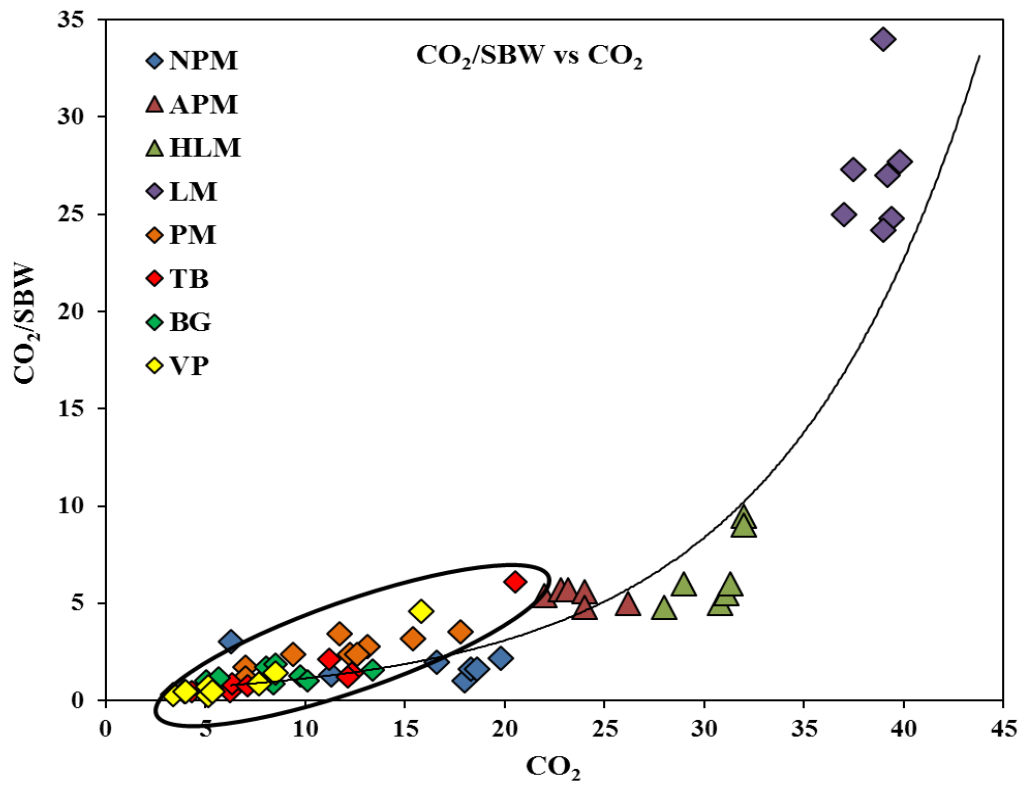


Figure 9.5: CO₂/SBW vs. CO₂ diagram, comparing data from analyzed Roman mortars (black circle) and from Moropoulou et al., 2005. (NPM: natural pozzolanic mortars; APM: artificial pozzolanic mortars; HLM: Hydraulic lime mortars; LM: lime mortars; PM: Piscina Mirabilis; TB: Terme di Baia; BG: Villa del Capo; VP: Villa del Pezzolo).

As regards raw materials, the provenance of lime and carbonatic fragments is still unknown, even if it is highly reasonable to think that they were produced on site using local material availability. The Geological Map of the Bay of Naples shows that Campania Plain is completely bordered by carbonatic deposits of Mesozoic age (Figure 9.6).

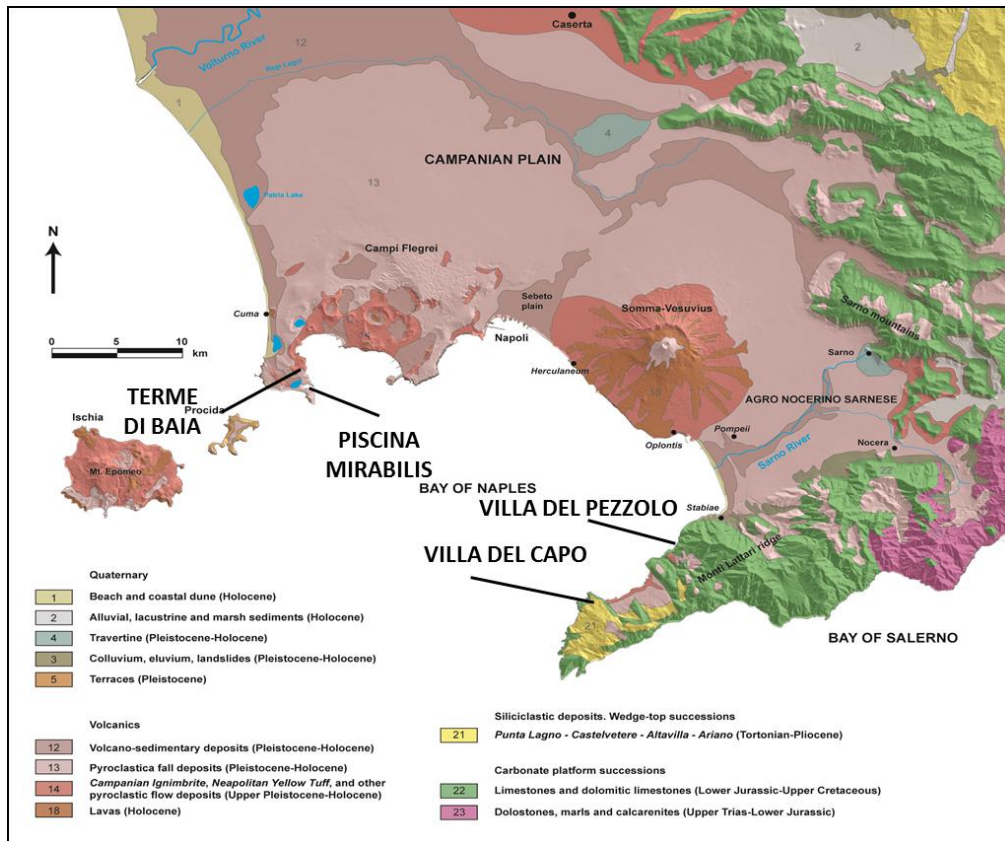


Figure 9.6: Geological sketch map of the Bay of Naples with location of investigated archaeological site (De Bonis et al., 2016).

Concerning the volcanic fragments, it was confirmed a local provenance:

- origin of volcanic aggregates retrieved in the mortar samples from *Piscina Mirabilis*, *Terme di Baia* and *Villa del Capo*, was ascribed to the Neapolitan Yellow Tuff formation, deriving from the volcanic activity of Campi Flegrei dated back to 15,000 years ago (de' Gennaro et al., 1999, 2000; Figure 9.7), due to their mineralogical-petrographic composition and, especially, to the typical mineralogical association of phillipsite > chabazite > analcime as revealed by XRPD and SEM-EDS analyses. This information was furtherly confirmed by the chemical analysis of pumice fragments that, according to TAS diagram, follow the compositional trend of the NYT (Figure 9.8).

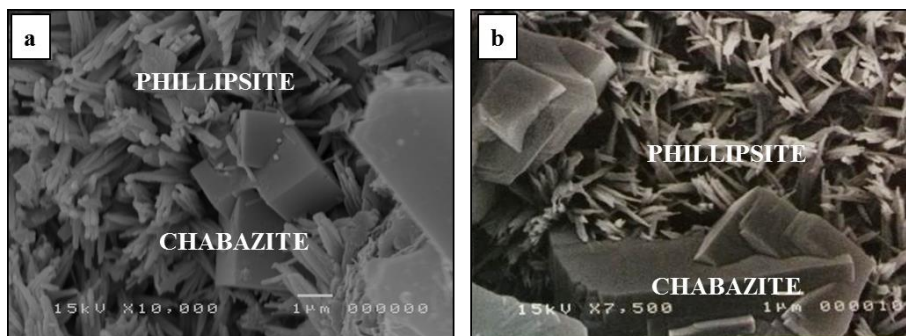


Figure 9.7: SEM images of phillipsite and chabazite in a) analyzed mortars samples; b) NYT deposit (de' Gennaro et al., 1999).

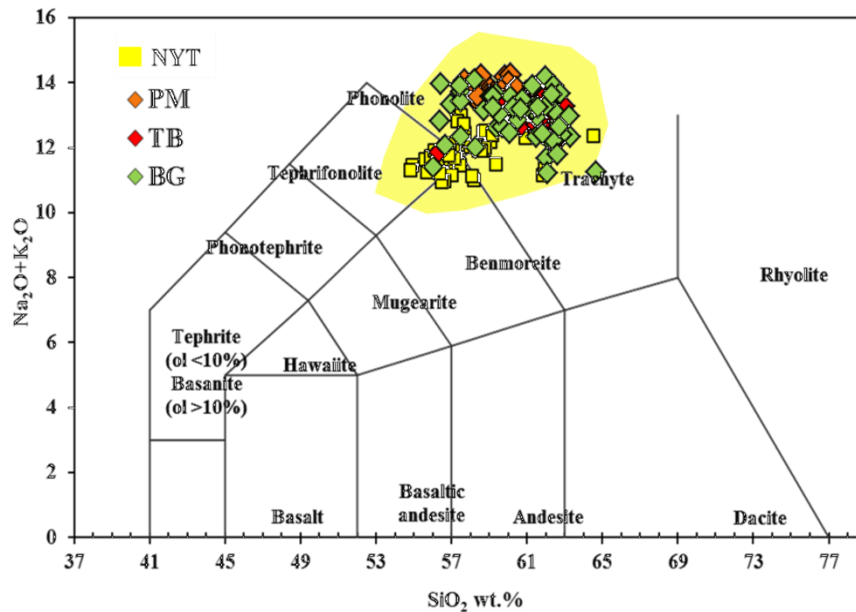


Figure 9.8: Classification of pumice fragments from investigated samples (Le Maitre et al., 1989) and geochemical comparison with NYT pumice (Morra et al., 2010)

- In some samples from *Villa del Capo* site, the presence of volcanic fragments (as aggregates), characterized by leucite-bearing scoriae and crystal fragments of garnets in the binder matrix, led to hypothesize that this particular aggregates could be associated to eruptive deposits from Somma-Vesuvius complex. In fact, EDS analyses of garnet show a solid solution between andradite (48.98 - 58.38 mol%) and grossular (25.91- 30.46 mol%), very close to that of with garnets from Somma-Vesuvius (andradite 46-70 mol% and grossularia 16-45 mol%; Scheibner et al., 2007 data on garnets from intrusive Somma-Vesuvius rocks. L. Melluso, personal communication).
- The volcanic aggregates of *Villa del Pezzolo* samples must be considered separately, according to different building phases that characterize the *Villa*.

Tuff fragments found in the first building phase are probably associated to the Campanian Ignimbrite formation, cropping out in the same geographical area (Figure 9.9a-b); this hypothesis was also confirmed by the presence of zeolitic phases (chabazite and analcime) and of glassy shards, partially devitrified and replaced by authigenic feldspar, a typical feature of the welded gray Campanian Ignimbrite lithofacies (CI-WGI - Langella et al. 2013 - Figure 9.10a-b).

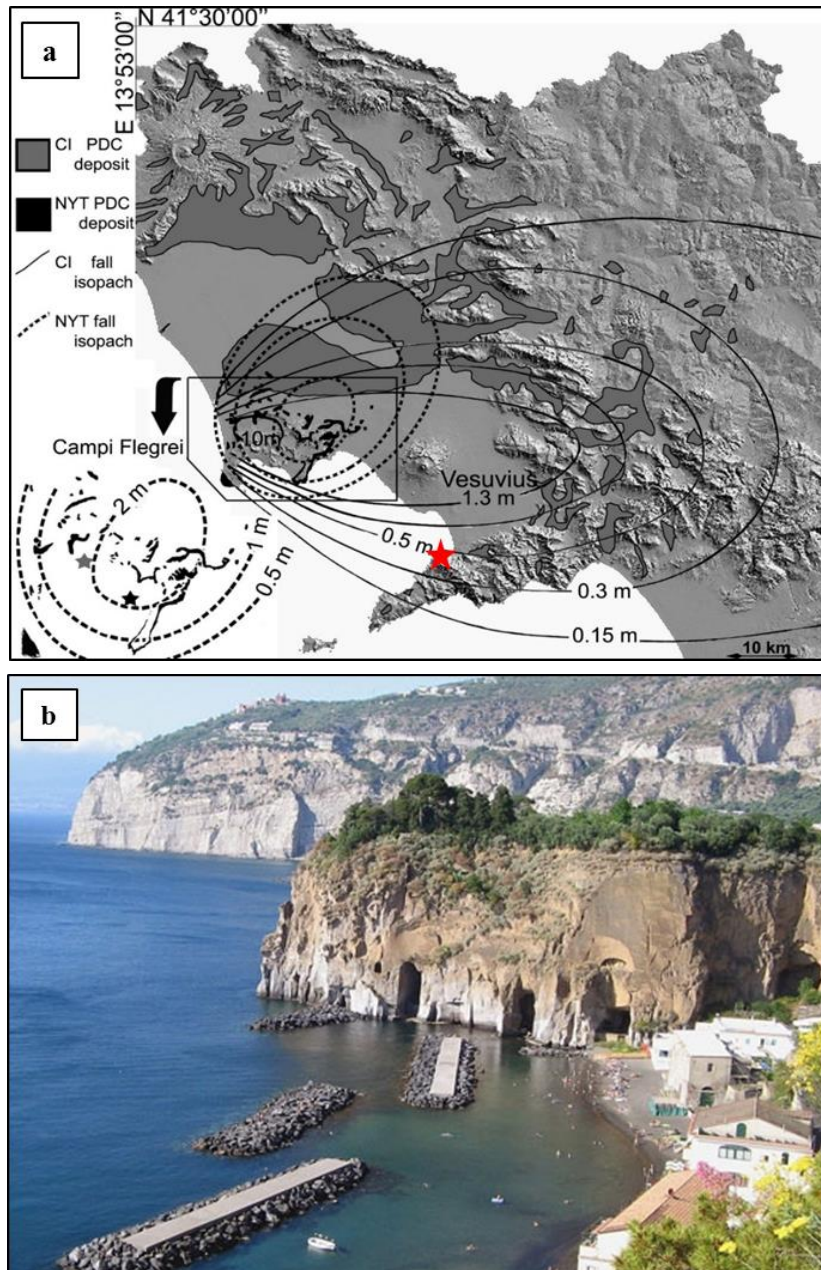


Figure 9.9: a) Distribution of Campanian Ignimbrite (CI) and Neapolitan Yellow Tuff (NYT) pyroclastic density current (PDC) deposits and fall deposits (modified after Scarpati, and Perrotta, 2012). Inset (left) shows their source area (Campi Flegrei) and presumed vent locations (black star—NYT vent; gray star—CI vent; b) CI-WGI cliff, Piano di Sorrento.

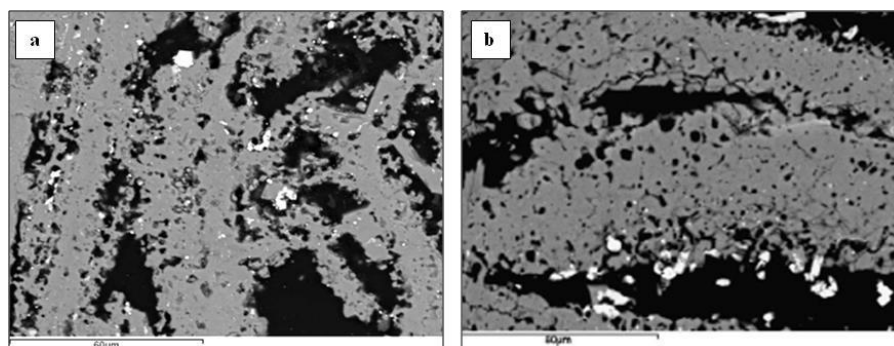


Figure 9.10: BSE-SEM images: a) glass shards coated by thin layer of micrometric feldspars in VP3 samples; b) devitrified glass shards, CI-WGI facies, from Langella et al., 2013.

Samples belonging to the second and third building phases (after A.D. 79 eruption of Mt. Somma-Vesuvius), showed differences in mineralogical composition and aggregates shapes (from angular to sub-rounded). The presence of volcanic scoriae, containing abundant leucite and garnet fragments, both in pumice and binder, allow us to consider these materials as belonging to eruptive products of Mt. Somma-Vesuvius.

SEM EDS chemical analyses, performed on pumice and garnet fragments, confirmed the use of Mt. Somma-Vesuvius materials. Chemical composition of pumice, plotted in the TAS diagram, follow the compositional trend of pumice belonging to A.D. 79 Somma-Vesuvius eruption, while chemical composition of garnets (solid solution between andradite 52.99 – 57.29 mol% and grossular 25.64- 28.65 mol%) is compatible with Somma-Vesuvius garnets (andradite 46-70 mol% and grossularia 16-45 mol%; Scheibner et al., 2007 data on garnets from intrusive Somma-Vesuvius rocks. L. Melluso, personal communication).

Furthermore, samples with sub-rounded shape of aggregates allow us hypothesizing the use of “*Durece*” (Cinque et al., 2009), the alluvial delta lithofacies formed by products of debris- and mud-flows emplaced after strong rainfalls following a large volcanic eruption.

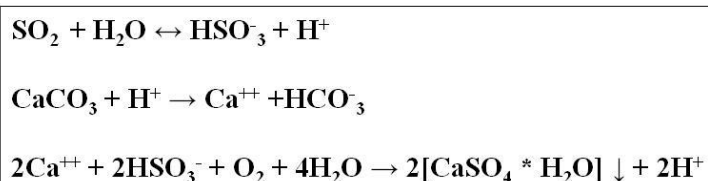
Analysis of samples of the third building phase (coating and floor mortars) showed the presence of ceramic fragments, completely lacking in the other two building phases. However, it was almost impossible to define their provenance due to the extreme differences among samples, that likely suggests a recycling of building materials. Actually, the great role played by such ceramic fragments was to confer hydraulicity to the mortars, as pointed out by the HI estimation.

As regards secondary minerogenetic processes, the composition of the cementitious binding matrix of analyzed mortars is extremely interesting. In detail, concomitant presence of gel-like C-S-A-H, calcite, gypsum, halite and tobermorite was retrieved in the *Piscina Mirabilis* mortar samples, while hydrocalumite occurs in *Villa del Capo* mortars.

- Gel C-A-S-H derived from reactions between lime and pozzolanic material (volcanic and ceramic materials):



- Usually, presence of calcite is related to the not-well reacted clasts of under-burned lime. Further, since the mortars have been stored in subaerial environment, carbonation processes from residual portlandite could have occurred.
- Gypsum, the main widespread neoformation mineral, is related to calcite sulphation as a consequence of the decrease in pH value, caused by dissolution of atmospheric SO₂ (de Gennaro et.at., 1993):



However, gypsum in *Terme di Baia* mortar samples can be also attributed to the presence of sulphurous waters. In fact, according to Di Bonito and Giammelli (1992), the archaeological site was located in proximity of hot water source with strong sulfurous rate, still used in the Middle Age (Amalfitano et al., 1990).

- The presence of halite is can be easily related to interaction of the materials with seawater or marine aerosol (Gulzar et al., 2013; Rispoli et al., 2015).
- Tobermorite, an unusual hydrothermal, calcium-silicate hydrate mineral with cation exchange properties (Jackson et al., 2017), was unexpectedly retrieved in relict voids of *Piscina Mirabilis* mortars. Formation of such mineral should not occur in conventional concretes, but its presence was found in Roman marine concretes (Stanislao et al., 2011; Jackson et al., 2013; Jackson et al., 2017), occasionally in hydrothermally altered volcanic rocks (such as basaltic tuff (palagonite) of Surtsey volcano, Iceland (Jackson et al., 2017) and as an alteration product at the cement-rock interface in toxic and nuclear waste repositories (Gaucher and Blanc, 2006; Jackson et al., 2017). Generally, tobermorite synthesizes at 120°-240°C (Jackson et al., 2017), but these temperatures are incompatible with those of lime-based materials. Moreover, it is well known that the heat of hydration in hydraulic mortars is definitely lower than ordinary cements (Collepari et al., 2009; Rispoli et al., 2015).

According to Jackson et al. (2016), it is possible to considering tobermorite crystallization in Roman concrete at lower temperatures, strictly referred to the *Campi Flegrei* deposits; in this site post-eruptive hydrolysis and dissolution of trachytic glass generated alkaline fluids from which zeolites originated.

Lime mortars mixed with zeolitized materials and seawater, a typical recipe of Roman engineers, created highly alkaline, but relatively short-lived, pozzolanic system buffered by calcium hydroxide, which produced C-A-S-H phase and tobermorite at < 95° C (Jackson et al., 2017).

Presence of tobermorite allows us identifying more precisely the mix design of *Piscina Mirabilis* mortars, suggesting the use of sea water during their production.

- Occurrence of hydrocalumite (Ca, Cl and Al hydroxide), identified in relict pores of *Villa del Capo* mortars, may be associated to the migration of Cl⁻ from sea-water saturated portlandite to the aluminium-rich sites.

Crystalline hydrocalumite microstructures have apparently sequestered Cl⁻ anions, which produce deleterious reactions, damaging expansions, and corrosion of steel reinforcements in modern Portland cement concretes (Brandon et al., 2014).

By contrast, the presence of this phase in the relict pores of ancient Roman mortars contribute to the long-term chemical durability of the mortars

Then, comparing the analyzed Roman mortars and standard hydraulic mortar (SHM) through thermal analyses it was highlighted that exists a fairy connection between the two-different kind of mortars, while mercury intrusion porosimetry (MIP) analysis revealed a difference.

The results of thermal analyses, according to with Moropoulou et al. (1995, 2005, see chapter 8 par. 8.2.1), suggest an overall high hydraulicity of ancient and modern mortars.

MIP analysis highlighted different values of both pore radii and total porosity between ancient mortars and SHM.

As far as MIP data are concerned, ancient roman mortars showed a maximum in pore radius distribution between 4 and 120 nanometres (nm) and total porosity between 38 -52 %, whereas in SHM, main distribution of pore radii ranges between 100 and 1000 nm and total porosity is around 28% (Figure 9.11). Thus, average pore size in ancient Roman mortars suggests a very little dimension of pore radii, about one order of magnitude less than modern conventional mortars.

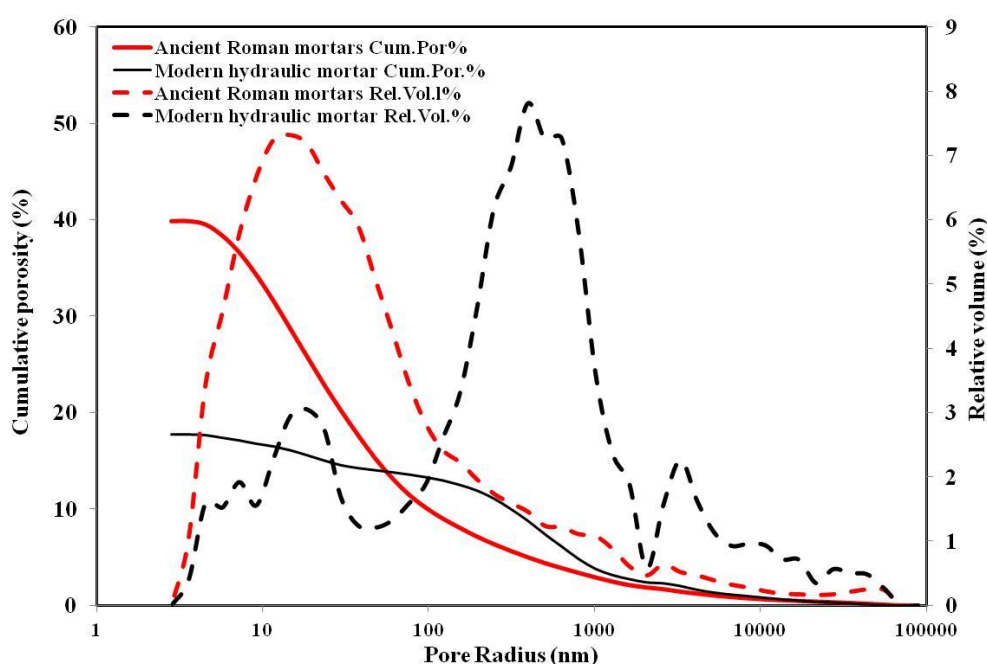


Figure 9.11: Cumulative and Relative pore size distribution in Roman mortars compared with SHM.

Results of porosity tests together with microstructural observations, suggest that in ancient Roman mortars the vesicular structure of pozzolanic materials (i.e. pumice) represents a fundamental feature of the complex pore's structure of the cementitious matrix; the products related to minerogenetic secondary processes such as: gel C-A-S-H, tobermorite and hydrocalumite settling in the porous of pozzolanic materials making mortars more resistant and ductible (Brandon et al., 2014).

So, peculiar vesicular nature pumice-bearing pozzolanic materials, led to low permeability (Brandon et al., 2014), and slowed the fluids diffusion through the mortar over time, leading to a relatively stable chemical system).

On the contrary, the higher pore size in modern mortars could account for their poor durability, thus making crucial to understand the reasons of such unusual pore structure of the ancient mortars, providing their extraordinary longevity.

Chapter 10

Conclusions

This research permitted not only a first minero-petrographic characterization of the raw materials used to produce the mortars from important archaeological sites such as: *Piscina Mirabilis*, *Terme di Baia*, *Villa del Capo* and *Villa del Pezzolo*, but also shed some light on the provenance and gave further information on the technology used for the preparation of different geomaterials used by ancient Romans.

- Building materials used in the studied archaeological sites had a local provenance, and are very well consistent with the surrounding geological setting. In fact, both pozzolanic materials such as volcanic fragments, scoriae, pumice and crystal fragments (i.e. clinopyroxene, feldspar and garnet) deriving from deposits of pyroclastic rocks of the *Campi Flegrei* district and from igneous rocks of Somma-Vesuvius complex, as inferred by the mineralogical and chemical composition.

In coating and floor mortars there is an addition of ceramic fragments that improve the pozzolanic aptitude of the mortar.

It was not possible to define their provenance due to strong differences among samples, which likely suggest a recycle of building materials.

- A common feature of the investigated mortars is their high hydraulicity, as shown by the reaction rims of pozzolanic materials (volcanic and ceramic fragments).

Such high hydraulicity is the result of an accurate selection, preparation and mixing of raw geomaterials, supplied by the geological availability of the area surrounding the different archaeological sites.

- Composition of cementitious binding matrix is definitely peculiar: it shows various products of reaction, including amorphous gel-C-A-S-H, calcite, tobermorite (*Piscina Mirabilis* samples) and hydrocalumite (*Villa del Capo* samples). In particular, these two latter secondary mineralogical products fill pore space and enhance bonding in pumice clasts (Jackson et al., 2017).

In addition, formation of tobermorite and hydrocalumite is also related to specific chemical elements (i.e. alkali cations and chloride), that in modern mortars and concretes generally produce unwanted expansion and corrosion of steel reinforcements, while in Roman mortars increase ductility and mechanical resistance (Jackson et al., 2017).

- The main difference between ancient Roman mortars and modern hydraulic mortars is related to porosity. The size distribution and cumulative volume of pores in the ancient mortars has the potential to strongly influence chemical and mechanical durability of structures, especially along beaches and intertidal environments. In these two settings, a continuous cycling of subaerial drying and moisture, and repetitive penetration of sea-water salts into the mortars fabric took place (Brandon et al., 2014). The volume and connectivity of pores in modern cementitious materials have important influences on fluids pathways through mortar and/or concrete, so comparisons of pore characteristics of ancient materials with conventional mortars may be a key factor to understand the exceptional resistance to decay of ancient Roman mortars. This research contributes to the knowledge and understanding of the technical skills achieved during Roman times. It may represent a valuable reference for the future restoration projects of investigated archaeological sites.

Moreover, this research project is a further demonstration that the manufacturing technology of the ancient Romans was really oriented to **innovation, quality, sustainability, durability** and **beauty**:

- mix-design, performance ► **quality**
- origin of pozzolanic material ► **sustainability**
- porosity of mortars ► **durability**

It is necessary to apply the teachings of the ancient Roman to our construction materials because innovation in ancient Rome is the state of the art of today.

ACKNOWLEDGMENTS

First of all, I wish to thank my supervisor, Prof. Piergiulio Cappelletti, for his invaluable guidance and for several scientific and academic opportunities that greatly improved my capacities and knowledges.

A special thank to Prof. Vincenzo Morra to have managed parts of the project, and his guide in these years.

Prof. Maurizio de' Gennaro is thanked to be our scientific father.

I want to thank also Dr. Emanuele Gotti to have hosted me at Italcementi. I thank him for the different kinds of supports and helps during my staying in Bergamo, and also to have showed me an unexpected and pleasant way to live the science.

I thank the ex “*Soprintendenza per i Beni Archeologici delle Campania*” in the persons of Dr. Tommasina Budetta and Dr. Perfrancesco Talamo that allowed and guided the sampling phase.

I'm also particularly grateful to Prof. Alessio Langella (University of Sannio) and Prof. Rocco (University of Bari) for the critical reviews of the manuscript.

Thanks are also to Prof. Leone Melluso, Prof. Luigi Franciosi, Dr Mara Cesarano, Dr. Sabatino Ciarcia, Dr. Ciro Cucciniello, Dr. Alberto de Bonis, Dr. Roberto de Gennaro, Dr. Claudia di Benedetto, Dr. Renata Esposito, Dr. Lorenzo Fedele, Dr. Chiara Germinario, Dr. Fabio Graziano, Dr. Celestino Grifa, Dr. Vincenza Guarino, Dr. Francesco Izzo, Dr. Mariano Mercurio, Dr. Silvia Minissale, Dr. Vincenzo Monetti, for the huge support during the analytical work.

Bibliography

- Adam J. P. (1988) - *L'arte di costruire presso i Romani. Materiali e tecniche (Art of Building in the Roman Civilisation. Materials and Techniques)* - Longanesi & Co., Milano, Italy.
- Amalfitano P., Comodeca G., Medri M. (1990) - *I Campi Flegrei, un itinerario archeologico.* - Marsilio, Venezia.
- Ascione A., Ciarcia S., Di Donato V., Mazzoli S., Vitale S. (2012) - *The Pliocene-Quaternary wedge-top basins of southern Italy: an expression of propagating lateral slab tear beneath the Apennines.* - Basin Res 24, p. 456–474.
- ASTM D4404 – 10: Standard Test Method for Determination of Pore Volume and Pore Volume Distribution of Soil and Rock by Mercury Intrusion Porosimetry.
- Aucelli P., Cinque A., Giordano F., Mattei G., (2015) - *A Geoarchaeological Survey of the Marine Extension of the Roman Archaeological Site Villa del Pezzolo, Vico Equense, on the Sorrento Peninsula, Italy.* - Geoarchaeology: An International Journal 00, pp. 1–9.
- Aucelli P., Cinque A., Mattei G., Pappone G. (2016) - *Historical sea level changes and effects on the coasts of Sorrento Peninsula (Gulf of Naples): New constraints from recent geoarchaeological investigations* - Palaeogeography, Palaeoclimatology, Palaeoecology 463, pp. 112–125.
- Bahlburg H. and Dobrzinski N. (2011) - *A review of the Chemical Index of Alteration (CIA) and its application to the study of Neoproterozoic glacial deposits and climate transitions* - Geological Society, London, Memoirs, Vol. 36, pp. 81-92.
- Bakolas A., Biscontin G., Contardi V., Franceschi E., Moropoulou A., Palazzi D. and Zendri, E., (1995) - *Thermoanalytical research on traditional mortars from Venice* - Thermochimica Acta 269/270, pp. 817-828.
- Barba, L., Blancas, J., Manzanilla, L. R., Ortiz, A., Barca, D., Crisci, G. M., Miriello, D., Pecci, A. (2009) - *Provenance of the limestone used in Teotihuacan (Mexico): a methodological approach* - Archaeometry, 51, pp. 525–545.
- Belfiore C.M., La Russa M.F., Mazzoleni P., Pezzino A., Viccaro M. (2009) - *Technological study of “ghiara” mortars from the historical city centre of Catania (Eastern Sicily, Italy) and petro-chemical characterisation of raw materials* - Environmental Earth Sciences, 61, pp. 995-1003.

- Bonardi G., Amore F.O., Ciampo G., de Capoa P., Miconnet P., Perrone V. (1988) - *Il Complesso Liguride Auct.: stato delle conoscenze e problemi aperti sulla sua evoluzione pre-appenninca ed i suoi rapporti con l'arco calabro.* - Mem Soc Geol Ital 41, pp.17–35.
- Bonardi G., Ciarcia S., Di Nocera S., Matano F., Sgrosso I., Torre M. (2009) - *Carta delle principali Unità Cinematiche dell'Appennino meridionale* - Nota illustrativa. Ital J Geosci 128:47–60 Scale 1:250000 1 sheet.
- Bonazza A., Ciantelli C., Sardella A., Pecchioni E., Favoni O., Natali I., Sabbioni C. (2013) - *Characterization of hydraulic mortars from archaeological complexes in Petra* - Periodico di Mineralogia (2013), Vol. 82, pp. 459-475.
- Boynton, R. S. (1966) - *Chemistry and technology of lime and limestone* - New York: John Wiley & Sons.
- Bragg W.L. (1913) - *The Diffraction of Short Electromagnetic Waves by a Crystal.* - Proceedings of the Cambridge Philosophical Society, Vol.17, pp. 43-57.
- Brancaccio L., Cinque A., Romano P., Roskopf C., Russo F., Santo A., Santangelo N. (1991) *Geomorphology and neotectonic evolution of a sector of the Tyrrhenian flank of the Southern Apennines, (Region of Naples, Italy).* - Zeit. Geo morph., N.F., Suppl. Bd. 82, pp. 47–58.
- Brandon C., Hohlfelder R. L. and Oleson J. P. (2008) - *The Concrete Construction of the Roman Harbours of Baiae and Portus Iulius: The ROMACONS 2006 Field Season.* - International Journal of Nautical Archaeology 37, pp. 374–92.
- Brando C.J., Hohlfelder R.L., Jackson M.D., Oleson J.P. (2013) - *Building for Eternity: The History and Technology of Roman Concrete Engineering in the Sea* - Oxford Books.
- Budetta T., De Martino R., Franchino R., Frettoloso C. (2013) - *The System of Environmental Networks for the use of Archaeological Sites in Areas of Natural Beauty* - Journal of sustainable architecture and civil engineering, pp. 4-8.
- Callebaut, K., Elsen, J., Van Balen, K. and Viaene, W. (2001) - *19th century hydraulic restoration mortars in the Saint-Michael' church (Leuven, Belgium): natural hydraulic lime or cement?* - Cement and Concrete Research 31(3), pp. 397-403.
- Carminati E., Lustrino M., Doglioni C. (2012) - *Geodynamic evolution of the central and western Mediterranean: tectonics vs. igneous petrology constraints* - Tectonophysics 579, pp. 173–192.

Carannante G., Ruberti D., Sirna M. (2000) - *Upper Cretaceous ramp limestones from the Sorrento Peninsula (southern Apennines, Italy): micro-and macrofossil associations and their significance in the depositional sequences.* - Sediment. Geol. 132 (1), pp. 89–123.

Ciarcia S., Mazzoli S., Vitale S., Zattin M. (2012) - *On the tectonic evolution of the Ligurian accretionary complex in southern Italy.* - Geol Soc Am Bull 124, pp. 463–483.

Cinque A., Robustelli G. (2009) - *Alluvial and Coastal Hazards Caused by Long-range Effects of Plinian Eruptions: The Case of the Lattari Mts. After the A.D. 79 eruption of Vesuvius.* - Geological Society, London, Special Publications, pp. 155–171.

Colleparidi M. (2003) - *La lezione dei romani: durabilità e sostenibilità delle opere architettoniche e strutturali* - Proceedings of III Convegno AIMAT “Restauro e Conservazione dei Beni Culturali: Materiali e Tecniche”, 3-4 October 2003, Cassino, Italy.

Colleparidi M., Colleparidi S., Troli R. (2009) - *Il nuovo calcestruzzo* - Enco S.r.l., Ponzano Veneto, Grafiche Tintoretto, 5th Ed., Villorba, Treviso.

Conticelli S., Melluso L., Perini G., Avanzinelli R., Boari E. (2004) - *Petrologic, Geochemical and Isotopic Characteristics of Shoshonitic to Potassic and Ultrapotassic Alkalic Magmatism in Central-Southern Italy: Inferences on its Genesis and on the Nature of its Mantle Source* - Periodico di Mineralogia 73, pp. 135-164.

Cosentino D., Cipollari P., Marsili P., Scrocca D. (2010) - *Geology of the central Apennines: a regional review. The geology of Italy: tectonics and life along plate margins.* - In: Beltrando M, Peccerillo A, Mattei M, Conticelli S, Doglioni C (eds). Journal of the Virtual Explorer, 36.

Cinque A., Robustelli G., Russo M. (2000) - *The consequences of pyroclastic fallout on the dynamics of mountain catchments: Geomorphic events in the Rivo d'Arco basin (Sorrento Peninsula, Italy) after the Plinian eruption of Vesuvius in 79 AD.* - Geografia Fisica e Dinamica Quaternaria, 23, pp. 117–129.

Cinque A., Robustelli G. (2009) - *Alluvial and coastal hazards caused by long-range effects of Plinian eruptions: The case of the Lattari Mts. after the A.D. 79. Eruption of Vesuvius.* - Geological Society, London, Special Publications, pp. 155–171.

Cullity B.D. (1978) - *Element of X-ray diffraction, Second edition* - Addison-Wesley publishing company, Inc.

D'Argenio B., Barattolo F., Budillon F., Cesarano M., Donadio C., Pappone G., Pugliese A. Putignano M.L., Aucelli P.P.C., Russo Ermolli E., Sgroso A., Terlizzi F., Ferrari G., Lamagna R., (2012) - *Carta Geologica della Regione Campania, Note Illustrative della Carta Geologica*

alla scala 1: 10.000, Foglio 484 Isola di Capri, Regione Campania - Assessorato Difesa del Suolo.

De Bonis A., Febbraro S., Germinario C., Giampaola D., Grifa C., Guarino V., Langella A., Morra V. (2016) - *Distinctive Volcanic Material for the Production of Campana A Ware: The Workshop Area of Neapolis at the Duomo Metro Station in Naples, Italy* - *Geoarchaeology* 31, pp. 437-466, doi: 10.1002/gea.2157.

De Feo G. and Napoli R. M. A. (2007) - Historical development of the Augustan aqueduct in Southern Italy: twenty centuries of works from Serino to Naples. *Water Sci. Technol. Water Supply* 7(1), pp. 131–138.

De Feo G., De Gisi S., Malvano C., De Biase O. (2010) - *The greatest water reservoirs in the ancient Roman world and the “Piscina Mirabilis” in Misenum.* - IWA Publishing 2010 *Water Science & Technology: Water Supply-WSTWS*, Department of Civil Engineering, University of Salerno.

de' Gennaro M., Colella C., Pansini M. (1993) – *Hydrothermal conversion of trachytic glass into zeolite. II Reactions with high-salinity waters* - *Neues Jahrbuch Far Mineralogie-Monatshefte*, 3, pp. 97-110.

de' Gennaro M., Incoronato A., Mastrolorenzo G. et al. (1999) – *Depositional mechanisms and alteration processes in different types of pyroclastic deposits from Campi Flegrei volcanic field (Southern Italy)* - *Journal of Volcanology and Geothermal Research*, 91, pp. 303-320.

de' Gennaro M., Cappelletti P., Langella A., Perrotta A., Scarpati C. (2000) - *Genesis of zeolites in the neapolitan yellow tuff: geological, volcanological and mineralogical evidence* - *Contribution to Mineralogy and Petrology*, Vol. 139, pp. 17-35.

De Luca R., Miriello D., Pecci A., Dominguez-Bella S., Bernal-Casasola D., Cottica D., Bloise A., Crisci G.M. (2015) - *Archaeometric Study of Mortars from the Garum Shop at Pompeii, Campania, Italy* – *Geoarchaeology*, pp. 330–351.

De Vita P., Napolitano E., Godt J.W, Baum R. L, (2012) - *Deterministic Estimation of Hydrological Thresholds for Shallow Landslide Initiation and Slope Stability Models: Case Study from the Somma-Vesuvius Area of Southern Italy* - *Landslides*, pp.1-16.

De Vivo B., Rolandi G., Gans P. B., Calvert A., Bohrsen W. A., Spera F. J., Belkin, H. E. (2001) - *New Constraints on the Pyroclastic Eruptive History of the Campanian Volcanic Plain (Italy)* - *Mineralogy and Petrology*, 73, pp. 47–65.

- Deino A. L., Orsi G., de Vita S., Piochi M. (2004) - *The age of the Neapolitan Yellow Tuff caldera-forming Eruption (Campi Flegrei caldera - Italy) assessed by $^{40}\text{Ar}/^{39}\text{Ar}$ dating method* - Journal of Volcanology and Geothermal Research 133, pp. 157-170.
- Di Bonito R., Giammelli R. (1992) - *Le Terme Dei Campi Flegrei* – Milano, Roma 1992.
- Hodge A. T. (2002) - *Roman Aqueducts & Water Supply*, 2nd edition. Gerald Duckworth & Co. Ltd, London, ISBN 0715631713.
- Di Maio R., Fabbrocino S., Forte G., Piegari E. (2014) - *A three-dimensional hydrogeological–geophysical model of a multi-layered aquifer in the coastal alluvial plain of Sarno River (southern Italy)* - Hydrogeology Journal, pp. 691–703.
- Duzgoren-Aydin N.S., Aydin A. (2003) - *Chemical heterogeneities of weathered igneous profiles: implications for chemical indices* - Environ. Eng. Geosci. 9, pp. 363–377.
- Elsen J. (2006) - *Microscopy of historic mortars - a review* - Cement and Concrete Research 36, pp. 1416–1424.
- Faccenna C., Davy P., Brun J.P., Funiciello R., Giardini D., Mattei M., Nalpas T. (1996) - *The dynamics of back-arc extension: an experimental approach to the opening of the Tyrrhenian Sea.* - Geophys J Int 126, pp. 781–795.
- Faccenna C., Becker T.W., Lucente F.P., Jolivet L., Rossetti F. (2001) - *History of subduction and back-arc extension in the Central Mediterranean.* - Geophys J Int 145, pp. 809–820.
- Fedele L., Scarpati C., Lanphere M., Melluso L., Morra V., Perrotta A., Ricci G. (2008) - *The Breccia Museo Formation, Campi Flegrei, Southern Italy: Geochronology, Chemostratigraphy and Relationship with the Campanian Ignimbrite Eruption* - Bulletin of Volcanology 70, pp. 1189-1219.
- Grifa C., De Bonis A., Langella A., Mercurio M., Soricelli G., Morra V. (2013) - *A Late Roman Ceramic Production from Pompeii.* - JASc, 40, pp. 810-826.
- Fedele L., Insinga D.D., Calvert A.T., Morra V., Perrotta A., Scarpati C. (2011) - *$^{40}\text{Ar}/^{39}\text{Ar}$ dating of tuff vents in the Campi Flegrei caldera (southern Italy): toward a new chronostratigraphic reconstruction of the Holocene volcanic activity* - Bulletin of Volcanology, Vol. 73 - 9, pp 1323–1336.
- Fernández R., Nebreda B., Vigil de la Villa R., García R., Frías M. (2010) - *Mineralogical and chemical evolution of hydrated phases in the pozzolanic reaction of calcined paper sludge* - Cement & Concrete Composites, 32, pp. 775-782.

Franzini M., Leoni L., Saitta M., (1975) - *Revisione di una metodologia analitica per fluorescenza: X. Basata sulla correzione completa degli effetti di matrice* - Rendiconti della Società Italiana di Mineralogia e Petrologia, 31, pp. 365-378.

Gaucher E.C, Blanc P. (2006) - *Cement/clay interactions – a review: experiments, natural analogues, and modeling* -Waste Manage, pp. 776–788

Gotti E., Oleson J.P., Bottalico L., Brandon C., Cucitore R., and Hohlfelder R.L. (2008) - *A Comparison of the Chemical and Engineering Characteristics of Ancient Roman Hydraulic Concrete with a Modern Reproduction of Vitruvian Hydraulic Concrete* - Archeometry, 50:4, pp. 576-590.

Howarth R.J. (1998) - *Improved estimators of uncertainty in proportions, point-counting, and pass-fail test results* - American Journal of Science, Vol. 298, pp. 594-607.

Iannace A., Merola D., Perrone V., Amato A., Cinque A., Santacroce R., Sbrana A., Sulpizio R., Budillon F., Conforti A., D'Argenio B. (2015) - *Note Illustrative della Carta Geologica d'Italia alla scala 1:50.000 fogli 466–485 Sorrento-Termini*.

Izzo F., Grifa. C, Mercurio M., Langella A. (2015) - *Simultaneous Thermal Analyses and Fourier Transform Infrared Spectroscopy of ancient mortars from Arch of Trajan and Roman Theatre (Benevento, Italy)* - Proceedings of the 1st International Conference on Metrology for Archaeology. Benevento, pp. 240–245.

Izzo F., Arizzi A., Cappelletti P., Cultrone G., De Bonis A., Germinario C., Graziano S.F., Grifa C., Guarino V., Mercurio M., Morra V., Langella A. (2016) - *The art of building in the Roman period (89 B.C. – 79 A.D.): Mortars, plasters and mosaic floors from ancient Stabiae (Naples, Italy)* - Construction and Building Materials 117, pp. 129–143.

Jackson M. D., Kosso C., Marra F., Hay R. (2006) - *Geological Basis of Vitruvius' Empirical Observations of Materials Characteristics of Rock Utilized in Roman Masonry* - Proceedings of the Second International Congress of Construction History Queen's College, University of Cambridge, 29 March – 2 April 2006, edited by Dunkeld M., Campbell J., Louw H., Tutton M., Addis B. and Thorne R., London: The Construction History Society, 2, pp. 1685-1702.

Jackson M. D. and Marra F. (2006) - *Roman stone masonry: Volcanic foundations of the ancient city* - American Journal of Archaeology, 110, pp. 403-436.

Jackson M. D., Deocampo D., Marra F. and Scheetz B. (2010) - *Mid-Pleistocene Pozzolan Ash in Ancient Roman Concretes* - Geoarchaeology: An International Journal, 25,1, pp. 36-74.

Jackson M.D., Chae S.R., Mulcahy S.R., Meral C., Taylor R., Li, P., Emwas A., Moon J., Yoon S., Vola G., Wenk H., Monteiro P. (2013) - *Unlocking the secrets of Al-tobermorite in Roman seawater concrete - Mineralogical Society of America -Volume 98*, pp. 1669–1687.

Jackson M. D., Gudmundsson M. T., Bach W., Cappelletti P., Coleman N. J., Ivarsson M., Jónasson K., Jørgensen S. L., Marteinsson V., Mc Phie J., Moore J. G, Nielson D., Rhodes J. M., . Rispoli C, Schiffman P., Stefánsson A., Türke, Vanorio T., Weisenberger T. B., White J. D. L, Zierenberg R., and Zimanowski B. (2015) – *Time A -lapse characterization of hydrothermal seawater and microbial interactions with basaltic tephra at Surtsey Volcano - Scientific Drilling*, 20, pp. 51–58.

Jackson M.D., Mulcahy S.R., Chen H., Li Y., Li Q., Cappelletti P., Wenk H.R. (2017) – *Phillipsite and Al-Tobermorite produced by cementitious water-rock reaction in Roman marine concrete – American Mineralogist (in press)*.

Jolivet L, Faccenna C, Goffé B, Burov E, Agard P (2003) - *Subduction tectonics and exhumation of High Pressure metamorphic rocks in the Mediterranean orogens.- Am J Sci* 30, pp. 353–409.

Le Maitre R.W., Bateman P., Dudek A., Keller J., Lameyre J., Le Bas M.J., Sabine P.A., Schmid R., Sorensen H., Streckeisen A., Woolley A.R., Zanettin B.(1989) - *A Classification of Igneous Rocks and Glossary of Terms: Recommendations of the International Union of Geological Sciences Subcommittee - Systematics of Igneous Rocks*. Blackwell, Oxford.

Laforgia E., Boenzi G., Amato L., Di Vito M. A., Fattore L., Stanzione M., Viglio F. (2009) - *The Vesuvian “Pomici di Avellino” Eruption and Early Bronze Age Settlement in the Middle Clanis Valley - Méditerranée* 112, pp. 101-107.

Langella A., Bish D.L., Cappelletti P., Cerri G., Colella A., de Gennaro R., Graziano S.F., Perrotta A., Scarpati C. and de Gennaro M., (2013) - *New insights into the mineralogical facies distribution of Campanian Ignimbrite, a relevant Italian industrial material.- Applied Clay Science*, pp. 72, pp. 55-73.

Lendering J. (2008) - *Constantinople (Istanbul): Basilica Cistern. Istanbul Turkey - <http://www.livius.org> (accessed 22 September 2009)*.

Leoni L., Saitta M., (1976) - *X-ray fluorescence analysis of 29 trace elements in rock and mineral standards - Rend. Soc. It. Miner. Petrol.* 32, pp. 497-510.

Ling R., 1979, *The “stanza di Venere” at Baia*, in *Archaeologia* 106, pp. 77-140.

- Locock A.J. (2008) - *An Excel spreadsheet to recast analyses of garnet into end-member components, and a synopsis of the crystal chemistry of natural silicate garnets* - Computers and Geosciences 34, pp. 1769-1780.
- Maniatis Y. e Tite M.S. (1981) - *Technological examination of Neolithic-Bronze Age pottery from central and southeast Europe and from the Near East* - Journal of Archaeological Science, 8, pp. 59-76.
- Malinverno A., Ryan W.B.F. (1986) - *Extension in the Tyrrhenian Sea and shortening in the Apennines as a result of arc migration driven by sinking of the lithosphere.* - Tectonics 5, pp.227–243.
- Marturano A., Aiello G., Barra D., Fedele L., Grifa C., Morra V., Berg R., Varone A. (2009) - *Evidence for Holocenic Uplift at Somma-Vesuvius* - Journal of Volcanology and Geothermal Research 184, pp. 451-461.
- Massazza F. (2001) - Pozzolana and pozzolanic cements - in: Hewlett P. C. (ed), *Lea's chemistry of cement and concrete*, 10, pp. 471-602.
- Mazzoli S., Ascione A., Buscher J.T., Pignalosa A., Valente E., Zattin M. (2014) - *Low-angle normal faulting and focused exhumation associated with late Pliocene change in tectonic style in the southern Apennines (Italy).* - Tectonics 33, pp. 1802–1818.
- Mazzoli S., D'Errico M., Aldega L., Corrado S., Invernizzi C., Shiner P., Zattin M. (2008) - *Tectonic burial and 'young' (< 10 Ma) exhumation in the southern Apennines fold and thrust belt (Italy).* - Geolog. 36, pp. 243–246.
- Melluso L., de' Gennaro R., Fedele L., Franciosi L., Morra V. (2012) - *Evidence of Crystallization in Residual, Cl-F-rich, Agpaitic, Trachyphonolitic Magmas and Primitive Mg-rich Basalt-Trachyphonolite Interaction in the Lava Domes of the Phlegrean Fields (Italy)* - Geological Magazine Volume 149, 3, pp. 532-550.
- Mehta P. K., Monteiro, P.J. (2006) - *Concrete: Microstructure, Properties and Materials* - 3rd ed. London: McGraw-Hill.
- Middendorf B. and Knöfel, D. (1998) - *Gypsum and lime mortars of historic German brick buildings: analytical results as well as requirements for adapted restoration material* - Conservation of Historic Brick Structures: Case Studies and Reports of Research', Editors: N.S. Baer *et al.* (Donhead Publishing Ltd, England, ISBN 1 873394 34 9).
- Middendorf B., Hughes J. J., Callebaut K., Baronio G. and Papayianni I. (2005) - *Investigative methods for the characterisation of historic mortars - Part 1: Mineralogical characterization*, Materials and Structures 38, RILEM, pp. 761-769.

Mingazzini, (1946) - *Forma Italiae: Latium et Campania, Surrentum* - Vol. 2, ed. De Luca.

Miriello D., Barca D., Bloise A., Ciarallo A., Crisci G. M., De Rose F., Gattuso C., Gazineo F., and La Russa M. F., 2010 - *Characterisation of archaeological mortars from Pompeii (Campania, Italy) and identification of construction phases by compositional data analysis* - Journal of Archaeological Science, 37, pp. 2207–2223.

Moore D.M. and Reynolds R.C.JR (1997) - *X-ray diffraction and the identification and analysis of clay minerals. Second edition* - Oxford University Press, Oxford and New York, pp. 378.

Moropoulou A., Bakolas A., Michailidis P., Chronopoulos M., Spanos C.. (1995) - *Traditional technologies in Crete providing mortars with effective mechanical properties* - Structural Studies of Historical Buildings Traditional Technologies 1 (50), pp. 151 – 161.

Moropoulou A., Bakolas A., Moundoulas P. and Camak A.S., (1999) - *Compatible restoration mortars for Hagia Sophia earthquake protection* - Earthquake Resistant Engineering Structures, Compatible Restoration, Ch. 78, pp. 522-531.

Moropoulou A., Cakmak A., Labropoulos K. C., Van Grieken R., Torfs K. (2004) - *Accelerated microstructural evolution of a calcium-silicate-hydrate (C-S-H) phase in pozzolanic paster using fine siliceous sources: Comparison with historic pozzolanic mortars* - Cement and Concrete research, 34, pp. 1-6.

Moropoulou A., Bakolas A., Anagnostopoulou S. (2005) - *Composite materials in ancient structures* - Cement & Concrete Composites, 27, pp. 295-300.

Morra V., Calcaterra D., Cappelletti P., Colella A., Fedele L, de' Gennaro R., Langella A., Mercurio M., de' Gennaro M. (2010) - *Urban Geology: Relationships between Geological Setting and Architectural Heritage of the Neapolitan Area, in The Geology of Italy: Tectonics and Life along Plate Margins* - M. Beltrando, A. Peccerillo, M. Mattei, S. Conticelli, C. Doglioni (eds.), Journal of the Virtual Explorer, Electronic Edition, 36, 27 (<http://virtualexplorer.com.au/journal/2010/36>).

Morra V., De Bonis A., Grifa C., Langella A., Cavassa L., Piovesan R. (2013) - *Minero-Petrographic Study of Cooking Ware and Pompeian Red Ware (Rosso Pompeiano) from Cuma (Southern Italy)*. - Archaeometry, 55, pp. 852-879.

Mostardini F, Merlini S. (1986) - *Appennino centro-meridionale: sezioni geologiche e proposta di modello strutturale* - Mem Soc Geol Ital 3, pp. 177–202.

Mottana A., 1988. *Fondamenti di mineralogia geologica*. Zanichelli, Bologna.

- Nesbitt H.W., Young G.M. (1982) - *Early Proterozoic climates and plate motions inferred from major element chemistry of lutites* - Nature 299, pp. 715–717.
- Ng C.W.W., Guan P., Shang Y.J. (2001) - *Weathering mechanisms and indices of igneous rocks of Hong Kong* - Quaterly Journal of Engineering Geology and Hydrogeology, 34, pp. 133-151.
- Ohta T., Arai H. (2007) - *Statistical empirical index of chemical weathering in igneous rocks: A new tool for evaluating the degree of weathering*- Chemical Geology 240, pp. 280–297.
- Pappone G., Casciello E., Cesarano M., D'Argenio B., Conforti A., Russo F., Esposito E., Porfido S., Perriello Z.S., Violante C., Conforti A., Sacchi M. (2010) - *Note Illustrative della Carta Geologica d'Italia alla scala 1: 50000, Foglio 467 Salerno, Regione Campania* - Assessorato Difesa del Suolo.
- Parker A. (1970) - *An index of weathering for silicate rocks* - Geol. Mag. 107, pp. 501–504.
- Passchier C., Schram W., D. (2005) - *Aqua Augusta. Serino (Italy)*. - www.cs.uu.nl/wilke/aquasite/index.html (accessed 22 September 2009).
- Picon M., Olcese G (1993). - *Per una classificazione in laboratorio delle ceramiche comuni. In: Ceramica romana e archeometria: lo stato degli studi. Atti delle giornate di studio (Castello di Montegufoni, Firenze)* - Quaderni del Dipartimento di Archeologia e Storia delle Arti, Sezione archeologica – Università di Siena, pp. 105-114.
- Pouchou J.L., Pichoir F., (1988) - *A simplified version of the PAP model for matrix corrections in EPMA* - Newbury DE (ed) Microbeam analysis. San Francisco Press, San Francisco, pp. 313-318.
- Prugnola, F. (2003) - *Il Cisternone. Formia (The “Cisternone”, Formia, Italy)*. - <http://www.comune.formia.it> (accessed 22 September 2009).
- Rispoli C., Graziano S.F., De Bonis A., Cappelletti P., Esposito R., Talamo P., (2015) - *Piscina Mirabilis: characterization of geomaterials* - Proceedings of the 1st International Conference on Metrology for Archaeology. Benevento, pp. 266–270.
- Ritter and Drake, (1945) - *Pressure porosimeter and determination of complete macropore-size distributions. Pressure porosimeter and determination of complete macropore-size distributions* - Ind. Eng. Chem. Anal., pp 787–791
- Rosenbaum G., Lister G.S. (2004) - *Formation of the arcuate orogenic belts in the western Mediterranean region*. - Geol Soc Am Special Paper 383, pp. 41–56.

Roure F., Casero P., Addoum B. (2012) - *Alpine inversion of the North African margin and delamination of its continental lithosphere.* - Tectonics. doi:[10.1029/2011TC00298](https://doi.org/10.1029/2011TC00298).

Russo M., (2006) - *La villa romana del Capo di Sorrento con i fondi agricoli acquistati dal Comune, Sorrento* - "Oebalus" I, pp. 299-309.

Sánchez-Moral S., Luque L., Cañaveras J. C., Soler V., Garcia-Guinea J., Aparicio A. (2005) - *Lime pozzolana mortars in Roman catacombs: composition, structures and restoration* - Cement and Concrete Research, 35, pp. 1555-1565.

Santacroce R., Cioni R., Marianelli P., Sbrana A., Sulpizio R., Zanchetta G., Donahue D. J., Joron J. L. (2008) - *Age and Whole Rock-Glass Compositions of Proximal Pyroclastics from the Major Explosive Eruptions of Somma-Vesuvius: a Review as a Tool for Distal Tephrostratigraphy.* - Journal of Volcanology and Geothermal Research 177, pp. 1-18.

Scarpati C. and Perrotta A. (2012) – *Erosional characteristics and behavior of large pyroclastic density currents* - Geology, V. 40, n° 11, pp. 1035-1038.

Scheibner B., Wörner G., Civetta L., Stosch H.G., Simon K., Kronz A. (2007) - *Rare earth element fractionation in magmatic Ca-rich garnets* - Contrib Mineral Petrol 154, pp.55-74.

Senatore, M., Ciarallo, A., and Stanley, J. (2014) - *Pompeii damaged by volcanoclastic debris flows triggered centuries prior to the 79 A.D. Vesuvius eruption* - Geoarchaeology.

Shiner P., Beccacini A., Mazzoli S. (2004) - *Thin-skinned versus thick-skinned structural models for Apulian Carbonate Reservoirs: constraints from the Val D'Agri Fields.* - Mar Pet Geol 21, pp. 805–827.

Sigurdsson H., Cashdollar S., Sparks S.R.J. (1982) - *The eruption of Vesuvius in AD 79: reconstruction from historical and volcanological evidence.* - Am. J. Archaeol. 1982, pp.39–51.

Silva D. A., Wenk H. R., Monteiro P. J. M. (2005) - *Comparative investigation of mortars from Roman Colosseum and cistern* - Thermochemica Acta, 438, pp. 35-40.

Stanislao C., Rispoli C., Vola G., Cappelletti P., Morra V., de Gennaro M. (2011) - *Contribution to the knowledge of ancient Roman seawater concretes: Phlegrean pozzolan adopted in the construction of the harbour at Soli-Pompeipolis (Mersin, Turkey)* - Periodico di Mineralogia vol. 80, pp. 471-488.

Taylor, H. F. W. (1997) - *Cement chemistry* - 2nd ed. London: Thomas Telford, pp. 113–128

Tian J., Guo Q., (2014) - *Thermal Decomposition of Hydrocalumite over a Temperature Range of 400–1500°C and Its Structure Reconstruction in Water* - Journal of Chemistry. Volume 2014, pp. 1-8.

Tite M.S., Kilikoglou V., Vekinis G. (2001) - *Review article: strength, toughness and thermal shock resistance of ancient ceramics, and their influence on technological choice* - Archaeometry, 43 (3), pp. 301-324.

Tolle-Kastenbein R. (2005) - *Archeologia dell'acqua (water archaeology)*. - Longanesi-Collana: Biblioteca di Archeologia.

UNI-EN 11305:2009 - *Beni culturali: Malte storiche, linee guida per la caratterizzazione mineralogico petrografica, fisica e chimica delle malte*.

UNI EN 196-1: 2005 - *Methods of testing cement - Part 1: Determination of strength*.

UNI EN 459-1:2010 - *Building lime - Part 1: Definitions, specifications and conformity criteria*.

Vignaroli G., Faccenna C., Rossetti F., Jolivet L. (2009) - *Insights from the Apennines metamorphic complexes, their bearing on the kinematics evolution of the Orogen*. - In: Van Hinsbergen DJJ, Edwards MA, Govers R (eds) *Geodynamics of collision and collapse at the Africa–Arabia–Eurasia subduction zone*. Geological Society London Special Publications, vol 311, pp. 235–256.

Vitale S, Ciarcia S (2013) - *Tectono-stratigraphic and kinematic evolution of the southern Apennines/Calabria-Peloritani Terrane system (Italy)* - Tectonophysics 583, pp. 164–182.

Vitale S, Ciarcia S, Tramparulo FDA (2013) - *Deformation and stratigraphic evolution of the Ligurian Accretionary Complex in the southern Apennines (Italy)*. - J Geodyn 66, pp.120–133.

Vitale S., Tramparulo F.D.A., Ciarcia S., Amore O., Prinzi E.P., Laiena F. (2016) - *The northward tectonic transport in the southern Apennines: examples from the Capri Island and western Sorrento Peninsula (Italy)* - Int J Earth Sci (Geol Rundsch). DOI 10.1007/s00531-016-1300-9.

Washburn E. W. (1921) - *The Dynamics of Capillary Flow* - Phys. Rev. 17, pp. 273.

Zanchetta G. - Sulpizio R. - Di Vito M. A. (2004) - *The Role of Volcanic Activity and Climate in Alluvial Fan Growth at Volcanic Areas: an Example from Southern Campania (Italy)* – Sedimentary Geology 168, pp. 249-260.

Zawawi R. (2006) - *Artificial hydraulic lime mortar obtained by calcining limestone and siliceous waste materials* - Jurnal of Advances in applied ceramics. Vol. 10 - 4, pp. 175-178.